Cavitation Nucleation and Dynamics in Biological Systems

by

Chunghwan Kim

A Dissertation Presented in Partial Fulfillment
of the Requirements for the Degree
Doctor of Philosophy

Approved October 2023 by the
Graduate Supervisory Committee:

Wonmo Kang, Chair
Abhinav Acharya
Jagannathan Rajagopalan
Jay Oswald
Jeonglae Kim

ARIZONA STATE UNIVERSITY

December 2023

ABSTRACT

Cavitation bubbles in the human body, when subjected to rapid mechanical load, are being increasingly considered as a possible brain injury mechanism during contact sports and military operations. Due to this great importance, it is essential to fundamentally understand the cavitation bubble dynamics in varying biological systems. In this dissertation, experimental and theoretical characterization of cavitation dynamics in soft matters from tissue simulant soft gels (e.g., agar, agarose, and gelatin) to actual live cells are performed.

First, cavitation nucleation and bubble growth in different types of tissue simulants are studied under translation impact. The critical acceleration that corresponds to onset of cavitation bubble burst is measured in the soft gels and individual gel types indicate significantly different trends in the critical acceleration and bubble shape (e.g., A gel-specific sphere-to-saucer transition) with increasing gel stiffness. Possible underlying mechanisms of the experimental observations are provided in the concepts of a damaged zone and crack propagation. This study sheds light on potential links between traumatic brain injuries and cavitation bubbles induced by translational acceleration, the overlooked mechanism in the literature.

Second, a drop-tower-based repetitive impact tester is newly designed to mimic biological systems under a wide range of impact conditions including high strain rate as well as repeated loadings. Theoretical approach based on a two-degree-of-freedom mass-spring-damper model simulates the transient dynamic response of the system with experimental validations. As one of main implications, a novel noncontact detecting method is developed to capture initial cavitation nucleation during successive drop events.

This study also observes impact characteristics dependent cavitation bubble responses, which have not been characterized by other methods (e.g., laser or ultrasound induced cavitation rheology).

Finally, although significant efforts have been made in the dynamic response of tissue simulants, there is a huge knowledge gap between the soft gels and actual live cells due to the lack of the experimental capability and of knowledge for complicated cell responses. Newly designed *in vitro* experimental setup and systematic characterization of specific cell types, i.e., Hs27 fibroblasts, enable a testing of spatio-temporal responses of cells under mechanical impact by controlling their static and dynamic behaviors.

ACKNOLEDGEMENTS

Finally, I would not successfully finish my graduate studies without the endless support and love from my parents. I wish to express my greatest gratitude to my parents for their unwavering support, kind, and encouragement, helping me successfully overcome the challenges during a Ph.D. degree.

TABLE OF CONTENTS

LIST OF FIGURES

LIST OF TABLES

1.   INTRODUCTION

1.1   Mechanically Induced Cavitation in Biological Systems

When a homogeneous liquid is subjected to a transient pressure drop below its saturated vapor pressure at a given temperature, small vapor cavities, referred to as *Cavitation* [1], can be formed inside the liquid media. Generally, cavitation can be classified into two types: *Inertial* and *Non-inertial*. The former describes rapid bubble dynamics that involve unstable bubble expansion and collapse typically triggered by a rapid change of pressure with a relatively large amplitude. The latter refers to much gentler bubble dynamics, e.g., the stable oscillation of a bubble around its equilibrium radius, typically driven by small periodic external pressure. Inertial cavitation dynamics, the focus of the work, involves multiple steps including nucleation, expansion, oscillation, and collapse. During the bubble expansion, the bubble works against the resistance of the surrounding media, i.e., liquid. During the bubble collapse, the energy stored in the media is released. This collapse is violent in nature because the energy release is very localized at very high rates, a phenomenon known as *microjetting*.

Traditionally, cavitation in liquid has been of great interest to many researchers due to its important implications for many industrial and military applications. For example, sudden pressure drops in liquid media can occur in many engineering systems that involve rapid acceleration of the media, such as propellers of submarines and ships, hydraulic pumps, water turbines, and industrial piping systems. Due to its violent nature, cavitation can damage even the strongest man-made materials and structures over time, significantly

shortening the life of these systems. Therefore, traditional research has focused on preventing cavitation-induced damage by predicting and avoiding the critical conditions that trigger cavitation nucleation.

There have been increasing research efforts to investigate cavitation in biological systems, e.g., a human body or tissue simulant. For example, significant progress has been made in shockwave lithotripsy (SWL) [2-6] by understanding the contribution of cavitation dynamics for biomedical applications [7-11]. Similarly, laser-induced cavitation has been used in ophthalmic microsurgery [12, 13]. Another biomedical application of cavitation is targeted drug delivery [14-16]. In these works, cavitation was used to release an encapsulated drug within a carrier, such as a liposome or polymeric nanoparticle, when the carriers were near the target site, e.g., tumor or cancer. Other than that, a microfluidic system with highly controllable bubbles also provides several advantages associated with understanding of cell injury mechanism or mechanotransduction via calcium signaling processes [17-19]. In the viewpoint of being possible for single-cell analysis, it is helpful to characterize shear stress-induced membrane deformation and the level of its poration.

More recently, several studies have reported that injuries that involve rapid acceleration of the human body by mechanical impact, e.g., car crash, collisions during sporting events, and bullet wounds, [20-23] can induce cavitation in the human body or a tissue simulant. Among the instances of cavitation in the human body, cavitation-induced traumatic brain injury (TBI) has received much increased attention because cavitation bubbles inside the human skull can result in tremendous brain damage [24-26]. Therefore, it is essential to understand the behavior of bubbles from the nucleation of the cavity to the collapse of the bubble and its effect in biological systems.

2

With biomedical applications of cavitation, there have been rapidly increasing demands for theoretical and experimental characterization of cavitation dynamics in biological systems to capture the unique interplay between cavitation and soft biological systems. Unlike homogeneous pure liquid, cavitation in soft biological systems exhibits highly complex behavior due to the viscoelastic properties [27-29] and heterogeneous microstructures [30, 31] of biological systems. In this regard, it is required for applying appropriate theoretical and experimental approaches for investigating cavitation dynamics in biological systems and biomedical applications.

In this regard, a drop-tower-based system, recently developed in the lab [32], can correlate a physical or mechanical property, i.e., acceleration or its gradients, to cavitation nucleation in different types of soft matters. This capability to directly correlate the onset of cavitation with acceleration would be quite helpful to understanding the underlying injury mechanism of biomaterials that are known to be sensitive to strain rates. The drop weight impact test is currently the only method that allows control of the input acceleration profile. This unique feature is crucial to revealing blunt injury mechanisms as one can mimic exact acceleration profiles for actual blunt injuries and study the biological responses of live cells or tissues. Furthermore, this integrated system is coupled with a sample holder and high-speed cameras to avoid direct contact between the biological sample and the impactor while optically observing the real-time material deformation of soft gels. Despite the key findings of cellular damage at the population level correlated with changes in transient acceleration and the following bubble growth [33], there are still remaining questions, i.e., how this system can be used to analyze deformation and damage of individual cells during impact loading. Therefore, an effort to add high-resolution real-

3

time imaging techniques, i.e., single-cell-level observations, to the current drop-tower-based system for in vitro studies would be critical to gain a fundamental understanding of the cavitation damage mechanisms at the single-cell/subcellular level.

1.2   Cavitation Nucleation and Its Ductile-to-brittle Shape Transition in Soft Gels under Translational Mechanical Impact

Biological materials, when subjected to rapid mechanical load, exhibit complex time-dependent material responses. These viscoelastic dynamic behaviors have garnered increasing attention in the scope of understanding blunt injury mechanisms under ballistic or impact exposures [22, 34-38]. These mechanical threats applied to the biological systems (e.g., the human body) can result in a wide range of injuries from considerable deformations of organs and rupture of injury-prone blood vessels [39, 40] to traumatic brain injury (TBI) [38, 41, 42].

In the cases of blunt impact head injuries, a human head experiences a rapid head motion that can be quantitatively defined by rotational and translational accelerations. It is well known that such accelerations result in acceleration-induced pressure inside a skull, deformation of brain, and flow of the CSF (cerebrospinal fluid) [43, 44]. The conventional census has been that the human brain is much more sensitive to rotational motion compared to translational motion because brain tissue is roughly five to six orders of magnitude softer under shear deformation from rotational motion, compared to tension/compression deformation induced by translational motion [45]. Understandably, the effect of translational head motion on TBI has been widely overlooked in the research community. A series of studies [46-49] evaluated the effect of rotational acceleration in causing brain

4

injury by using live subhuman primates and physical models. They concluded that angular acceleration contributes more than linear one to the occurrence of concussive injuries, diffuse axonal injuries, and subdural hematomas due to severe shear deformation. Holbourn et al. [50] suggested that rotation acceleration could explain the most portion of traumatic injuries due to the nearly incompressible properties of brain tissue. In sum, bulk modulus of brain tissue is much larger than its shear modulus and, as a result, shear deformation has been used as an indicator of traumatic brain injury associated with diffuse axonal injuries [51-53] and the damage of the blood brain barrier [54].

Despite the census, a series of recent studies have strongly suggested that translational acceleration could be one of the main mechanisms of acute traumatic brain damages [25, 55-57] due to cavitation nucleation and its violent dynamics in biological systems. The local pressure gradient to induce cavitation nucleation can be likely created by translational impact since the CSF pressure induced by the rotational impact is likely much lower than that of translational one due to a decrease in skull deformation [58, 59]. More specifically, Kang et al. [28, 29] have developed an integrated drop-tower system and quantified the critical translational linear acceleration (a_{cr}) for different tissue simulants including gelatin, agarose, and collagen. Their studies have revealed that a_{cr} strongly depends on both sample size and stiffness. For example, a_{cr} for 1.0% (8 kPa) and 7.5% (60 kPa) gelatin samples were 482 g and 581 g, respectively [28] where g is gravitational acceleration. Also, a_{cr} values of pure water in 10-mm, 40-mm, and 60-mm tall containers were 1300 g, 300 g, and 175 g, respectively [28, 33]. Note that a_{cr} sharply decreases with increasing sample size. Due to this size-dependent a_{cr}, it was argued that cavitation could be triggered well below 175 g inside the human skull considering its average size (~150

mm). This critical point has been experimentally validated by using a full scale human head surrogate [60] as cavitation bubbles were observed around 100 g.

The recent results above indicate that cavitation may occur in the brain when impact-induced linear acceleration is near or even below 100 g with a time period in a range of 1~10 milliseconds. It is important to point out that, although 100 g seems very high, sports players [61, 62] and military personnel [63, 64] are often exposed to near or even higher linear acceleration. For example, it has been reported that an upper range of linear acceleration measured among college football players was 60~120 g. Similarly, reported recoil acceleration of a shoulder mounted weapon was consistently about 250 g. The fundamental understanding of how soft materials respond under translational impact becomes increasingly relevant for the accurate prediction and evaluation of cavitation-induced damage to the biological materials.

Despite the increasing demand and a few recent studies [28, 29, 32, 65], the underlying mechanisms that govern the onset of cavitation nucleation in biological materials and the transient dynamic responses of cavitation bubbles particularly under translational impact are not fully understood. Unlike cavitation in pure water without structural rigidity [66, 67], a cavitation bubble in a soft biomaterial directly interacts with the complex fluid- and solid-like characteristics of the surrounding material. Therefore, it is crucial to characterize and reveal how cavitation nucleation and subsequent bubble dynamics are influenced by complex material responses of biomaterials arising from their soft and labile features, nonlinear material deformation, and strain-rate-dependent material properties [68-71].

Here, transient cavitation bubbles in four different tissue simulants (agarose, agar, and gelatin A/B) are experimentally and theoretically considered so that the correlation between cavitation dynamics and properties of soft materials (e.g., stiffness, surface tension, and fracture toughness) can be systematically investigated. Individual soft gel samples prepared at different gel concentrations in pure water are considered to simulate a wide range of bulk material properties of biological systems (e.g., from 0.1 to 10 kPa for brain tissues to 100 kPa for human aorta [72]) and their dynamic response under mechanical impact. The experimental results have revealed that the critical acceleration for cavitation nucleation and the shape of cavitation bubbles during bubble growth strongly depend on both gel types and stiffness. Interestingly, a bubble shape transition from a sphere to saucer in agarose and agar with increasing gel stiffness has been observed. This is very different from spherical cavitation bubbles observed in gelatin A/B regardless of their gel stiffness. In order to explain this gel-type and -stiffness-dependent transition, the concepts of both a damaged zone at a bubble-gel interface and fracture mechanics have been utilized. The theoretical analysis predicts that a damaged zone in agarose and agar, while consistently small (tens of nanometers) in gelatin A/B, becomes much larger with increasing gel stiffness (> 100 times increase). The larger damaged zone in stiffer agarose and agar allows formation of longer cracks and the subsequent activation of crack propagation due to a substantial increase in a stress concentration factor.

1.3   Characterization and Detection of Acceleration-induced Cavitation in Soft

Matters Using a Drop-tower-based Repetitive Impact System

Soft materials, comprising a variety class of substances such as polymer, elastomers, hydrogels, and foam, play a crucial role in the field of biomedical engineering and biomaterial development including artificial organ (e.g., cartridge and hip implant), wound healing process [73], tissue regeneration [74, 75], as well as stretchable soft bioelectronics for human skin surface [76, 77]. Their unique mechanical properties, i.e., flexibility, viscoelasticity, high deformability, and recovery characteristics, make them indispensable by replacing and/or mimicking a native tissue [78, 79]. Due to a continuously increasing demand for soft matters as tissue surrogate materials, accurate characterization of their properties garnered much attention such that various testing methods have been developed over the years [31, 80-82]. However, the use of the instruments for characterizing biomaterials (e.g., hydrogels or tissues) remains challenging because of their soft and highly compliant nature. Under an external mechanical insult, biological materials show complex responses that are associated with their fluid like- and solid like nature, which leads to strain rate dependent material properties [83, 84]. On top of that, due to high water contents, the biomaterials are likely to experience fatigue- or accumulated damage induced failure in a brittle manner mostly after the multiple, repetitive loadings [85-87].

The atomic force microscopy (AFM) and rheological-based tester have been widely used to characterize tissue response under various modes of deformation (e.g., shear, compression, and tension) [88]. These techniques have several advantages such as being capable of measuring both elastic and viscous properties and of testing biological samples

in vivo. These aspects are important for understanding their nonlinear stress-strain relations and quantifying their accurate characteristics in their native state where they need to function. However, these methods are necessary to use direct contact between target samples and probe or loading frame such that there are unwanted problems related with how the surface- and surface-substructure of the target materials interplay with a probe or indenter such as sample plastic damage, cone- and microcracks as well as probe contamination [89]. To avoid contact-induced problems, contactless measurements can be an alternative to the contact methods. For example, the use of elastohydrodynamic (EHD) interactions in a liquid or magnetic resonance imaging elastography non-invasively assesses mechanical properties of the soft sample [89]. Despite these modifications, all of these techniques are still incapable of evaluating dynamic properties of the soft samples in high frequencies or high strain rate loading conditions ($> 10^2/s$) [81].

Other methods such as split Hopkinson pressure bar (SHPB) [90, 91] and laser cavitation rheology (LCR) [27, 92, 93] have been used to measure dynamic mechanical properties of bio-soft materials at high-strain rates ($10^2 \sim 10^4/s$ and $\sim 10^8/s$, respectively). In order to apply SHPB to soft materials, researchers have made several modifications to reduce a drastic mismatch of impedance between specimen and the bars: 1) replacement of a metal bar with viscoelastic or hollow bars showing low-impedance (e.g., polycarbonate or hollow aluminum bars) [91, 94], 2) reduction of the specimen thickness [95], and 3) more sensitive measurement methods to improve the ratio of signal to noise by using electromagnetic loading [96] or quartz piezoelectric transducers [97]. For accurate characterization of biomaterials using LCR, Sacchita et al. introduce laser absorbing seed microspheres in order to avoid nonlinear dielectric breakdown of the testing

medium, leading to less dependency on the optical properties of the testing samples [92]. However, despite the above advances, both techniques still face unresolved challenges in terms of unwanted nonuniform stress or strain field [98] as well as laser-induced thermal damage [99], respectively. These aspects make them less suitable for examining dynamic properties of biological samples particularly under repetitive loading conditions.

Previously, Kang et al. developed a drop-tower-based integrated system by modifying conventional drop tower system with adaptations [100]. The integrated system allows us to non-invasively characterize soft, labile materials in a way of applying rapid, smooth acceleration profile at a relatively broad range of strain rates ($1 - 10^5/s$) [101]. This sudden acceleration change can induce a pressure gradient in the soft medium, which leads to cavitation nucleation. The capability to associate physical parameters (i.e., acceleration and its change over time) with the onset of cavitation can be helpful to understand underlying injury mechanisms in the situation of rapid acceleration of the human body or tissue simulant via mechanical input such as collision during contact sports and bullet or shock wounds during military operations. However, compared to the previously mentioned rheological-based testers, this integrated system is not able to offer continuous, repetitive mechanical inputs (i.e., acceleration profiles) on the testing sample with tightly controlled experimental conditions (e.g., impact frequency and amplitude). Furthermore, due to limitations on relatively small sample sizes, the applied critical acceleration (i.e., an acceleration leads to the onset of cavitation) is significantly higher than what is normally expected in human body injury situations ($\sim150g$) [102].

Here, a drop-tower-based repetitive impact system is presented for characterizing soft biomaterials under varying mechanical loading conditions that a human body frequently encounters. Further advances have been made by integrating the previous integrated system with a motor system, a unique sample holder and testing platform, as well as a novel triggering algorithm. These modifications offer the following advantages: 1) precisely controllable impact characteristics (i.e., the number of impacts over time and impact amplitude) by changing the motor gear designs, 2) utilization of various size of the testing samples, which are directly relevant to different human organ scales, and 3) an automatic detection of initial cavitation burst synchronized with the corresponding optical and mechanical data sets. In this paper, the dynamic characteristics of our developed repetitive impact tester are theoretically evaluated based on experimental validation. The theoretical and experimental approaches show that an impact-induced acceleration can be systematically tuned by a series of springs and dampers placed between a movable mass and the sample holder. Moreover, repetitive drop experiments are performed on individual agarose gels to quantify size- and impact characteristics-dependent cavitation properties, which are not possible with other cavitation induced rheology such as lasers or ultrasound. Finally, the novel non-optical detection method of initial cavitation during continuously repeating impacts is proposed, triggered by the structural resonance of a sample holder perpendicular to the impact direction.

1.4   Mechanisms of Cell Damage Due to Mechanical Impact – an in Vitro

Investigation

Trauma is one of the leading causes of death in the world [103] and has garnered much interest in recent years due to the realization of the breadth of impact-related pathologies that vary in severity, level of ability for accurate diagnosis, and time scales over which the effects are observed. For instance, blunt liver trauma is often associated with a single severe traumatic incident and might involve immediate surgical intervention once identified [104]. However, traumatic brain injuries (TBI) associated with active military personnel often have a singular traumatic event, yet can manifest as a combination of physical, cognitive or emotional ailments over time that can be misdiagnosed as post-traumatic stress syndrome [105]. Furthermore, the recently discovered prevalence of chronic traumatic encephalopathy (CTE) in contact sports athletes is associated with compounding effects of less-severe, yet still traumatic events over time that can only be accurately diagnosed posthumously [106].

Many resources and efforts have been utilized over the years to better understand the pathophysiology of blunt impact injuries. Typically, animal models that utilize injury mechanisms to the organ of interest in conjunction with end-point assays, such as immunohistochemistry, have been a common platform to identify injury related biomarkers or to assess cell/tissue damage [107]. However, the mechanisms underlying post-trauma cellular damage or death remain poorly understood [108], likely in part due to the lack of standard testing procedures and the complexity of interpreting animal models [109]. This has prompted research efforts to focus on simpler *in-vitro* platforms, allowing

12

researchers to investigate potential underlying injury mechanisms at the cellular or molecular level [110]. However, in many of these *in-vitro* platforms, it has proven technically challenging to accurately apply injury-relevant pressure forces to the cell population in question in tightly controlled environments [111].

The human body is exposed to considerable linear acceleration in the range of 80-250g during mechanical collisions, e.g., football and boxing matches [61, 62] or military operations [112, 113]. Such rapid acceleration of the human body results in various traumatic injuries including blunt liver trauma [114, 115] or traumatic brain injury [37, 61, 62, 112]. It is important to note that acceleration alone is the most commonly used criteria for assessment of blunt injury.

Dynamic cavitation in the brain is increasingly considered a potential damage mechanism for traumatic brain injury [116-120]. In this regard, one notable advance is in the characterization of cavitation properties for soft biomaterials under an impulsive force [121-123]. In these studies, the critical acceleration that corresponds to the onset of the bubble formation and bursts has been experimentally and theoretically characterized utilizing biologically relevant soft biomaterials including collagen, agarose, and gelatin. These studies have established a range of mechanical acceleration for potential cavitation-induced brain injury. Further, these studies have shown that the acceleration-induced local pressure strongly depends on the sample size, and therefore, in addition to acceleration, the size of biological system experiencing trauma, e.g., head, should be considered for accurate assessment of potential injuries.

Despite the recent progress on the dynamic response of tissue simulant, experimental studies on the spatio-temporal response of live cells under well-characterized acceleration-induced pressure are very limited in the literature largely due to the lack of such experimental capability. Some of the key experimental challenges include: 1) maintenance of consistent in vitro conditions during the experiments and observation periods; 2) a capability to probe cells in time, in particular before and after impact; 3) a high throughput approach for analyses of multiplexed cell populations. The combination of these capabilities is necessary for revealing cellular behavior associated with injury mechanisms and ensures statistical significance considering the heterogeneous nature of cell response. For example, understanding and characterizing the cell-line specific senescence for *in-vitro* platforms is of paramount importance to accurately probe underlying mechanisms and ensure reproducible results.

Here, damage mechanisms of live cells are investigated to address a key question of "what are the key injury mechanisms, e.g., acceleration or pressure, and injury criteria associated with mechanical impact?" Towards this fundamental question, a new experimental approach for the application of well-controlled impact to live cell populations in vitro has been developed and utilized. First, a new drop-tower-based experimental setup designed to apply a wide range of blunt injury mimicking accelerations to live cell populations is described, while also optically monitoring the in vitro cell culture. Then pressure in a cell culture chamber during impact to establish an acceleration-pressure relation during impact is theoretically considered. Utilizing the new experimental capability, damage to cells is experimentally evaluated, by using fibroblast cells as a model, during impact. Finally, the acceleration- and cavitation-induced pressure during impact are

14

quantified and it is shown that the latter is the critical injury mechanism to cells due to the dynamic nature of the cavitation.

1.5   Hs27 Fibroblast Response to Contact Guidance Cues

Although the previous in vitro cell culture setup offers an experimental capability for studying cellular spatial- and temporal responses under a translational loading, there are still knowledge gap between cavitation-induced injury and cell caused by different cellular static and dynamic behaviors under its natural conditions. For example, in brain, endothelial cells which form blood-brain barrier (BBB) are known to be elongated and align along a collagen fiber from extracellular matrix (ECM) as well as along a surrounding blood flow in order to regulate the passage of intracellular molecules [124, 125]. It has been well known that the cell morphology and mobility are closely correlated mechanical properties of its plasma membrane [126-128]. In this regard, I reasoned that the response of a cell to cavitation-induced injury can be influenced by its different morphological and dynamic behaviors under its natural conditions. For Chapter 5, with the use of contact guidance, how ECM scaffolding modulates the cell static and dynamic responses will be investigated.

Cellular responses to topographical cues, known as contact guidance, has been studied for several decades [129-131] and the influence of topography on cell behaviors has been also investigated mainly from bio-chemical and -physical viewpoints. The fundamental understanding of the cell-substrate interactions can provide better insight into the complicated relations between cells and surrounding natural extracellular matrix (ECM) [132]. In addition, the underlying mechanisms in the cell-ECM relations become relevant

for revealing key biomedical processes such as wound healing, cancer dissemination, tissue and organ formation and regeneration as well as development of next generation biomaterials [133-137]. Various studies performed using different types of cells show considerable changes in cell morphology and mobility in response to topographic cues [138-141]. Several techniques, such as nano/microfabricated grooves, functionalized surface patterns, and fibers in hydrogels [140, 142-144], have been developed and utilized to achieve well-controlled anisotropic topographical cues and quantify topography-dependent cell responses including cell morphology, movement, viability, proliferation and differentiation [141, 144, 145].

Previous studies in the contact guidance field have shown that cellular anisotropic behavior takes place on a micro- and nano grooved substrate of varying dimensions [138, 146-148]. In general, these studies show that (1) cells tend to elongate along the groove direction (i.e., the longitudinal direction of ridge and groove patterns) and (2) a degree of elongation and alignment is strongly influenced by lateral and vertical dimensions of the patterns (grooves and/or ridges). However, the results are still inconsistent and specific contributions from each topographic feature, namely, groove depth (G_D), ridge (R_w) and groove (G_w) widths, are not fully characterized. As a result, there are controversial conclusions on which topographic feature is the most dominant effect on cellular behavior. For example, G_D was identified as the dominant factor for cell elongation and alignment of baby hamster kidney (BHK) cells [138] and corneal epithelial cells [139]. However, another study using rat dermal fibroblasts [147] reported a considerable increase in the cell elongation and alignment ratios with a smaller R_w and concluded that that R_w is the most dominant dimension compared to G_w and G_D.

16

Similar to the static cell behavior, dynamic cellular responses to contact guidance are cell specific. Neutrophils [149], endothelial [150], osteoblasts [151], human cervical and lung cancer cells [152] on patterned topographies show strongly directional and fast cell migration along the longitudinal direction of contact guidance patterns compared to control experiments on flat surfaces. However, the cell mobility of human aortic endothelial cells [150] and corneal keratocytes [153] are not strongly influenced by surface patterns. Such inconsistency in cell responses can be partially due to complex cell responses that are sensitive to cell types and associated with a lack of parametric studies for individual cues since the intrinsic morphology and/or variation of respective cell type in the intracellular population are closely related with their physicochemical functions [154]. Many studies have simultaneously varied two dimensions, R_w and G_w, while poorly controlling over the other (G_D), which can lead to inaccuracy in predicting cell behaviors because of inconclusive data generated by intertwined topographic effects.

Despite the inconsistency, it has been well accepted that contact guidance technologies considerably alter cell morphology [139, 155, 156] and migration [153, 156] and, as a result, have been considered as a possible mechanism to enhance wound healing processes, e.g., by guiding cells to wound sites and controlling their elongation, alignment, and directionality. In this regard, fibroblasts become relevant due to their important roles in wound healing process including breaking down fibrin clots and repairing ECM and collagen structures [157]. However, experimental characterizations of anisotropic morphological behaviors of fibroblasts on contact guidance surfaces are still limited to a relatively small range of topographical dimensions, i.e., G_w and $R_w \leq 2\,\mu m$ or $G_D \leq 300\,nm$ [139, 153, 156]. Furthermore, the effect of contact guidance on dynamic cell

behavior has been rarely performed and, to the best knowledge, the available results are limited to G_w and $R_w \leq 2\ \mu m$ with $G_D \leq 300\ nm$ and G_w and $R_w = 3, 5,$ and $10\ \mu m$ with $G_D \leq 300\ nm$ [153, 156]. However, considering typical dimensions (diameter $>$ $10\ \mu m$ and thickness $\sim 550\ nm$) of fibroblasts [158], it is worth investigating cell anisotropic behaviors on the substrate having intermediate feature sizes of widths and depths ($2\ \mu m \leq G_w$ and R_w, and $300\ nm \leq G_D \leq 1000\ nm$) since each fibroblast can spread on enough number of topographical cues to impose constraints along the groove direction, which is sufficient to affect their morphology and migration.

Beyond the necessity of a contact guidance study for fibroblasts with a broad range of topographical dimensions, it would be highly desirable to independently evaluate a contribution for individual topographic features. To the best knowledge, no effort has yet been made to perform a parametric study for fibroblasts in order to reveal each topographical effect, while holding one-dimension constant with varying the others. The quantitative characterization of cellular behaviors under influence of well controlled yet diverse combinations of geometrical cues is still challenging due to lack of a fabrication technique that allows precise control of small-scale topographic features and multiplexed cell studies under identical extracellular environments. Without such unique capabilities, characterizing the correlation between individual effects of topographical cues and the corresponding cellular behavior with statistical significance becomes non-trivial. On top of that, several hypotheses have been proposed to explain their underling mechanisms; some studies suggest that mechanical interlocking or capillary force results from the groove of the substrates [159, 160] and others present that cells lying on the microtextured surfaces are able to reorganize their fibers network for balancing internal and external forces [161,

18

162]. Characterizing the specific effects of individual topographical features, using a time-effective high throughput method, is crucial to explore possible mechanisms for cell-type dependent anisotropic cell behaviors and to provide effective design space for biomedical applications of contact guidance.

In here, the morphological and dynamic responses of Hs27 fibroblasts on multiplexed monolithic quartz chips [163] with a wide range of topographical dimensions well beyond what has been previously reported are characterized. The multiplexed approach allows quantitative characterizations of $R_w, G_w,$ and G_D dependent cell responses while minimizing unwanted biological variations during cell culture. First, static analyses on three different morphological measurements, such as cell spread area, aspect ratio and cell alignment degree, due to their biological and biomedical relevance are performed. Then, the directional cell migration in the scope of effectively guided cell motion is quantified. Finally, both the cell membrane deformation and focal adhesion models are utilized to offer mechanistic explanations for the observed cell behavior of HS27 fibroblasts on the multiplexed contact guidance chips.

2. CAVITATION NUCLEATION AND ITS DUCTILE-TO-BRITTLE SHAPE TRANSITION IN SOFT GELS UNDER TRANSLATIONAL MECHANICAL IMPACT

2.1 Materials and Methods

2.1.1 An Integrated Drop Tower System

The integrated drop-tower system (Figure 2-1) consists of a conventional drop tower impact system (Model DW750L, STEP Lab, Treviso, Italy), a high-speed camera (FastcamSA-X2RV, Photron, San Diego, CA), a cuvette and holder, accelerometers, and a data acquisition system. Soft gel samples are prepared inside standard plastic cuvettes for ease of sample handling. Each cuvette is sealed with a cap and then glued onto the cuvette holder which consists of two horizontal plates connected by four vertical columns. The cuvette holder is rigid enough to sustain impacts while preventing damage to the cuvette. Soft silicone sheets are placed at the bottom and/or top of the cuvette holder to control characteristics of impacts, e.g., applied force on the holder and resultant acceleration. It is important to emphasize that the integrated drop-weight tower system is designed to apply smooth acceleration profile to a soft gel without generating shock waves. The magnitude of each mechanical impact is controlled by adjusting a vertical drop height of a movable impactor with respect to the cuvette holder. Upon release, the impactor falls toward the cuvette holder by gravity until collision. At the onset of impact, a high-speed camera with 2x magnification lens (Tokina at-X PRO M 100mm F2.8 D Macro lens and Kenko TELEPLUS HD DGX 2x) and 50 kfps frame rate and an accelerometer (model #356A01, PCB Piezotronics, Depew, NY) are triggered for synchronized optical observation and

acceleration measurement at 10^{-6} s sampling rate. Result data is collected by NI PXIe-8135 embedded controller and an NI PXI-6115 multifunction I/O module with SignalExpress 2014 data acquisition software (National Instruments Corporation., Austin, TX). A representative acceleration profile (raw data without any filter or postprocessing) during each drop experiment is shown in Figure 1. Detailed characterization of the
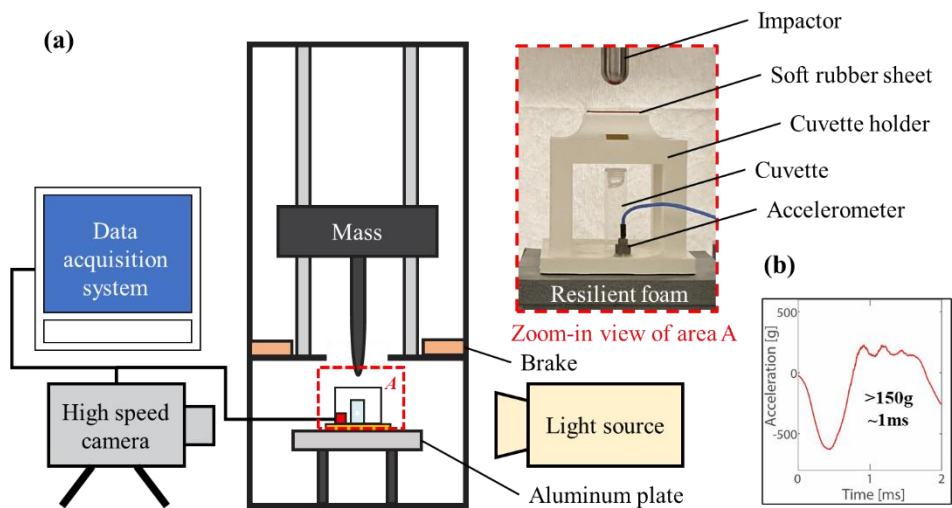
Figure 2-1. (a) A schematic of the integrated drop-tower system consisting of a drop-tower system, high-speed camera, cuvette holder, cuvette with a soft gel sample, accelerometer, and computer for data acquisition. A cuvette holder is placed on an anvil in *area A* for each drop experiment. A high-speed camera is mounted on a camera stand. (b) A representative acceleration profile. Note that the profile is smooth without characteristics of shock waves due to use of a soft rubber sheet and a resilient foam as dampers.

integrated drop-weight tower system has been reported elsewhere [28, 29, 32].

2.1.2 Materials and Sample Preparation

For pure water samples, the 4 ml ultrapure water was poured into each new cuvette by a micropipette. The agarose (Ultrapure, Invitrogen, Cat # 16500-100), agar (supplied by Sigma), and gelatin from porcine skin (supplied by Sigma, Type A/B, Lot # SLBX2973) were prepared in ultrapure water (>18 MΩ-cm resistivity; LabChem, ACS Reagent Grade,

21

Zelienople PA) at different gel concentrations (%w/w). For agarose samples, 100 ml of room temperature water was dispensed into a Pyrex beaker with a magnetic stir bar. Then 0.3, 0.58, 0.75, 0.9, 1.1, 1.3, and 1.5g of agarose powder were gradually added to the beaker to form 0.3, 0.58, 0.75, 0.9, 1.1, 1.3, 1.5% agarose samples, respectively. Similarly, 1, 1.5, 2.5, 4, 5, and 7g were added to 100 ml to create 1, 1.5, 2.5, 4, 5, and 7% gelatin A/B samples, respectively. Then, each beaker with a Pyrex beaker cover was placed on a hot stir plate. The set temperatures were 60~80 °C for gelatin A/B and 100 °C for agarose and agar, respectively, for 30 min. The solution was continuously mixed by a stirrer at 160 rpm. The total weight of the solution was measured before and after heating and the pure water was added to each beaker to compensate the difference due to evaporation. 4 ml of hydrogel solutions was inserted into the individual cuvettes using a 10 ml disposable serological pipette. Agar and agarose samples were cured at room temperature (20 °C) overnight (12 hours) while gelatin samples were kept in a refrigerator at 4 °C for 3 hours and then the drop-tower experiment was performed.

2.1.3   Quantitative Measurement of the Critical Acceleration for Cavitation

The following experimental procedure has been developed and utilized to measure the critical acceleration (a_{cr}). The main goal is to minimize the number of drops on the same sample by actively adjusting initial drop height based on accumulated experimental data and, therefore, avoid possible sample damage. First, several pure water samples were characterized and quantified the critical drop height that is sufficient to induce preferably a single cavitation bubble. Second, the first gel sample of each gel type was tested starting from the lowest concentration. For the first sample, the critical drop height of pure water was used as the initial drop height. The drop experiments were repeated on the same first

sample while the height of each drop incrementally increased by 20 mm until cavitation bubble(s) was(were) observed via the high-speed camera. After cavitation, the sample was replaced by a new one. For the subsequential experiments, the initial drop height was adjusted slightly lower than the measured critical drop height from the previous experiment so that cavitation occurred typically within 1-3 drop experiments. The initial drop height for each type of gel at each concentration was independently characterized and adjusted as discussed here. After each drop experiment, the input acceleration from the accelerometers and the corresponding deformation of each gel from high-speed camera images (1 pixel = 33 µm) were processed together using MATLAB software to determine the critical acceleration (a_{cr}) and the corresponding time (t_{cr}). The smallest cavitation bubble size that can be optically detected by the high-speed camera is about 100 µm.
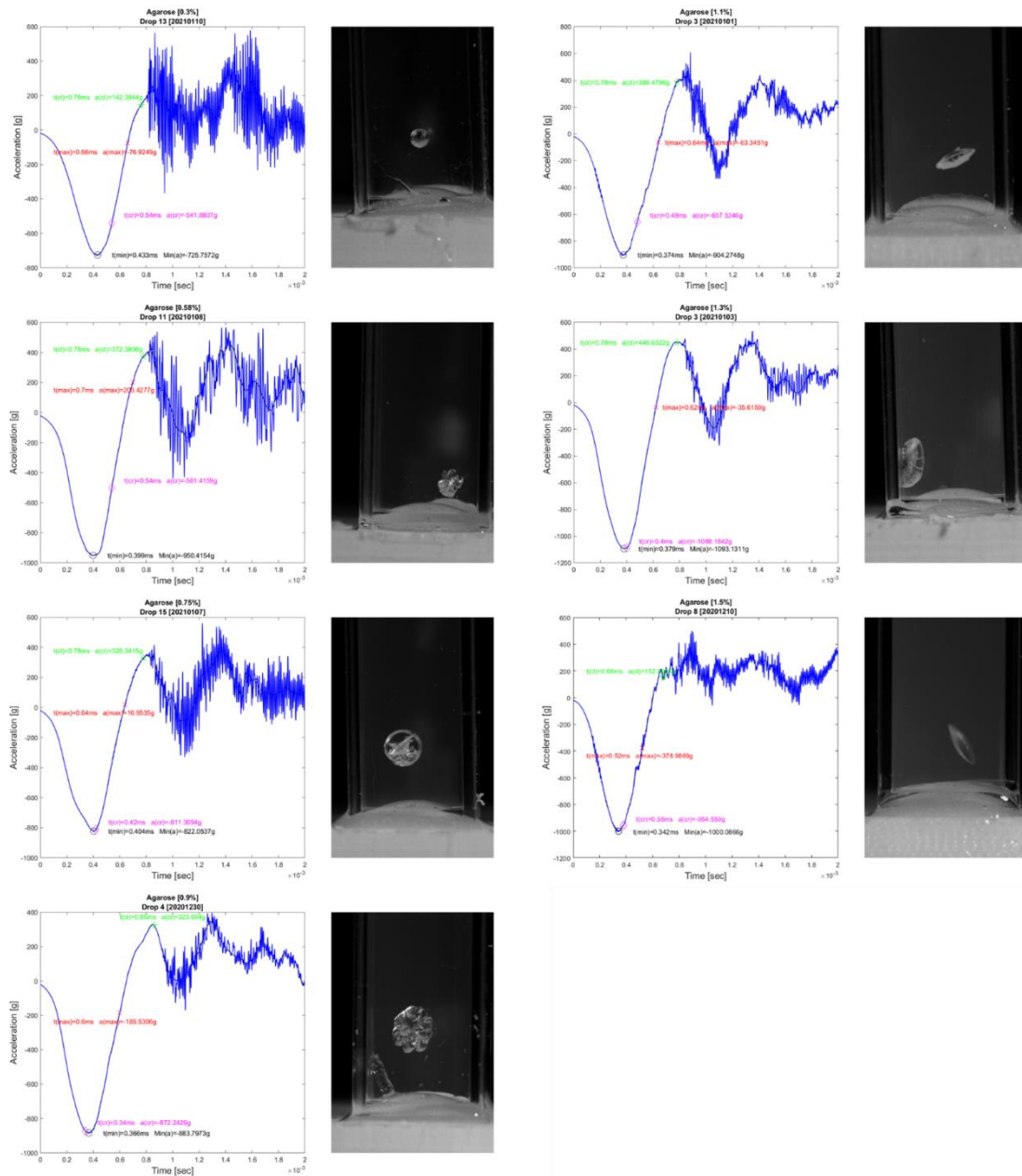
Figure 2-2. Representative acceleration profiles for agarose with respect to each concentration (0.3, 0.58, 0.75, 0.9, 1.1, 1.3, and 1.5w/v%). Each right-side image represents the maximum size of the cavitation bubble. Circle, diamond, X, and star marks represent the minimum and critical acceleration, the acceleration at the maximum bubble size and at the bubble collapse, respectively.

It is worth noting that the acceleration induced pressure in pure water or gel samples is

near the critical pressure value because the drop height incrementally increases until the

onset of cavitation nucleation is triggered. This allows nucleation of a single (or very few) cavitation bubble(s). As an example, nucleation and growth of the second cavitation bubble
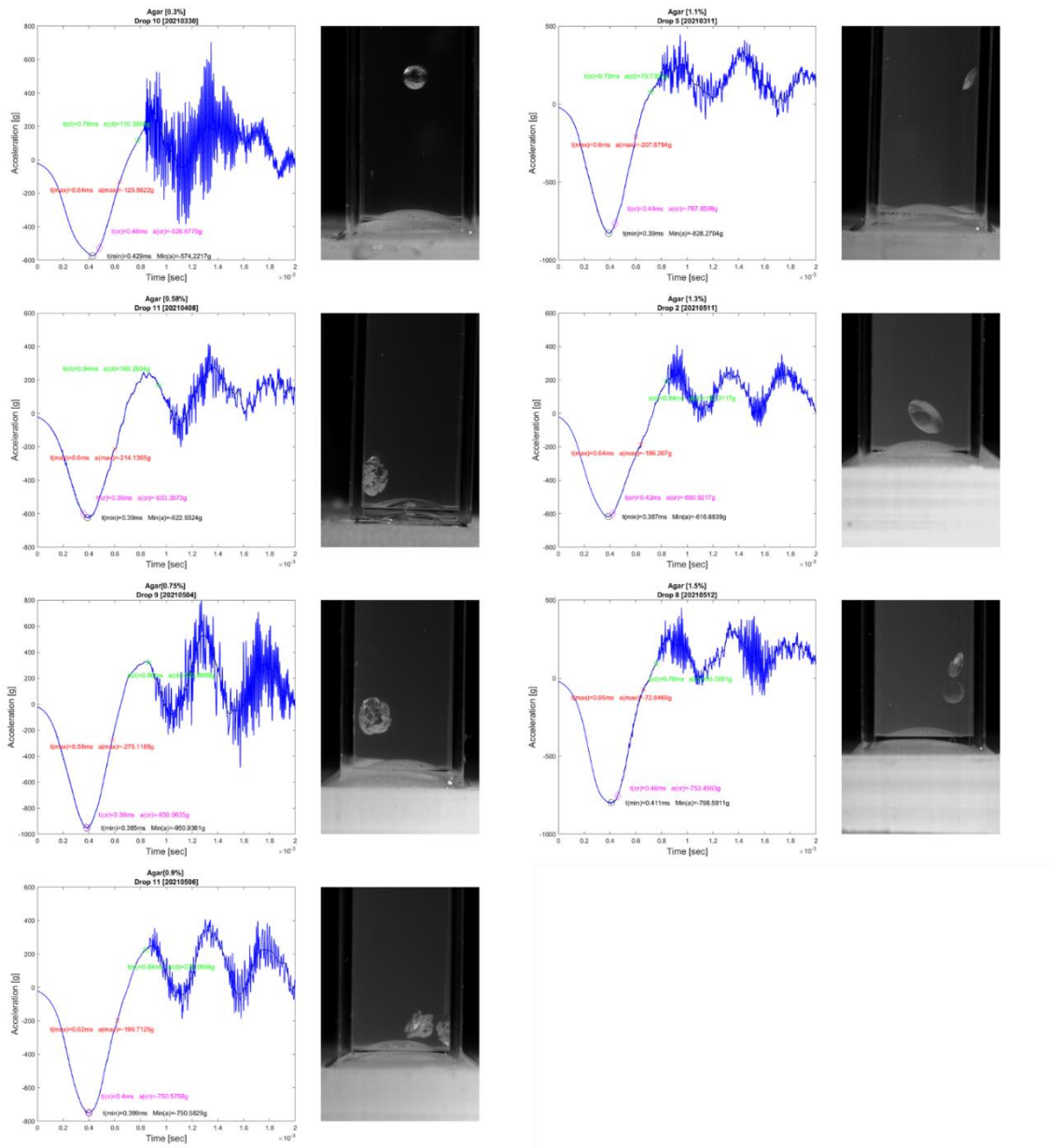
Figure 2-3. Representative acceleration profiles for agar with respect to each concentration (0.3, 0.58, 0.75, 0.9, 1.1, 1.3, and 1.5w/v%). Each right-side image represents the maximum size of the cavitation bubble. Circle, diamond, X, and star marks represent the minimum and critical acceleration, the acceleration at the maximum bubble size and at the bubble collapse, respectively.

will require slightly higher acceleration (or equivalently pressure) in order to overcome

compressive pressure gradient in pure water or gel induced by the growth of the first

cavitation bubble. More details on the experimental method can be also found elsewhere
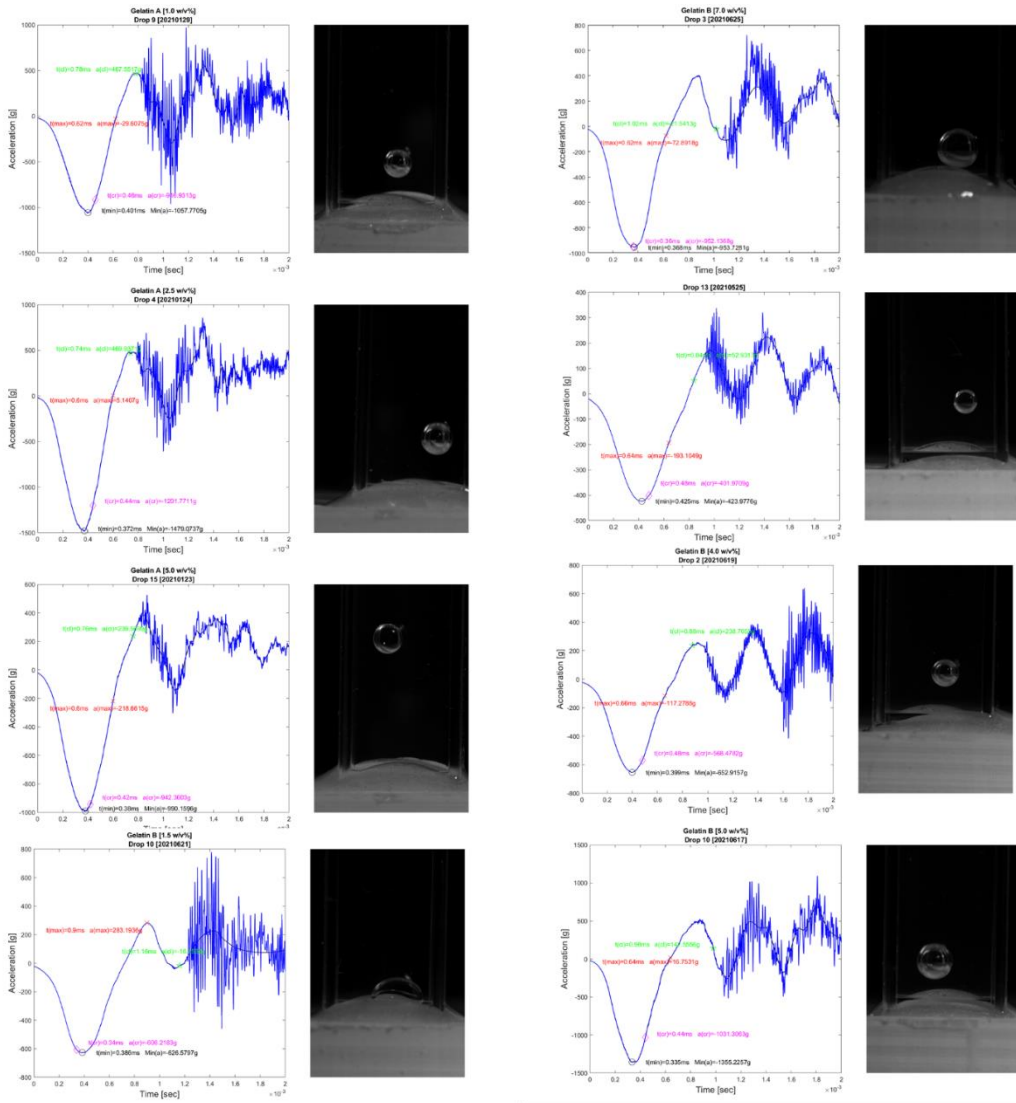
Figure 2-4. Representative acceleration profiles for gelatin A and B with respect
to each concentration (gelatin A: 1.0, 2.5, and 5.0w/v%, gelatin B: 1.5, 2.5,
4.0, 5.0, and 7.0w/v%). Each right-side image represents the maximum size of
the cavitation bubble. Circle, diamond, X, and star marks represent the
minimum and critical acceleration, the acceleration at the maximum bubble
size and at the bubble collapse, respectively.

[28, 32].

Note that several samples (> 10 samples) were prepared and tested for each gel type at each concentration for capturing the stochastic nature of cavitation nucleation in soft matter and making experimental conclusions with statistical significance. Individual gel samples in a transparent cuvette were carefully inspected under an optical microscope, before each drop-tower experiment, to avoid any pre-existing bubbles or visible defects. Figure 2-2, Figure 2-3, and Figure 2-4 show a representative acceleration measurement and the corresponding gel deformation with cavitation bubble in a gel during a drop experiment. Note that the critical acceleration that corresponds to the onset of cavitation nucleation can be quantified by currently using both optical observation and acceleration measurement.

2.1.4 Statistical Analysis
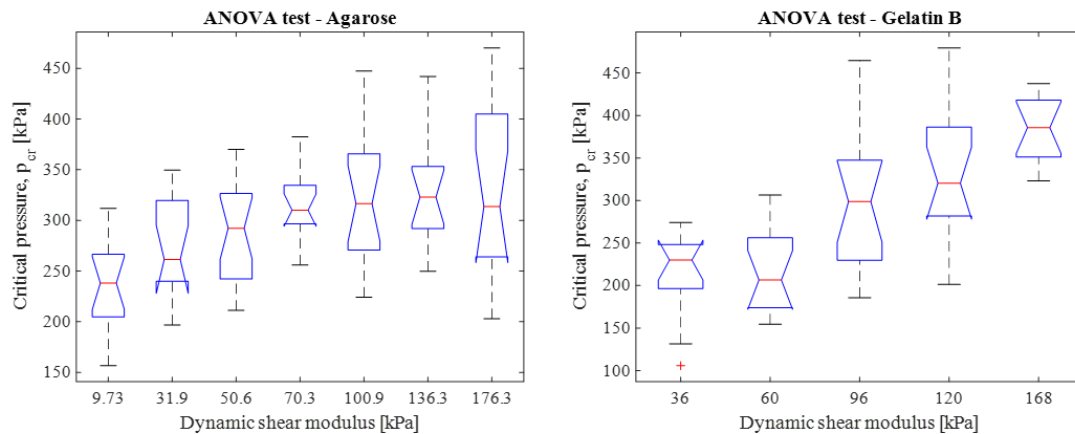
Figure 2-5. The results of our one-way ANOVA tests for agarose (left) and gelatin B (right) with respect to the corresponding dynamic shear modulus

All data were presented as $mean \pm 2 \cdot standard\ deviation$ in Figure 2-6. For the detailed statistical study, the built-in functions of MATLAB (*mean* and *std*) are used to calculate the mean and standard deviation of the critical accelerations in Figure 2-6 and Figure 2-13 (b). To consider the statistical significance between the theoretical and experimental data in Figure 2-13 (b), one-way ANOVA tests (null hypothesis: the critical

27

threshold is independent of gel stiffness, see Figure 2-5) were performed. The corresponding p-values for agarose and gelatin B are 5.38×10^{-5} and 5.46×10^{-10}, respectively. These p-values reject the null hypothesis and indicate that the critical pressure values are very likely dependent on gel stiffness (or equivalently gel concentration).

2.2   Experimental Results

Inertial cavitation nucleation and subsequent bubble dynamics in different types of soft gels (agarose, agar, and gelatin A/B) are experimentally characterized under translational impact. These soft gels are selected due to their biological relevance, i.e., commonly used as tissue simulant [164, 165] and in 3D cell culture [166, 167]. For instance, mechanical properties of agarose at a concentration of 0.4~0.6% are close to that of brain tissues [164] and gelatin has been considered as a promising candidate for regeneration of neural tissue [168].
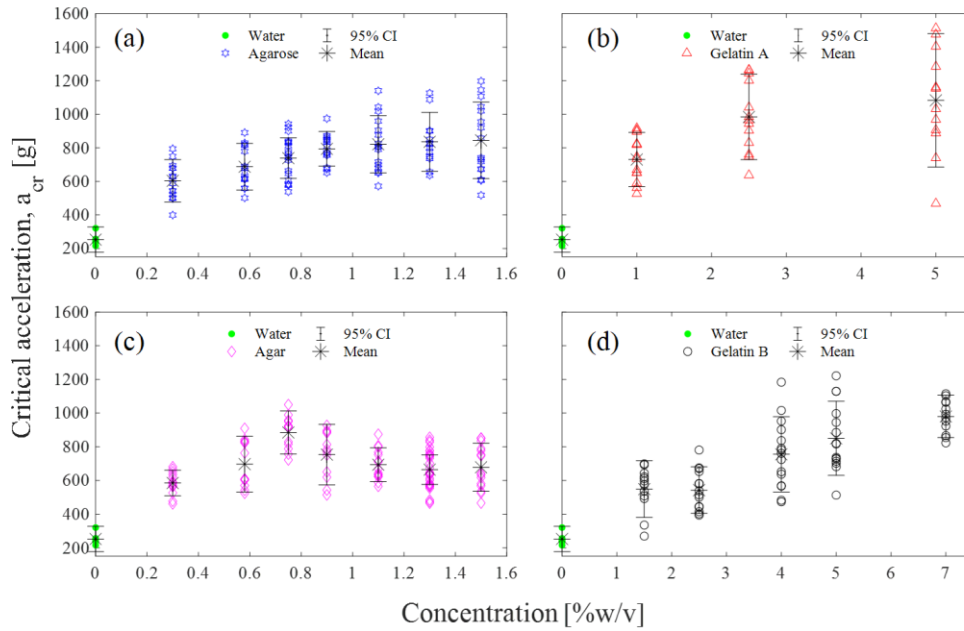
Figure 2-6. The critical acceleration of cavitation nucleation as a function of a gel concentration (*c*): a) agarose, b) gelatin A, c) agar, and d) gelatin B. The critical acceleration values for pure water (green circles) are added to each figure for comparison and CI indicates the confidence interval. *g* is gravitational acceleration.

The mechanical properties of soft gels depend on their concentration [70, 169-171]. This feature offers an advantage to mimic mechanical properties of biological systems, such as tissues and organs. In this work, the four different gel types as tissue simulants are prepared and tested to explore the gel-type-dependent and gel-property-dependent dynamic responses of soft samples during translational impact. For quantitative characterization of cavitation behavior in the gels, a recently developed integrated drop-tower system [32], offering a unique capability to control profiles of linear acceleration during translational impact, was utilized. A series of optical images were taken during impact by a high-speed camera for optical detection of cavitation nucleation and analysis of bubble shape.

Figure 2-6 shows the critical acceleration (a_{cr}) of pure water and the four different gels—agarose, agar, and gelatin A and B —as a function of a gel concentration (c). Each data point (i.e., individual markers) corresponds to an independent drop test (as shown in Figure 2-2, Figure 2-3, and Figure 2-4) using different gel samples. The mean values of the critical acceleration are designated by "∗" with the 95% confidence intervals. Note that the mean values of a_{cr} for gels are considerable higher compared to pure water regardless of gel types, but its specific trend with increasing gel concentrations (i.e., the $a_{cr} - c$ relations) appears to be dependent of gel types.
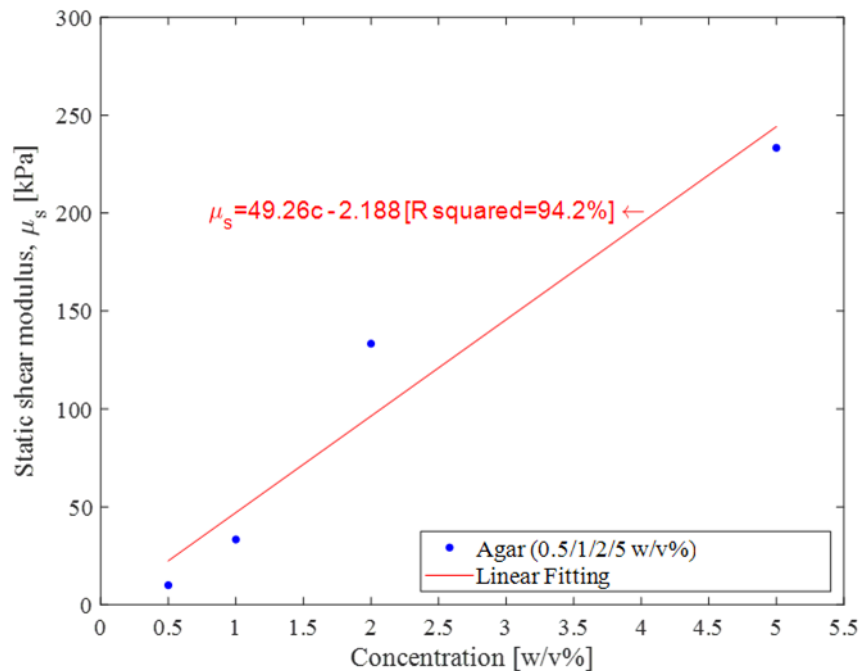
Figure 2-7. Extrapolation for the static shear modulus of agar gel. Blue dots and a red solid line represent the experimental data points and the corresponding linear fitting ($\mu_s = 49.26 * c - 2.188 \ with \ R^2 = 0.94$), respectively [70].

The bulk material properties of the four different types of gels are summarized in Table 2-1. These values are to show how the critical acceleration of different gels depend on their bulk properties. The key properties that are relevant to cavitation in soft matter were

30

obtained through extensive literature survey [28, 69, 70, 169, 170, 172-178] or extrapolation of known material properties shown in Table 2-1. For example, static shear modulus of agar, to the best knowledge, is available only within a limited range of gel concentrations. Therefore, unknown values of static shear modulus of seven different concentrations (i.e., 0.3, 0.58, 0.75, 0.9, 1.1, 1.3, 1.5 w/v%) are extrapolated from the known values of 0.5, 1, 2, 5 w/v% [70] using a linear regression method (see Figure 2-7). For agarose, its elastic modulus has been relatively well characterized and, therefore, an empirical equation given by, $E = 85c^{1.8}$ kPa [169] was used to estimate the shear modulus at different concentrations.

For gelatin type A/B, their bloom numbers, i.e., rigidity measure of gelatin gels [179], are 300 g Bloom and 225 g Bloom, respectively. The gelatin A has a higher bloom number likely due to the higher concentration of alpha chains that mainly contribute to the gel strength and viscosity [171, 179, 180]. For example, it is known that mechanical modulus of gelatin linearly increases with alpha chains [171]. It is assumed that the shear modulus of gelatin A is 33.3% higher than gelatin B based on the gelatin A to B ratio of their bloom numbers. It is worth noting that the dynamic shear modulus (μ_D) of agarose, agar, and gelatin A/B, obtained at high strain rates ($> 10^3 s^{-1}$) [69, 70, 181], can be significantly larger than their static shear modulus (μ_s). Hence, $\mu_D = 3\mu_s$ is used for agarose and agar [70], and $\mu_D = 9\mu_s$ is used for gelatin [69], where μ_s and μ_d are static and dynamic moduli, respectively.

For quantitative comparison, Figure 2-6 (a) shows the mean a_{cr} values of all gel types as a function of dynamic shear modulus (μ_D) for each gel type using both Figure 2-6 and

31

Table 2-1. At lower μ_D (< 100 kPa), a general trend for all gel types is that the mean a_{cr} monotonically increases with an increase of μ_D. The higher stiffness of soft materials results in increasing resistance against bubble expansion and, as a result, higher input acceleration is required to provoke cavitation nucleation and bubble growth. At higher μ_D (> 100 kPa), the difference in the $a_{cr} - \mu_D$ relation becomes more distinctive for each gel type. For example, a decrease of a_{cr} becomes noticeable for agar while a_{cr} keeps increasing for gelatin A/B and levels for agarose. The different trends of the $a_{cr} - \mu_D$ relations for each gel type suggest that μ_D alone cannot explain the measured critical accelerations and, therefore, other material properties such as v_k (kinetic viscosity), γ (surface energy), and G_c (fracture toughness) may need to be included to explain the observed behaviors. For example, consider the mean a_{cr} values near $\mu_D = 40$ kPa. Agarose and gelatin A samples may have higher critical acceleration than gelatin B samples due to larger v_k and γ as shown in Table 2-1. Additional theoretical analyses will be performed in the following section to assess the contribution of v_k and γ to the gel-type-dependent a_{cr} trends.
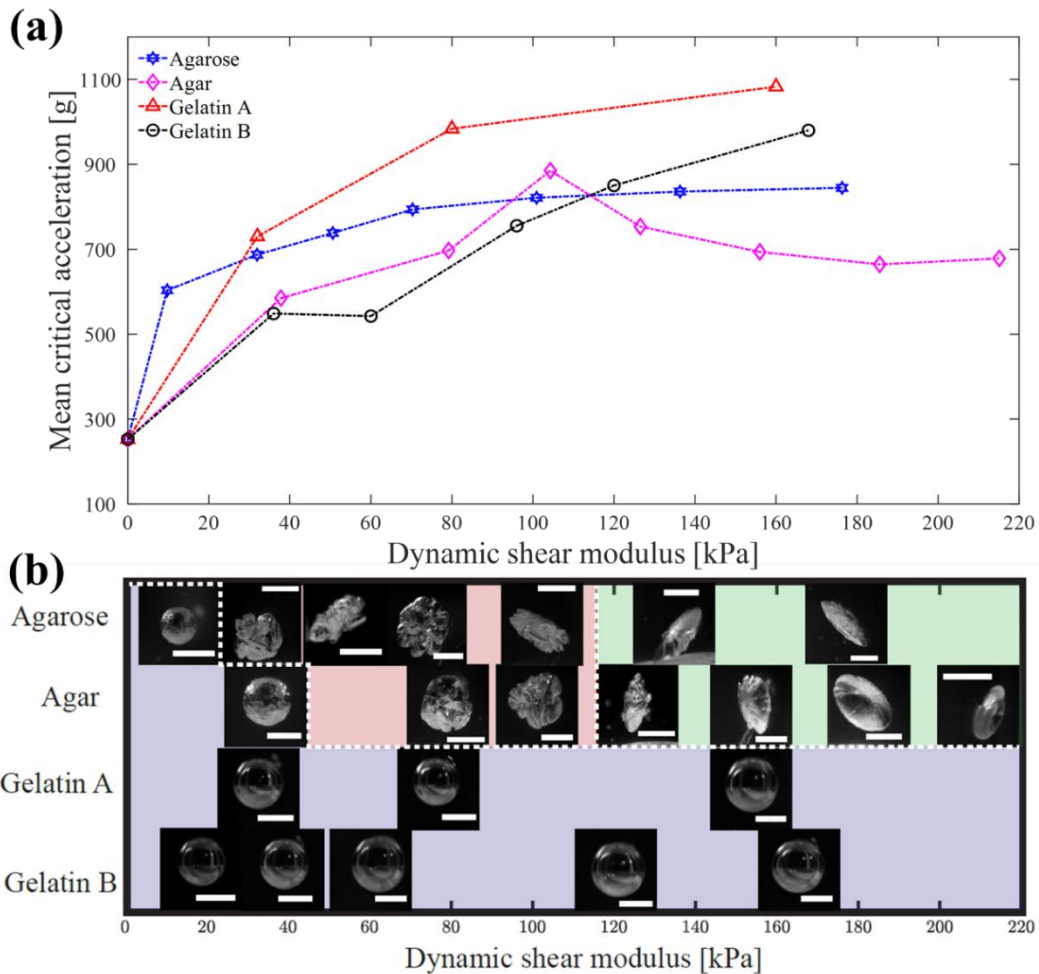
Figure 2-8. (a) The mean values of the critical acceleration (a_{cr}) for Agarose (blue hexagon), agar (pink diamond), gelatin B (black circle), and gelatin A (red triangle) as a function of dynamic shear modulus. (b) Image analysis of a cavitation bubble during bubble growth. Each image was captured when a bubble was its maximum size in each sample during an individual impact experiment. To highlight a transition in bubble shape, the images of the maximum bubbles are organized by gel type (vertical) and stiffness (horizontal, dynamic shear modulus). Note that three different bubble shapes, namely, sphere, transitional shape (i.e., bumpy and elongated bubbles), and saucer, are observed and designated by light blue, red, and green colors, respectively. An inserted white scale bar is 2 mm.

33

Gel type	Properties	Concentration [w/v%]							Ref
		0.3	**0.58**	**0.75**	**0.9**	**1.1**	**1.3**	**1.5**	
Agar	μ_s [kPa]	12.6	26.4	34.8	42.2	52.0	61.9	71.7	[70]
	μ_D [kPa]	37.8	79.2	104.3	126.5	156.0	185.6	215.1	
	ν_k [m^2/s]				5 X 10^{-6}				[172]
	γ [N/m]				0.154				[170]
	G_c [J/m^2]	7	8	9	10	11	12	14	[173]
Agarose	μ_s [kPa]	3.28	10.6	16.9	23.4	33.6	45.4	58.8	[169]
	μ_D [kPa]	9.73	31.9	50.6	70.3	100.9	136.3	176.3	
	ν_k [m^2/s]				5 X 10^{-6}				[172]
	γ [N/m]				0.154				[170]
	G_c [J/m^2]				6.5				[174]

Gel type	Properties	Concentration [w/v%]						Ref
		1	**1.5**	**2.5**	**4**	**5**	**7**	
Gelatin A	μ_s [kPa]	3.56	5.33	8.89	14.2	17.8	24.9	*
	μ_D [kPa]	32.0	48.0	80.0	128.0	160.0	223.9	
	ν_k [m^2/s]			10^{-6}				[176]
Gelatin B	μ_s [kPa]	2.67	4	6.67	10.7	13.3	18.7	[69, 175]
	μ_D [kPa]	24	36	60	96	120	168	
	ν_k [m^2/s]			10^{-6}				[176]
	γ [N/m]	0.086	0.085	0.083	0.082	0.082	0.081	[28]
	G_c [J/m^2]	2.02	3.12	5.3	8.59	10.8	15.15	[177, 178]

Table 2-1. Summary of materials properties of agar, agarose, and gelatin A/B. $\mu_s, \mu_D, \nu_k, \gamma,$ and G_c are the static -, dynamic shear modulus, kinematic viscosity, surface energy, and fracture toughness of each gel as a function of a gel concentration (*: The extrapolated values based on the bloom strength difference between gelatin A/ B).

In addition to the critical acceleration, image analysis of cavitation bubbles in each gel sample during bubble growth was performed. This study revealed that cavitation bubble shape depends on both gel types and stiffness as summarized in Figure 2-8 (b). Note that each high-speed camera image in the figure corresponds to the maximum bubble size in a different gel sample during an independent impact experiment. The images are organized by gel types (vertical axis) and gel stiffness (horizontal axis) where three different background colors are used to designate three different bubble shapes: (light blue) *sphere*, (light red) *transitional shape*, and (light green) *saucer*. In the figure, cavitation bubbles with bumpy and elongated profiles are categorized as transitional shape. The bubble shape transition can be also seen in Figure 2-8 (b). Three important observations are 1) cavitation bubbles in gelatin A/B are spherical regardless of gel stiffness (see the light blue area), 2) cavitation bubbles in agarose and agar change its shape from a sphere to saucer and the transition occurs within $30 < \mu_D < 100$ kPa (see the light blue and green areas separated by the light red area), and 3) the bumpy patterns at the bubble-gel interface become less pronounced after the completion of the shape transition ($\mu_D > 100$, see the light green area). The mechanisms of these observations will be theoretically considered in the following section.

Table 2-2. The percentage occurrence of saucer-shaped bubbles at each gel concentration. The three numbers inserted in the parentheses denote the number of spherical, transitional, and saucer cases from left to right, respectively, at each gel concentration.

	Gel type	Concentration [w/v%]						
		0.3	**0.58**	**0.75**	**0.9**	**1.1**	**1.3**	**1.5**
Occurrence of saucer-shaped bubbles (%)	**Agarose**	0 (6/0 /0)	0 (0/1 2/0)	0 (0/8 /0)	0 (0/8 /0)	64.3 (0/5 /9)	100 (0/0 /7)	100 (0/0 /9)
	Agar	0 (9/0 /0)	0 (1/5 /0)	0 (0/6 /0)	12.5 (0/7 /1)	63.6 (0/4 /7)	87.5 (0/2 /14)	100 (0/0 /11)

Table 2-2 summarizes the percentage occurrence of saucer-shaped bubbles in agarose and agar where bubbles nucleated at or near the walls of a gel container (i.e., a transparent cuvette) were excluded to eliminate the possible effect of walls on bubble shape. For agarose, a very sharp transition occurs within a relatively small range of dynamic shear modulus. As an example, the percentage occurrence of saucer-shaped bubbles increases from 0% at 31 kPa (0.58 w/v%) to 64.3% at 101 kPa (1.1 w/v%) and 100% at 133 kPa (1.3 w/v%). For agar, the transition begins at higher μ_D=126.5 kPa (0.9 w/v%) and the rate of change from translational to saucer shape is slower as about 10% of cavitation bubbles were transitional (bumpy/elongated shape) even at μ_D=185.6 kPa (1.3 w/v%) than that of agarose (see Figure 2-9, Figure 2-10, Figure 2-11, and Figure 2-12).

37
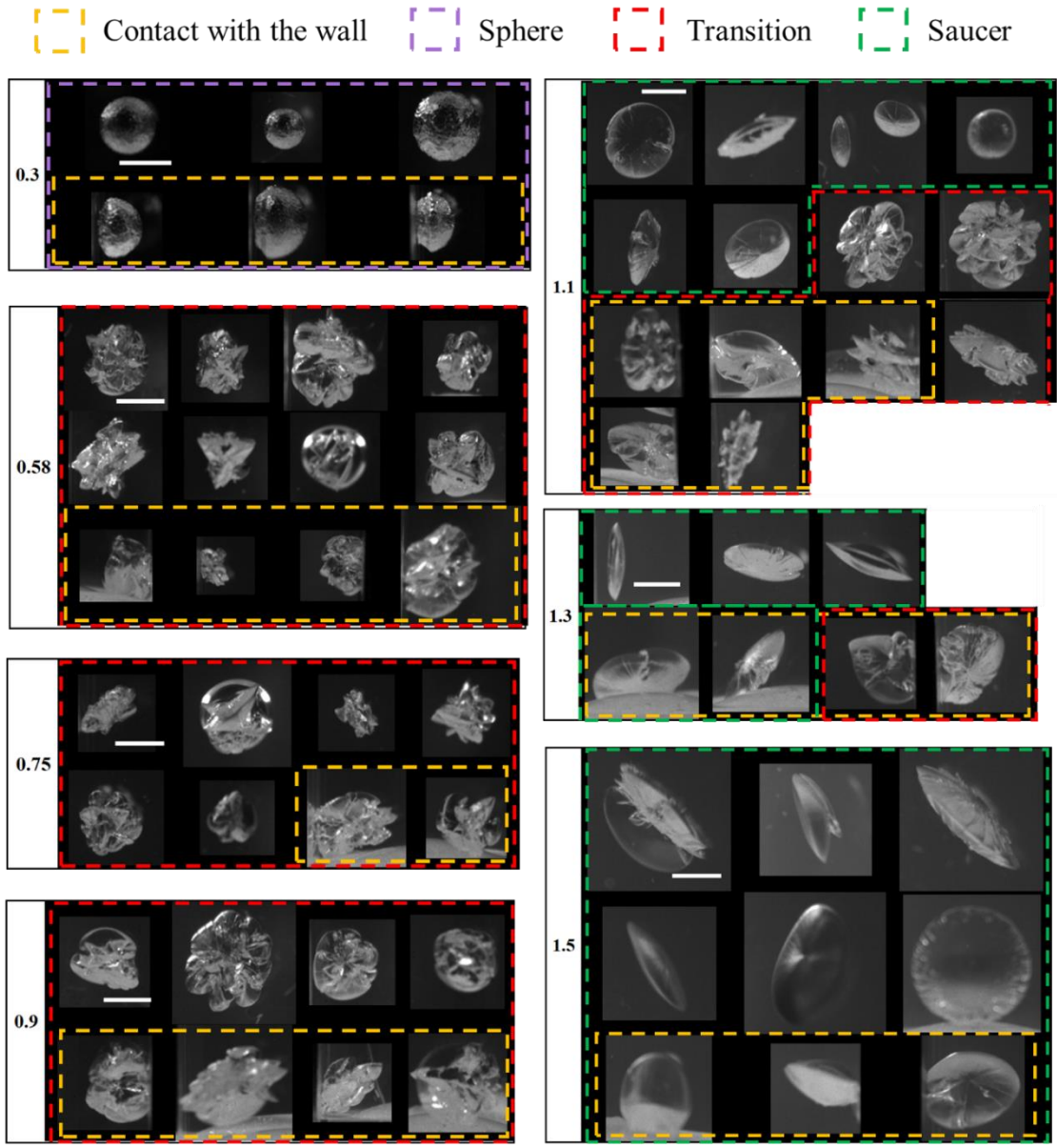
Figure 2-9. Bubble shape at the maximum radius and the number in the first column denotes w/t% concentration for agarose gels and the dotted yellow, purple, red, and green borders represent "bubble contact with the wall", sphere, transition, and saucer bubble shape, respectively. The white bar present 2mm scale.
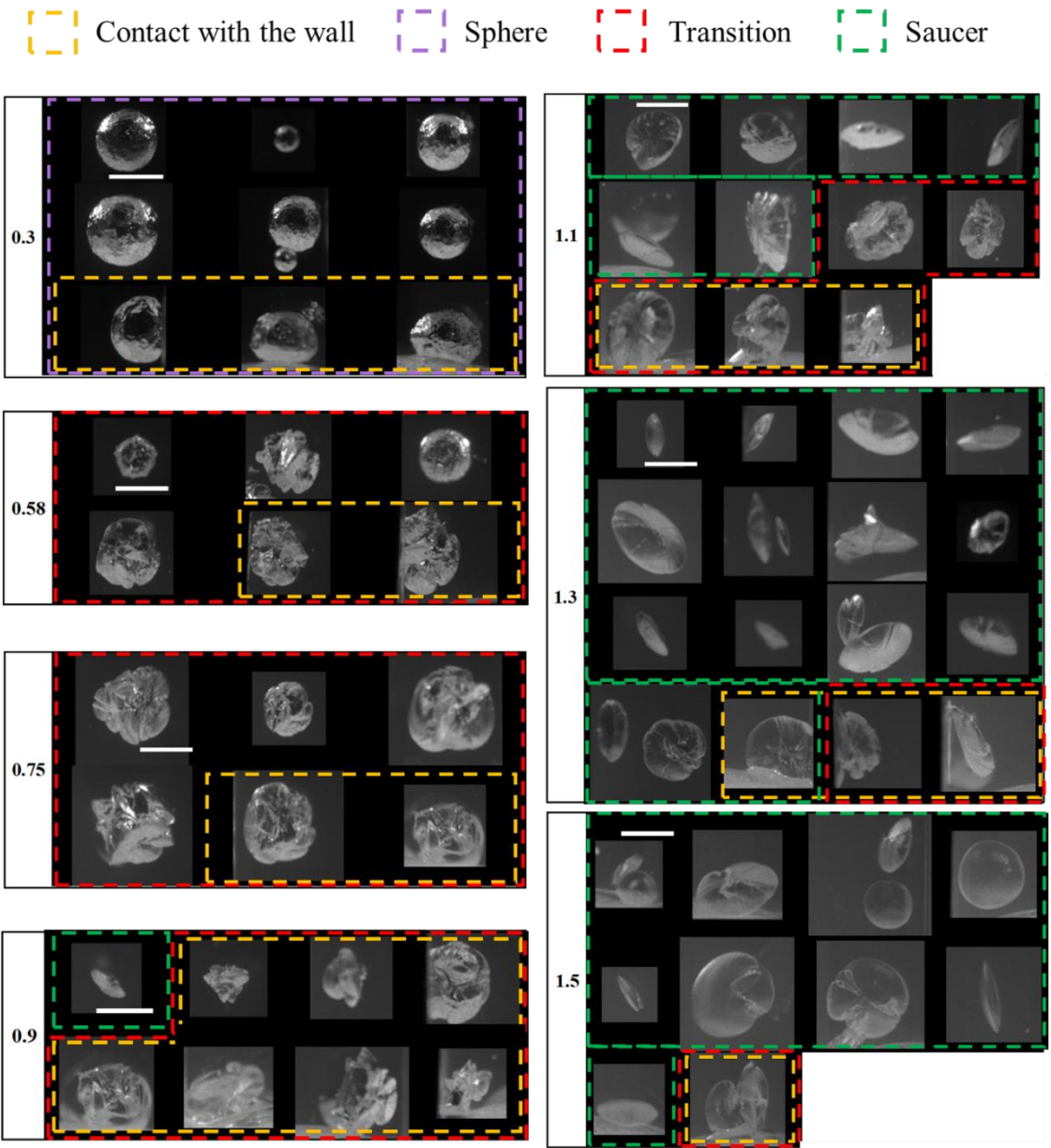
Figure 2-10. Bubble shape at the maximum radius and the number in the first column denotes w/t% concentration for agar gels and the dotted yellow, purple, red, and green borders represent "bubble contact with the wall", sphere, transition, and saucer bubble shape, respectively. The white bar present 2mm scale.
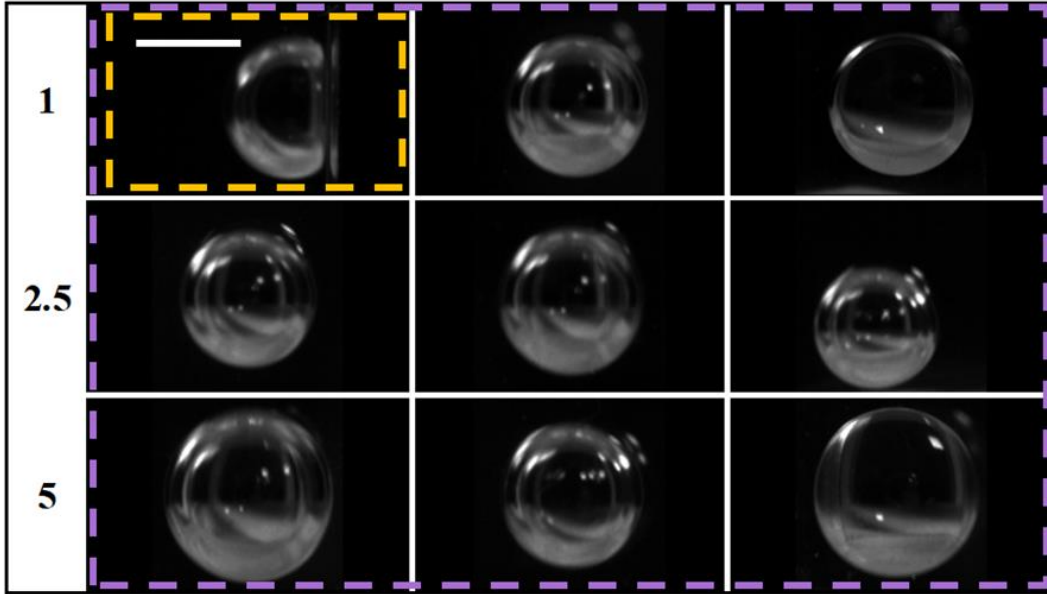
Figure 2-11. Corresponding bubble shape at the maximum radius and the number in the first column denotes w/t% concentration for gelatin A gels and the dotted yellow and purple borders represent "bubble contact with the wall" and spherical bubble shape, respectively. The white bar present 2mm scale.
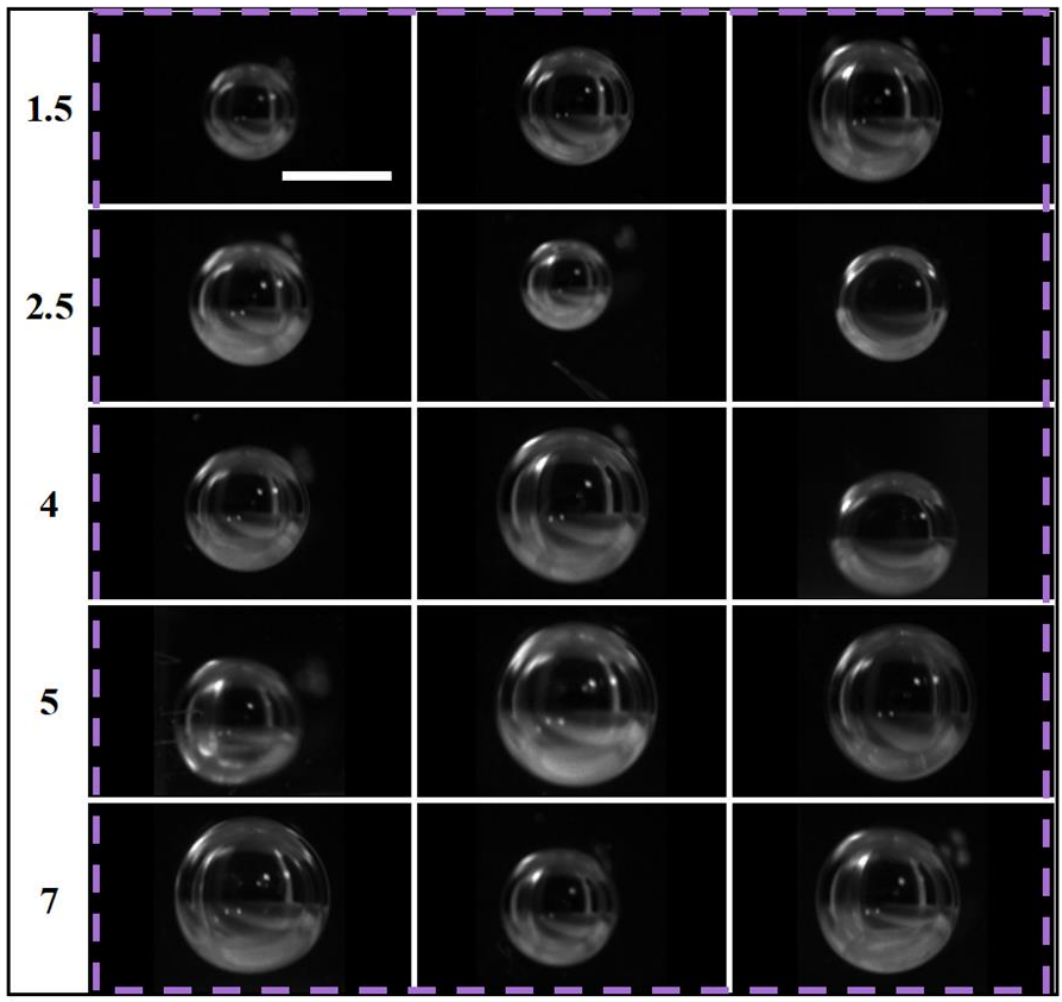
Figure 2-12. Corresponding bubble shape at the maximum radius and the number in the first column denotes w/t% concentration for gelatin B gels and the dotted yellow and purple borders represent "bubble contact with the wall" and spherical bubble shape, respectively. The white bar present 2mm scale.

Gel type	C(w/v%)	0.3	0.58	0.75	0.9	1.1	1.3	1.5	Average
Agar	Surface cavitation occurrence (%)	35.7 (5/14)	53.8 (7/13)	41.7 (5/12)	25 (3/12)	13.3 (2/15)	39.3 (11/28)	26.7 (4/15)	34%
Agarose		53.8 (7/13)	14.3 (2/14)	33.3 (4/12)	42.9 (6/14)	22.2 (4/18)	38.5 (5/13)	18.8 (3/16)	31%

Gel type	C(w/v%)	1	1.5	2.5	4	5	7	Average
Gelatin A	Surface cavitation occurrence(%)	58.3 (7/12)		23.1 (3/13)		16.7 (2/12)		32.4%
Gelatin B			41.7 (5/12)	38.5 (5/13)	46.7 (7/15)	13.4 (2/15)	25 (3/12)	32.8%

Table 2-3. Surface cavitation occurrences for the respective gel as a function of its concentration.

For the intermediate concentration levels (0.58~1.1w/v%) of agar or agarose, the direction of crack propagation appears to be randomly distributed (see Figure 2-9, Figure 2-10, Figure 2-11, and Figure 2-12). However, cracks in high concentration agar/agarose gels (>1.1w/v%) appear to have a preferred orientation, i.e., 45-degree with respect to the horizontal axis. These interesting observations are still preliminary and would require additional studies with the use of two high speed cameras to be conclusive. One possible explanation for the preferred orientation is that the linear acceleration induces axial loading conditions and, as a result, the maximum shear stress occurs along the principal direction oriented at 45-degree. In addition, the image analyses indicate that the probability of surface cavitation (i.e., nucleation at the cuvette-gel interface) is about 31~34% for all gel types and concentrations, while 66~69% of bubbles occur within a gel as summarized in Table 2-3.

2.3 Theory

2.3.1 Cavitation Nucleation in Soft Gels

The Rayleigh-Plesset equation (RP) with a Kelvin-Voigt viscoelastic model [68, 70, 182, 183] is utilized to analyze the experimentally observed cavitation nucleation and subsequential bubble dynamics in gels. In the following analytical study, it is assumed that gels are the Neo-Hookean material, one of the common material models for the nonlinear stress-strain behavior of hyperelastic gels with large deformations [27, 184, 185]. The governing equation for the dynamic behavior of a spherical bubble in a *h*-tall sample can be described as follows [29]:

Equation 2-1

$$\frac{p_v - p_{in}(t, a_{in}, h)}{\rho} + \frac{p_{g0}}{\rho}\left(\frac{r_0}{r}\right)^{3k} = r\ddot{r} + \frac{3}{2}\dot{r}^2 + \frac{4v\dot{r}}{r} + \frac{2\gamma}{\rho r} + \frac{\mu_D}{2\rho}\left[5 - \frac{4r_0}{r} - \left(\frac{r_0}{r}\right)^4\right]$$

where p_v is a vapor pressure, p_{in} is a input pressure, ρ is the material density, p_{g0} is the initial partial pressure of the gas in a bubble, i.e., $p_{g0} = p_\infty(0) - p_v(T_\infty) + 2\gamma/r_0$, p_∞ and T_∞ are the ambient pressure and temperature, r_o and r are the initial and current bubble radius, $k, \mu_D, v,$ and γ are the polytropic index ($k = 1$), dynamic shear modulus, viscosity, and surface tension of the gels, respectively, and the overdot and double overdot describe the first and second derivative with respect to time (*t*). Note that Equation 2-1 is used for the prediction of cavitation nucleation where the initial bubble size is less than a few micrometers. Because of the small bubble size near cavitation nucleation, it is assumed an isothermal process (k=1). Equation 2-1 can be numerically solved using MATLAB, i.e.,

ODE45 function with the given initial conditions, $r(0) = r_0$ and $\dot{r}(0) = 0$, from experiments.
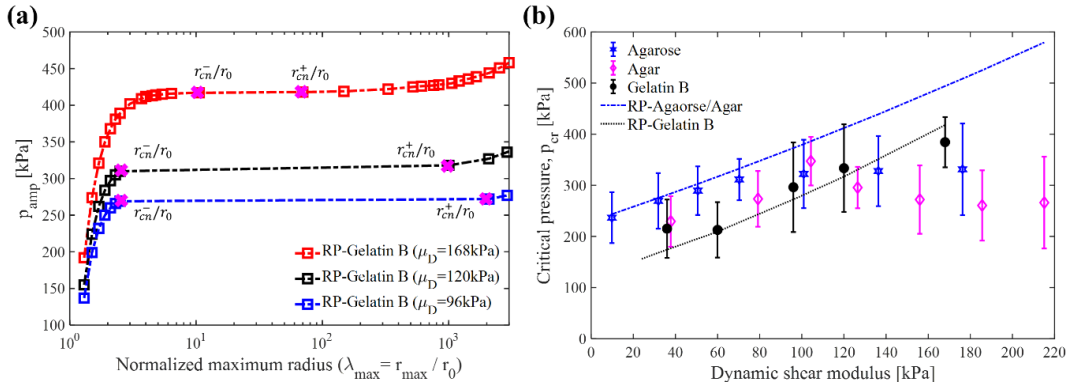
Figure 2-13. Theoretical predictions using the Rayleigh-Plesset (RP) equation with the Neo-Hookean material model. (a) The normalized maximum bubble radius $(\lambda_{max} = r_{max}/r_0)$ for three different dynamic shear moduli (i.e., $\mu_D = 96$, 120, and 168 kPa) with increasing amplitude of input pressure (p_{amp}). "x" markers indicate a rapid bubble radius change from r_{cn}^-/r_0 to r_{cn}^+/r_0 at $dp_{amp}/d\lambda_{max} \approx 0$. (b) The experimental data and theoretical predictions for the critical pressure (p_{cr}) are directly compared. The blue dash-dotted and black dotted lines are the theoretical predictions of p_{cr} for agarose/agar and gelatin B, respectively, based on the RP equation. The blue hexagon, pink diamond, and black solid circle denote the experimental mean values for agarose, agar, and gelatin B, respectively, where the error bars indicate 95% confidence intervals.

It is important to note that a direct measure of an initial bubble radius (r_0) is experimentally very challenging although use of accurate r_0 is important for studying cavitation nucleation [29]. To address this, Equation 2-1 is used to estimate reasonable initial bubble size in pure water by substituting the well-known properties of pure water [186]. It has been found that the experimental results in Figure 2-6 and theoretical predictions using Equation 2-1 match well to each other when $r_0 = 0.474$ μm, which is also consistent with the previous studies [29]. Because all gel samples were prepared using the same high purity water, it is assumed that the same initial bubble size for all samples

44

in the following analyses. Like pure water, the material properties summarized in Table 2-1 are substituted into Equation 2-1 for individual gel samples.

In addition, the dynamic shear modulus (μ_D) is used for all types of gels due to large strain rates ($\approx 10^5 s^{-1}$ [101]) associated with cavitation bubble dynamics. Following the previous studies [28, 29], the acceleration-induced stress is estimated by $p_{in}(t) = \rho(a_{in} - g)h$ where ρ and h are the density and height of a sample ($h = 40$ mm), and a_{in} is input acceleration applied to the sample. To mimic the input experimentally measured acceleration profile, the acceleration is given by $a_{in}(t) = -a_{amp}\sin(\omega t)$ where $\omega = 1000\pi$ s^{-1} is used to capture the experimentally characterized time scale of the impact event, i.e., the largest negative a_{in} occurs at 0.4-0.5 ms.

To predict the critical pressure (p_{cr}) at cavitation nucleation, Equation 2-1 is numerically solved with increasing input pressure magnitude (p_{amp}) for each gel type. For example, Figure 2-13 (a) shows how the normalized maximum bubble radius (λ_{max}) and the amplitude of acceleration induced pressure (p_{amp}) are correlated for gelatin B with three different dynamic shear moduli ($\mu_D = 96, 120,$ and $168\ kPa$). The corresponding ν_k and γ values given in Table 2-1 are used for each shear modulus. All three cases exhibit similar trends: (1) the slope of the $p_{amp} - \lambda_{max}$ (i.e., $dp_{amp}/d\lambda_{max}$) decreases with increasing λ_{max} within $\lambda_{max} < 10$, and then (2) a jump in λ_{max} as $dp_{amp}/d\lambda_{max}$ approaches to zero. The sudden jumps in λ_{max} from r_{cn}^-/r_0 to r_{cn}^+/r_0 (see "x" markers in Figure 2-13 (a)) are the key signature of cavitation nucleation and burst [1, 187] and are due to the change in the dominant mechanism of cavitation dynamics from surface tension to inertia effects with increasing bubble radius [29]. Note that the amplitude

of the λ_{max} jump becomes smaller with increasing shear modulus because larger energy is required to deform stiffer gels.

Figure 2-13 (b) summarizes the experimentally and theoretically obtained critical pressure values of three different types of gels including agarose, agar, and gelatin B. The experimental results, i.e., the mean critical pressure ($\bar{p}_{cr}$) with 95% confidence intervals, are directly compared with the theoretical results of agarose/agar (a blue dash-dotted line) and gelatin B (a black dotted line). Note that the direct comparison for gelatin A is not feasible because the surface energy of gelatin A, to the best of knowledge, is not available in the literature. Similarly, the reported surface tension (γ) of agarose and agar are also

Agarose	μ_D [kPa]			
	9.73-31.9	9.73-50.6	9.73-70.3	9.73-100.9
R-squared	0.8532	0.8277	0.7687	0.1214

Gelatin B	μ_D [kPa]
	36-168
R-squared	0.8356

Table 2-4. R-squared values for the measured critical pressures of agarose and gelatin B compared with the theoretical results obtained from Equation 2-1.

somewhat limited and, therefore, the simulation results for agarose and agar are overlapped to each other. These factors highlight the experimental challenges in quantitative characterization of soft gels under dynamic load.

For gelatin B in Figure 2-13 (b), the theoretical results (the black dotted line) capture the experimental measurements (black solid circles) accurately over the entire range of dynamic shear modulus ($R^2 \approx 0.8$ without using any fitting parameters as shown in Table 2-4). For agarose, the experimental p_{cr} (blue hexagons) follows the same trend of the

theoretical predictions (the blue dash-dotted line) up to about 70 kPa ($R^2 \approx 0.8$ in Table 2-4), but the discrepancy between them considerably increases when $\mu_D > 100$ kPa ($R^2 \approx 0.1$ as illustrated in Table 2-4). Agar samples also qualitatively follow the similar trend of agarose, although their experimental P_{cr} means (pink diamonds) do not quantitatively match well with the predictions. As pointed out above, the quantitative disagreement for agar is likely due to a lack of available material properties in the literature. These results showing a good agreement between theory and experiments within a lower bound of μ_D indicate that the assumptions on initial bubble size (r_o) and shear modulus (μ_D) are indeed reasonable to analyze the bubble dynamics in soft gel samples.

Even though the RP equation offers good prediction of different gels at lower μ_D ($<$ 70 kPa), the theory-experimental discrepancy for agarose/agar at higher μ_D (> 100 kPa) remains unsolved. The image analysis suggests that the discrepancy is likely attributed to the shape transition because a spherical bubble is the key assumption for the RP equation. In other words, the RP equation is not valid anymore for agarose and agar after the bubble shape transition. In the following sections, a new theoretical approach that provides insights into the mechanisms of the bubble shape transition in different gels will be considered.

Accurate characterization of soft biomaterial properties, including biological hydrogels or tissues, remains challenging due to their soft, labile nature, nonlinear material response, and strain-rate-dependent material properties and understandably, material properties of many hydrogels are not readily available including their surface tension and fracture toughness. Although surface tension and fracture toughness would strongly influence

47

cavitation nucleation, growth, and collapse in soft matters, this will remain as future work due to a lack of available experimental measurements on these properties.

2.3.2 The Ductile-to-brittle Shape Transition
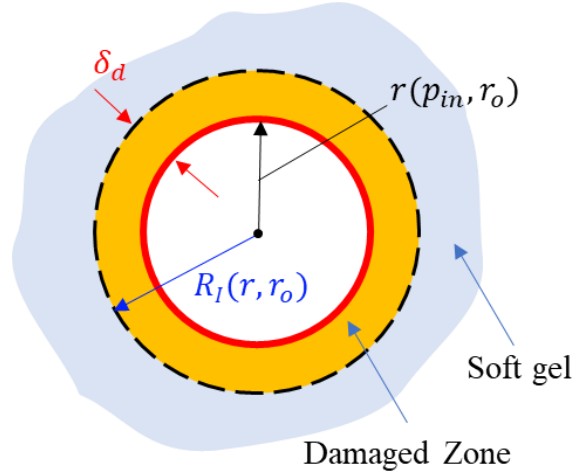
Figure 2-14. A schematic of a damaged zone model. $\delta_d, r(p_{in}, r_o)$, and $R_I(r, r_o)$ are the damaged zone thickness, current bubble radius due to input pressure p_{in}, and interfacial radius between the damaged and undamaged zones in the soft gel.

In the previous section, the theoretical analyses of impact-induced cavitation nucleation in different gels were performed and it was found that the theory-experiment discrepancy for agarose and agar likely due to the bubble shape transition. Here, the possible mechanisms that give rise to the different bubble growth behavior in a soft gel, namely, ductile (spherical shape) and brittle (saucer shape) bubble growth are theoretically explored. To consider bubble shape during bubble burst, it is assumed that an inertial cavitation bubble is already nucleated in an initially purely elastic gel and the initial bubble shape is spherical. While a spherical bubble keeps growing in an elastic gel in time, the gel deforms to accommodate the volume change of the bubble. The work done associated with the volume change will be stored in the gel as strain energy without any energy loss.

48

As a reminder, the main emphasis is placed on the theoretical analysis on the bubble shape transition from sphere to saucer during bubble growth as shown in Figure 2-8 (b). To understand this gel-type and gel-concentration dependent transition, a spherical bubble in an infinitely large, incompressible gel is considered as shown in Figure 2-14. Due to the simplicity, it is assumed that the bubble radius (r) changes quasi-statically with input pressure (p_{in}), i.e., time-dependent behavior is ignored. In addition, dynamic fracture toughness of gels at high strain rates is not readily available in the literature. As mentioned above, the current bubble size r is assumed to be larger than a threshold radius for cavitation bubble burst because the current focus is on different bubble growth modes during bubble burst. Following recent work [185, 188, 189], it is assumed that material damage in gel induced by bubble growth is concentrated at the spherical-bubble and gel interface with the thickness (δ_d), referred to as *a damaged zone*, as schematically shown in Figure 2-14. Note that $\delta_d > 0$ when current bubble radius r is larger than the critical radius (r_f) that corresponds to the onset of gel damage.

Let the interfacial radius between the undamaged and damaged zones in the gel be $R_I(r, r_o) = r(p_{in}, r_o) + \delta_d$. Due to the incompressibility, the gel satisfies $R^3 - r^3 = R_o^3 - r_o^3$ or

Equation 2-2

$$R_o = [R^3 - r^3 + r_o^3]^{\frac{1}{3}}$$

where R_o and R are radial coordinates of the same position in soft matter with respect to r_o and r, respectively [184, 185]. Note that material damage is forming in the gel when $r \geq r_f$ as the damaged zone does not contribute toward the mechanical

49

resistance against bubble growth. Also, during the damage accumulation, the interfacial

radius (R_I) satisfies the following relations:

$$\frac{R_I}{R_o} = \frac{r + \delta_d}{R_o(r + \delta_d)} = \frac{r + \delta_d}{((r + \delta_d)^3 - r^3 + r_o^3)^{\frac{1}{3}}} = \frac{r_f}{r_o} = \lambda_f$$

In order to find R_I (the interface between the damaged and undamaged zones) within

the gel, the material property (λ_f) as given in **Equation 2-3** is used. Note that **Equation 2-2**

is substituted into **Equation 2-3** to obtain new R_o values that are corresponding to $R_I =$

$r + \delta_d$ for $\delta_d > 0$ by using the incompressibility condition. This new R_o is allowable

to exclude the damaged zone from the initial bubble size after the onset of the damaged

zone. In other words, the total volume (i.e., the sum of the damaged and undamaged zones)

of gel does not change, but the volume of undamaged zone decreases with increasing δ_d

and, therefore, the effective R_o increases (detailed derivation can be found in [185]).

By using both **Equation 2-2** and **Equation 2-3**, the thickness of the damaged zone can

be written as [185]

$$\delta_d = \begin{cases} 0, & if\ \dfrac{r}{r_o} \leq \lambda_f \\ \lambda_f \left[\dfrac{r^3 - r_o^3}{\lambda_f^3 - 1} \right]^{\frac{1}{3}} - r, & otherwise. \end{cases}$$

Note that while $r_o = 0.474\,\mu m$ has been obtained in the previous analysis, the reasonable values of the normalized critical radius (referred to as the failure stretch ratio, $\lambda_f = r_f/r_o$) is still required to evaluate δ_d for each type of gel.

In this regard, the Griffith's criterion-based fracture model is utilized. The stored elastic strain energy due to the bubble growth from r_o to r in Figure 2-14. A schematic of a damaged zone model. $\delta_d, r(p_{in}, r_o)$, and $R_I(r, r_o)$ are the damaged zone thickness, current bubble radius due to input pressure p_{in}, and interfacial radius between the damaged and undamaged zones in the soft gel. can be written as [184, 190, 191]

Equation 2-5

$$U_E = \int_{r_o}^{r} 4\pi W(r, r_o) r^2 dr$$

where $W = \frac{\mu_s}{2}[5 - 4(r/r_0)^{-1} - (r/r_0)^{-4}]$. Using Equation 2-5, the change of stored elastic energy per bubble surface area (i.e., $\partial U_E/\partial A$) can be obtained as shown below:

Equation 2-6

$$-\left(\frac{\partial U_E}{\partial A}\right)\bigg|_V = 2r_o f(\lambda) \geq G_c \quad \text{and} \quad f(\lambda) = \lambda^4 \frac{\partial\left(\epsilon^{-3}\int_1^\epsilon W\lambda_a^2 d\lambda_a\right)}{\partial \epsilon}\bigg|_{\epsilon=\lambda}$$

where $A = 4\pi r^2$, $\lambda = r/r_0$, λ_a and ϵ are dummy indices, and G_c is fracture toughness. Note that the onset of material damage to gel occurs when $2r_o f(\lambda = \lambda_f) = G_c$. Both equations in Equation 2-6 for λ_f are numerically solved with an incremental increase of λ (step size=0.1). As a reminder, $r_o = 0.474\,\mu m$ for all gels and the material properties of different gel types summarized in Table 2-1 are used.
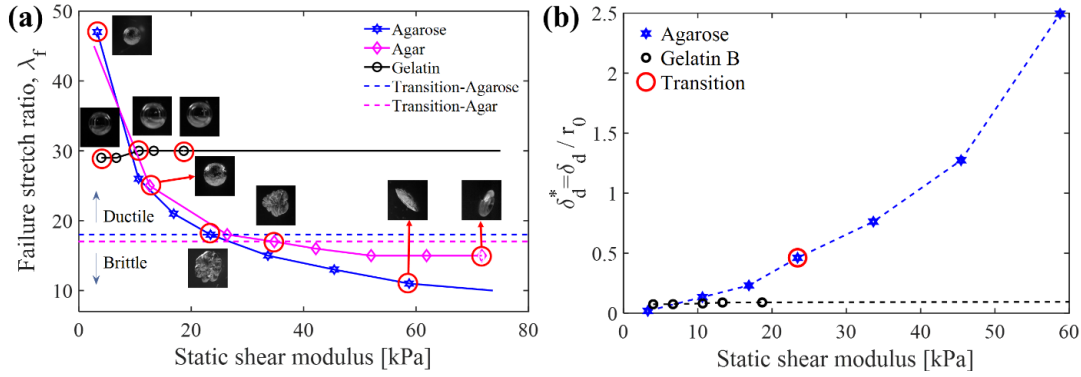
Figure 2-15. (a) Failure strain ratio (λ_f) as a function of the static shear modulus for agarose and agar gels after respective transition point. The inset images show bubble shape for each gel at different static shear modulus. (b) A normalized damaged zone thickness (δ_d^*) as a function of the static shear modulus and the red dotted line corresponds to the respective transition point for agarose and agar gels.

Figure 2-15 (a) presents the failure stretch ratio (λ_f) of agarose and agar gels with respect to the static shear modulus (μ_s). For both agarose (a blue line) and agar (a pink line), λ_f exponentially decreases with increasing μ_s. This result indicates that a large bubble expansion during bubble burst cannot be accommodated by pure elastic deformation of the gels for stiffer gels or equivalently at higher concentrations and, as a result, the gels likely form a larger damaged zone with reduction of λ_f. For comparison, the representative bubble shapes of each sample are directly added to the corresponding μ_s values (see optical images near red circles). Note that $\lambda_f = 17 \sim 18$ corresponds to the transitional shape of agarose and agar as spherical and saucer bubbles were observed for $\lambda_f > 18$ and < 17, respectively (see dotted lines in Figure 2-15 (a)). Unlike agarose and agar, λ_f for gelatin B is in a range of $29 \sim 30$ (a solid black line), which is considerably larger than where the shape transition occurs for agarose and agar, and insensitive to its μ_s value. These considerably different trends in the $\lambda_f - \mu_s$ relations provide mechanistic

insights in why cavitation bubbles in gelatin B are spherical regardless of μ_s (i.e., no bubble shape transition).

As discussed above, it appears that the gel-type-dependent fracture toughness (G_c) dominates the bubble shape during rapid bubble growth as larger G_c increases stretchability of gels. This conclusion offers qualitative explanation for the observed shape

Agarose	Static shear modulus (μ_s)						
	3.28	10.6	16.9	23.4	33.6	45.4	58.8
r_{max} (mm)	2.84	3.35	3.05	3.83	3.66	3.98	4.72

Gelatin B	Static shear modulus (μ_s)				
	4	6.67	10.7	13.3	18.7
r_{max} (mm)	2.59	2.61	3.13	3.43	3.45

Table 2-6. Experimental averaged maximum bubble radius for agarose and gelatin B gels as a function of static shear modulus (μ_s).

	μ_s (kPa)						
	3.28	10.6	16.9	23.4	33.6	45.4	58.8
δ_d (μm)	0.009	0.064	0.110	0.219	0.362	0.604	1.183

Table 2-5. Thickness of the damaged zone for agarose gel.

transition for different gels. However, it is important to note that the λ_f values (< 50) in Figure 2-15 (a) are much smaller than the λ_{max} values ($10^2 \sim 10^3$) after bubble burst (see the jumps from r_{cn}^-/r_0 to r_{cn}^+/r_0 in Figure 2-13 (a)). Because of $\lambda_{max} \gg \lambda_f$ after the onset of bubble burst, $\delta_d > 0$ is expected and the effect of the damaged zone on the bubble shape transition must be appropriately considered. To obtain δ_d, Equation 4 can be solved using both λ_f presented in Figure 2-15 (a) and the experimentally measured maximum bubble radius from the image analyses of high-speed camera images. The

average values of the measured $r_{max} (= 3\sim5$ mm) for agarose and gelatin B at different gel concentrations are given in Table 2-6.

	μ_s (kPa)					
	2.67	4	6.67	10.7	13.3	18.7
δ_d (μm)	0.0354	0.0357	0.0386	0.0424	0.0426	0.0457

Table 2-7. Thickness of the damaged zone for gelatin B gel.

Figure 2-15 (b) shows the normalized damaged zone thickness ($\delta_d^* = \delta_d/r_0$) for agarose and gelatin B with increasing μ_s. The increasing rate of δ_d^* for agarose is much fast compared to gelatin B. For example, δ_d for agarose increases from 0.009 µm at $\mu_s =$
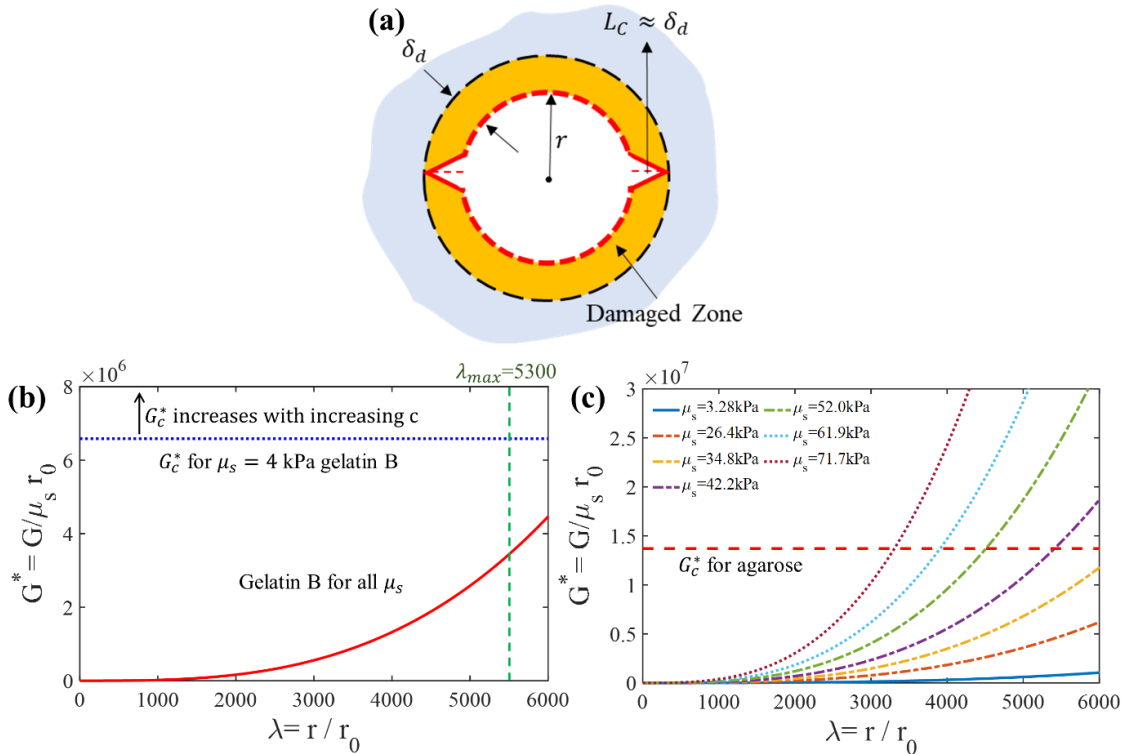
Figure 2-16. (a) A schematic of a cavitation bubble with symmetric cracks in the damaged zone where L_C is the crack length. (b)-(c) The normalized energy release rates ($G^* = G/\mu_s r_o$) for gelatin B and agarose where $G_c^* = G_C/\mu_s r_o$ is the normalized fracture toughness.

3.28 kPa to 0.219 μm at $\mu_s = 23.4$ kPa (see Table 2-5 for more details) while δ_d^* is consistently small (35~45 nm) for gelatin B (also summarized in Table 2-7).

For further analysis, it is assumed that cracks in gel can occur only within the damaged zone as schematically shown in Figure 2-16 (a), and they are preferably oriented in the radial direction due to circumferential tensile stress. The assumptions are allowable to estimate crack length (L_c) by the damaged zone thickness (i.e., $L_c = \delta_d$). For the gelatin B case, a stress concentration factor at the tip of a L_c-long crack is not significant due to extremely small δ_d (~40 nm) as shown in Figure 2-15 (b). On the other hands, the crack length in agarose is very sensitive to gel stiffness (i.e., δ_d increases by 131 times from $\mu_s = 3.28$ to 58.8 kPa) and, therefore, the L_c-dependent stress concentration needs to be explored to determine the conditions for crack propagation and arrest, corresponding to brittle and ductile bubble growth, respectively.

Following [189], the energy release rate (G) of gel with an L_c-long crack can be written as $G = 2\Gamma(\lambda)W(\lambda)L_c$ where $W(\lambda)$ is the strain energy density function of Neo-Hookean material and $\Gamma(\lambda)$ is a dimensionless function that depends on the current bubble state. Using $L_c \approx \delta_d$, it can be shown that the energy release rate of a cavitation bubble in a gel with the two L_c-long cracks can be estimated by

Equation 2-7

$$G = \frac{2L_c}{\lambda} \left(\frac{1.513\lambda^{\frac{3}{2}} - 0.076}{\lambda^{\frac{3}{2}} - 0.6325} \right) \left(\frac{\mu_s(\lambda^3 + \lambda^{-3} - 2)}{2} \right)$$
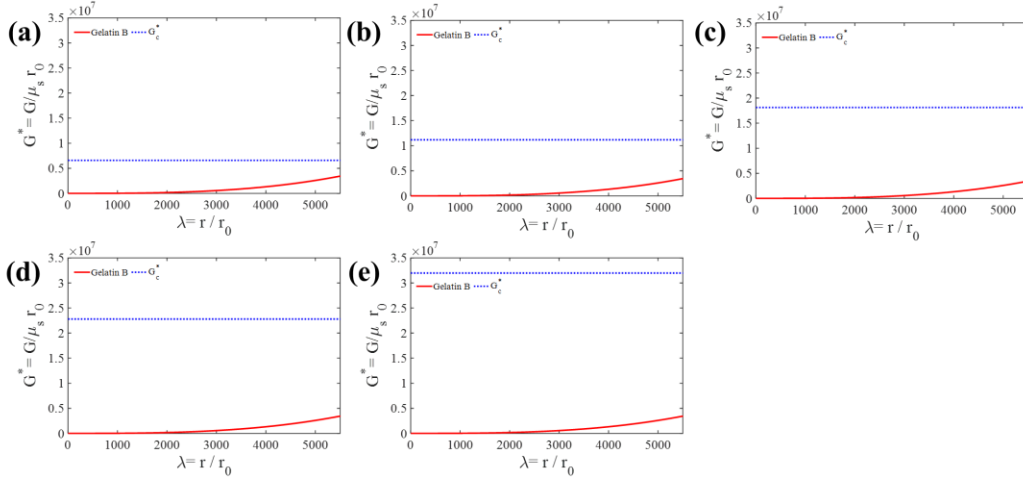
Figure 2-17. The normalized energy release rate (G^*) for gelatin B gel as a function of λ based on the λ_f from Figure 5 (a). (a), (b), (c), (d), and (e) represent the relation G^* and λ with respect to the corresponding μ_s.

Using Equation 2-7, the normalized energy release rates ($G^* = G/\mu_s r_o$) for gelatin B

and agarose are shown in Figure 2-16 (b) and (c), respectively. Again, $G \geq G_C$ is used as

a criterion for crack propagation.

For gelatin B, δ_d is small (about 40 nm) and insensitive to μ_s and, as a result, the

solid red line in Figure 2-16 (b) represents the $G^* - \lambda$ relations for all gel concentrations

(or equivalently for all μ_s). The blue dotted line indicates the known G_C^* value for a 1.5

w/v% gelatin B sample ($\mu_s = 4$ kPa). As expected, G^* increases as a bubble grows due

to larger material deformation and the corresponding elastic energy stored in the gel.

Interestingly, $G^* < G_C^*$ even when $\lambda = 6000$, which predicts that a crack in gelatin B

cannot propagate during the bubble burst. To quantitatively compare these predictions with

the experiment results, the maximum bubble size (r_{max}) in 1.5 w/v% gelatin B samples

was experimentally estimated using the high-speed camera images. The measured average

r_{max} is about 2.5 mm, which gives $\lambda_{max}(= r_{max}/r_o \approx 5300)$ (see the green dotted line

in Figure 2-16 (b)). Note that $G^* < G_C^*$ at $\lambda_{max} = 5300$ regardless of gel concentrations

and, therefore, spherical bubble growth is expected for the gelatin B samples. It is important to emphasize that the concentration-dependent fracture toughness of gelatin B increases with increasing concentration (c). Due to higher G_C^*, crack propagation beyond the damaged zone becomes even less likely among the gelatin B samples with higher c (see Figure 2-17 for more details).

When compared to gelatin B, agarose in Figure 2-16 (c) qualitatively exhibits a similar trend, i.e., G^* increases with λ, but presents quantitatively different behavior. For example, the increasing rate of G^* strongly depends on μ_s because a stiffer gel forms much longer cracks within a thicker damaged zone ($L_c = \delta_d$). As a result, the critical condition $G^*(\lambda_{cr}) = G_C^*$ satisfies, depending on its modulus, at significant different λ values (e.g., $\lambda_{cr} \approx 3000$ for $\mu_s = 71.7$ kPa while $\lambda_{cr} \gg 6000$ for $\mu_s = 3.28$ kPa). This result indicates that a crack in stiffer agarose becomes unstable at much lower λ. Note that G_C^* for agarose (see a dotted red line) is insensitive to μ_s.

Again, $r_{max} \approx 2.8$ mm and $\lambda_{max} \approx 6000$ are experimentally estimated from spherical bubbles observed in 0.3 w/v% agarose for quantitatively comparing the theoretical and experimental results. It is worth noting that radius measurements from non-spherical bubbles, observed in higher-concentration agarose samples due to the ductile-to-brittle transition, becomes non-trivial. At $\lambda_{max} \approx 6000$, $G^* < G_C^*$ for $\mu_s = 3.28$, 26.4, and 34.8 kPa while $G^* \geq G_C^*$ for $\mu_s = 42.2$, 52.0, 61.9 and 71.7 kPa. These theoretical predictions clearly indicate that there is the critical value of μ_s that triggers crack propagation. In other words, bubble grows spherically below the critical value (e.g., $\mu_s = 3.28$, 26.4, and 34.8 kPa) because cracks are bounded within the damaged zone.

57

Bubble shape undergoes the transition near the critical μ_s value accompanied with transitional bubble shape, and then becomes saucer shape after the completion of the shape transition due to crack propagation from the damaged zone.

In sum, the concepts of the damaged zone and maximum crack length in soft gel have been combined together to provide the theoretical interpretation of the experimentally observed transition in cavitation bubble growth. The key predictions of the theoretical approach are 1) for gelatin B, $G_C^* > G^*$ for all μ_s and, hence, spherical cavitation bubble growth is expected without any shape change, 2) for agarose, there is a transition from $G_C^* > G^*$ to $G_C^* \leq G^*$ due to $\mu_s(c)$-dependent crack length. This change in the material response from formation and expansion of the damaged zone to crack formation and propagation gives rise to the unique ductile-to-brittle transition for agarose and agar. These predictions match well with the experimental summaries in Figure 2-8 (b). With this, it has been concluded that the energy-based approach to check the stability of crack offers reasonable explanation for the gel-type dependent ductile-brittle transition and how it correlates with gel concentration, i.e., $\mu_s(c)$.

It is worth noting that the effect of gel stiffness and fracture toughness on cavitation nucleation as well as gel-type and gel-concentration-dependent bubble shape during growth have been mainly considered. Considering the complexity of the human head, it will be interesting to study how head shape and size as well as micro/molecular structures and heterogeneity of brain tissues are related with characteristics of cavitation in the scope of brain injury mechanisms, prediction, and prevention under rapid mechanical loading.

2.4   Discussion

2.4.1   Cavitation to TBIs (traumatic brain injuries)

To the best knowledge, there is no conclusive clinical evidence that directly correlates specific types of loading (inertial and blast) to cavitation-induced brain injury even after considering cavitation as a traumatic injury mechanism for more than 50 years. The main reasons are imaging resolution limit [192], a lack of reliable cavitation threshold in the human brain, ethical concerns, and the transient nature of cavitation [193]. However, theoretical and experimental studies, using simplified computational and physical head models due to the complexity of the human head, have suggested that cavitation is a likely head injury mechanism for mild to severe TBIs under mechanical loadings. For example, finite element simulation studies predict that the induced pressures and time durations under realistic blast scenarios make it possible to accommodate the cavitation phenomenon [194, 195]. The corresponding threshold pressure for cavitation nucleation [196] indicates that the cavitation might be possible under extreme blast cases as well as the relatively mild blunt head impact during sports events and vehicle accidents [37, 117, 197-199] in the contrecoup region [200].

In addition to computational models, there are numerous experiment methods to observe the cavitation bubble bursts with the use of cadaver skull replicas or tissue surrogate materials loaded by rapid mechanical loading such as impactors [60, 196, 201] and shock waves [202]. Utilizing the Split-Hopkinson pressure bar, different groups [192]·[117] seeded small bubbles near rat hippocampal slices and demonstrated that the cavitation bubble collapse could cause diffuse focal injuries and brain deformation. Again,

these studies emphasize the importance of reliable cavitation nucleation conditions in biological systems. Lang et al. [60] showed cavitation bubble formation near the contrecoup regions by applying relatively small linear acceleration (~100 g) to an artificial transparent head surrogate. This study also suggested that cavitation bubbles inflict severe damage to their brain model and generate shock waves traveling within the entire skull structure. The experimental studies using simplified head models reveal 1) the extremely transient nature of cavitation bubbles and 2) the formation of cavitation bubbles at a relatively low linear acceleration range.

Experimental animal models exposed to blast shock waves provided a possible correlation between microcavitation and blast injury [203]. Studies using a diffusion tensor imaging (DTI) technique, a non-invasive method for head injury detection, showed reduced fractional anisotropy (FA) and a brain abnormality metric in the superficial cortex. These results match with the simulation results of the human [194] and rat brain [204] that predict the brain and CSF boundary as preferred spots for cavitation nucleation. This result could also be associated with white matter abnormalities among Iraq and Afghanistan War veterans. The region-specific reduction in FA among the veterans was observed in the left retrolenticular part of the internal capsule, which might be cavitation preferential spots due to a stiffness mismatch between the thalamus and cerebral hemisphere for mild TBIs [205, 206]. Huang et al. [207] found that traumatic cerebral contusion and intracerebral hemorrhages can be induced by cavitation dynamics, mimicked by intravenous injection of microbubbles and application of extracorporeal shock waves. In-vitro studies [33, 208, 209] also provide possible links between cavitation and TBIs. While these studies support

cavitation as a potential TBI mechanism, a critical question, i.e., "under what conditions does cavitation nucleate in complex soft biological systems?", has not been fully addressed.

Due to a lack of fundamental understanding of cavitation behavior in soft biological systems, accurate prediction of cavitation nucleation and the subsequential bubble growth are not possible yet even in relatively simple and homogeneous soft tissue simulants. In this regard, this study, quantifying cavitation nucleation conditions and characterizing different bubble growths in different types of tissue simulants, would be an important step for revealing material-property-dependent cavitation responses and ultimately developing more accurate and reliable criteria for cavitation events in soft biomaterials. For instance, accurate head injury predictions, e.g., by utilizing the concept of digital twins (i.e., digital representation) of the human heads, will require reliable threshold values of the onset of cavitation nucleation and a fundamental understanding of bubble growth mechanisms.

2.4.2   Initial Bubble Size

In this work, the initial bubble size in pure water (see Section 4) is estimated and it is assumed that the same initial bubble size ($r_0 = 0.474$ µm) for all soft gel samples. Because it is well known that the critical threshold for cavitation nucleation in pure water as well as soft matter strongly depends on initial bubble size, numerical parametric studies have been performed by using different r_0 values from 0.2 µm to 0.8 µm in different types of gels (see Figure 2-18). The results confirm that the above assumption is likely reasonable due to two reasons: 1) a good match between theoretical predictions and experimental data and 2) relatively large pore size in gels compared to $r_0 = 0.474$ µm. For clarification, the pore in gels is defined as a small volume within gel without fiber networks.
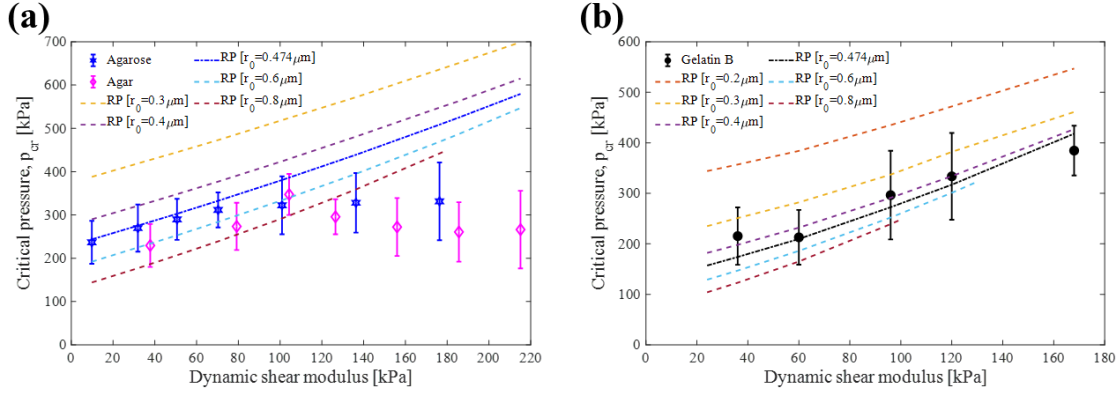
Figure 2-18. The simulation results of the critical pressure (p_{cr}) as a function of dynamic shear modulus (μ_D) with a different initial bubble radius ($r_0 = 0.2\sim0.8\ \mu m$): (a) Agarose/agar and (b) Gelatin B, respectively. Note that the results of agarose and agar for $r_0 = 0.2\ \mu m$ are not shown in (a) because the corresponding p_{cr} values are >700 kPa (well beyond the range of the current vertical axis).

First, consider how the critical threshold changes with different r_0 in agarose and gelatin B. For agarose (see Figure 2-18 (a)), the critical pressure values for $r_0 = 0.3$ μm are considerably larger (about >150 kPa) than the measured values. $r_0 = 0.8$ μm is also very unlikely because such large bubbles would have been detected during sample inspection under a high-resolution optical microscope. $r_0 = 0.4$ μm and 0.6 μm correspond to lower and upper bounds of the initial radius. Similarly, the critical pressure values for gelatin B (see Figure 2-18 (b)) match well with theoretically predicted values when $r_0 \approx 0.474$ μm. The results also indicate that $r_0 = 0.6$ and 0.8 μm are unlikely because the analysis predicts that rapid cavitation bubble burst is not expected over $\mu_D = 130$ and 100 kPa, respectively (note that the dotted lines end at these μ_D values Figure 2-18 (b)). With both increasing initial bubble size and gel stiffness, the energy associated with the surface tension of a bubble becomes relatively small compared to elastic strain

62

energy and, as a result, a bubble burst triggered by a sudden transition in dominant energy terms does not occur.
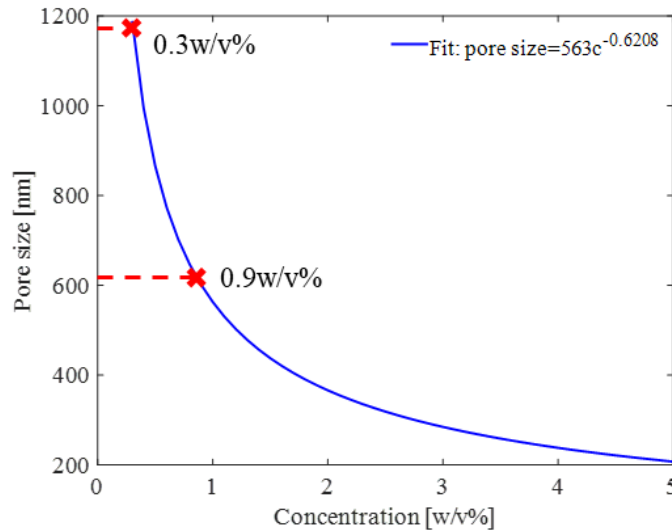
Figure 2-19. Agarose's pore size distribution with respect to its concentration [141].

Second, it is also important to consider a possible correlation between initial bubble size and gel concentration because size of pre-existing bubbles could be limited by the pore size of gels. It is important to note that pore size decreases with increasing gel concentration [210-212]. For example, the known pore sizes are about 0.6 and 1.2 μm in 0.9 and 0.3w/v% agarose [210], respectively (see Figure 2-19), while much larger pores (~100 μm) form in gelatin [211, 212]. $r_0 = 0.474$ μm is similar to or smaller than the range of pores in agarose and gelatin and, therefore, it is argued that the correlation between initial bubble size and gel concentration is likely weak for such small r_0. To support this argument, note that $r_0 = 0.67$ μm in agarose 0.3w/v% was measured by inertial microcavitation-based high strain-rate rheometry [213]. The values of initial bubble size in this work cannot be directly compared with the previously reported values [213] because they are likely sensitive to sample preparation protocols, purity of water and gel powder,

etc. However, this result supports that relatively large initial bubbles can form within pores of agarose. Another possible explanation is that the gel network may form around pre-existing bubbles in pure water when gel powder is mixed into the water and, as a result, the bubble size is consistent regardless of gel types and concentrations.

2.5   Conclusion

In this article, four different types of soft gels, i.e., agarose, agar, and gelatin A/B, have been characterized by monitoring their dynamic responses under translational mechanical impact. It has been shown that, through a series of impact experiments, that the critical acceleration (a_{cr}) at the onset of cavitation nucleation and burst gradually increases with increasing sample stiffness regardless of gel types. This initial trend can be explained by the existing theoretical framework (i.e., the Rayleigh-Plesset equation with the Kelvin-Voigt and Neo-Hookean models). The trend continues until dynamic shear modulus of the different gels approaches to about 70~100 kPa. Above this, two distinctive trends, depending on gel types, have been observed: (*Trend I*) a_{cr} keeps increasing, which again matches well with the existing theory and (*Trend II*) a_{cr} plateaus or even decreases with increasing shear modulus, and the theory-experiment discrepancy in a_{cr} becomes more pronounced. Careful image analyses of cavitation bubbles have suggested that the emergence of the two distinctive trends is closely linked with how a bubble grows in each gel type. For example, cavitation bubbles in gelatin A/B follow Trend I, i.e., spherical regardless of their gel stiffness. On the other hands, agar and agarose follow Trend II and cavitation bubbles in these gels undergo a shape transition from sphere at lower μ_s to saucer at higher μ_s, respectively. The theory-experiment discrepancy for Trend II can be

easily understood because the Rayleigh-Plesset equation is derived for a spherical bubble and, therefore, is not applicable for non-spherical bubbles. However, theoretical understanding of the underlying mechanism that governs the shape transition is non-trivial.

In this regard, an innovative theoretical concept based on both formation of a damaged zone in gel and stability of a crack in the zone have been developed. For validation of new approach, concentration-dependent material properties of different gel types have been extensively surveyed. Using the known material properties, despite limited to a few gel types, the theoretical analyses provide the theoretical interpretation of the experimentally observed transition in cavitation bubble shape. The key predictions are twofold. First, fracture toughness (G_C) of gelatin B is larger than an energy release rate (G) for the entire arrange of experimentally tested gel concentrations (c). As a result, spherical cavitation bubble growth is expected in gelatin B regardless of its c-dependent shear modulus. Second, for agarose, there is a transition from $G_C > G$ to $G_C \leq G$ because crack length sharply increases with increasing shear modulus, namely, shear modulus dependent crack length. This change in the main mechanisms of material response from formation of the localized damaged zone to crack propagation gives rise to the gel-type- and gel-concentration-dependent ductile-to-brittle transition. It has been concluded that, through the integrated experimental and theoretical approach, that the predictions of the continuum-based model match well with the experimental results.

With increasing concerns on cavitation-induced brain injury, mechanical response of soft gels under translational impact becomes increasingly relevant and deserves more thorough investigations. The current work characterizes cavitation nucleation and growth

in different soft tissue simulants and offers the theoretical interpretations of experimentally observed unique dynamic responses of cavitation bubbles, e.g., when a cavitation bubble nucleates and how it grows in soft materials depend on gel types and their concentrations. The in-depth experimental and theoretical studies would shed light on the link between traumatic brain injury and acceleration-induced cavitation bubbles, the overly overlooked mechanism until very recently.

3. CHARACTERIZATION AND DETECTION OF ACCELERATION-INDUCED CAVITATION IN SOFT MATTERS USING A DROP-TOWER-BASED REPETITIVE IMPACT SYSTEM

3.1 Experimental Procedure

3.1.1 Repetitive Impact Tester with an Integrated Drop Tower System
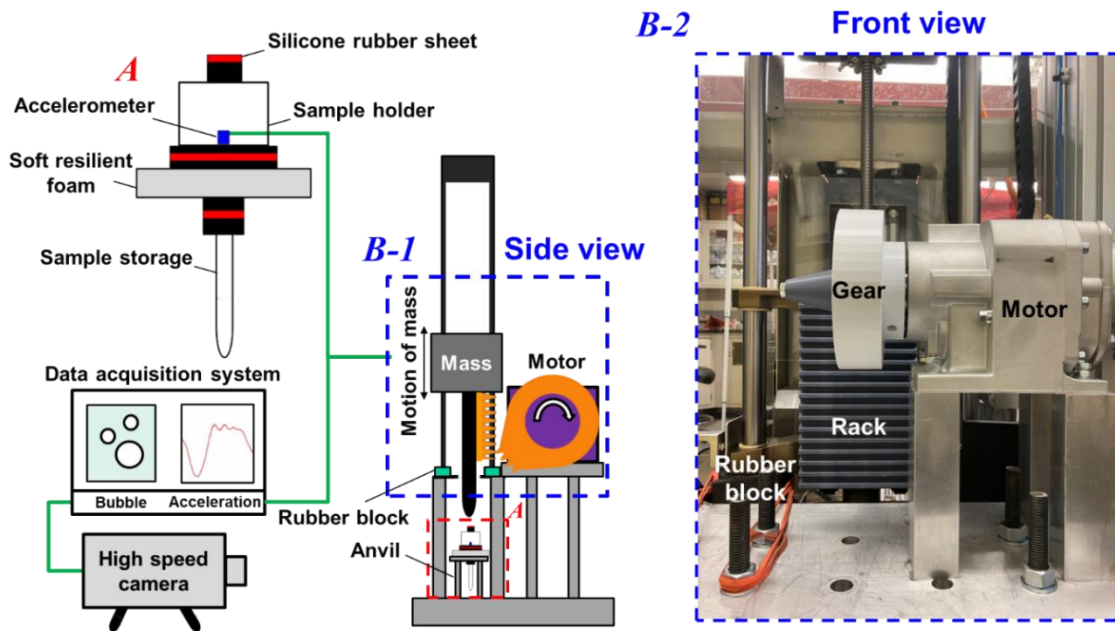
Figure 3-1. Schematic of a repetitive impact tester for soft material samples. A zoom-in view of area A shows a sample holder connected with data acquisition. Area B-1 and B-2 indicate a schematic diagram for a side view of motor system and an actual image of experimental setup for a motor system at the front view, respectively.

A similar experimental setup (i.e., integrated drop tower system) as previously reported by Kang et al [100] is utilized to develop a repetitive impact tester. The repetitive impact tester consists of a conventional drop weight tower, high speed camera, sample holder, accelerometers, data acquisition system, and motor system (see Figure 3-1). Soft gel

samples are stored inside clear long plastic tubes (16 x150 mm) for simulating size-dependent mechanical response of soft gels. Individual tubes are sealed with a cap and glued into a tube ring connected to the tube holder. The tube holder is linked with the sample holder which consists of two horizontal plates connected by four vertical columns. All the parts except the tube are connected to each other via M3 bolts and nuts, and silicone rubber sheets are placed in between each part to avoid any unwanted solid-solid collision. The soft resilient foam and silicone rubber sheet are attached to the bottom and top of the sample holder to control the impact characteristics and the induced acceleration during the impact. Note that this system is able to continuously apply rapid and smooth acceleration trajectories to a soft sample without any shock waves.

The assembled sample holder is placed on the impact anvil (see area *A* in Figure 3-1). Weight and height of the impactor as well as the number of impacts over time are three main parameters that determine the total amount of kinetic energy during a specific time. For continuous and repetitive impact events, the motor system is developed, which converts rotational motion into translational motion by using a rack and pinon gear (see area *B-1* and *B-2* in Figure 3-1) attached to the impactor and motor, respectively. With the rack and pinion, the rotation of the pinion causes linear motion of the rack. The linear travel distance of rack depends on the number of continuous gear teeth with a fixed pinion pitch diameter, which is directly related to the drop height (i.e., a vertical drop height of a movable impactor with respect to the sample holder) as well as impact-induced acceleration magnitude. With a constant motor rotational speed, a different number of gaps between continuous gear teeth arcs is introduced to control an impact frequency (i.e., total number of impacts over time). In sum, the number of continuous gear teeth arcs and number

68

of gear teeth along each arc are used to control the impact frequency and -magnitude, respectively. The motor platform configuration includes rubber bands and thick rubber sheets to dampen any unwanted vibrations during the repetitive impact testing.

As a data acquisition system, a high-speed camera with 2x magnification lens (Tokina at-X PRO M 100-MM F2.8 D Macro lens and Kenko TELEPLUS HD DGX 2x) and 50 kfps frame rate is triggered by the onset of impact or initial cavitation nucleation and synchronized with the corresponding acceleration profile at 10^{-6} s sampling rate. Resultant data sets are obtained via NI PXIe-8135 embedded controller and an NI PXI-6115 multifunction I/O module with SignalExpress 2014 data acquisition software (National Instruments Corporation., Austin, TX). More details about a presentative acceleration profile during repetitive drop experiment and initial cavitation detection algorithm are forthcoming in the following sections.

3.1.2 Motor System

Gear design parameters	
Tooth profile	Involute
Pressure angle	20°
Number of teeth	48
Diametral pitch	6 in
Resulting tooth angle	7.5°

Table 3-1. Summarized gear design parameters

	Image	Slip height [cm]	Gear engagement height [cm]	Drop height [cm]
Gear 1		2.31	1.39	6
Gear 2		2.31	2.78	7.4
Gear 3		2.22	4.16	8.6
Gear 4		2.38	5.55	10.3

Table 3-2. *S*lip, gear engagement height, and drop height for different number of gear teeth along single arc.

The motor system utilizes a rack and pinion system where the pinion is only a partial gear. This partial or crescent gear allows the rack to engage and then release continuously in a vertical direction, stemming from the constant rotational motion of the motor. The motor used in this system is a Nord AC Gearmotor that operates at a constant 28 revolutions

per minute with a maximum torque of 124 N-m. This motor is controlled with an on/off switch through the power supply.

The motor is connected to the drop tower setup using a custom-built platform that screws into the threaded grid patterned base plate of drop tower. Eight high strength steel threaded rods cut to a length of 75 cm are used to hold up an aluminum platform (see Figure 3-1). The eight rods provide adequate strength to secure the motor in position in all directions, even when under load. The aluminum plate is needed to mount the motor to the threaded rods and thus align the motor to the drop tower plunger apparatus. The aluminum plate is connected to the threaded rods with nuts which allows the platform to be raised or lowered to properly align the rack and pinion gears. The motor is mounted to the aluminum platform with 8-inch-long screws and 6-inch-long aluminum spacers. This leaves ample space below the motor for the threaded rod adjustment length (see Figure 3-1).

The rack and pinion gear mechanisms are constructed of 3D printed polymer. This polymer is eSUN PLA PRO 3D Printer Filament. The pinion gear is press fitted on to a Metal Gear (McMaster 6867K4) which keys on to the motor shaft. This metal gear provides ample surface area to transfer the motor forces to the polymer gears without causing areas of high stress. The 3D printed rack press fits onto the drop tower plunger mass and is secured with a screw ring.

The design of the gears is based on the involute tooth profile. The gear design parameters given in Table 3-1 dictate the shape of the gears utilized in this experiment. The 3D printing of the gears allowed for rapid change of the tooth profiles. The design of the partial/crescent pinion controls the impactor drop frequency and magnitude/drop height. With the given

gear design parameters (see Table 3-1), each tooth on the pinion gear accounts for 7.5 degrees out of an entire gears 360 degrees profile. An arc of gear teeth is created by cutting the pinion gear such that only a select number of gear teeth remain.

There are two slip conditions that occur with a crescent pinion gear design, the pre-slip condition and the post-slip condition. When the teeth first make contact, a slipping motion between the two teeth occurs until the gear teeth are fully engaged or mated. When fully engaged, no slipping occurs, and the gears operate as expected. After the final tooth in a crescent gear gets pulled out from the fully engaged position, another slipping condition occurs between the pinion teeth and the rack teeth. These two slipping conditions result in a consistent vertical height profile no matter the arc size of the crescent gear. In other words, the slipping between the two gears between no-contact to fully engaged contact has a consistent height which is around 2.3 cm (see Table 3-2) for the given gear profile. The drop height for a given gear profile is two times the slip height plus the height from the arc length of the pinion gear crescent. This controllable height from the gear arc is called the gear engagement height (see Table 3-2). The center of the motor axis to the gear rack is approximately 10.5 cm which, for one tooth with an arc of 7.5 degrees results in an arc length of 1.37 cm in accordance with Table 3-2. Controlling the drop height magnitude is thus done through the number of teeth in the crescent gear.

The frequency of the drops can be controlled by putting more than one crescent of gear teeth on one pinion gear. However, a frequency ceiling arises which limits the number of crescents on one gear. This ceiling is due to the settling time of the drop tower system. The plunger must have adequate time to settle before the next engagement of the pinion gear. Otherwise, misalignment will occur and damage to the system can result.

Due to the slipping (i.e., friction) of the gear teeth, the gear and rack experience significant wear over time. This is expected and is one key reason why 3D printed polymer gears are used. It is cheap and quick to make new gears. For this system, the 3D printed gears are treated as a consumable, needing to be replaced after extended use. Since the motor system is constructed of high strength steel, and the gears are constructed of relatively weak polymer, if an issue arises, such as misalignment of the gear teeth at contact, then the polymer gears will break before the rest of the motor system. This prevents costly damage and provides rapid development of new testing procedures.

3.1.3 Dynamic Mechanical Analysis of Soft Resilient Foam

Dynamic mechanical tests are conducted by DMA 3200, New Castle, DE. The cylindrical soft resilient foams with dimensions of 1 cm radius with 1.4 cm thickness are examined on the 1.25 cm radius compression plate having maximum 500 N capacity. Tests are performed to study the strain- and strain rate-dependent mechanical properties (i.e., storage and loss modulus, and damping ratio) of the soft resilient foam with different displacements (i.e., 0.2, 0.6, 1.0, 2.0 mm) using frequency weep mode ranging from 0.1 to 100 Hz at a constant room temperature. Three specimens of each condition are tested for dynamic mechanical analysis.

3.1.4 Soft Gel Preparation

The equipment used to prepare the samples includes an electronic balance, hot plate and stirrer, 1000 mL glass beaker, electronic pipette, pure ponta weigh boats, ultra-pure DI water, and agarose (Invitrogen, REF 16500-100, LOT0001189939).

For the testing in this study, the samples were made one day before testing, in batches of approximately 15 samples. The sample preparation process begins by adding 300 mL of DI water into the 1000 mL beaker and setting it on the hot plate at 350 Celsius. Next, a pure Ponta weigh boat is zeroed on the electronic balance. The necessary sample in powdered is poured onto the weigh boat and measured to the desired weight. The weight is found from the desired concentration and the known water volume, most commonly, 300 mL. For 0.75w/v% agarose gel, dissolved into 300 mL, 2.25 grams of powdered sample is needed. When the water on the hot plate is just starting to boil, the stirrer is engaged, and the powder sample is slowly and continuously poured in. Ample time is given to let the powder completely dissolve into the water. Water is also continuously added in small quantities to maintain the 300 mL volume. During the dissolving process, 15 clear sample tubes are rinsed three times each in the sink using de-ionized water. After complete dissolving of the sample, the hot plate temperature is reduced to 35 Celsius and set to cool with the stirrer still running. After cooling, the pipette is used to fill the sample tubes to their desired fill height. For this experiment, the clear sample tubes are filled to approximately 14 centimeters in height of sample which corresponds to 15 cm long. The samples are then cooled at room temperature.

3.2   Experimental Characterization
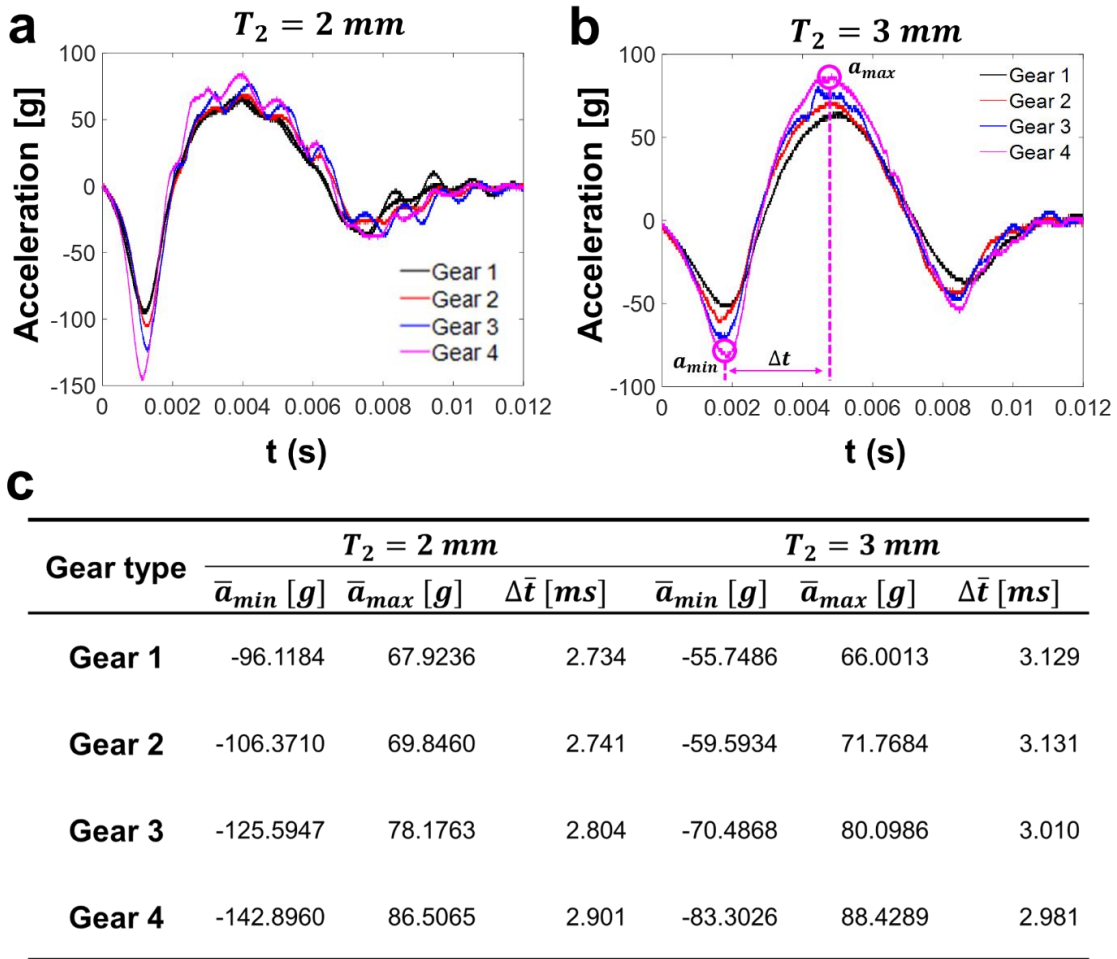
Figure 3-2. (a) and (b) Measured acceleration profiles for different gear designs with different silicone rubber sheet thicknesses ($T_2 = 2\ mm\ (a),\ and\ 3\ mm\ (b)$). a_{min}, a_{max}, and Δt represent minimum and maximum acceleration, and time interval between them, respectively. (c) The average maximum and minimum accelerations (i.e., $\bar{a}_{max}$ and $\bar{a}_{min}$) and time intervals ($\Delta \bar{t}$) between (a_{max} and a_{min}) of different types of gear design.

For experimental characterization of the developed repetitive impact tester, the clear 14 cm long plastic tube is mainly utilized with 0.75w/v% Agarose. To control the characteristics of impacts, the number of gear teeth along an arc (hereinafter cited as teeth number) and thickness of the silicone rubber sheet (i.e., T_2) are changed (see Figure 3-2

(a) and (b), respectively). Firstly, the system capability of repeated impact without any significant change in impact response of the sample holder is confirmed by repeating 3 successive drops from each condition (see Figure 3-3). Individual measured mechanical quantities (i.e., minimum and maximum acceleration as well as time intervals between them) are averaged (i.e., denoted as $\bar{a}_{min}$, $\bar{a}_{max}$, and $\overline{\Delta t}$, respectively) and summarized in Figure 3-2 (c). As shown in Figure 3-2 (a) and (b), vertical acceleration (i.e., acceleration along the impact direction) responses of the sample holder from the same gear types are relatively consistent for all the cases. Since a greater number of teeth result in a higher drop height, as shown in Table 3-2, the amplitude of the first trough gradually increases as the number of teeth increases. In addition, the $\bar{a}_{min}$ of each gear type is linearly proportional to drop height (fit equation: $\bar{a}_{min}\,[g] = -14.46 \cdot h\,[cm]$ (i.e., drop height) for $T_2 = 2\,mm$ with $R^2 = 0.9$ and $\bar{a}_{min}\,[g] = -8.27 \cdot h\,[cm]$ for $T_2 = 3\,mm$ with $R^2 = 0.9$). The use of larger T_2 reduces the induced $\bar{a}_{min}$ amplitude and even increases response time interval (i.e., $\overline{\Delta t}$) between the first and second trough of the acceleration profile. This is due to the greater spring and damping coefficient of $T_2 = 3\,mm$ compared to $T_2 = 2\,mm$. Interestingly, the $\bar{a}_{max}$ values do not show any noticeable change between $T_2 = 2$ and $3\,mm$ as shown in Figure 3-2 (c). It is worth noting that the acceleration of the sample holder goes back to equilibrium state (i.e., $0g$ acceleration) within $0.012\,s$ for all cases. This confirms that the prior impact response of the sample holder would not affect the next drop event while applying repetitive impacts.
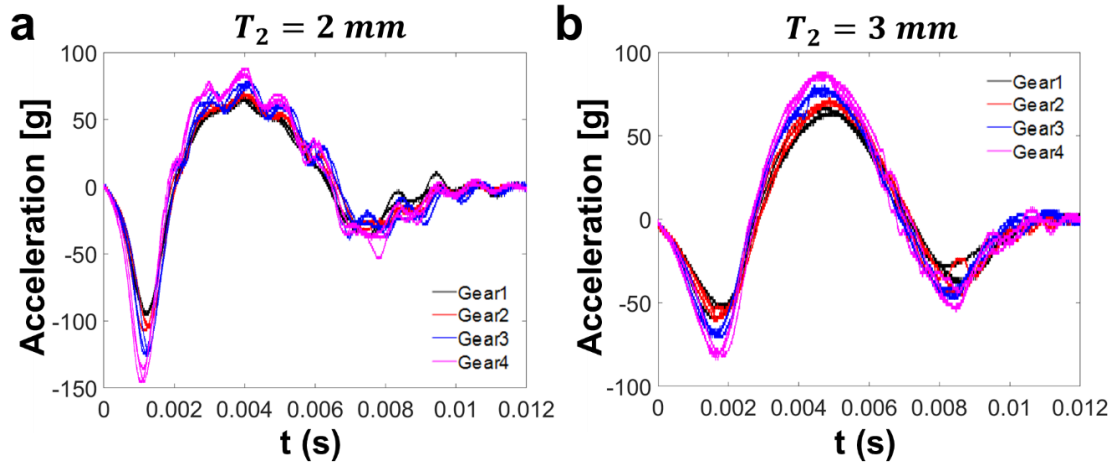
Figure 3-3. (a) and (b) Measured 3 successive acceleration profiles for different gear designs with different silicone rubber sheet thicknesses ($T_2 = 2\ mm\ (a)$, and $3\ mm\ (b)$).

3.3 Theoretical Modeling
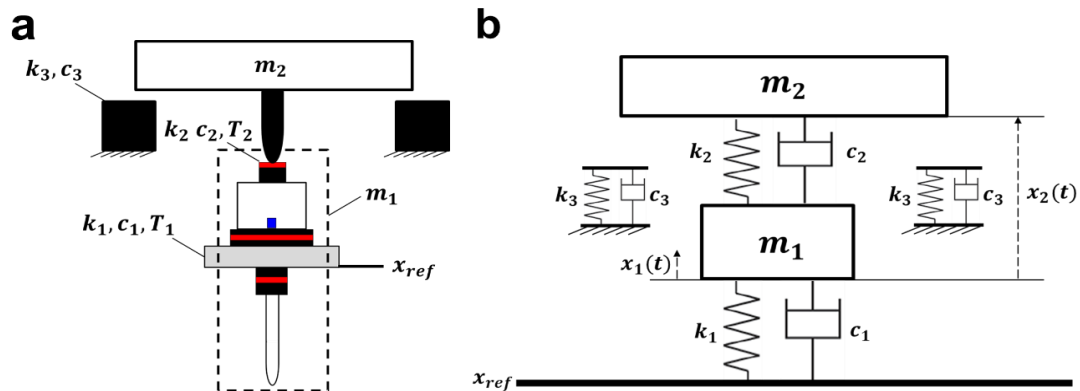
Figure 3-4. (a) Schematic of the simplified repetitive impact tester. (b) A free body diagram of the multiple impact tester with soft foam (k_1 and c_1), sheet (k_2 and c_2), and block (k_3 and c_3) for modeling.

In order to consistently apply the well-controlled acceleration profile to soft material samples, thorough understanding of the impact responses between the sample holder and impactor is necessary. In this regard, a systematic theoretical approach is performed to characterize the transient dynamic response of the system (*A* in Figure 3-1 and Figure 3-4 (a)). The main focus will be placed on providing high-strain rate conditions, characterized by a smooth, consistent acceleration to the sample holder.

Figure 3-4 (b) represents a two-degree-of-freedom schematic model of the system. Two movable masses denote the sample holder (m_1) and impactor (m_2), respectively. Three sets of a linear spring (k_i) and damper (c_i) represent the soft resilient foam and silicone rubber sheet with thickness (T_1 and T_2, respectively) as well as the rubber block where $i = 1, 2,$ and 3. When m_2 is dropped at drop height, h, it freely falls until an engagement happens between the silicone rubber sheet and m_2. The silicone rubber sheet and the soft resilient foam are attached to m_1 which is in a stationary state on the rigid anvil (x_{ref}). Note that when the impactor contacts the rubber block, there is an offset distance ($d_e = 1\ mm$) between m_2 and m_1 without the silicone rubber sheet. However, with a relatively thick silicone rubber sheet ($T_2 > 1\ mm$), the m_2 first contacts with the silicone rubber sheet and then, when a travel distance of the m_2 after the first engagement with the rubber sheet is more than $T_2 - d_e$, another contact occurs between m_2 and the fixed rubber block. This avoids excessive contact depth of the silicone rubber sheet, due to a large m_2 mass.

Material properties			
ζ_1	0.2	k_2	392.50 kPa ($T_2 = 2\ mm$) 261.67 kPa ($T_2 = 3\ mm$)
ζ_2	0.001	k_3	1.0383 MPa
ζ_3	0.0892	M	14.2857
k_1	187.35 kPa	T_1	0.014 mm
A_1	8743 mm^2	A_2	78.5 mm^2

Table 3-3. Material properties of soft foam, sheet, and block utilized in numerical simulation.

79

For simplicity, it is furtherly assumed that m_1 and m_2 move only along a vertical impact direction. This assumption is fairly reasonable by considering that (1) the impactor motion is guided by metal guide rails (see Figure 3-1) and (2) motion of the sample holder is constrained by the center hole of the anvil, which helps the impactor and sample holder align each other along the vertical axis. Again, the focus is to characterize the transient, dynamic, but repetitive response of the system such that the above constraints would provide better system stability and repeatability during the long-time operation. The initial condition of the theoretical analysis is when m_1 and m_2 first contact each other via the silicone rubber sheet (see Figure 3-4). The corresponding mathematical notation is $x_2(t) - x_1(t) = T_2$ at t (i.e., time) $= 0$ in which $x_2(t)$ and $x_1(t)$ describe the vertical location of the impactor (m_2) and the sample holder (m_1) in time (i.e., displacement) from the initial position of the sample holder ($x_1(0)$), respectively.

The governing equation of the two-degree-of-freedom system in Figure 3-4 (b) can be described as follows:

Equation 3-1

For m_1: $m_1\ddot{x}_1 + c_1\dot{x}_1 + c_2(\dot{x}_1 - \dot{x}_2) + k_1x_1 + k_2(x_1 - x_2 + T_2) = -m_1g$

Equation 3-2

For m_2:

$$\begin{cases} m_2\ddot{x}_2 + c_2(\dot{x}_2 - \dot{x}_1) + k_2(x_2 - x_1 - T_2) = -m_2g, \text{ if } x_2(t) \geq d_e \\ m_2\ddot{x}_2 + c_2(\dot{x}_2 - \dot{x}_1) + k_2(x_2 - x_1 - T_2) + c_3\dot{x}_2 + k_3(x_2 - d_e) = -m_2g,, \text{ if } x_2(t) < d_e \end{cases}$$

where $d_e (= 1\,mm)$ is the offset distance between the impactor and rubber block when $m_1 - m_2$ initially contact through the silicone rubber sheet and g is the

80

gravitational acceleration. Note that depending on $x_2(t)$, the spring-damper of the rubber block is either active $(x_2(t) < d_e)$ or not $(x_2(t) \geq d_e)$. On top of that, the dynamics of the system in Equation 3-1 and Equation 3-2 can be further decomposed into four additional phases which are triggered by the onset of specific events: contact and separation between m_1 and anvil (x_{ref}) or between the m_1 and m_2. For this step, the detailed phase equations are listed as follows (previous work from Kang et al. [100]):

(*phase 1*) m_1 and x_{ref} as well as m_1 and m_2 $(0 \geq x_1(t) > -T_1$ and $T_2 \geq x_2(t) - x_1(t) > 0)$ are in contact with the soft resilient foam and silicone rubber sheet (i.e., $k_1 - c_1$ and $k_2 - c_2$ are both active);

(*phase 2*) m_1 and m_2 are in contact $(T_2 \geq x_2(t) - x_1(t) > 0)$ are in contact with the silicone rubber sheet, but separation happens between m_1 and the soft resilient foam $(x_1(t) > 0)$ (i.e., $k_2 - c_2$ is only active);

(*phase 3*) m_1 and x_{ref} is in contact with the soft resilient foam $(0 \geq x_1(t) > -T_1)$, while separation happens between m_1 and m_2 $(x_2(t) - x_1(t) > T_2)$ (i.e., $k_1 - c_1$ is only active);

(*phase 4*) m_1 and x_{ref} as well as m_1 and m_2 $(x_1(t) > 0$ and $x_2(t) - x_1(t) > T_2)$ are separated each other (i.e., $k_1 - c_1$ and $k_2 - c_2$ are both inactive);

The above governing equation (Equation 3-1 and Equation 3-2) will be properly adjustable depending on the specific phase of the system.

To simplify the analysis of this system dynamic behavior, $y_1(t) = x_1(t), y_2(t) = x_2(t), y_3(t) = \dot{x}_1(t)$, and $y_4(t) = \dot{x}_2(t)$ are defined such that the state vector is $Y =$

$(y_1\ y_2\ y_3\ y_4)$ which represents the complete internal state of the dynamic system at a specific time. After the first-time derivative of the state vector (i.e., $\frac{dY}{dt}$), the corresponding $\frac{dY}{dt}$ of Equation 3-1 and Equation 3-2 for each phase will be represented as follows:

(phase 1)

$$\frac{dY_1}{dt} = \begin{cases} y_3(t) \\ y_4(t) \\ -(\omega_1^2 + \omega_2^2 M) \cdot y_1(t) + \omega_2^2 M \cdot y_2(t) - (2\omega_1\zeta_1 + 2\omega_2\zeta_2 M) \cdot y_3(t) \ldots \\ \qquad +2\omega_2\zeta_2 M \cdot y_4(t) + \alpha - g \\ 2\omega_2\zeta_2\big(y_3(t) - y_4(t)\big) + \omega_2^2\big(y_1(t) - y_2(t)\big) + \beta - g \end{cases}$$

(phase 2)

$$\frac{dY_2}{dt} = \begin{cases} y_3(t) \\ y_4(t) \\ -2\omega_2\zeta_2 M \cdot (y_3(t) - y_4(t) - \omega_2^2 M \cdot (y_1(t) - y_2(t)) + \alpha - g \\ 2\omega_2\zeta_2\big(y_3(t) - y_4(t)\big) + \omega_2^2\big(y_1(t) - y_2(t)\big) + \beta - g \end{cases}$$

(phase 3)

$$\frac{dY_3}{dt} = \begin{cases} y_3(t) \\ y_4(t) \\ -\omega_1^2 \cdot y_1(t) - 2\omega_1\zeta_1 y_3(t) + \alpha - g \\ \beta - g \end{cases}$$

(phase 4)

$$\frac{dY_4}{dt} = \begin{cases} y_3(t) \\ y_4(t) \\ -g \\ -g \end{cases}$$

where $\alpha = -2\omega\zeta_2 M \cdot T_2$, $\beta =$

$$\begin{cases} -2\omega_3\zeta_3 \cdot y_4(t) - \omega_3^2 \cdot (y_2(t) - d_e) + 2\omega\zeta_2 M \cdot T_2, \; y_2(t) \le d_e \\ 2\omega\zeta_2 M \cdot T_2, y_2(t) > d \end{cases}$$, $\omega_1 = \sqrt{\frac{k_1}{m_1}}$, $\omega_2 =$

$\sqrt{\frac{k_2}{m_2}}$, $\omega_3 = \sqrt{\frac{k_3}{m_2}}$, $\zeta_1 = \frac{c_1}{2m_1\omega_1}$, $\zeta_2 = \frac{c_2}{2m_2\omega_2}$, $\zeta_3 = \frac{c_3}{2m_2\omega_3}$, and $M = \frac{m_2}{m_1}$.

While running the dynamic system, hard impacts can occur between m_1 and x_{ref} or m_2 and m_1 when $y_1(t) = -T_1$ or $y_2(t) = y_1(t)$, respectively. The hard impacts are assumed as inelastic collisions with a coefficient of restitution e (= 0.8) based on linear momentum conservation. The state vector immediately after the above hard impacts can be written as follows:

Equation 3-7

$$m_1 \text{ and } x_{ref}: \; M_{m_1}(Y) = \begin{cases} y_1(t) \\ y_2(t) \\ -ey_3(t) \\ y_4(t) \end{cases}$$

$$m_2 \text{ and } m_1: \; M_{m_1-m_2}(Y) = \begin{cases} y_1(t) \\ y_2(t) \\ (eM(y_4(t) - y_3(t)) + y_3(t) + My_4(t))/(1 + M) \\ (e(y_3(t) - y_4(t)) + y_3(t) + My_4(t))/(1 + M) \end{cases}$$

During the system operation, its dynamic responses are composed of different smooth profiles for individual phases such that a jump condition is required to link respective events (i.e., contact, separation, or hard impact event). Following the previous work studied

by Kang et al. [100], the contact, separation or hard impact event bring about the use of a different state vector described from Equation 3-3 to Equation 3-7 and for numerically solving the dynamic system, 6 event surfaces are utilized as follows:

Event 1: $C_{m_1} = y_1(t)$ when $y_3(t) < 0$ for a contact between m_1 and x_{ref}.

Event 2: $C_{m_1-m_2} = y_2(t) - y_1(t) - T_2$ when $y_4(t) - y_3(t) < 0$ for a contact between m_1 and m_2.

Event 3: $S_{m_1} = y_1(t)$ when $y_3(t) > 0$ for a separation between m_1 and x_{ref}.

Event 4: $S_{m_1-m_2} = y_2(t) - y_1(t) - T_2$ when $y_4(t) - y_3(t) > 0$ for a separation between m_1 and m_2.

Event 5: $I_{m_1} = y_1(t) + T_1$ when $y_3(t) < 0$ for an impact between m_1 and x_{ref}.

Event 6: $I_{m_1-m_2} = y_2(t) - y_1(t)$ when $y_4(t) - y_3(t) < 0$ for an impact between m_1 and m_2.

The event surfaces allow us to monitor various events as well as their transitions, in time, while numerically simulating the dynamic system. In addition, through the connectivity map between the individual segments of the dynamic trajectories, the complicated correlation between the state vector fields and corresponding event surfaces is successfully organized. More details are explained in [100].

The initial conditions of the numerical simulations are $y_1(0) = y_2(0) = y_3(0) = 0$, while the velocity of the impactor (i.e., m_2) corresponds to $-\sqrt{2gh}$ by assuming energy conservation during its free fall from the drop height (i.e., h) induced by different gear types (see Table 3-2). In this regard, the initial conditions satisfy the *phase 1* equation

criterion such that the governing equation initially starts with Equation 3-3. All other material properties used in the simulation are summarized in Table 3-3. The spring constant of soft resilient foam and silicone rubber sheet are estimated using $k_i = E_i A_i / T_i$ in which E_i, A_i, and T_i are elastic modulus, cross-sectional area thickness of the soft resilient foam ($i = 1$) and silicone rubber sheet ($i = 2$). The elastic modulus and damping coefficient of silicone rubber sheet (E_2 and ζ_2, respectively) is referred from [214], while that of soft resilient foam (E_1 and ζ_1, respectively) is measured using the dynamic mechanical analysis (see Figure 3-6). On top of that, the mechanical properties of the rubber block (i.e., k_3 and $\zeta_3 = \frac{c_3}{2m_2\omega_3}$) are numerically fitted into $m_2 \ddot{x'}_2 + c_3(\dot{x'}_2) + k_3(x'_2) = -m_2 g$ where x'_2 is a displacement of m_2 only affected by the rubber block by using lsqcurvefit function in MATLAB based on simple mass-spring-damper system (see Figure 3-5). Again, a contact between the impactor and the rubber block can always occur after the contact between the impactor and the silicone rubber sheet since relatively thicker silicone rubber sheet ($T_2 = 2$ or 3 mm) which is greater than d_e is used.
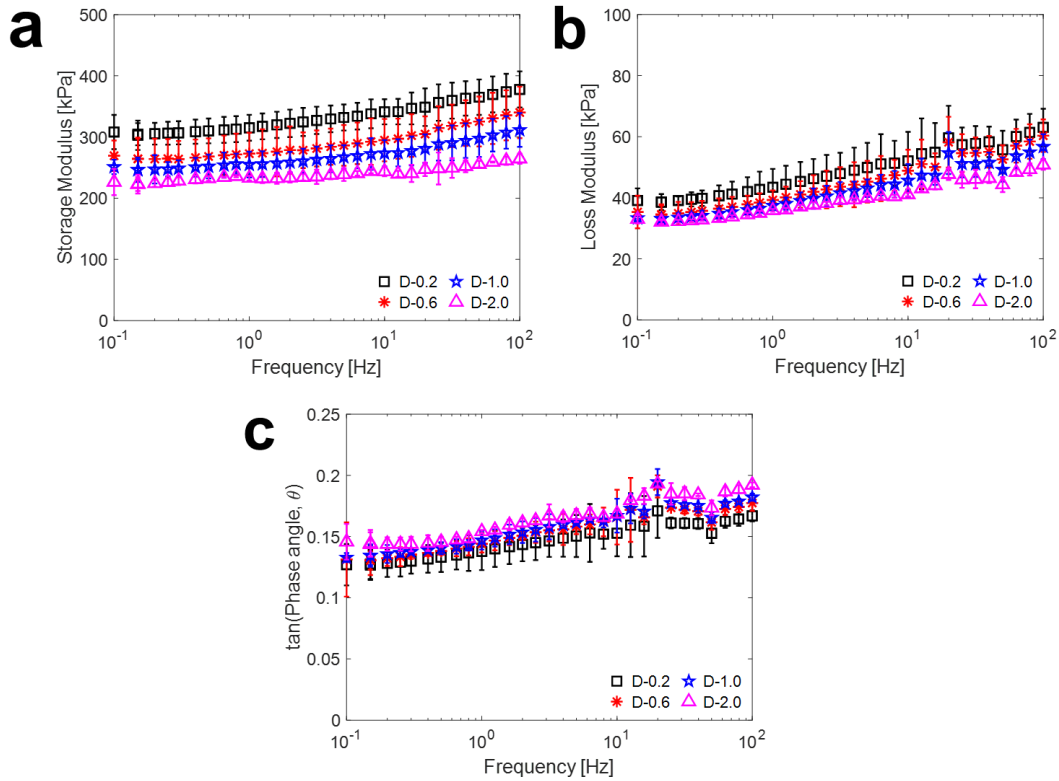
Figure 3-6. Dynamic mechanical analysis of lower soft foam with different displacements (0.2, 0.6, 1.0, and 2.0 mm). The storage (a) and loss modulus (b), and phase angle (i.e., damping ratio) of lower soft foam are measured via dynamic compression test.
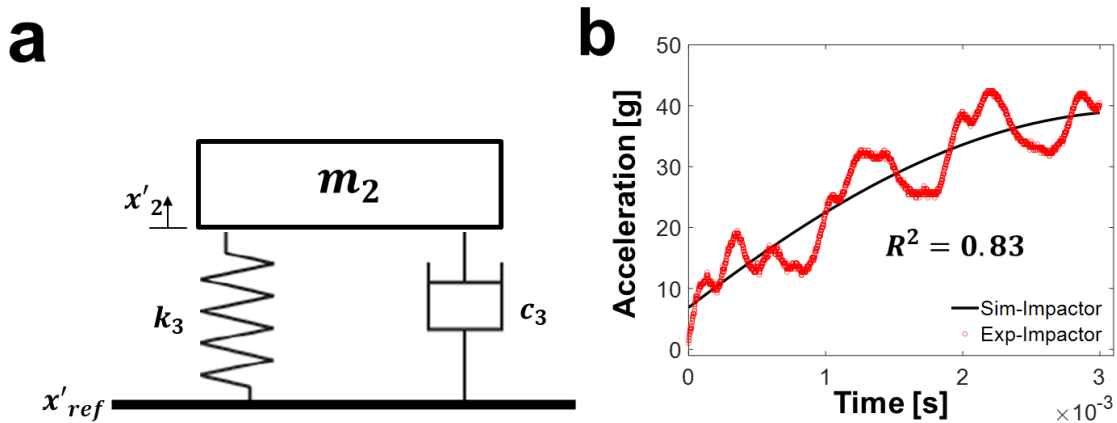
Figure 3-5. Numerical estimation of rubber block mechanical properties: (a) A free body diagram of impactor and the rubber block and (b) experimental and simulated results of impactor acceleration with the use of fitted ζ_3 and k_3. x'_2 is a displacement of m_2 only affected by the rubber block. The R^2 value for the use of fitted ζ_3 and k_3 is 0.83.
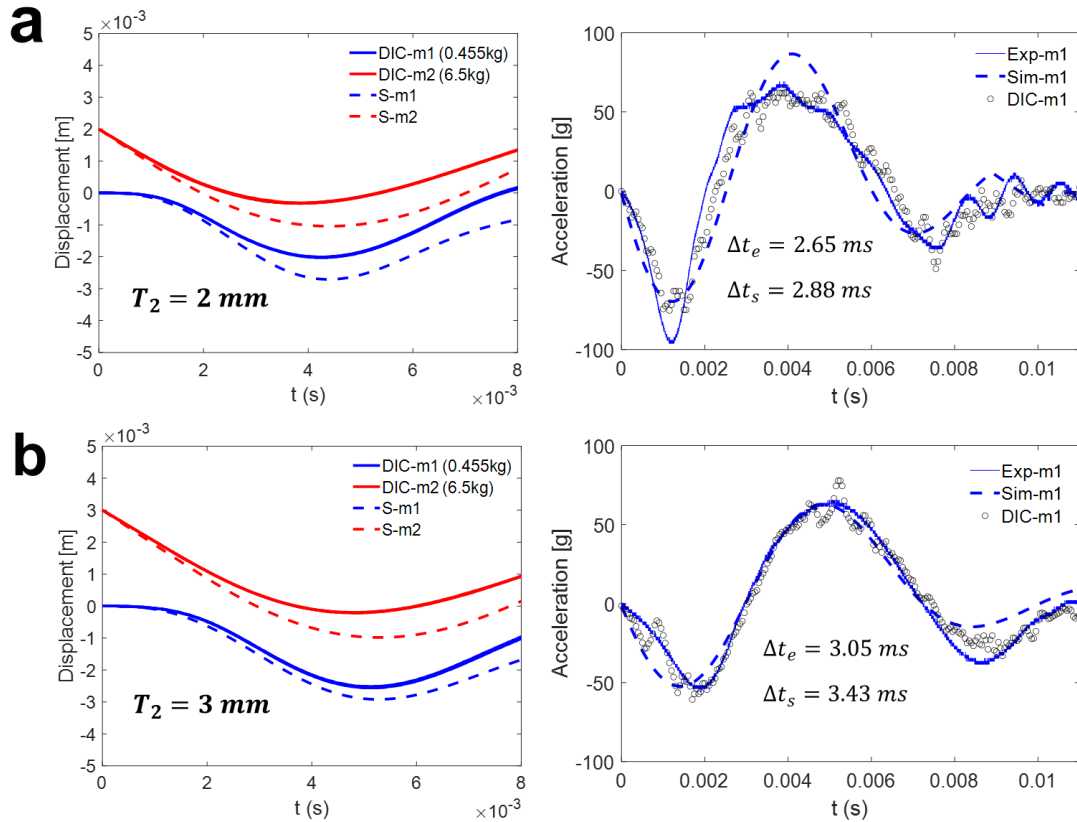
Figure 3-7. Experimental validation of numerical simulation: displacement and acceleration profiles of Impactor (m_2) and sample holder (m_1) with (a) $T_2 = 2\ mm$ (b) $T_2 = 3\ mm$ upper soft rubber sheet. Δt_e and Δt_s represent the time intervals between minimum and maximum acceleration for experimental and simulated measurements, respectively.

To find the appropriate conditions for using the repetitive impact system to test soft samples, 2 representative cases are explored with the consideration of the realistic mechanical properties (listed in Table 3-3) as well as drop height ($h = 60\ mm$ induced by Gear type 1) by only changing thickness of the silicone rubber sheet (T_2). First of all, the left columns of Figure 3-7 (a) and (b) show the corresponding experimental measurements (solid line) and numerical prediction (dotted line) of displacement trajectory for the sample holder (m_1, blue) and impactor (m_2, red) with $T_2 = 2$ and $3\ mm$, respectively. By using a DIC (digital image correlation) method, the corresponding displacement fields for

87

impactor (m_2) and sample holder (m_1) are experimentally measured. For enhanced displacement resolution, a series of images have been taken by the high-speed cameras for all cases which were recorded with a camera frame rate of 20,000 frames per second.

Interestingly, there is no discontinuous jump of both m_1 and m_2 displacement profiles, which indicates that a hard impact induced by collision between the m_1 and m_2 does not occur regardless of T_2. This is because, compared to the previous study [100], the engagement of the rubber block having relatively higher spring and damping coefficient with m_2 when $x_2(t)$ or $y_2(t) \leq d_e$, prevents further deformation of the silicone rubber sheet. Therefore, as shown in Figure 3-7 (a) and (b), even with a higher drop height ($h = 60 \ mm$), the maximum displacement changes are only $2 \ (T_2 = 2 \ mm)$ and $3 \ mm \ (T_2 = 3 \ mm)$ for m_1 and $2 \ (T_2 = 2 \ mm)$ and $2.5 \ mm \ (T_2 = 3 \ mm)$ for m_2 from the DIC, and $3 \ (T_2 = 2 \ mm)$ and $4 \ mm \ (T_2 = 3 \ mm)$ for m_1 and $2.7 \ (T_2 = 2 \ mm)$ and $2.9 \ mm \ (T_2 = 3 \ mm)$ for m_2 from the simulation (frame step $= 0.5 \ ms$). It is also important to note that during the time interval ($0 \leq t \leq 0.008 \ s$), there is no phase change such that the governing equation considered here is a phase 1 equation (Eq. (3)). The experimental trend of the m_1 and m_2 displacement profiles are matched with those of the simulation, while the deviations between the experiment and simulation results increase as an increase of the m_1 and m_2 displacement changes. This is possibly due to the strain-dependent non-linear behavior of the silicone rubber sheet, soft resilient foam, and rubber block, which are not considered here for simplicity.

To rigorously evaluate the system performance based on the main goal, it is necessary to characterize the impact-induced acceleration profile for a soft gel in the sample holder

(m_1). For experimental measurement of the induced acceleration of m_1, two different methods are utilized: 1) the use of an accelerometer attached onto the sample holder and 2) numerical differentiation of the DIC-based displacement measurement in time. For the second approach, 'spline' and 'fnder' functions are used in MATLAB for reducing data nosiness and performing interpolation, as well as piecewise derivatives. The theoretical predication for the m_1 acceleration is quantified by invoking the state vector of m_1 into the corresponding phase equation.

The right columns of Figure 3-7 (a) and (b) indicate the measured and estimated m_1 acceleration profiles (i.e., blue solid line for the accelerometer measurement, black dot for the numerical differentiation of the DIC-based displacement, and blue dotted line for the simulation). First of all, for repeatedly applying rapid, smooth acceleration profiles onto the soft sample, it is required to confirm whether the acceleration of m_1 approaches zero (i.e., stationary state) before another impact event happens. Considering the highest motor speed (i.e., 28 rpm), the shortest time scale of respective impacts is approximately the second or sub-second time scale. According to Figure 3-7 (a) and (b), the m_1 accelerations for both T_2 thicknesses return to a stationary state within $0.011\ s$, which allows this system to continuously and independently inflict a series of impact to the sample. Furthermore, due to an increase of T_2, the stiffness of silicone rubber sheet decreases, leading to a decrease of ω_2, but an increase of the displacement change. Therefore, it can be expected lower amplitude of first peak acceleration for larger $T_2\ (= 3\ mm)$ based on the impulse-momentum theorem. To be specific, the extended deformation distance (i.e., displacement change) increases the time over which the change in momentum occurs, resulting in lower acceleration. This hypothesis can be confirmed by

similar total impulse amounts between two cases ($0.491\ kg \cdot m/s$ for $T_2 = 2\ mm$ and

$0.451\ kg \cdot m/s$ for $T_2 = 3\ mm$) during half cycles of the respective acceleration profile

(i.e., peak-to-peak time period). Note that the half cycle (i.e., Δt_s and Δt_e which denote

the time intervals of peak-to-peak acceleration from simulation and experiment,

respectively) for $T_2 = 3\ mm$ is longer than that for $T_2 = 3\ mm$, while the former has

lower first peak acceleration value than the latter one, as shown in Figure 3-7 (a) and (b).

How T_2 influences the dynamic characteristics (e.g., displacement and induced

acceleration) of the repetitive impact is investigated. Based on the theoretical and

experimental analyses, it is concluded that a smooth, rapid, and consistent acceleration

profile, which is important for systematic material characterization, would be

accomplished with the developed repetitive impact tester. Moreover, the impact

characteristics of the target sample will be tightly controlled by not only adjustment of the

drop height but by modifying the impact surface.

3.4   Repetitive Impact Effect on Soft Gels

Three key results from the experimental and theoretical analysis are 1) smooth and

rapid dynamic trajectories of the sample holder, 2) to continuously apply consistent impacts

on the sample holder, and 3) a control of the impact characteristics (i.e., acceleration

profile) by using different gear types and impact surface conditions. These capabilities

achieve versatile applications of the repetitive impact tester, which befit various simulated

situations. Here, the capability of the developed repetitive impact tester by quantitatively

measuring critical acceleration (a_{cr}) associated with the onset of cavitation nucleation in

soft materials after several impact with different impacts amplitudes is experimentally demonstrated.

3.4.1 Critical Acceleration for Cavitation

To demonstrate the capability of the repetitive impact tester for soft samples, the critical acceleration (a_{cr}) that triggers the onset of cavitation in agarose 0.75w/v% is quantified with different impact numbers and amplitudes which are controlled by system operation time and gear type, respectively. Agarose is chosen for demonstration since it is a well-used biomaterial, as a tissue simulant [215]. Again, the ultimate goal is to characterize soft gel responses (e.g., cavitation) with respect to continuously repetitive impacts. Based on the experimental and theoretical results, it is important to point out that the largest peak acceleration magnitude (142.8960 g) from gear type 4 with $T_2 = 2\ mm$ is considerably lower than the a_{cr} of 0.75w/v% agarose in 14 cm long tube from single impact (234.522 g, see Figure 3-8). In this regard, this system is appropriate for characterizing mechanical response of soft gel under repeated impacts (i.e., Total number of applied impacts on individual samples > 1) since the cavitation nucleation will not occur with a single drop event.
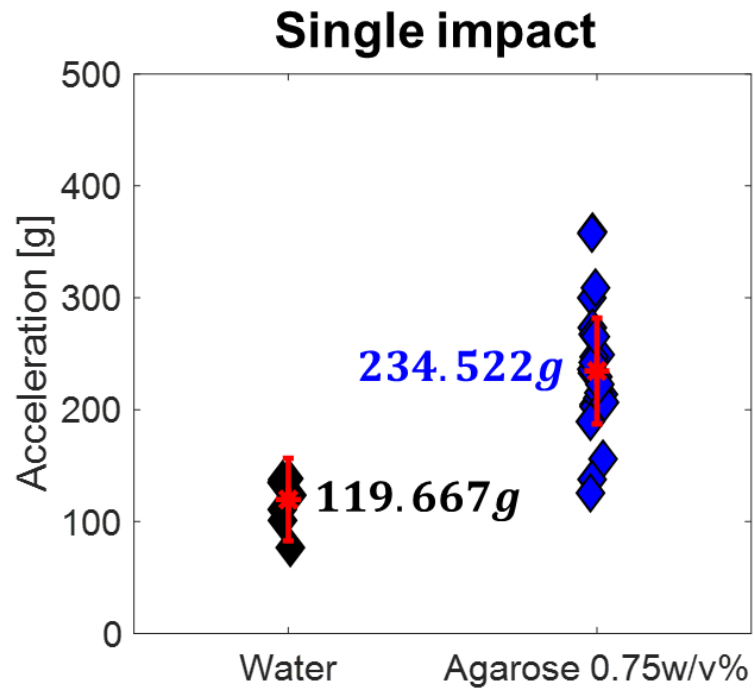
Figure 3-8. Critical acceleration (a_{cr}, the corresponding acceleration at the onset of cavitation) for water and 0.75w/v% agarose gel under single impact condition.

3.4.2 Detection of Initial Cavitation Nucleation While Applying Repeated Impacts
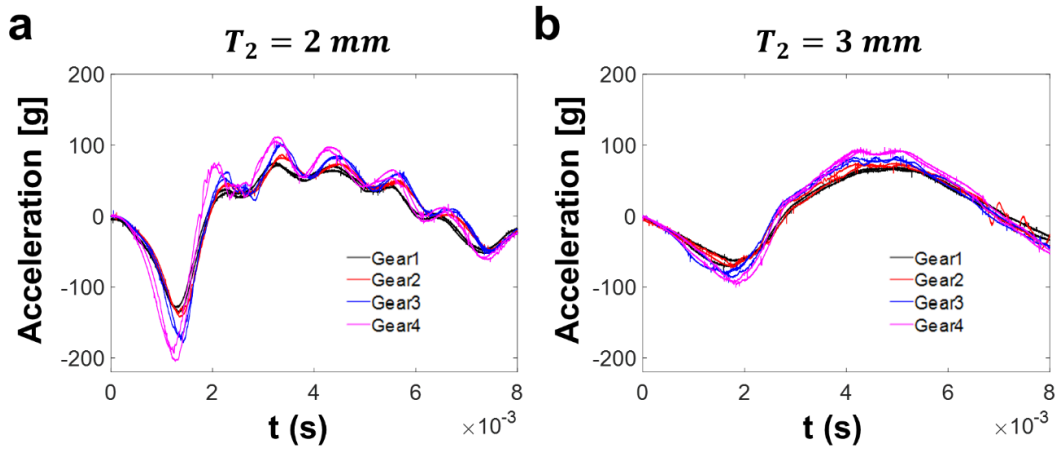
Figure 3-10. (a) and (b) Measured 2 successive acceleration profiles for different gear designs with different silicone rubber sheet thicknesses ($T_2 = 2$ mm (a), and 3 mm (b)). Accelerometer is located on the tube ring.
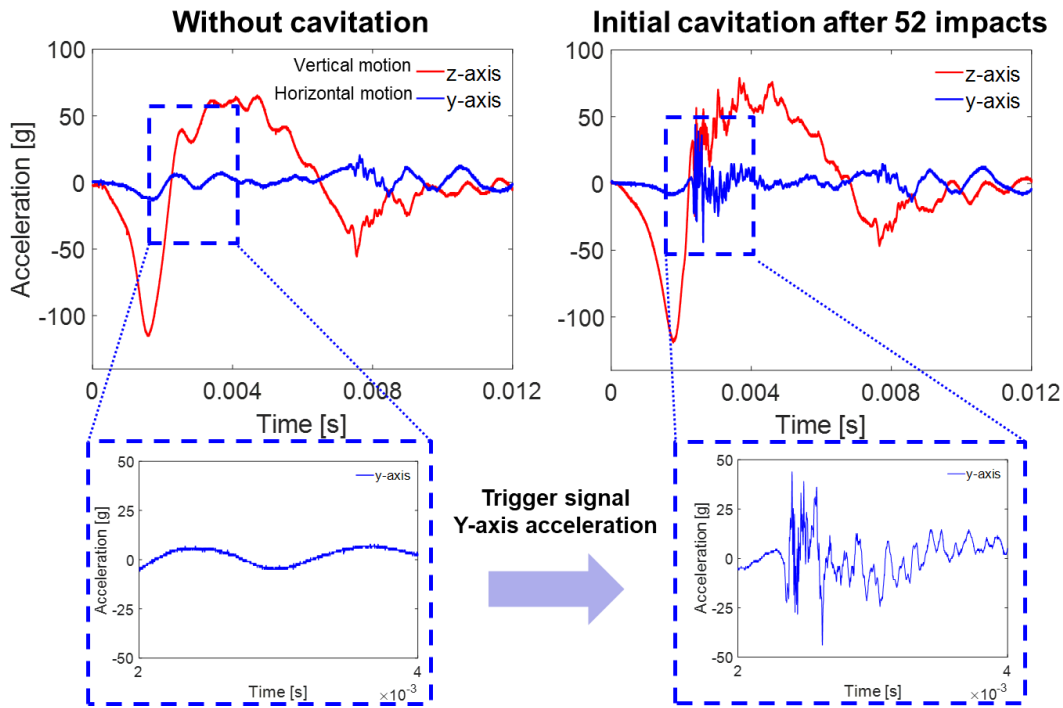
Figure 3-9. Initial cavitation in 0.75w/v% agarose. Left and right graph indicate the corresponding acceleration profiles without and with cavitation. Red and blue curves in each graph show vertical and horizontal acceleration, respectively. To timely trigger the data acquisition system, the horizontal acceleration (i.e., along perpendicular to the impact direction) is used for capturing first cavitation after multiple impacts.

Detecting the first onset of cavitation in a soft gel material subjected to repetitive impacts can be challenging due to a lack of knowledge regarding the relation between applied impact characteristics and soft material properties. To overcome this challenge, it is necessary to find a noticeable difference between post and prior the onset of cavitation. When a cavitation bubble collapses, it releases a significant amount of energy that can be enough to excite the resonance vibration of the sample holder. This large vibration can lead to high frequency as well as amplitude change of the induced acceleration profile. In this regard, the high-frequency and amplified acceleration trajectory will be used to detect the initial onset of cavitation.

First of all, an accelerometer is placed on the tube ring in order to clearly identify the amplified acceleration signal by being close to the target sample. Although measured peak acceleration magnitudes on the tube ring are larger than those on the sample holder, both values are still less than the a_{cr} of 0.75w/v% agarose with single impact for testing a repetitive impact influence on a soft material's response (see Figure 3-10). In addition, a closer accelerometer location to the sample provides more accurate acceleration measurements of soft samples as well as better sense of cavitation induced resonance of the material. Next, a threshold of the acceleration signal value along the horizontal direction (i.e., perpendicular to impact direction, y-axis) is defined rather than the vertical direction (i.e., impact direction, z-axis). This is because the first peak acceleration along the z-axis results from the drop impact event (see red solid line in Figure 3-9), while that for the y-axis comes from the amplified acceleration caused by the cavitation collapse (blue red solid line for the case of "Initial cavitation after 52 impacts" in Figure 3-9). In other words, if the detection threshold of the acceleration value is defined along the vertical

direction, the data acquisition system will be firstly triggered by the applied continuous impacts, not collapse-induced acceleration change. This indicates that the vertical movement cannot be used as standard for detecting the first cavitation. On the other hand, there is a clear difference in the prior to cavitation y-axis acceleration profile and the post cavitation y-axis acceleration amplitude profile. This difference in profiles can be used as a nonvisual signature to trigger the designed algorithm. As already explained in the previous section, specific drop induced acceleration profile is continuously applied onto the sample until the initial cavitation is detected. Once the cavitation collapse induced trigger occurs, the data acquisition system is controlled by using SignalExpress software to send a transistor-transistor logic (TTL) pulse to the high-speed camera and then, to save both pre- and post-trigger data and image sets. As a result, the detected acceleration signal is correlated to a series of images from the high-speed camera in time with a particular emphasis on the signature events of the initial cavitation, i.e., nucleation and collapse.
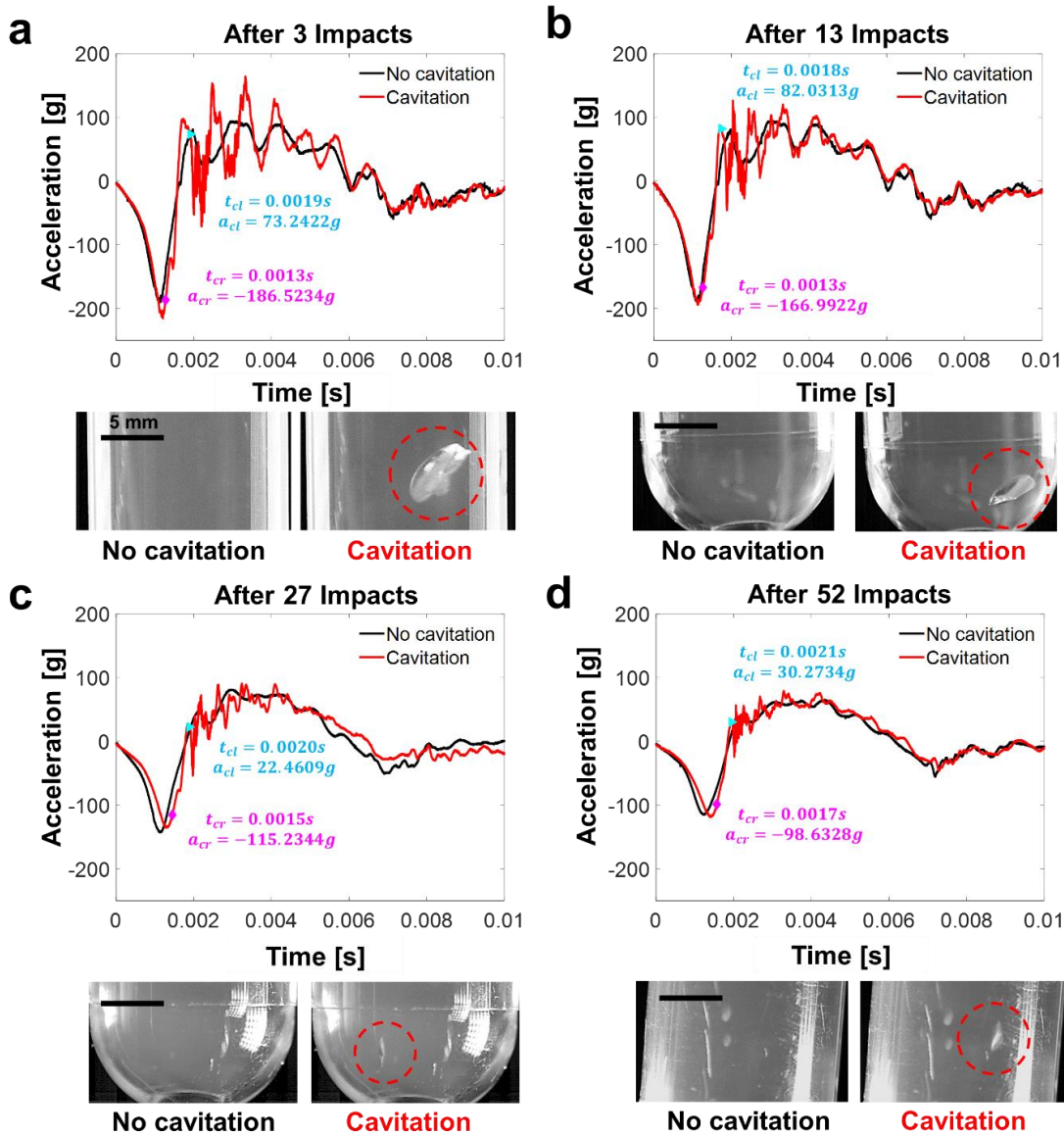
Figure 3-11. Preliminary results of repetitive impact response to agarose 0.75w/v% gel with different number of impacts and gear types. The acceleration profiles with the corresponding high-speed images (i.e., no cavitation (left) and cavitation (right)) are shown: a) cavitation after 3 impacts with gear type 3, b) cavitation after 13 impacts with gear type 3, c) cavitation after 27 impacts with gear type 1, and d) cavitation after 52 impacts with gear type 1. $a_{cr}, a_{cl}, t_{cr},$ and t_{cl} represent the acceleration and time values for cavitation nucleation and collapse, respectively.

Figure 3-11 shows representative experimental results from individual 0.75w/v%

agarose gels with the use of a different number of impacts and gear types for nucleating a

cavitation event: a) 3 impacts with gear type 3, b) 13 impacts with gear type 3, c) 27 impacts with gear type 1, and d) 52 impacts with gear type 1. As discussed earlier, cavitation nucleation and collapse events, as denoted by a solid magenta diamond and cyan triangle, respectively, are obtained from high-speed camera images. In addition, the corresponding acceleration and time values (i.e., a_{cr}, a_{cl}, t_{cr}, and t_{cl} represent the acceleration and time values for cavitation nucleation and collapse, respectively) are written in each acceleration profile. For visual comparison of the soft sample response between without and with cavitation cases, both high-speed images are attached underneath the corresponding acceleration profile (black solid line: no cavitation and red solid line: cavitation). Note that cavitation nucleation consistently happens during the first trough for all 4 cases. This is possibly because of a larger ratio of the first to second acceleration peaks, which results from damping effects of the soft resilient foam and silicone rubber sheet.

Three noticeable observations are that 1) the number of impacts to nucleate a cavitation event increases from 3 to 52 with a decrease of input first peak acceleration (i.e., first minimum peak value of a black solid line in Figure 3-11) from to $190.4297\ g$ to $115.2344\ g$, 2) magnitude of the a_{cr} significantly decreases for 0.75w/v% agarose samples from $186.5234\ g$ to $98.6328\ g$ as an increase of the number of impact, and 3) higher frequency signals are captured after cavitation collapse for every case. The first and second observations indicate the impact characteristics dependent cavitation response. The third observation has been already addressed in the previous section through how cavitation collapse is related to the high frequency signals. On top of that, from Figure 3-11, higher a_{cr} gives rise to a larger cavitation bubble whose major axis length ranges from $2.5\ mm$ ($a_{cr} = 98.6328\ g$) to $5.5\ mm$ ($a_{cr} = 186.5234\ g$). Presumably, this is due to a larger

97

amount of the acceleration-induced inertial energy, resulting in more significant pressure gradients which lead to the formation of a larger bubble.
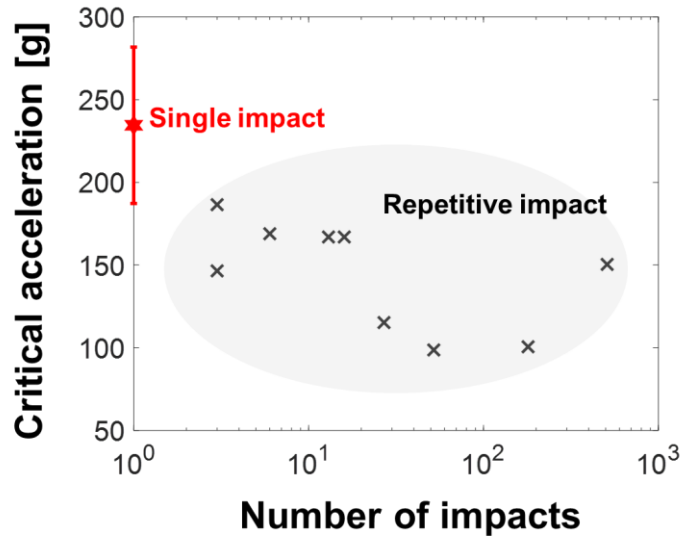
Figure 3-12. Critical acceleration of 0.75w/v% agarose gel as a function of the number of impacts applied onto the agarose gel until capturing an initial cavitation event. The mean critical acceleration of the agarose gel with a single impact are denoted as the red hexagon with 95% confidence interval. All other data points from the repetitive impacts are denoted as a black x marker in the plot.

The relationship between the critical acceleration (a_{cr}) and the impact number (i.e., the total number of applied impact until capturing an initial cavitation nucleation) for agarose 0.75w/v% is considered as shown in Figure 3-12. Interestingly, the a_{cr} values with repetitive impacts (i.e., impact number is greater than 1) are well below the mean a_{cr} (i.e., 234.522 g) with a single impact. For the case of relatively larger impact number (>20), their a_{cr} values are close to the mean a_{cr} of pure water (i.e., 119.667 g, see Figure 3-8). Note that with the consideration of system size, the mean a_{cr} values of agarose 0.75w/v% and pure water with the use of 14 cm tube, which height is similar with human brain size, reasonably match with their known values using 4 cm cuvette in the previous

studies ($710\ g$ and $304\ g$, respectively)   One possible implication of these results is that the effect of impact number on the cavitation property is considerable such that cavitation may occur in the brain after receiving significant number of repetitive impacts during contact sports and military operation which upper range of linear acceleration are $120\ g$ and $250\ g$, respectively. These interesting observations are still preliminary and would require additional studies with the complex impact number-a_{cr} relationships in multivariate biological systems.

3.5   Discussion

The impact-induced acceleration trajectories explored in this study are closely related to external threats that have been frequently measured during contact sports (e.g., boxing game, ice hockey and American football) and military operations. For example, football players receive head impacts whose mean acceleration is $56\ g$, with an upper range more than $100\ g$ (i.e., a threshold of $100\ g$ as a cutoff for detecting possible concussions) during gameplay within a relatively short time scale of impact to peak linear acceleration (a few milliseconds) [216, 217]. For the case of firing a shoulder-fired weapon, the mean maximum recoil acceleration ranges from $200\ g$ to $255\ g$ with sub-millisecond time scales. In terms of severe head injuries, not only impact magnitude, but a characteristic time scale of each impact can also be important since brain tissues (e.g., pons, cortex, and cerebellum) are known to have less or minimal energy dissipation rate particularly at the fast strain rate regions (>20 Hz), likely leading to a decrease of impact energy dissipation efficiency to the microstructures [218]. This strain and/or strain-rate dependent material property can provide the reason for why concussive injury mostly occurs at specific impact

characteristics (i.e., impacts with accelerations of 100 g or greater and durations of 1-10 milliseconds) of which the impact parameters examined in this study are representative.

Another important consideration in this study is that the mechanical response of the 0.75w/v% agarose sample significantly depends on not only the impact amplitude and time scale, but also the total number of impacts applied on individual samples before the onset of initial cavitation. This implies that biomechanical threshold for injury can be impact number dependent. According to injury statistics, individuals with a prior history of TBI are more vulnerable to a second injury; a player who received substantially lower peak acceleration of the impacts than the cutoff acceleration ($\ll 100\ g$) was diagnosed with concussions [219]. To be specific, female ice hockey players reported the average peak acceleration ($43\ g$) related with concussive brain juries with three to five successive impacts per day. As an *in vivo* experiment, a cortical impact study in mice represents a sharp decrease in shear modulus of the damaged brain region which can last for several days [220]. In vitro studies also show that cells result in increased cell damage and degradation of their extracellular matrix (ECM) after a second injury [221, 222]. Although these alternations may not be acute initially, long-lasting changes in biological systems would affect how they react to subsequent mechanical threats in terms of repetitive injuries.

3.6   Conclusion

In summary, the unique integrated drop-tower based repetitive impact tester is developed to study mechanical responses of soft materials under smooth, rapid, repeated loading conditions. On top of benefits from previously designed integrated drop tower systems such as noncontact between sample and impactor, real-time optical

characterization of material deformation, and an environmental isolation of testing sample, the newly developed instrument is additionally able to test sample size- and impact characteristic-dependent material properties. The use of 14 cm tube for storing biological samples allows us to mimic different sizes of human organs (e.g., kidney, liver, lung and heart) and study how varying sample sizes affect the mechanical responses of the target soft sample with the same input acceleration profile. Furthermore, the motor system enables continuously applying a well-controlled acceleration profile by changing the type of gear design. More importantly, a novel trigger condition via resonance measurement has been also defined along orthogonal impact direction, as a non-optical detecting method, to automatically capture the onset of initial cavitation which is one of violent material deformations caused by the rapid mechanical loading. This setup also enables a synchronization of real-time material deformations with the corresponding accelerations.

As a preliminary study for this system, the critical acceleration corresponding to the cavitation nucleation in 7.5% agarose gel is quantified. This study shows that with a single impact, the critical acceleration for agarose samples in the tube ($235\ g$) is significantly smaller than that for the cuvette in the previous study ($800\ g$) [223]. One possible explanation for the lower acceleration threshold for the large tube sample (sample size along impact direction, $h = 14\ cm$) compared to the cuvette ($h = 4\ cm$) is that the acceleration-induced pressure is linearly proportional to h and, as a result, the critical acceleration associated with cavitation nucleation would significantly decreases with increasing h from 4 to 14 cm. Most notably, it is found that the critical acceleration for the agarose sample significantly drops (about a 58% decrease) when the number of impacts prior to the initial cavitation nucleation increases from single to 52. This result supports

others suggesting that soft materials subjected to continuous quasi-static cyclic loading suffer from progressive stress softening behavior resulting from accumulation of inelastic damages such as detachment or breakage of polymer chains and chain slippage [224]. When taken together, the newly developed repetitive impact tester allows future work to answer fundamental questions such as: how does prior impact history of soft, biomaterials affect their response on another insult? Furthermore, this system could be expanded to different sizes of organs or tissues, which minimizes a knowledge gap of their mechanical responses under a variety of impact conditions.

4.   MECHANISMS OF CELL DAMAGE DUE TO MECHANICAL IMPACT – AN IN VITRO INVESTIGATION

4.1   Method

4.1.1   Cell Culture and Image Analysis

For initial validation of this platform, Hs27 fibroblast cells (ATCC, CRL-1634) cultured in DMEM (ATCC 30-2002) and 10% FBS (ATCC 30-2020) are used for all experiments. Fibroblasts are initially plated in several T25 flasks (Corning), with at least one flask solely used to measure and characterize cell confluence as a function of passage. A separate flask is harvested during its logarithmic growth phase (typically ~ 25-80% confluence) to plate cells for subsequent drop tower experiments. For each drop tower culture set up, 50,000 or 100,000 fibroblasts are plated in 1mL of complete media. Each cell-culture is then monitored in real-time while incubating with a 10x phase objective and 25 regions of interest (ROI) at a frequency of every 30 minutes (Incucyte, Essen Bioscience). Confluency of each individual culture is calculated via automated segmentation of each ROI utilizing an image recognition algorithm trained on Hs27 cells offered through the Incucyte software. The resulting growth-curve of a single culture set up is the average of 25 individual ROI confluence measurements. Typically, eight cell culture setups are prepared and monitored in parallel. After the cultures reach the approximate middle of the logarithmic growth phase (approximately 35~40% confluence), each cell culture setup is assembled with the holder for drop tower experiments (Step-ii in Figure 4-1 (b)). Each drop tower test takes approximately 15 minutes and is conducted under aseptic conditions, minimizing deviations of *in-vitro* conditions. For each batch of

experiments, one culture set up remains in the incubator as a reference, while another

undergoes the same steps and conditions of a drop tower test without any impact forces
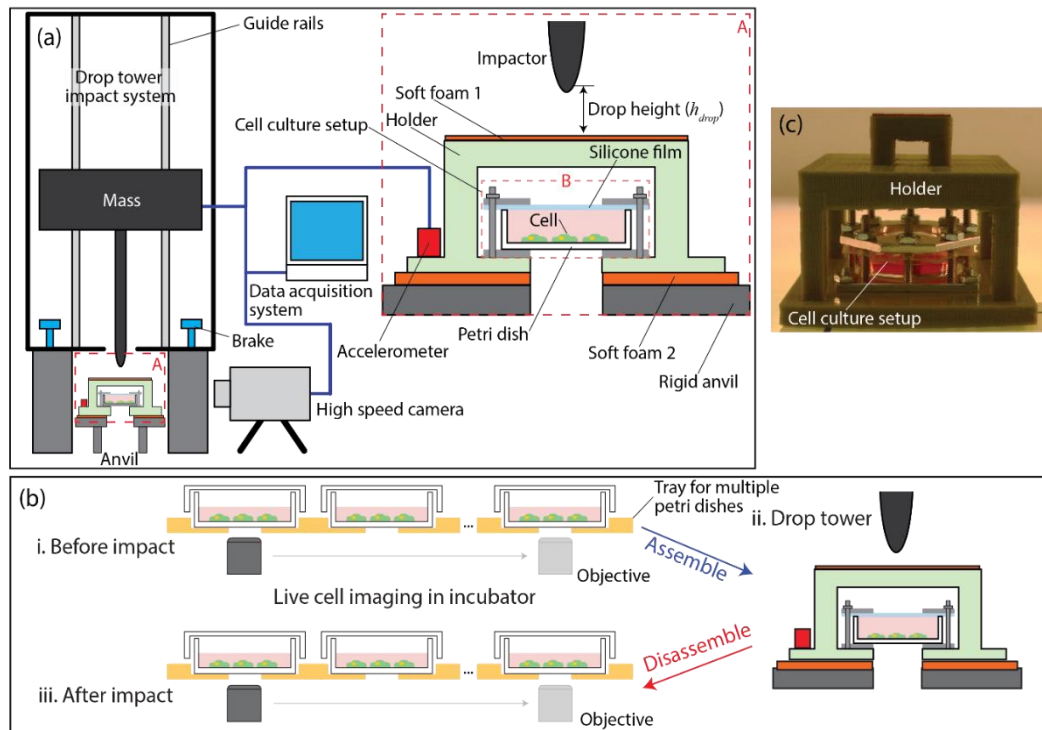
Figure 4-1. (a) Schematic of the drop-tower-based integrated system for characterizing the biological response of live cells due to rapid acceleration associated with mechanical impact. The inset (zoom-in view of *Area A*) on the right shows the structures of the cell culture setup (highlighted by *Area B*) and the holder with electrical connections for data acquisition. (b) shows the experimental protocol to study acceleration-induced cell damage utilizing both the live cell microscopy and drop tower-based instrument. (c) An image of an assembled holder with a cell culture setup for a drop tower experiment. (b-i) Prepare multiple cell culture petri dishes and monitor them using live cell imaging capability in the incubator. All the prepared cell culture dishes are placed on a tray in a cell culture incubator and a motorized optical objective is used to take live cell images for all dishes at specific time intervals (see the arrows). When cell populations reach a specific target stage, e.g., 35-40% confluency in the cell growth curve, (b-ii) each petri dish is assembled with a holder for drop tower experiments (C shows a petri dish assembled with a cell culture setup, see Figure 4-2 for more details). (b-iii) After a drop tower experiment, a petri dish is disassembled from the cell culture setup and placed in a cell culture incubator for continuing live cell imaging.

being distributed on the culture as a control. The remaining cultures are utilized for drop

tower tests.

To access the plasma membrane integrity, propidium iodide (PI, ~700 Da, abcam ab14083, Cambridge, UK) is used. During the assembly of the cell culture setup (Figure 4-1 (b)), PI solution diluted in cell culture media is added into a petri dish to achieve the final PI concentration of $10\mu g/ml$. After completion of a drop tower experiment, each petri dish is washed with PBS and then regular cell culture media is added for live cell imaging of the fibroblasts during cell culture.

4.1.2   Drop Tower Experiments

To simulate realistic mechanical impact on biological systems, a recently developed system, called the integrated drop tower system [121], is utilized. The integrated drop tower system (Figure 4-1 (a)) consists of a conventional drop tower impact system (Dynatup 9210, Instron, Norwood, MA), two high speed cameras (Fastcam SA-X2RV, Photron, San Diego, CA), a cell culture setup (see the SI), A three-axis ICP-based accelerometer (model #356A01, PCB Piezotronics, Depew, NY), and a data acquisition system (National Instruments Corp., TX). One or two independent high-speed cameras are mounted on two camera stands such that the cameras can concurrently capture the front or/and side views of the cuvette, typically at 50k frames per second (fps). The plastic sample holder is manufactured using a MakerBot Replicator 2 (MakerBot Industries, LLC, Brooklyn, NY) 3D printer using MakerBot PLA (polylactic acid) plastic filament. Printing is done using default settings, with the exception of the infill being set to 100%. The accelerometer is glued onto the holders using 5-min epoxy. We use *soft form 1* (1mm thick, 50A silicone rubber, McMaster-Carr, Princeton, NJ) and *2* (12mm thick, silicone polymer closed cell sponge #7904, MTI Groendyk Inc., Richmond, VA) to control the characteristics of impact. Data acquisition is performed using a system consisting of an NI PXIe-8135 embedded

controller and an NI PXI-6115 multifunction I/O module using SignalExpress 2014 data acquisition software (all from National Instruments Corp., Austin, TX). The accelerometer (model #356A01, PCB Piezotronics, Depew, NY) is connected to three channels of the data acquisition system through an ICP signal conditioner (model #480B21, PCB Piezotronics). Data are acquired at a rate of 1 MHz and triggered off the vertical axis of the accelerometer. A pre-trigger buffer is used to capture the entirety of the signal event. Upon triggering the data acquisition system is programed through SignalExpress to output a TTL pulse to the two Photron cameras which are set up with a pre-trigger buffer equal in time to the data acquisition system's buffer. The time delay between the triggering of the data acquisition system and output of the TTL is less than a single sample ($< 1 \mu s$). To reliably measure pressure, a PCB 113B21 pressure sensor was used (PCB Piezotronics, Depew, NY). This has a 2758 kPa max range, with a rise time of less than 1 μs.

4.1.3 Experiment Setup – in Vitro Setup for Blunt Injury Mechanisms

Here, a new technique for studying cell injury mechanisms is presented by applying biologically relevant mechanical impact to in vitro cell culture. This new approach is for maintaining consistent in vitro conditions during experiments, accommodating multiple cell populations, and monitoring each population in real-time while the impact-induced accelerations which mimic blunt injury are quantified with regards to amplitude and time scale. These multiplexed, environmental control capabilities are critical for studying the relationships between mechanical impact and cell injury due to the complex nature of interpreting input-output relationships in multivariate biological systems.

Acceleration for typical blunt injuries, as discussed above, is in the range of 80-250g within 0.1-10 millisecond. Considering these specifications, it is important to control

collisions so that they closely represent biologically relevant blunt injury events during in vitro studies. In this regard, a new in vitro setup that can be integrated with a drop-tower-based system as well as a multiplexed, live cell-imaging instrument, as shown in Figure 4-1 (a) has been developed and utilized.

The system consists of a conventional drop tower impact system, two high speed cameras, a cell culture setup, accelerometers, and a data-acquisition system. For applying impact on the cell culture setup, a weight is vertically lifted to a specific height and then released. Upon the release, the weight impacts a holder with an integrated cell culture setup causing the cells and cell culture media to rapidly accelerate in the similar way biological systems would accelerate, e.g., inside the abdomen or skull. During impact, velocity, acceleration, and impact force are quantified using various sensors, while optically monitoring the cell culture setup utilizing high-speed cameras. Before and after an impact experiment, the cell culture petri dish is kept in incubator (Figure 4-1 (b-i and –ii)) for various analyses via live cell microscopy.
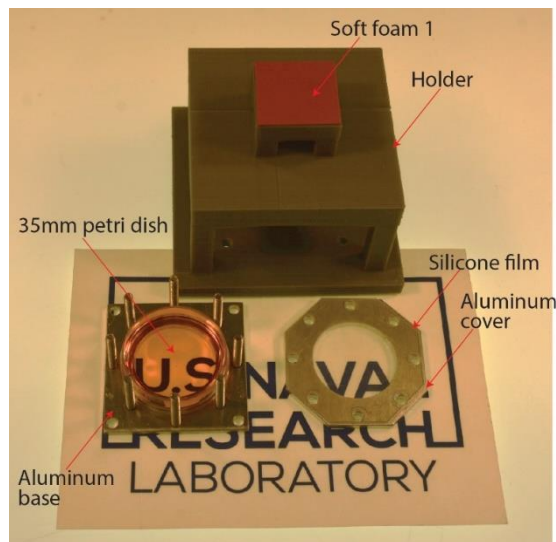
Figure 4-2. An optical image of a cell culture setup for a drop-tower experiment.

The cell culture setup (*Area B* in Figure 4-1 (a)) consists of a commercially available 35-mm cell culture petri dish, aluminum plates, and a transparent silicone film. Each petri dish is assembled/disassembled with the cell culture setup by standard bolts and nuts with other components. Two major technical challenges for any *in-vitro* experimental platform are environmental control and cell heterogeneity. First, cells are sensitive to changes in their environment and, as a result, minimizing and eliminating unwanted perturbations to cellular environments during in vitro studies is imperative for accurate interpretation and reproducibility of results. Second, both individual and collective cellular behavior is heterogeneous in nature, potentially confounding the interpretation of cellular response associated with the injury mechanism. The cell culture setup is designed to address these challenges by integrating with a multiplexed, live cell-imaging instrument as schematically shown in Figure 4-1 (b-i and –iii) (see Figure 4-2 for structural details of the cell culture setup).

It is important to note that the holder is rigid enough to sustain impacts while preventing direct impact to the cell culture setup. The two soft foam layers (*Soft foam 1* and *2* in Figure 4-1 (a)) are used at the top and bottom of the holder, critical to achieve desired impact in terms of both amplitude and time scale of acceleration. The top layer (*Soft foam 1*) is thinner (1mm) and stiffer (4MPa) to prevent direct solid-solid surface impact, which would generate shock waves, while effectively accelerating the holder (see Figure 4-3). The bottom layer (*Soft foam 2*) is thicker (12mm) and softer (0.4MPa) so that the holder can vertically move against the small stiffness of the layer. These parameters are specifically chosen to simulate common blunt injury scenarios, i.e., $>150g$ and <1ms. This experimental setup is generalizable so that the system parameters, e.g., the soft foams, can

be tuned to mimic characteristics of different blunt injury cases as reported in great detail [121].

The new approach allows continuous optical observation of multiple cell culture setups (currently up to 12 separate culture setups) without the need to take cells out from an incubator for observation. Additionally, the multiplexing capability of multiple cell
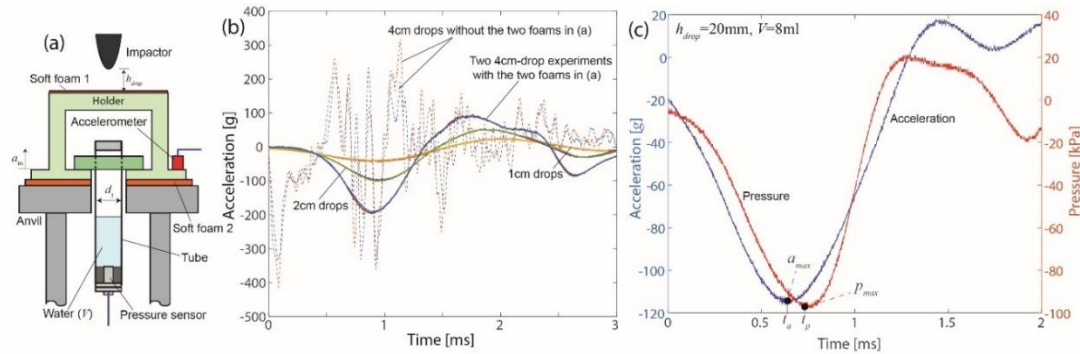
Figure 4-3. (a) Schematic of the experimental setup, (b) Acceleration response of the holder with and without use of soft foams and (c) the experimental comparison of acceleration and pressure with use of the foams during impact. The significant difference is observed in the measured acceleration signals in (b) when compared the two cases, i.e., with and without the soft foams. Compared to the latter (dotted lines in b), the former (solid lines in b) has much smoother acceleration profiles with much longer time scale (~1ms).

populations in parallel offers a unique dynamic window into how cells respond to mechanical input by directly comparing the same population of cells before and after impact in real-time. These attractive capabilities are essential for probing the injury mechanisms of cells while minimizing batch-to-batch and/or population-to-population variations in cell response due to heterogeneities.

4.2   Experimental Results

4.2.1   Theoretical Analysis on Acceleration-induced Pressure

Acceleration-induced pressure profiles during impact are a primary mechanism for blunt injuries. Therefore, it is necessary to characterize the pressure-acceleration relationship in the cell culture setup to understand the intimate connection between cell damage and mechanical impact.
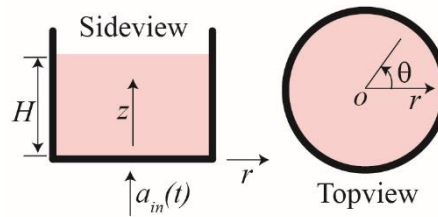
Figure 4-4. Transverse and cross-sectional views of the cell culture setup denoted by a cylindrical polar coordinate system.

Consider the transverse and cross-sectional views in Figure 4-4 that presents the cell culture setup with a focus on the time-dependent pressure profile in the cell culture media during impact where d and H are the diameter and height of the cell culture chamber, respectively. r, θ, and z are the radial, angular, and vertical coordinates with respect to the origin at the center of the bottom surface of the cell culture chamber. Upon mechanical impact on the holder, the cell culture setup is rapidly accelerated by a_{in} that results in acceleration-induced pressure (p_a) in the cell culture media where a_{in} and p_a are functions of time (t).

In the following analysis, it is assumed that the cell culture media is incompressible Newtonian fluid. Due to the axial symmetry of the cylinder-shaped cell culture chamber about z-axis, the pressure gradient (p_{in}) in the cell culture media depends on two

110

coordinates, r and z, only, and as a result all terms with a partial derivative of θ are zero, i.e., $\partial/\partial\theta = 0$. It is also assumed that no slip conditions along the solid-liquid interfaces at $(r, z) = (d/2, z)$ and $= (r, 0)$. Note that all external forces acting on the cell culture media during impact are associated with the no slip boundary conditions at the solid-liquid interfaces. Because all external forces are in z-direction, it is assumed the velocity of the cell media in r- and θ-directions is zero. Based on the experimental observations, it has been shown that the above assumptions on the velocity are reasonable between the time points from the onset of impact to maximum amplitude of input acceleration.

Using the assumptions above, the governing equation of motion for incompressible Newtonian fluid, i.e., the Navier-Stokes equations[225] with constant density of cell culture media (i.e., $\rho(r, \theta, z, t) =$ constant), in the cylindrical polar coordinates can be simplified as below

Equation 4-1

$$\rho(a_{in}(t) - g) = -\frac{\partial p_a}{\partial z}$$

where g is gravity. By solving Equation 4-1 using the free surface boundary ($p_a(z = H) = 0$), the acceleration-induced pressure in the cell culture media can be written as

Equation 4-2

$$p_a(z, t) = -\rho(H - z)(a_{in}(t) - g)$$

Note that the pressure in the cell culture media is linearly proportional to depth of cell culture media $(H - z)$ and input acceleration (a_{in}). The most important location is the cell

culture surface at z = 0 in which the pressure applied to cells is $p_a(0, t) \approx -\rho H a_{in}(t)$ for $a_{in} \gg g$.

4.2.2   The Key Injury Mechanism

Acceleration is the most commonly used criteria for blunt injury mainly due to ease of quantification, e.g., when compared to direct pressure measurements inside the human body. In addition to the easier measurement, it can be argued that acceleration could be a good representation of time-dependent pressure gradient in biological systems because acceleration and acceleration-induced pressure are intrinsically coupled during blunt impact, as suggested by Equation 4-2. However, the acceleration-based injury criteria have greatly overlooked the fact that acceleration-induced pressure also depends on the characteristic length of the biological systems, i.e., the height of cell culture media (H) in Equation 4-2. In addition, the recent experimental work utilizing collagen as tissue simulant has shown a non-linear acceleration-induced pressure for soft biomaterials [123], e.g., tissue, indicating that liquid-based experiments may even underestimate the sensitivity of cells to H.

To explore possible effects of size on blunt injury mechanisms, a cell culture chamber ($H = 10$ mm) is utilized and changes in cell response of fibroblast associated with mechanical impact are characterized. The focus is on quantifying the critical input acceleration for cell damage by monitoring cell confluency and cell membrane perturbations. Then the possible underlying mechanism(s) that govern the correlation between the critical input acceleration and the onset of the detectable damage to cell populations is considered.

4.2.3 Multiplexed in Vitro Cell Cultures

For the experimental study of cell damage due to mechanical impact, multiple cell culture petri dishes are firstly prepared and monitored by using live cell imaging capability in an incubator, as indicated in Figure 4-1 (b-i). After the cells cultured on an individual petri dish reached a specific target stage, e.g., 35-40% confluency in the cell growth curve, additional cell culture media was added to the dish before assembling with a holder for the drop tower experiments, Figure 4-1 (b-ii). Note that two dishes were always dedicated for control experiments (specific conditions for the *controls* are discussed below), while *other dishes* were for drop tower experiments. To quantify cell population, the local confluency at each area from A3 to E3 (see the inset in Figure 4-3) as well as the average confluency of each dish (the average over the nine areas) are continuously monitored during cell culture concurrently for both the *controls* and *other dishes*. The confluency is the ratio of the area covered by cells to the total area, evaluated based on image analysis of cells.

It is important that extra cell culture media was added to the maximum capacity of a petri dish (~10mm in height) only during the assembly of the drop tower holder as shown in Figure 4-1 (b). This step ensured 1) 3-5mm deep cell culture media was maintained during regular cell culture and 2) excessive air was removed from the cell culture setup during drop tower experiments. First, the shallow cell culture media is important for CO_2 exchange that ensures media pH stability during culture [226]. Second, it has been found that a trapped air pocket between cell culture media and a silicone film (Figure 4-1 (a), *Area B*) during the assembly of the cell culture setup could result in unwanted cell damage during impact. As an example, it has been observed that the trapped air was inserted into

113

the cell culture media during violent impact. In this case, cells could be damaged when directly exposed to the air, which is not a biologically relevant mechanism.

Unless stated otherwise, the same volume of cell culture media, like the other dishes, was added to the negative *control dishes* for maintaining consistent in vitro conditions during experiments. After adding media, one dish (*Control 1*) was immediately returned to an incubator without being assembled with the cell culture setup while a second (*Control 2*) underwent the exact conditions of the *non-control dishes*, i.e., assembled and stored in a temperature-controlled box for ~10 min, except for application of impact. *Control 1* and *2* were designed to quantify possible cell damage associated with the assembly procedure
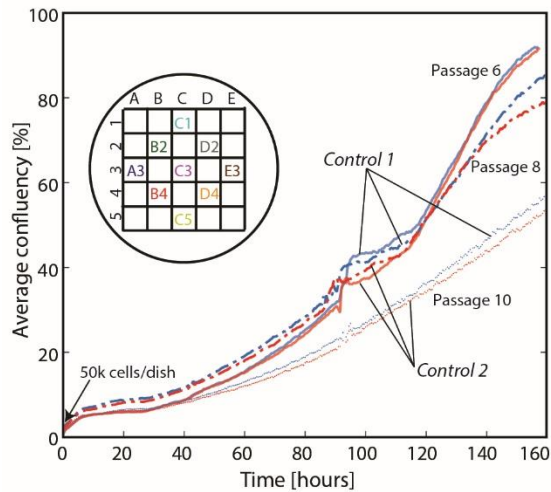
Figure 4-5. The average confluence of two *controls* without being exposed to mechanical impact for Hs27 cells. The average confluency was evalutaed from the nine areas on each 35mm petri dish (A3 to E3). *Control 1*: Additional cell media was added and immediately returned to an incubator (i.e., stayed in an incuvator during entire experiments). *Control 2*: After adding additional cell media, *Control 2* underwent the exact conditions of the *non-control dishes*, i.e., assembled and stored in a temperature-controlled box for ~10 min, except for application of impact.

of the cell culture setup.

Figure 4-5 shows the average confluency of fibroblast cells for *Control 1* and *2* prepared from *passages 6, 8, and 10*, respectively. The confluency curves of the two controls are very comparable to each other in all three passages. This study indicates that the new in vitro cell culture setup minimizes unwanted perturbations to cell cultures for ~1 week.
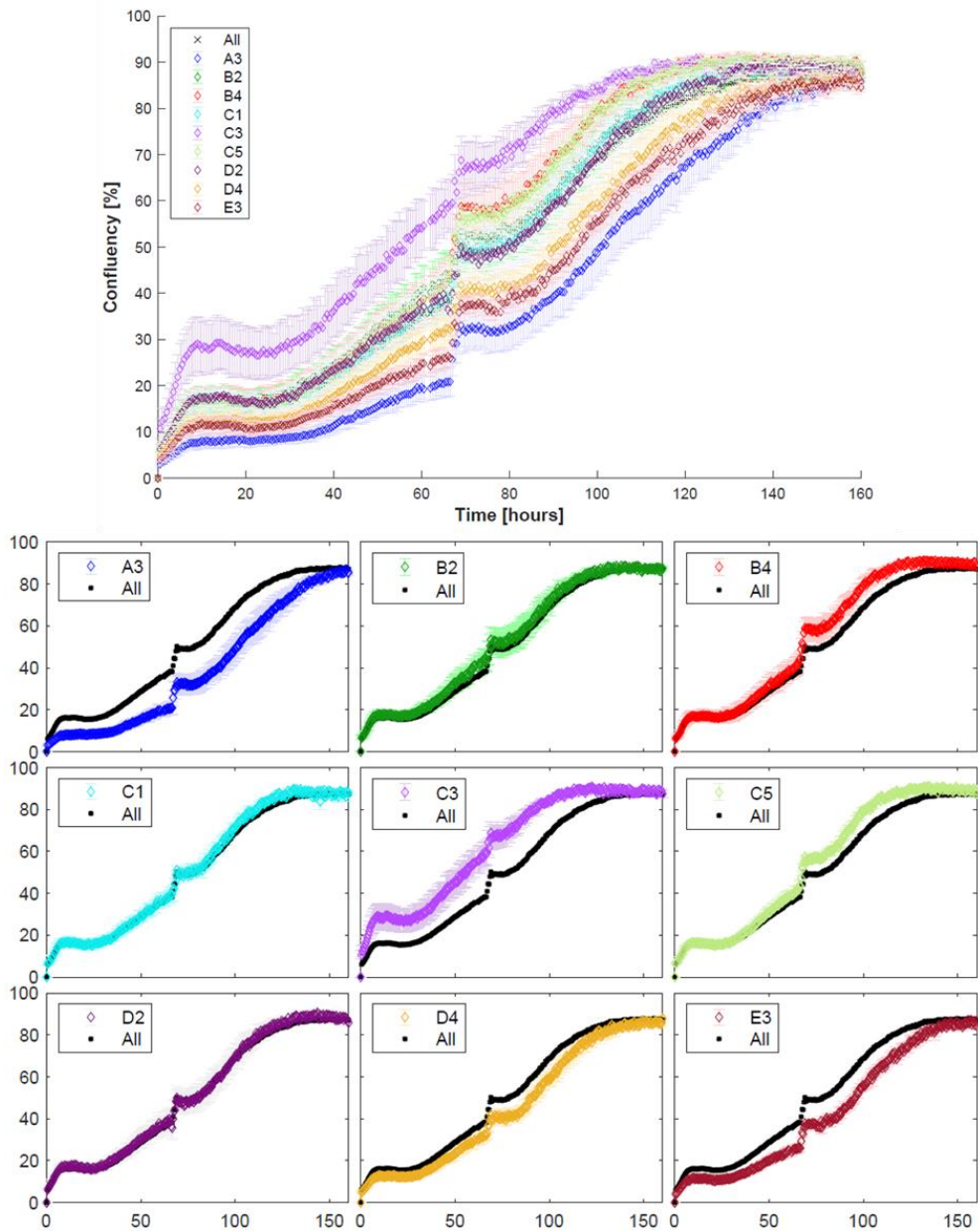
Figure 4-6. Local and average confluency curves for Control 1 from Passage 11. The upper panel shows the confluency curves at each ROI with the standard error (95% interval) and the average confluency curve (designated by "all" in legend) from the nine ROIs. The lower panel shows detail from each ROI where the local confluency curve is compared with the average confluency curve (see the legend in each plot). The horizonal and vertical axes are Time [hours] and Confluency [%], respectively.
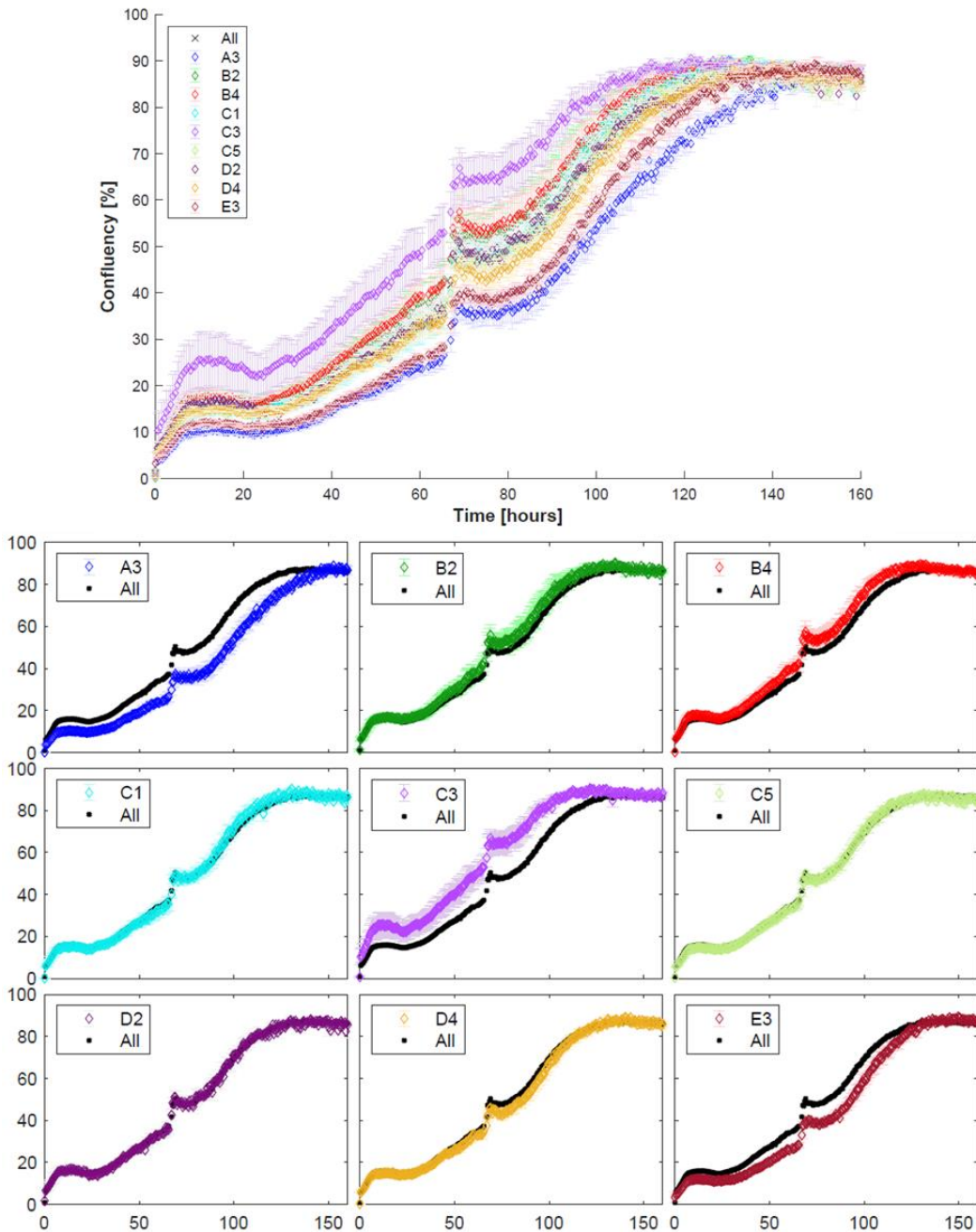
Figure 4-7. Local and average confluency curves with the standard error (95% interval, error bars are shown each plot) for Control 2 from Passage 11 (the average confluency curves are shown in Figure 4-12 (d)). The upper panel shows the confluency curves at each ROI and the average confluency curve (designated by "all" in legend) for the nine ROIs. The lower panel shows details for each ROI with the standard error where the local confluency curve is compared with the average confluency curve (see the legend in each plot). The horizonal and vertical axes are Time [hours] and Confluency [%], respectively.

117
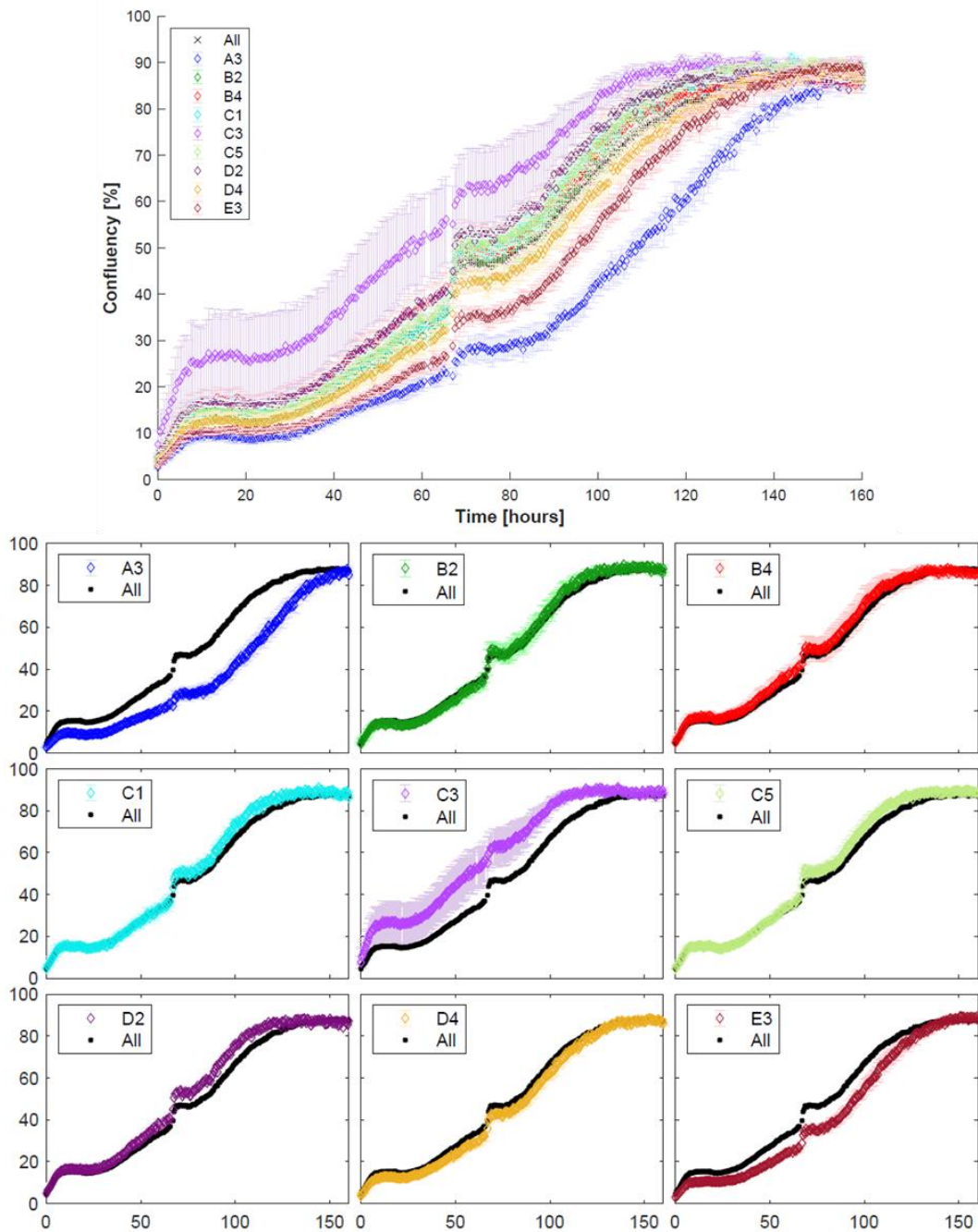
Figure 4-8. Local and average confluency curves with the standard error (95% interval, error bars are shown each plot) for 30cm drop 1 from Passage 11 (the average confluency curves are shown in Figure 4-12 (d)). The upper panel shows the confluency curves at each ROI and the average confluency curve (designated by "all" in legend) for the nine ROIs. The lower panel shows details for each ROI with the standard error where the local confluency curve is compared with the average confluency curve (see the legend in each plot). The horizonal and vertical axes are Time [hours] and Confluency [%], respectively.

118
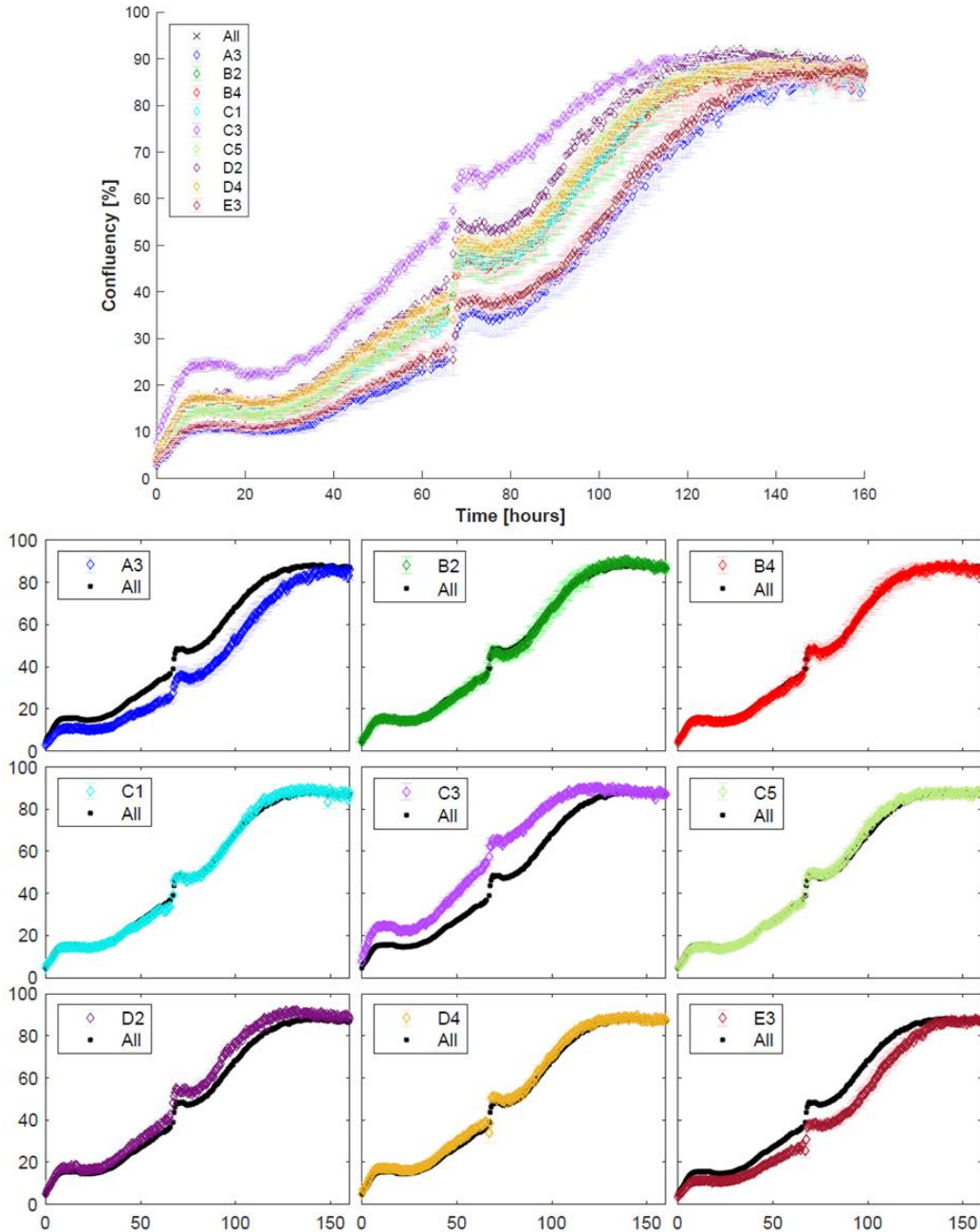
Figure 4-9. Local and average confluency curves with the standard error (95% interval, error bars are shown each plot) for 30cm drop from Passage 11 (the average confluency curves are shown in Figure 4-12 (d)). The upper panel shows the confluency curves at each ROI and the average confluency curve (designated by "all" in legend) for the nine ROIs. The lower panel shows details for each ROI with the standard error where the local confluency curve is compared with the average confluency curve (see the legend in each plot). The horizonal and vertical axes are Time [hours] and Confluency [%], respectively.

119
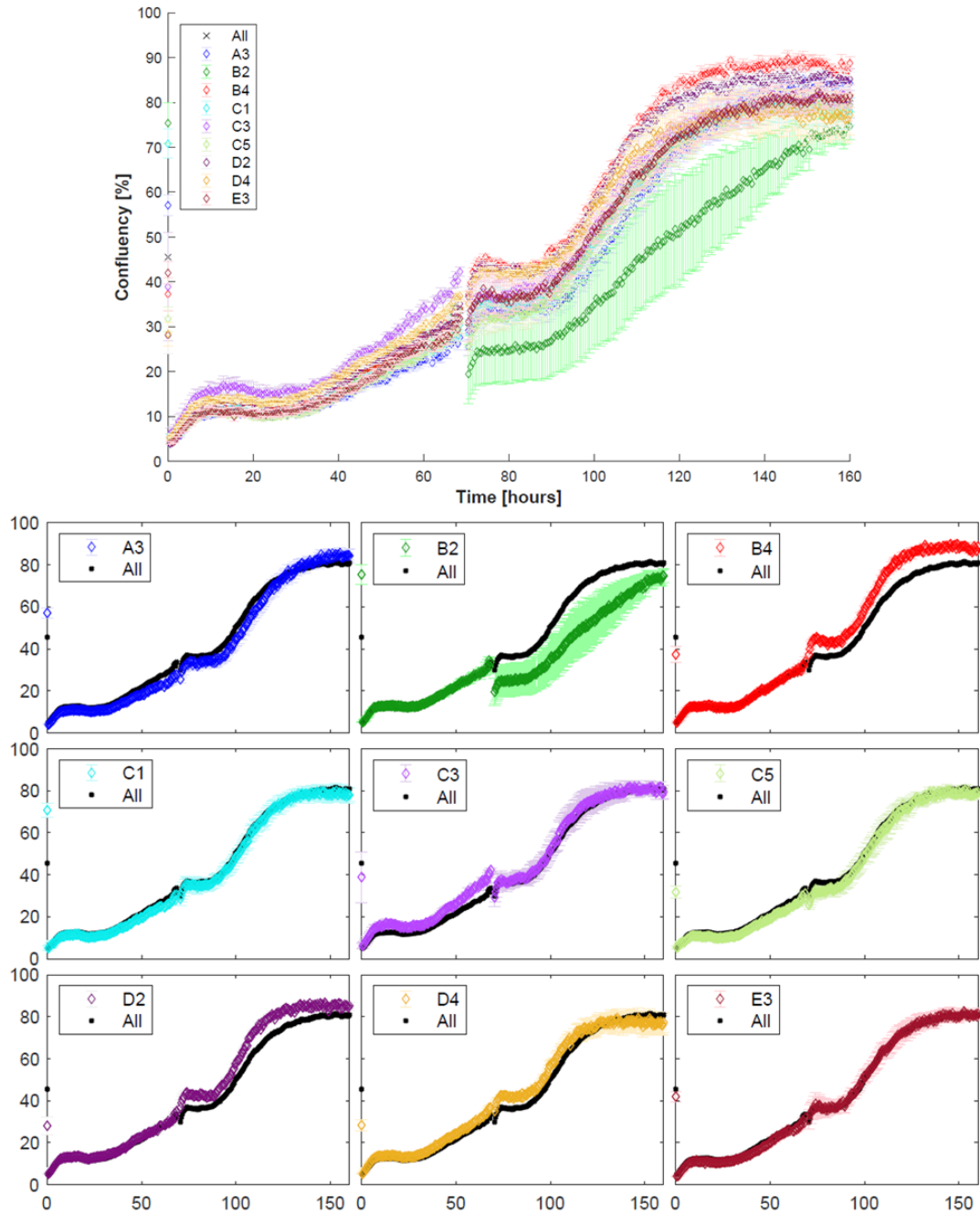
Figure 4-10. Local and average confluency curves with the standard error (95% interval, error bars are shown each plot) for 45cm drop 1 from Passage 11 (the average confluency curves are shown in Figure 4-12 (d)). The upper panel shows the confluency curves at each ROI and the average confluency curve (designated by "all" in legend) for the nine ROIs. The lower panel shows details for each ROI with the standard error where the local confluency curve is compared with the average confluency curve (see the legend in each plot). The horizonal and vertical axes are Time [hours] and Confluency [%], respectively.

120
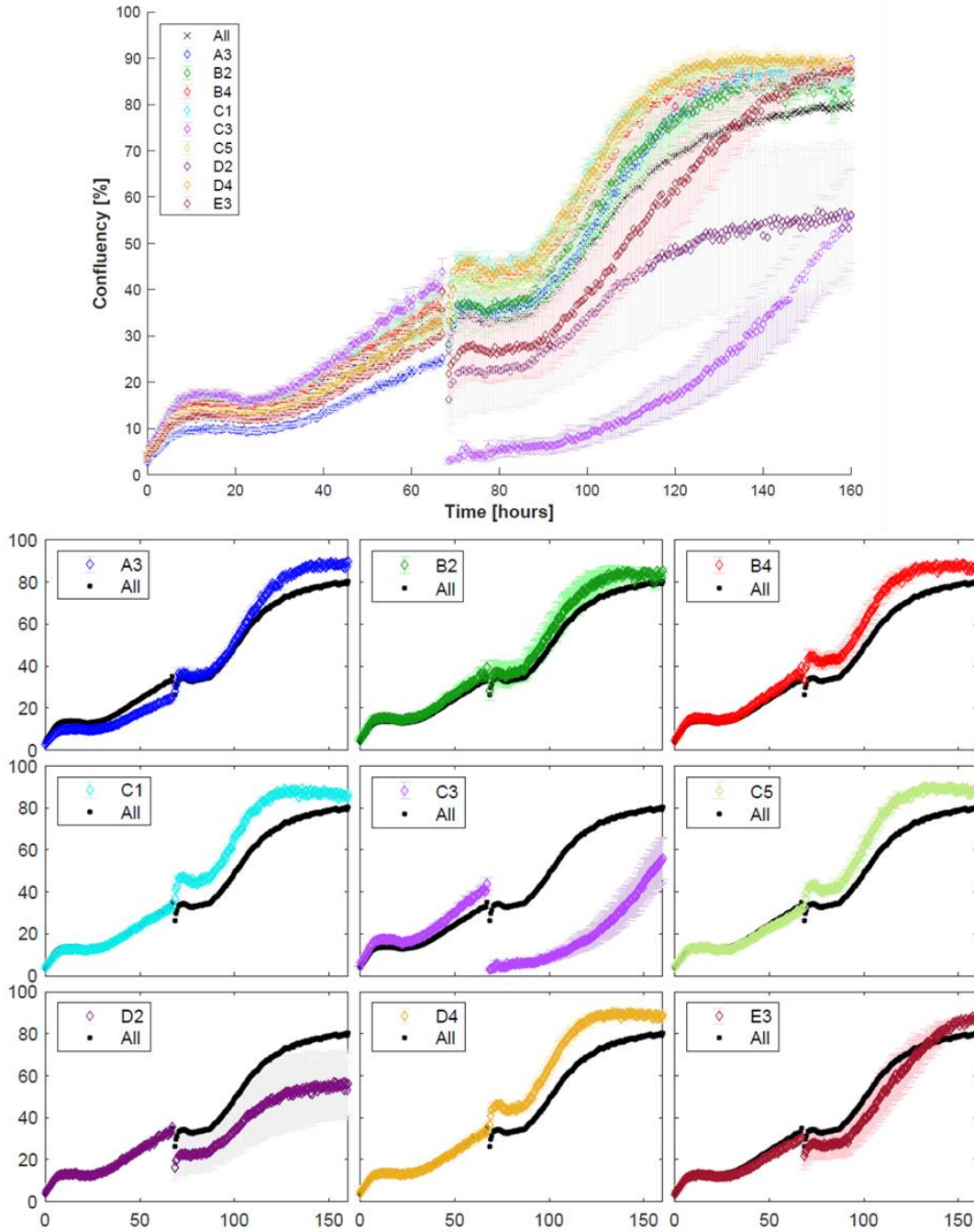
Figure 4-11. Local and average confluency curves with the standard error (95% interval, error bars are shown each plot) for 40cm drop 2 from Passage 11 (the average confluency curves are shown in Figure 4-12 (d)). The upper panel shows the confluency curves at each ROI and the average confluency curve (designated by "all" in legend) for the nine ROIs. The lower panel shows details for each ROI with the standard error where the local confluency curve is compared with the average confluency curve (see the legend in each plot). The horizonal and vertical axes are Time [hours] and Confluency [%], respectively.

121

There are a number of interesting observations by making multiplexed, real-time measurements of the growth as opposed to the more typical end-point assay approach to in vitro studies. For instance, in Figure 4-5, the growth rate becomes noticeably slower for *passage 10* compared to the previous passages, which is important for identifying passage-dependent responses. In addition, local confluency curves of each region of interest can be significantly different from the average values (see Figure 4-6, Figure 4-7, Figure 4-8, Figure 4-9, Figure 4-10, and Figure 4-11). The observed, intrinsic temporal and spatial cell heterogeneity could mask or mislead studies on injury mechanisms. As will be shown below, fmaking conclusions based on the data from a localized small area could be misleading because each area even on the same petri dish could have significantly different cell population/behavior/growth compared to the average cell behavior. The examples above highlight the attractive features of the approach including 1) characterization of the multiple, identical cell culture populations in real time to a variety of impact accelerations and pressure gradients and 2) a capability to analyze a sufficiently large cell population for statistically significant results.

4.2.4 The Critical Blunt Injury Conditions

Here, the critical blunt injury conditions that resulted in cell damage to fibroblast cells are quantified. For this study, several cell cultures prepared from passages 6, 8, and 11 (the same cell culture used in Figure 4-5) were subjected to a range of drop tower heights from 5cm to 40cm during the middle (35-40%) of their logarithmic growth phase (see "Impact" in Figure 4-12 (a-f)). Note that Figure 4-5 and Figure 4-12 are based on more than 20 independent petri dishes (e.g., each curve in Figure 4-5 and Figure 4-12 (a-c) is obtained from independent individual petri dishes) and at least two petri dishes were cultured and

tested under the same conditions. The cell cultures that were exposed to less than 40cm drop, both single/multiple impact conditions, show the average as well as local confluency curves that are very similar to the corresponding *Control 2* results (see Figure 4-12 (a-b) and (d-f) for the average and local confluency curves, respectively). On the contrary, the average confluency after the 40cm-drop experiment decreased from 48% to 35% (Figure 4-12 (c)). Furthermore, the local confluency curves (Figure 4-12 (d-f)) indicated that the cell damage after 40cm-drop was not homogeneous over the entire petri dish as significant cell population losses were localized to C3, D2, and E3 (Figure 4-12 (f)). As an example, the local confluency in C3 significantly dropped from ~40% to ~3%. This dramatic change is also shown in g-i and -ii, live cell images before and after 40cm-drop, respectively. Note that the orange lines in g-i and -ii highlight the contours of cells.

Based on the experimental data summarized in Figure 4-12, it has been concluded that the critical drop height associated with the noticeable loss of cell population was >30cm. Interestingly, the maximum amplitude of input acceleration for 30cm-drop was 990-1000g (see the inset in Figure 4-12 (c)), significantly larger than the commonly used criteria (150g) for blunt head injury. Equation 2 could provide a feasible explanation for this. The
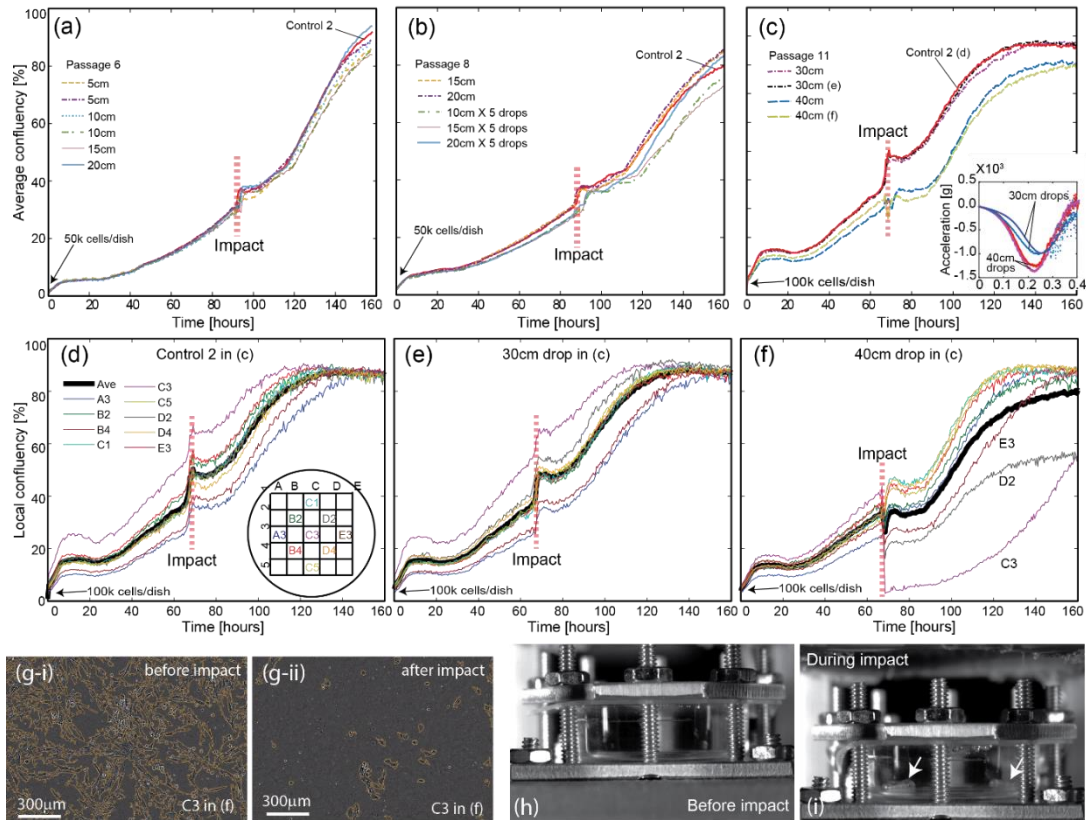
Figure 4-12. Characterizatinon of the critical mechanical impact for cell injury using Hs27 cells using an average confluency metric (a)-(c) versus a local area confluency metric (d)-(f), monitored over 160 hours. The average confluency curves (a) 5cm-, 10cm-, 15cm-, and 20cm-single-drops, (b) 15cm-/20cm-single-drops as well as 10cm-, 15cm-, and 20cm-five-drops, (c) 30cm- and 40cm-single-drops on the cell cultures. Passage 6, 8, and 11 were used for (a), (b), and (c), respectively. The acceleration measured during 30cm- and 40cm-drops are shown in the inset of (c). The local confluency curves for *Control 2*, 30cm-drop, and 40cm-drop from (c) are shown in d-f, respectivly. g-i and -ii are live cell images corresponsding to area C3 in (f) before and after the impact, respectivly. (h) and (i) are high speed camera images of the cell culture setup during 40cm-drop. Cavitation bubbles are observed on the petri dish (see the arrows in (i)).

124

maximum acceleration-induced pressure is linearly proportional to the size of biological system and, as a result, the critical input acceleration associated with cell damage would significantly increase with decreasing size of biological systems.

Another unexpected observation was a sudden increase in localized cell death for 40cm-drops, rather than globally and incrementally increasing cell death, where the corresponding amplitude of acceleration was 1280-1370g (see the inset in c). To identify the specific damage mechanism that seems to be activated for >1000g, high-speed camera movies were utilized (see Figure 4-12 (h-i)). The high-speed images in h-i show that cavitation bubbles, likely responsible for localized cell damage considering violent nature of cavitation dynamics, formed at the bottom of a petri dish for 40cm-drops. this cavitation-induced mechanism for cell damage is discussed later.

To support the two conclusions above, the detailed confluency curves with the standard error (95% interval) are shown from Figure 4-6 to Figure 4-11. The emphasis is placed on experimental data presented in Figure 4-12 (c) because the figure can be used to determine the critical drop height that triggers statistically relevant decreases in the confluency curves. Note that among Figure 4-6 to Figure 4-11, statistically relevant cell damage was observed only for the 40cm drop experiments and was limited to local ROIs, (e.g., see B2 in Figure 4-10 and C3 and D2 in Figure 4-11).
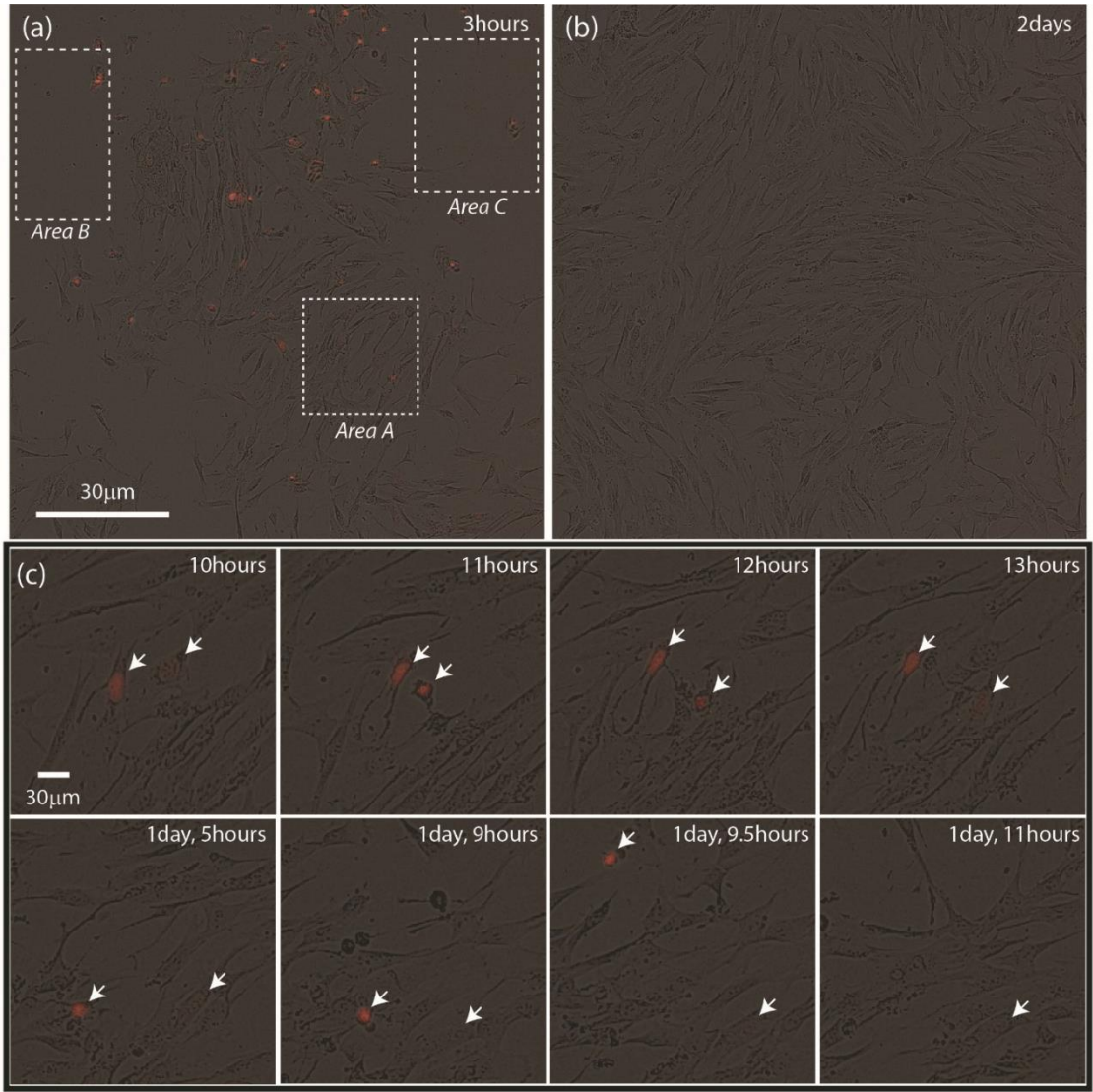
Figure 4-13. Propidium iodide (PI) fluorescence intensity overlaid with phase imagery highlighting PI of fibroblasts post-impact as a function of time. (a)-(b) are 3 hours and 2 days, respectively, after the 40cm-drop impact where *Area B* and *C* highlight localized loss of cell population due to cavitation. (c) is time lapse of *Area A* in (a).

To further highlight the importance of system size, note that the critical acceleration (~300g) at the onset of cavitation in pure water was recently quantified using a 40mm-height cuvette. Note that ~1300g, which triggers cavitation in the10mm-height cell culture setup, is about four times larger due to size dependent acceleration-induced pressure

(Equation 4-2). Note that the incorporation of a pressure measurement probe in the cell culture setup, while desirable, is still very challenging because insertion of such a sensor will likely contaminate cell culture.

Because of the importance of cell membrane integrity in cell injury mechanisms, membrane permeabilization associated with pressure gradients is considered. For example, it is well known that mechanical damage to cell membranes could result in irreversible cell death by necrosis [227] by glutamate release from the damaged cells or off balance of intracellular ion concentrations [228]. To monitor the plasma membrane integrity of individual cell populations in real time after the 40cm-drop, a propidium iodide (PI) assay is implemented. Cells stained with this dye indicate a compromised plasma membrane because PI is impermeable to healthy cells (see the method section for detailed procedure). Figure 4-13 (a) shows significantly damaged areas (see *Area B* and *C*) on a petri dish. Among the remaining cells, approximately 10% of fibroblasts in this region were stained by PI 3 hours after impact. Interestingly, 48 hours after impact, the cell population had doubled and no cells stained with PI were observed (Figure 4-13 (b)).
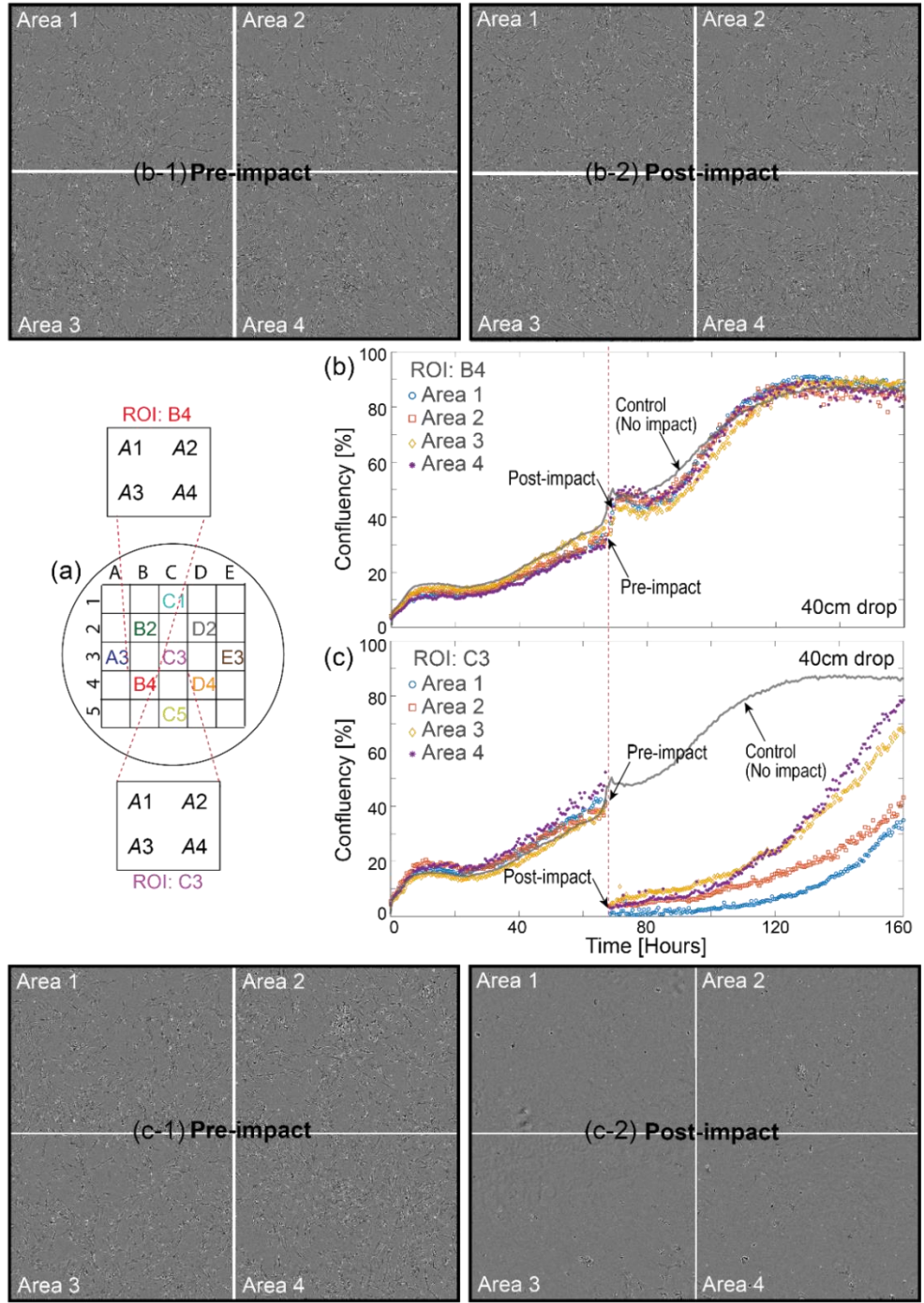
Figure 4-14. Identification of damaged areas due to applied impact. (a) Region of interests on a petri dish. Each ROI consists of four areas (*A*1, *A*2, *A*3, and *A*4). To determine damaged areas, the image analysis algorithm discussed in the method section is used to monitor confluency in each area. (b) and (c) show confluency curves in B4 and C3, respectively. Note that confluency curves in b and c have very different trend after impact. (b-1 and -2) and (c-1 and -2) show the live cell images just before and after impact in B4 and C3, respectively.
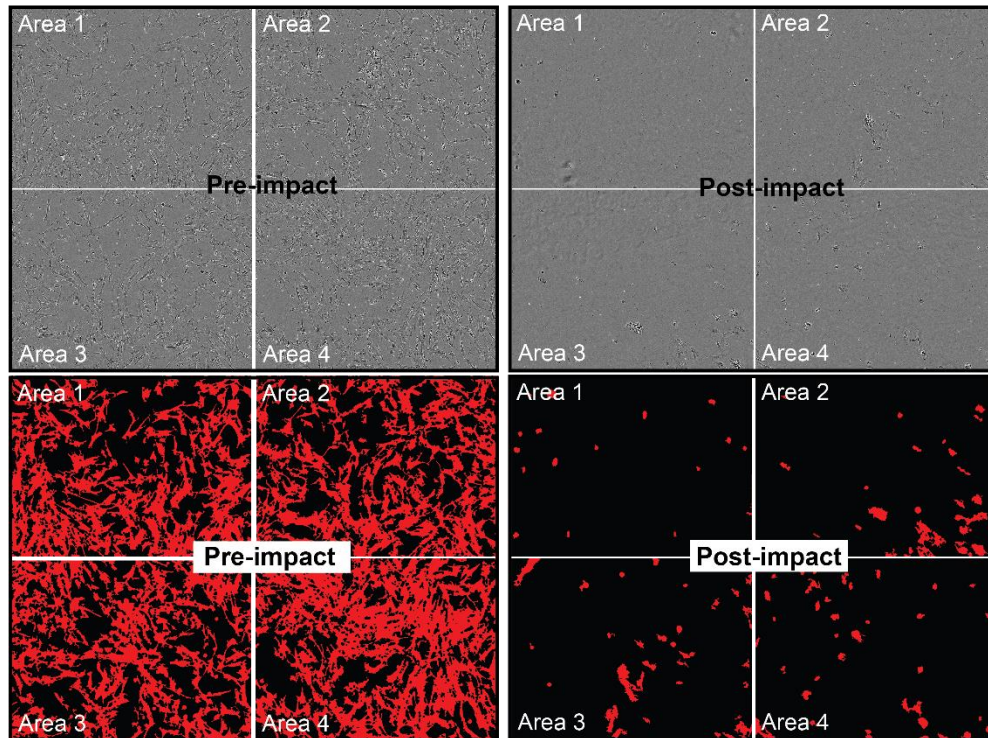
Figure 4-16. Upper panel: live cell images Figure 4-14 (c-1) and (c-2). Lower panel: the corresponding area of cells (red areas) recognized by software.
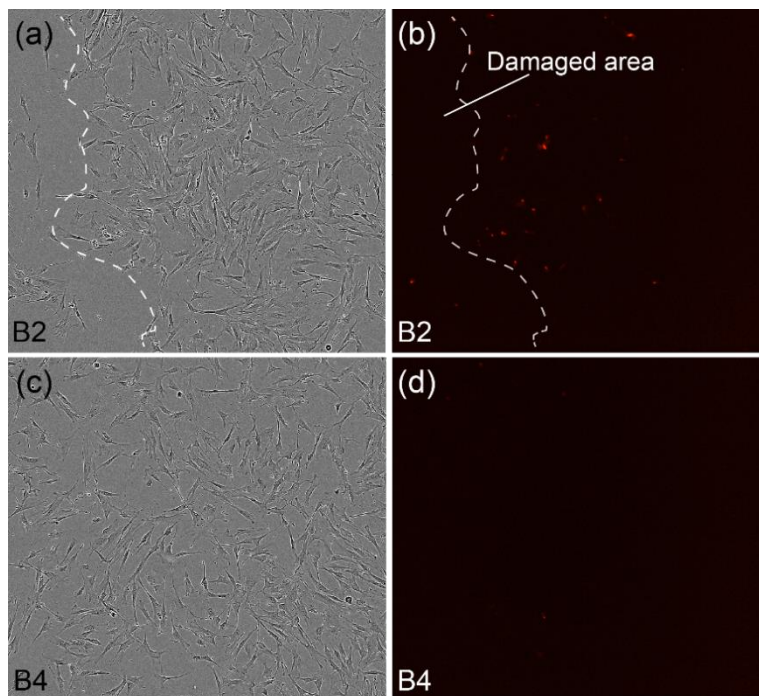
Figure 4-15. Phase and red fluorescence images after 40cm-drop impact: (a)-(b) near the damaged area (B2) by cavitation and (c)-(d) a few millimeters away from B2 (see Figure 4-5 and Figure 4-12).

129

To assess the fate of cells showing positive PI staining, the relative PI levels in individual cells are analyzed over time. Figure 4-13 (c) is the zoom-in view of *Area A* in (a) and shows time lapse imagery of a cluster of cells initially stained with PI (arrows). The morphology and positions of the cells changed over the course of 24 hours, indicating that the fibroblasts were motile after impact. One cell exhibited a significantly reduced fluorescence intensity after 3 hours, whereas the 2nd cell exhibited a more gradual reduction in fluorescence intensity over the course of 25 hours. At 24 hours, a new cell stained with a large fluorescence intensity entered the region, suggesting that the reduction in cell PI staining was not due to photobleaching. 48 hours after impact, no PI staining was observed in the cell population, indicating that fibroblasts plasma membrane was repaired over time. It is worth noting that cell PI staining was observed only near damaged areas, which indicates that the cavitation-induced membrane damage is localized (see Figure 4-16 and Figure 4-15).

So far, it has been concluded that acceleration alone does not damage fibroblasts even when the applied acceleration ($\sim 1000g$) is significantly greater than the conventional injury criterion, $150g$. In contrast, mechanical impact corresponding to the onset of cavitation bubbles results in sudden cell damage. Because the dynamics of cavitation bubbles is stochastic and localized, significant loss of cell population is limited to randomly distributed, localized spots on a 2D cell culture plate in the cell culture chamber. Among the remaining cells in the damaged spots, cell membrane damage has been detected utilizing fluorescent imaging techniques. While these results are consistent with membrane poration, more studies are needed for quantitative conclusions for acceleration-induced cell

membrane permeabilization as well as for fundamentally understanding cavitation's role in cell membrane damage.

4.2.5   The Main Injury Mechanism: Cavitation

Interestingly, acceleration-induced pressure did not result in cell detachment nor change in cell growth curves when $a_{in} < a_{cr}$ where a_{in} is the amplitude of input acceleration and a_{cr} is the critical acceleration for cavitation. In this case, the acceleration-induced pressure at the bottom of a petri dish (where cells are growing) during the impact event ($0 < t < 1$ ms) was expected to be tensile using Equation 4-2. In addition, the amplitude of tensile pressure would be less than the critical pressure for cavitation nucleation in pure liquid, 110 kPa [117, 121]. On the other hand, the cells that were directly under the influence of cavitation bubbles were significantly damaged.
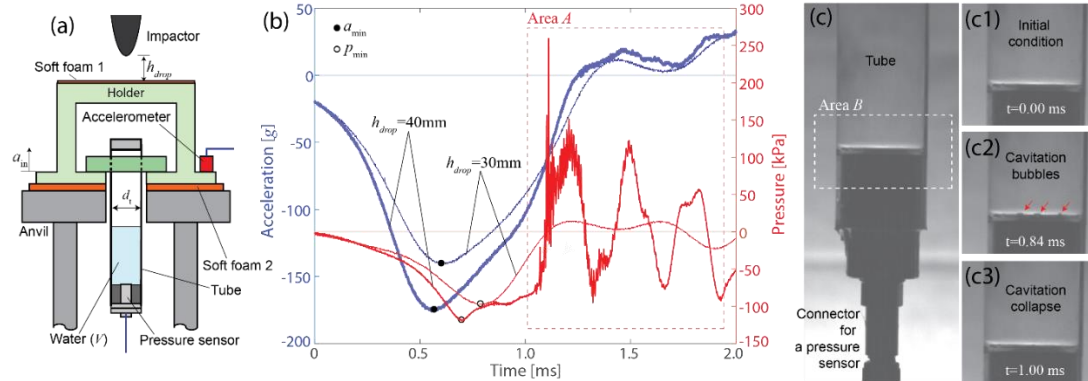
Figure 4-17. Direct comparison between acceleration (a_{in}) and acceleration-induced pressure (p_m) during impact. (a) Schematic of an experimental setup for concurrently monitoring acceleration and pressure. (b) Experimental data to compare acceleration (vertical axis on the left, blue) with the corresponding pressure (vertical axis on the right, red) in time for pure water (V=6ml) in a transparent plastic tube. (c) High speed camera images of the tube during 40mm-drop.

One possible explanation for this significant difference in cell response before/after impact is that the amplitude of cavitation-induced pressure may be much larger than acceleration-induced pressure. However, a recently study reported that pressure associated with bubble collapse of thermally induced cavitation is about 56 kPa [119], which is considerably smaller than the critical pressure, using a pressure sensitive film. Another possible mechanism is that cavitation-induced pressure, i.e., a rate of the pressure change in time, is much faster than acceleration-induced pressure and, as a result, viscoelastic response of cells, i.e., cell damage response, at different loading rates could be significantly different [229].

To quantitatively consider the two possible damage mechanisms above, transparent plastic tubes with an inserted pressure sensor are prepared for measuring time-varying pressure at the bottom of the tube. Figure 4-17 (a) and (c) show a schematic and an optical image of a transparent plastic tube filled with 6ml pure water where a pressure sensor is inserted at the bottom. This experiment setup allows concurrent measurements of acceleration and pressure at the liquid-plate interface, which mimics the cell culture media and plate interface at the bottom of the cell culture chamber.

The experimental setup was designed to achieve a higher probability of cavitation bubbles nucleation directly on a pressure sensor. First, while cavitation nucleation is stochastic in nature, bubbles would most likely form at the bottom of the tube where the amplitude of acceleration-induced pressure (see Equation 4-2) becomes maximum. Second, assuming a cavitation bubble occurs at the bottom plane, the expected distance between cavitation bubbles and a fixed-area pressure sensor effectively decreases by decreasing a cross sectional area of a tube. As an example, the probability of having a

cavitation bubble directly on a pressure sensor ($d\sim5.5$mm) could increase by more than 8 times by simply decreasing a cross section from d $\sim$35mm (petri dish) to $\sim$12mm (tube) due to an increase in the ratio of sensor to available surface areas where d is diameter.

Figure 4-17 (b) shows acceleration and acceleration-induced pressure for 30mm and 40mm drop experiments utilizing a plastic tube filled with 6ml pure water ($H\sim40$mm). For $h_{drop} = 30$mm, the smooth profile of the acceleration signal and measured pressure was very similar with a small shift in phase likely due to the viscosity of water. The measured amplitudes of acceleration and pressure were $a_{min} = -140.2g$ and $p_{min} = -96.9$kPa, respectively. In addition, shock waves, i.e., pulse-like signals (see the dotted lines in Figure 4-3 (b)), were not observed in the pressure measurement. Note that the critical tensile pressure for cavitation nucleation in water is about 110kPa.

For $h_{drop} = 40$mm, qualitative trends within $t < 1$ ms were very similar to $h_{drop} = 30$mm. As expected, the amplitudes of acceleration and pressure increased to $a_{min} = -174.7\,G$ and $p_{min} = -118.6\,$kPa, respectively, due to the increasing drop height. Although the qualitative acceleration profiles of both drops did not change much, the corresponding pressure measurement for $h_{drop} = 40$ mm became significantly different for $t > 1$ ms, i.e., rapid tensile/compressive pressure cycles superposed with much higher frequency acceleration signals.

To reveal a main mechanism that corresponds to the sudden changes in pressure, the image analysis of high-speed camera movies that were synchronized with acceleration and pressure measurements in time is performed. Figure 4-17 (c1-c3) shows the zoom-in view of *Area B* in (c), which is a likely cavitation nucleation site due to the maximum local

pressure, at different time points. The cavitation nucleation was first detected around $t = 0.64$ms. The bubbles grew in size until $t = 0.84$ms and then fully collapsed after $t = 1.00$ms, which correlates with the rapid tensile/compressive pressure cycles observed in Figure 4-17 (b). These images strongly indicate that the sudden changes in the pressure were mainly associated with dynamics of cavitation bubbles, in particular, cavitation collapse.

Two important conclusions from the experimental data in Figure 4-17 are 1) the amplitude of cavitation-induced pressure is considerably larger than acceleration-induced pressure and 2) a rate of pressure changes for cavitation-induced pressure is significantly faster than acceleration-induced pressure. Upon impact, the amplitude of acceleration-induced pressure gradually increases from 0 at $t = 0$ ms to 118.6kPa at $t = 0.70$ms. On the other hands, cavitation-induced pressure increases from -72.9 to 259.2kPa within 0.05ms where the maximum pressure occurs at $t = 1.11$ ms. Note that the corresponding rates of pressure change for acceleration- and cavitation-induced pressure are 169 kPa/ms and 6642 kPa/ms, respectively. It is worth mentioning that the pressure measurement is an average over the entire sensor and, therefore, the localized pressure must be even higher near the cavitation event.

It is worth discussing that the acceleration-induced pressure ($t < 1$ ms) for both $h_{drop} = 30$ and $= 40$mm strongly suggests that the 1mm-thick foam at the top of the sample holder effectively eliminates possible propagation of shock waves to the liquid and pressure in the liquid is indeed acceleration-induced. One possible implication of these

results is that the effect of shock waves on mild blunt injury is dampened because the human body is protected by soft skin, which would behave as the thin foam layer.

4.3   Conclusion and Discussion

Mechanical impact and the resulting acceleration-induced pressure gradient on the human body is one of the main mechanisms for traumatic injury. Fundamental understanding of injury mechanisms associated with mechanical impact is essential toward the development of reliable injury criteria and more accurate prediction of injury. In addition, such knowledge could pave the way for innovative protective equipment designs and effective strategies for post-injury treatment.

Here, a novel platform capable of applying well-characterized and reproducible acceleration-induced pressure gradients that is compatible with long-term and environmentally controlled live-cell microscopy has been introduced. This in vitro platform allows close monitoring of multiple cell populations, down to individual cells, to deduce how impact effects cell viability and mitosis, as well as assays for investigating the molecular mechanisms of cell injury, such as membrane permeabilization due to pressure gradients.

The drop tower studies using the cell culture setup in vitro reveal that even a seemingly very large acceleration ($\sim 1000g$) does not result in apparent cell damage due to the small size (e.g., height) of the cell culture setup (~ 10 mm). This result indeed emphasizes the importance of appropriately considering the effect of biological system size, in addition to acceleration, for accurate assessment of blunt injury. As an example, human head size

could be an important factor to predict blunt head injury among different sample populations, e.g., female vs male or child vs adult, for a given acceleration.

In addition, it has been shown that sudden cell death is triggered by the onset of cavitation bubbles, which apply localized compressive/tensile pressure cycles to cells, in the culture chamber. It has been found the cavitation-induced pressure is much more violent than acceleration-induced pressure due to a very rapid rate of pressure changes in time and large pressure amplitudes relative to when no cavitation is present.

This platform offers a novel window into fundamental mechanisms of cell injury due to impact. The integration with standard cell culture platforms allows future work to address fundamental questions such as: how does impact affect cell adhesion, motility, and mitosis? Indeed, novel migration or adhesion assays conducted on standard cell culture dishes could be incorporated into the in vitro impact tower set up described here. Furthermore, this platform could be expanded to a plethora of cell lines, such as neurons, or in vitro conditions, such as serum free media or altered substrate stiffness.

The focus of the current work is placed on assessing cellular damage at the population level associated with rapid mechanical acceleration and the subsequent onset of cavitation bubbles. Because the current experimental setup does not allow real-time measurements of deformation of individual cells during impact, fundamental mechanistic information on critical parameters required to assess damage at the single cell level is lacking. To elucidate critical parameters for single cell damage, future efforts will integrate the current system with high resolution imaging techniques to quantitatively correlate the critical impact amplitudes, pressures, and cell deformation with a specified damage to individual cells.

5.   Hs27 FIBROBLAST RESPONSE TO CONTACT GUIDANCE CUES

5.1   Materials and Methods

5.1.1   Fabrication of Platforms
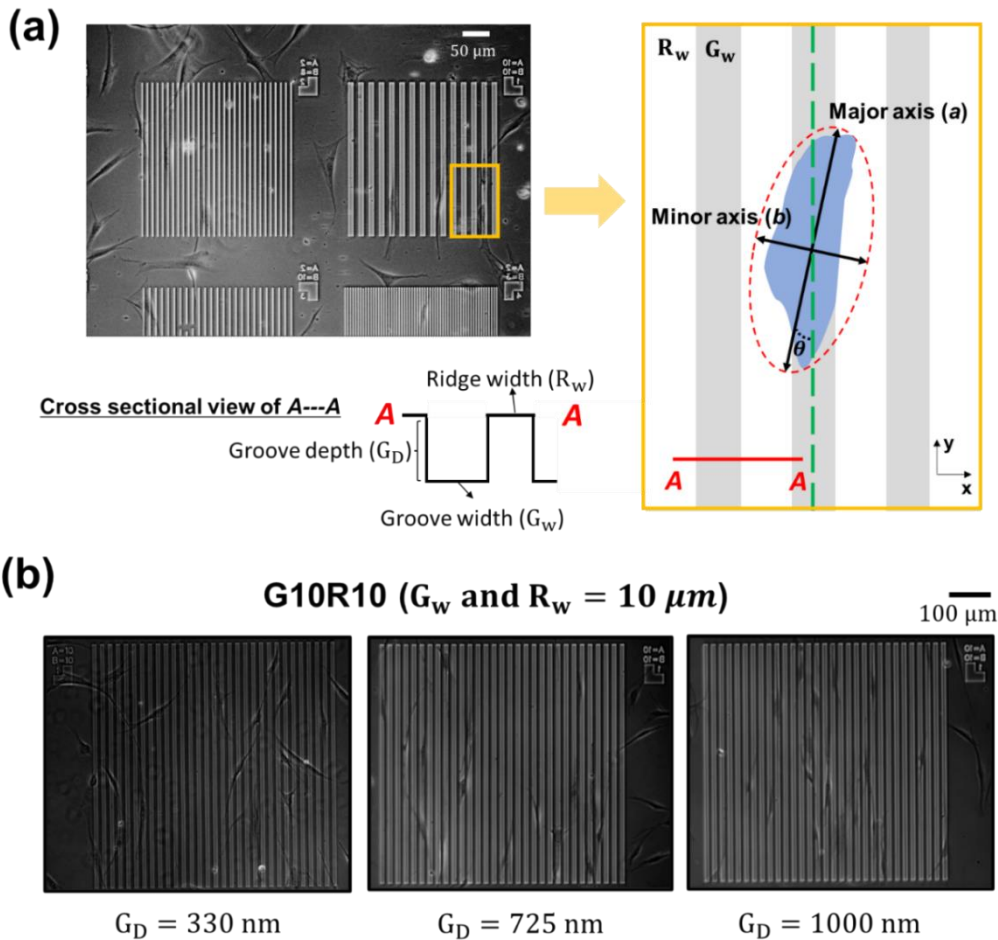
Figure 5-1. (a) A monolithic quartz contact guidance platform (left) and a schematic diagram of how cell topography is characterized on the micropatterned substrate (right). A---A is a cross sectional view of the platform showing groove (Gw) and ridge (Rw) widths, and groove depth (GD). The outline of a cell is fitted by an ellipse to estimate a length ratio of the major to minor axes and a cell alignment angle (θ) between the major axis and the direction of the groove patterns. (b) Optical images of live Hs27 cells on $G_w = R_w = 10\,\mu m$ (i.e., G10R10) with (left) G_D =330 nm, (middle) =725 nm, and (right) =1000 nm, respectively.

137

To examine the effects of substrate anisotropy on cellular alignment, multiplexed patterns are created with an emphasis on achieving uniform smoothness on the entire substrate including the patterns. The surface topographical cues consist of ridge and groove widths, and groove depths using deep etching process and seeded Hs27 fibroblasts on the etched substrates as shown in Figure 5-1 (a). To be specific, a 20 nm Cr thin film was e-beam evaporated onto 25 mm diameter fused silica coverslips and subsequently coated with AZ1518 photoresist (Microchemicals GmbH) and baked on a vacuum hot plate at 100°C for 90 seconds. The photoresist was patterned in a Heidelberg VPG200++ laser pattern generator at a dose of 60 μC/cm^2 and developed with the use of using AZ developer (Microchemicals GmbH) and rinsed in DI water. The patterned Cr film acted as hard mask, allowing only the exposed fused silica area to be etched (Oxford PlasmaLab 100 ICP380 system) by CHF$_3$ and Ar, with flow rates of 10 and 15 sccm, respectively, at 3 mTorr and 20°C to achieve various topographical conditions (more details are given in [163]). To systematically control topographical cues, ridge and groove widths (R_w and G_w, respectively) ranging from 2 to 10 μm with different R_w-to-G_w ratios were cofabricated on each multiplexed contact guidance chip. Three different groove depths (i.e., G_D = 330, 725, and 1000 nm) were used to quantify the effect of groove depth on cell response. The detailed dimensions of the contact guidance chips are presented in Table 5-1. The lower limit of $R_w = 2$ μm was motivated by the size of typical mature FAs [230, 231], whereas the upper limit of ridge or groove width is 10 μm, which is large enough not to confine focal adhesions and is also about the diameter of the nucleus [232].

Groove depth (nm)	Ridge, R (μm)	Groove, G (μm)
	2	2
	2	3
	2	4
	2	6
	2	8
	2	10
330	3	2
	3	3
725	4	2
	4	4
1000	5	5
	6	2
	6	6
	8	2
	8	8
	10	10

Table 5-1. Dimensions of nano- and micro features on the substrate surfaces.

5.1.2 Cell Culture

For cell culture, Hs27 cells (ATCC, CRL-1634, Lot #7006836) were cultured in DMEM (ATCC, 30-2002) with 10% FBS (ATCC, 30-2020, Lot #802500) at 37°C and 5% CO_2 as per manufacturer instructions, without antibiotics. The contact guidance chips and surrounding chambers were assembled under aseptic conditions. Ethanol was introduced to the chambers for 5min and then N_2 dried for additional sterilization of the contact guidance chips. FN at 25µg/mL in 10mM PBS was drop coated directly onto the chips and allowed to adsorb for 1 hour at room temperature, and subsequently rinsed 5x with DMEM to remove any excess FN. The contact guidance chambers were then allowed to equilibrate

Zeiss microscopes featuring environmental chambers at 37°C, 5% CO_2 and 95% humidity for at least 30 minutes before the introduction of cells. Hs27 cells were harvested for contact guidance experiments between 30-60% confluence in their logarithmic growth phase. Complete media was aspirated and replaced with 0.25% Trypsin-EDTA (Gibco, #25200-056) for 5 min at 37°C, after which serum free media was introduced.

5.1.3 Data Analysis

$$G10R10 \; (G_w = R_w = 10\mu m, and \; G_D = 330 \; nm)$$

100 μm

Original image   Processed image
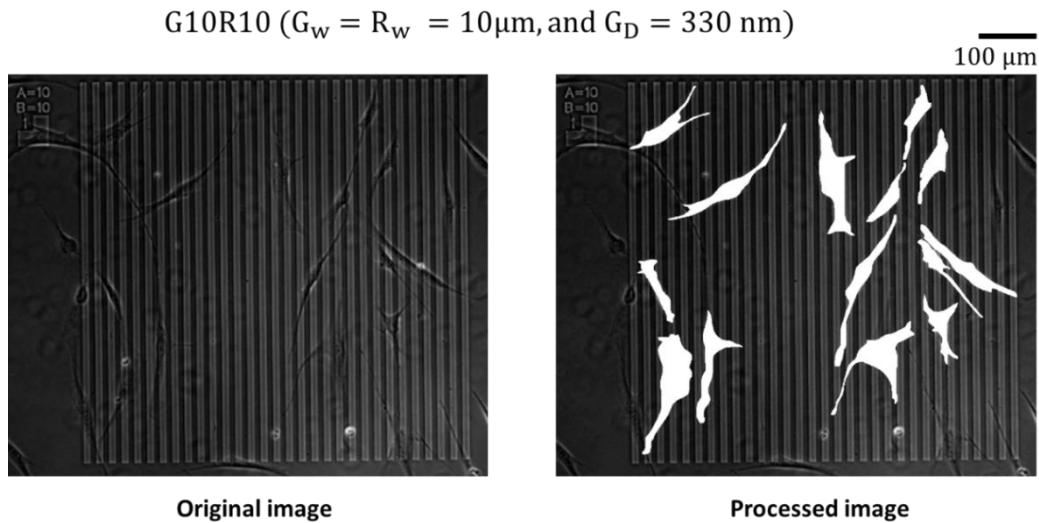
Figure 5-2. An original optical image of live Hs27 cells on $G_w \; (width \; of \; groove) = R_w(width \; of \; ridge) = 10\mu m \; with \; G_D \; (groove \; depth) = 330 \; nm$ (left). The processed image of the left original image with the outline of each cell (right).

The morphology of Hs27 fibroblasts cultured on the monolithic quartz platform was evaluated by analyzing the shapes of all cells adhering to patterned geographies. Image analysis was conducted under 10x phase microscopy and those images were acquired every 10 min and converted into TIFF files using Zen software. For example, the optical images, taken 24 hours after initial cell seeding using a 10x phase objective, in Figure 5-1 (b) shows Hs27 cells on G10R10 ($G_w = R_w = 10$ μm) with $G_D = 300$, 725, and 1000 nm from left

140

to right, respectively. The images show that the cells exhibit clearly different cell shapes depending on G_D. By using ImageJ (version 1.41, NIH), the outline of each cell on the substrates was manually drawn) and then, quantitatively measured the area of individual cells (see Figure 5-2). The cell outline was then fitted using an ellipse to estimate the cell aspect ratio (α) using a length ratio of the major to minor axes and then obtain the cell alignment angle (θ) between the major axis and the direction of groove patterns (see Figure 5-1 (a)).

The cell's time-dependent coordinates were measured by tracking its nucleus and this data has been used to compute several dynamic measurements (directional orientation, angular displacement, speed, mean square of distance, directionality ratio, and velocity autocorrelation). For all image analyses, more than 20 cells for each of the topographical dimensions are characterized including control experiments on a flat substrate. For precise analysis of cellular static behaviors, the following two cases are ruled out: (1) cells underwent mitosis and (2) cells spread over both flat and patterned areas of a substrate. Statistical analysis was performed by one-way analysis of variance (ANOVA) and Tukey's post hoc test using MATLAB and SPSS software for the estimation of significance level. All data figures were prepared by MATLAB where the central mark indicates the median, and the bottom and top edges of the box point to the 25% and 75%, respectively. The outliers are plotted individually if they are more than $q_3 + 1.5 \cdot (q_3 - q_1)$ or less than $q_1 - 1.5 \cdot (q_3 - q_1)$, indicated by the '+' symbol in which q_1 and q_3 are the 25th and 75th percentiles of the data set, respectively.

5.2   Results

Cell morphology and migration of Hs27 fibroblast on the monolithic quartz contact guidance platform are experimentally characterized. The goal is to systematically quantify the effect of lateral (ridge width (R_w), groove width (G_w)), and vertical (groove depth (G_D)) dimensions on static and dynamic behavior of fibroblast cells. For the lateral dimensions, three different cases are considered, namely, G2NR, GNR2, and GNRN. First, G2RN indicates fixed groove width (i.e., $G_w = 2$ µm) with different combinations of ridge width (i.e., $R_w = 2, 3, 4, 6, 8,$ and 10 µm). Similarly, GNR2 corresponds to $R_w = 2$ µm with different G_w values (i.e., $G_w = 2, 3, 4, 6,$ and 8 µm). G2RN and GNR2 are designed for independent characterization of the R_w- and G_w-dependent cell responses, respectively. Finally, GNRN represents topographical cues with $R_w / G_w = 1$ where $R_w = 2, 3, 4, 6, 8,$ and 10 µm for exploring the G_w-R_w coupling effect. To reveal the effect of groove depth (G_D), live cell experiments on G2NR, GNR2, and GNRN are performed and analyzed with three different groove depths (i.e., $G_D = 300, 725,$ and 1000 nm).

5.2.1   Cell Morphology

In this section, three key cell morphological parameters (spread area (A_{cell}), aspect ratio (α), and alignment angle (θ)) of fibroblast cells are quantified by performing image analyses of live cells on a contact guidance (see Figure 5-1 (a)). Quantitative characterization of cell morphologies associated with a wide range of microfabricated surface patterns is relevant to understanding and guiding cell behavior for several biological applications. For example, cell spread areas have been studied in the context of cell differentiation and proliferation [233], migration [234, 235], and transfection [236].

Note that the cell spread area becomes important for fibroblasts as it regulates cell migration in wound healing process [237]. It is also known that cell shape, often quantified by a cellular aspect ratio, is related to regulation of division-coupled interspersion for cells [238, 239]. Lastly, aligned organization of cells, also known as a cell polarity, contributes to tissue maturation [240], regeneration growth [241], differentiation [242], and proliferation [243] and, as a result, a capability to control cell alignment is crucial for engineering functional tissue equivalents.

The image analysis on the cell spread area indicates that cells on the patterned substrate tend to have smaller spread areas compared those on the flat control substrate (see Figure 5-3). As a reminder, image analysis techniques are discussed in Section 2. The spread area (A_{Cell}) on the control substrate ($=2816.8\ \mu m^2$) is considerably larger than that on the
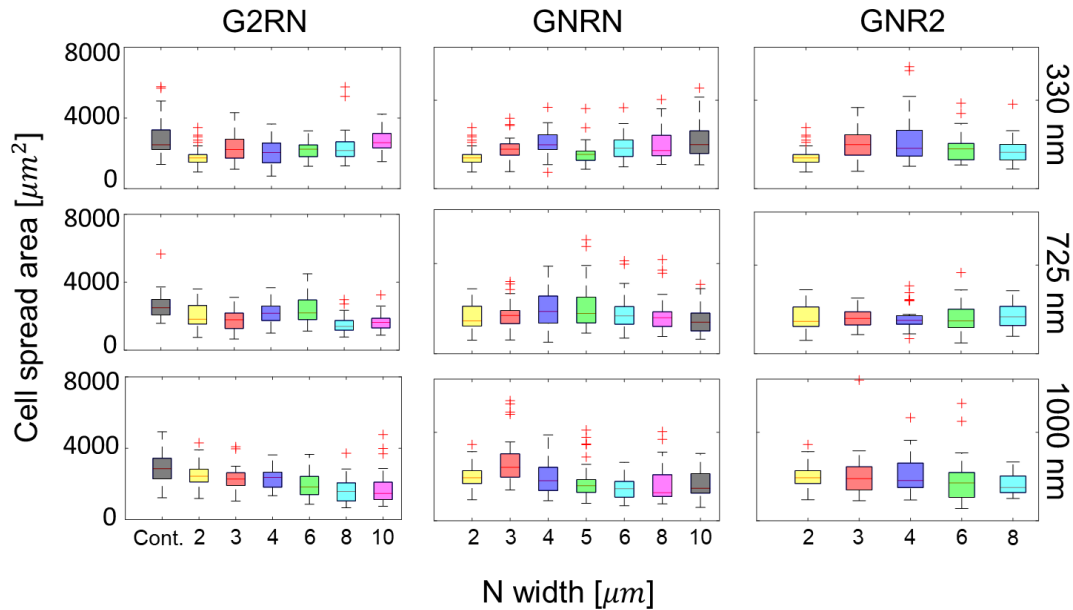
Figure 5-3. Box-and-whisker diagrams of cell spread area with respect to individual topographic conditions. Each column represents three different cases: (from left to right) G2RN ($G_w = 2\ \mu m$ and $R_w = N\ \mu m$), GNRN ($G_w = R_w = N$), and GNR2 ($G_w = N\ \mu m$ and $R_w = 2\ \mu m$). Each row indicates different groove depths: (from top to bottom) $G_D = 330$, 725, and 1000 nm. Cont. indicates a control experiment on a flat control substrate.

topographical cues, but the variation in A_{Cell} among different topographical cues is statistically insignificant ($A_{Cell} = 2365.3, 2115.3$ and $2259.4 \, \mu m^2$ on $G_D = 330, 725$, and 1000 nm, respectively). Consistent with the results, a similar trend was observed for NH3T3 fibroblast cells cultured on micropatterned polydimethylsiloxane (PDMS) substrate [238].
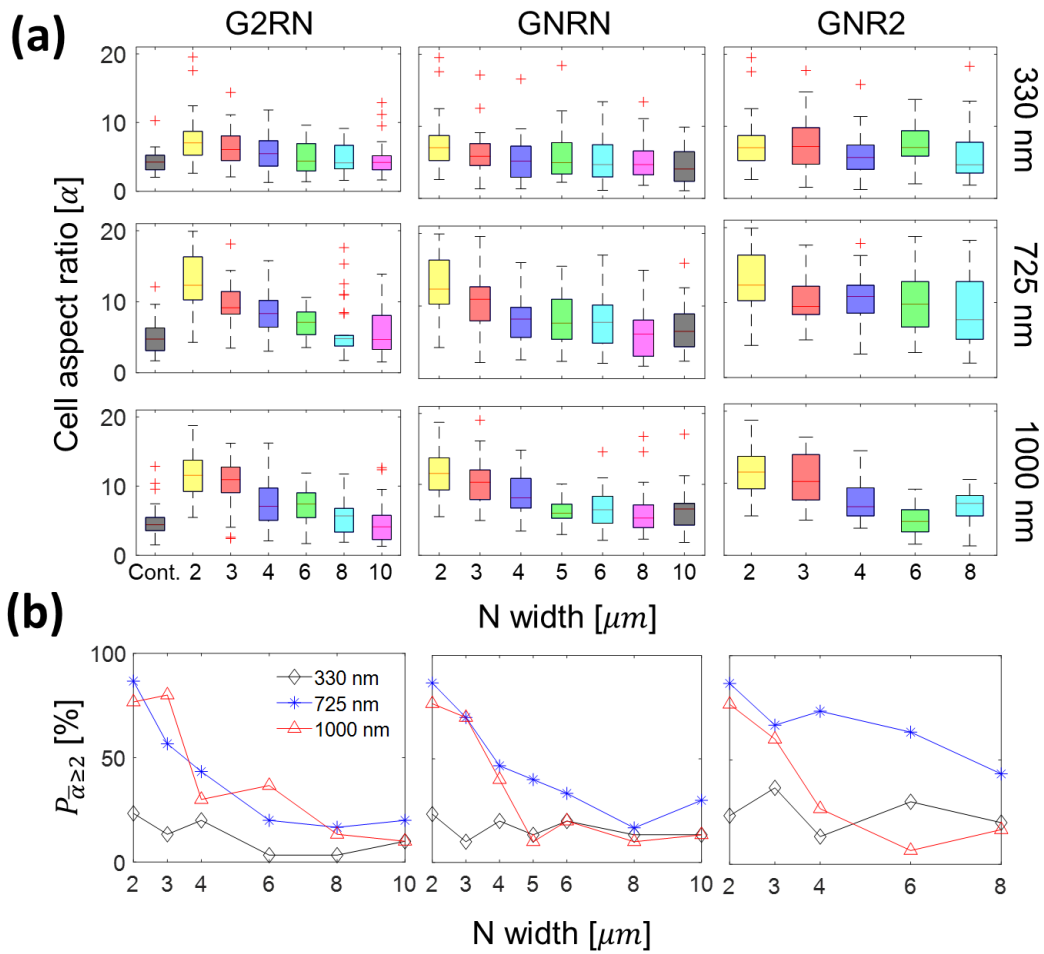
Figure 5-4. (a) A cell aspect ratio (α) for different topographic conditions. Each column represents three different cases: (from left to right) G2RN ($G_w = 2\ \mu m$ and $R_w = N\ \mu m$), GNRN ($G_w = R_w = N\ \mu m$), and GNR2 ($G_w = N\ \mu m$ and $R_w = 2\ \mu m$). Each row indicates different groove depths: (from top to bottom) $G_D =330, 725$, and 1000 nm. Cont. indicates a control experiment on a flat control substrate. (b) $P_{\bar{\alpha} \geq 2}$ is the percentage population of elongated cells ($\bar{\alpha} \geq 2$) for (left to right) G2RN, GNRN, and GNR2, respectively.

Figure 5-4 shows the elongation of cells. More specifically, Figure 5-4 (a) summarizes

the cellular aspect ratio (α) as a function of N (the size of lateral widths) for three different

cases: G2RN ($G_w = 2$ μm and $R_w = N$ μm), GNRN ($G_w = R_w = N$ μm), and GNR2

($G_w = N$ μm and $R_w = 2$ μm). In addition, different groove depths ($G_D=330, 725$, and

1000 nm) are considered. Note that *Cont.* indicates control experiments on flat control

substrates. For clarification, the results of cell alignment and cell speed will be presented in the same way in the later sections to be consistent.
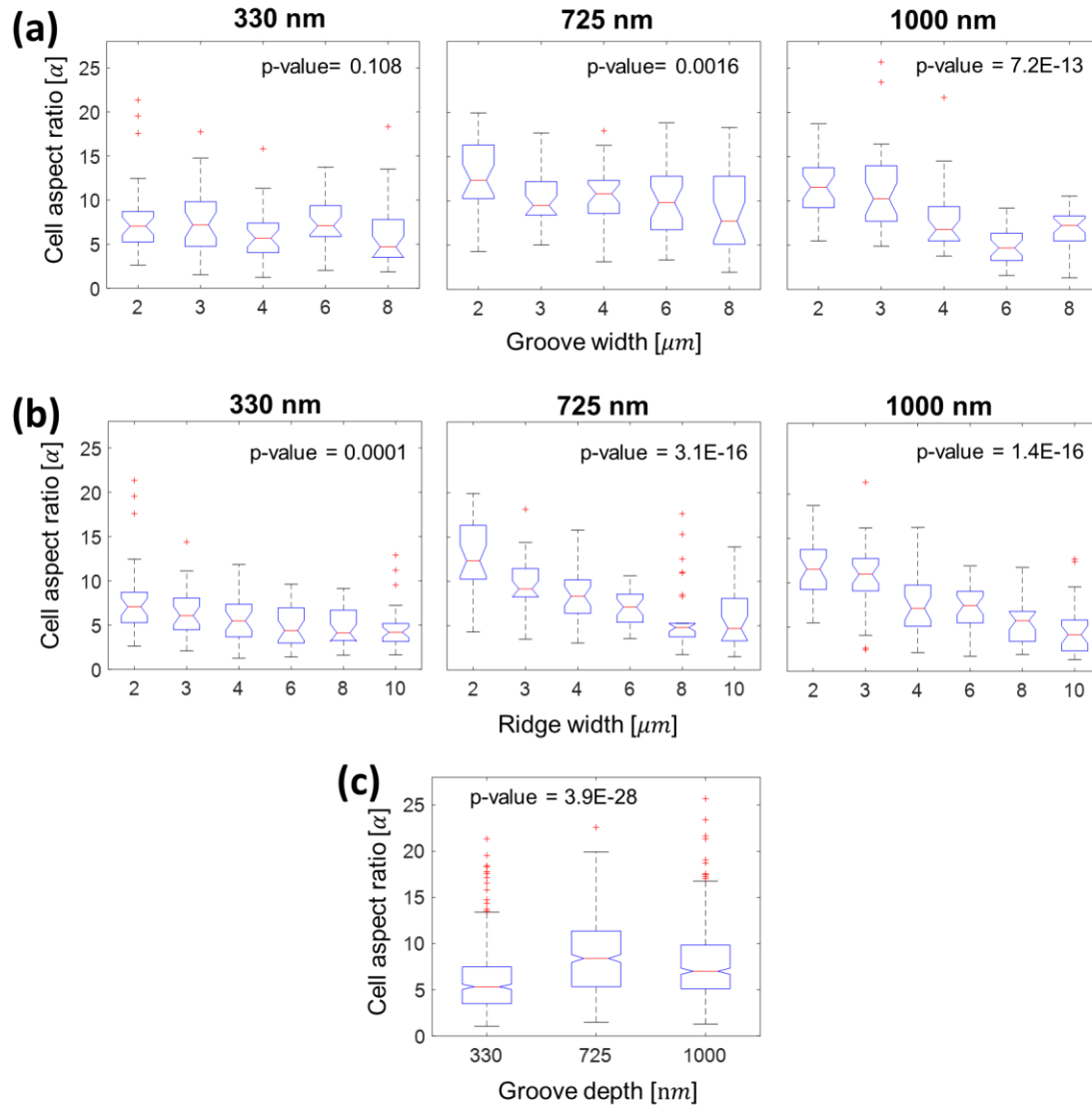
Figure 5-5. Box-and-whisker plot of the cell aspect ratio as a function of groove widths (a), ridge widths (b), and groove depths (c) with the corresponding p-value from one-way ANOVA test.

Consider the cellular aspect ratios from G2RN (see the first column in Figure 5-4 (a)). Two general trends are (1) α decreases with increasing R_w and (2) α increases with increasing G_D. For instance, α values of $G_D = 725$ nm decrease from $\alpha = 13.06$ (G2R2)

146

to $\alpha = 5.81$ (G2R10). Also, the distribution of the α values is sensitive to G_D, e.g., a rate of decreasing α with increasing R_w is much faster for $G_D = 725$ and 1000 nm compared to $G_D = 330$ nm. The strong G_D dependency in G2RN can be again validated by comparing the average aspect ratio (α_{ave}) for each G_D. For example, $\alpha_{ave} = 8.66$ and 7.64 for $G_D = 725$ and 1000 nm, respectively, are considerably larger than $\alpha_{ave} = 5.92$ for $G_D = 330$ nm and $\alpha_{ave} = 4.81$ for the flat substrate (control). One-way ANOVA (see Figure 5-5) confirms that the effect of G_D on α is statistically significant ($p \ll 0.001$). The results of GNRN (second column) and GNR2 (third column) show somewhat similar qualitative trends of G2RN. However, the statistical test shown in Figure
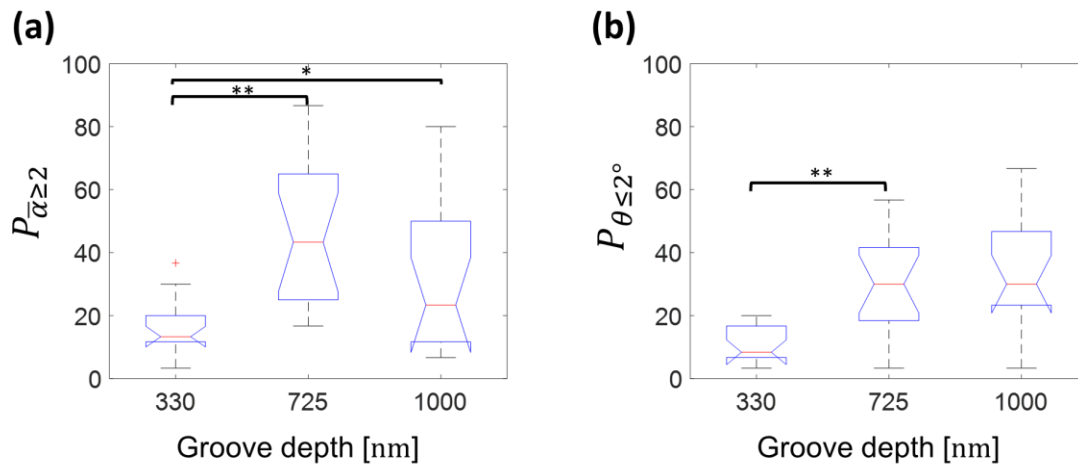
Figure 5-6. Box-and-whisker plot of the percentage population of the elongated, $\alpha \geq 2$, (a) and aligned, $\theta \geq 2°$, cells (b) as a function of groove depths (330, 725, and 1000 nm). *P < 0.05 and **P < 0.001 via one-way ANONA test.

S3 reveals that the p-values for varying R_w are much smaller than those for G_w regardless of G_D and, therefore, it is concluded that R_w has stronger effect on the cell aspect ratio compared to G_w.

It is important to acknowledge that α values depend on cell type as well as cell culture conditions. For example, different α values have been reported for cells on flat control

147

substrates, e.g., $\alpha = 2\sim 2.3$ for NIH 3T3 fibroblasts and myofibroblasts [238, 244]. To account for a natural tendency of such cell-type and cell-culture dependent behavior, here all the aspect ratios are normalized by the aspect ratio of cells on the control substrate (i.e., $\bar{\alpha} = \alpha/\alpha_{Cont}$). Following the previous studies [238, 244, 245], the percentage population ($P_{\bar{\alpha}\geq 2}$) of elongated cells are quantified by using $\bar{\alpha} \geq 2$.

Equation 5-1

$$P_{\bar{\alpha}\geq 2_i} = a + b \cdot G_{w_i} + c \cdot R_{w_i} + d \cdot G_{D_i} + e \cdot G_{w_i} \cdot R_{w_i} + f \cdot G_{w_i} \cdot G_{D_i} + g \cdot R_{w_i} \cdot G_{D_i} + h \cdot G_{w_i} \cdot R_{w_i} \cdot G_{D_i}$$
$$\begin{cases} i = 1,2,3, \dots, 32 \text{ for Case 1} \\ i = 1,2,3, \dots, 48 \text{ for Case 2} \end{cases}$$

Figure 5-4 (b) shows $P_{\bar{\alpha}\geq 2}$ values as a function of dimensional parameter N for cells on (left to right) G2RN, GNRN, and GNR2. In each plot, black diamonds, blue asterisks, and red triangles indicate G_D=300, 725, and 1000 nm, respectively. First, $P_{\bar{\alpha}\geq 2}$ for $G_D = 330$ nm is much less sensitive to N compared to the deeper groove depths. As an example, due to the change in N from 2 to 8 μm, $P_{\bar{\alpha}\geq 2}$ of G2RN decreases from 86.7% to 16.7% on $G_D = 725$ nm and from 76.7% to 13.3% on $G_D = 1000$ nm, respectively. The similar trend can be seen in GNR2 as the corresponding $P_{\bar{\alpha}\geq 2}$ values are 86.7% ($G_D = 725$ nm)

Data sets			Coefficient								R^2
		a	b	c	d	e	f	g	h		
Case 1	Control, 330 and 725 nm		-2.76	-2.07	122	0.541	-1.90	-9.78	0.127		0.835
		4.44				p-value					
			0.214	0.244	2.52E-9	0.138	0.682	0.0124	0.859		
		a	b	c	d	e	f	g	h		
Case 2	Control, 330, 725, and 1000 nm		4.69	-1.34	115	-0.198	-17.4	-10.5	1.63		0.612
		4.44				p-value					
			0.0739	0.517	3.82E-11	0.636	1.68E-4	2.95E-3	0.0150		

Table 5-2. Regression results of normalized elongated cell population ($P_{\bar{\alpha}\geq 2}$) with respect to G_w, R_w, G_D, and their cross terms. Frist and second represent estimated coefficients and their p-value with R^2 value for case 1 (Control, 330, and 725 nm) and case 2 (Control, 330, 725, and 1000 nm), respectively.

and 76.7% (G_D = 1000 nm) at N = 2 μm and 43.3% and 16.7% at N = 8 μm, respectivtly. Clearly, $P_{\bar{\alpha}\geq2}$ for G_D = 725 and 1000 nm decreases with an increase of N at a much faster rate compared to G_D = 300 nm, which indicates a strong depth dependent cell behavior. To further consider the correlation between cell elongation and groove depth for all lateral dimensions (R_w and G_w), the average $P_{\bar{\alpha}\geq2}$ values for each depth, including all G2RN, GNRN, and GNR2 cases, are shown in see Figure 5-6 (a). The average $P_{\bar{\alpha}\geq2}$ values are 4.44%, 16.5%, 31.9%, and 25.0% on G_D = 0 (control), 330, 725, and 1000 nm, respectively.

The effect of individual topographical features (R_w, G_w and G_D) and their products on $P_{\bar{\alpha}\geq2}$ are quantitively characterized by conducting multiple linear regression analyses. Because $P_{\bar{\alpha}\geq2}$ strongly depends on G_D and changes its trend between G_D=725 nm and =1000 nm, the linear regression analyses are performed twice using G_D = 0~725 nm (Case 1) and G_D = 0~1000 nm (Case 2), respectively, as summarized in Table 5-2. For clarity, G_D, G_w, and R_w = 0 for the flat substrates (control) are used as no topographical effect is expected on cell responses and, as a result, a constant term in the multiple linear
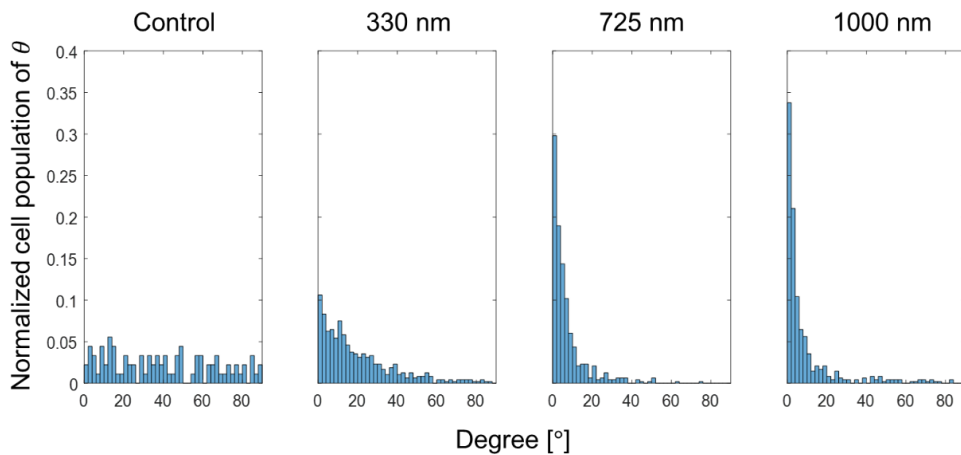
Figure 5-7. Normalized cell population as a function of cell alignment degree with respect to surface patterns: (from left to right) control, 330, 725, and 1000 nm. The bin size is 2°.

regression model (see Equation 5-1) becomes the $P_{\bar{\alpha}\geq2}$ value for the control substrates. A few key conclusions are (1) R^2 values for Case 1 and 2 are considerably different (i.e., 0.835 for Case 1 and 0.612 for Case 2, respectively) and (2) despite the different R^2 values, the coefficient associated with G_D, for both cases, is 1~2 orders of magnitude larger than other coefficients with statistical significance ($p < 10^{-8}$). The smaller R^2 value for Case 2 may confirm a change in the $P_{\bar{\alpha}\geq2}$ trend for $G_D > 725$ nm.

Finally, Figure 5-7 shows the normalized cell population as a function of the cell alignment angle (θ) on the control and patterned substrates with three different groove depths (G_D). Despite significantly different population distributions shown in the figure, the average values of the cell alignment angle (θ_{ave}) for $G_D = 0$ (control), 330, 725, and 1000 nm are 39.68 °, 19.70 °, 7.23 °, and 9.27 °, respectively. For clarification, each average value for each G_D includes G2RN, GNRN, and GNR2 and, therefore, the effect of G_D is considered for all R_w and G_w. Note θ_{ave} for the patterned substrates are significantly smaller than that of the control substrate and their distributions are also statistically different with p-value $\ll$ 0.001 as shown in see Figure S5. The cells on the control substrates exhibit a uniform distribution of alignment angle distribution unlike the patterned substrates. This expected trend can be also seen in the linear increasing cumulative distribution function (CDF) plots shown in Figure 5-8.
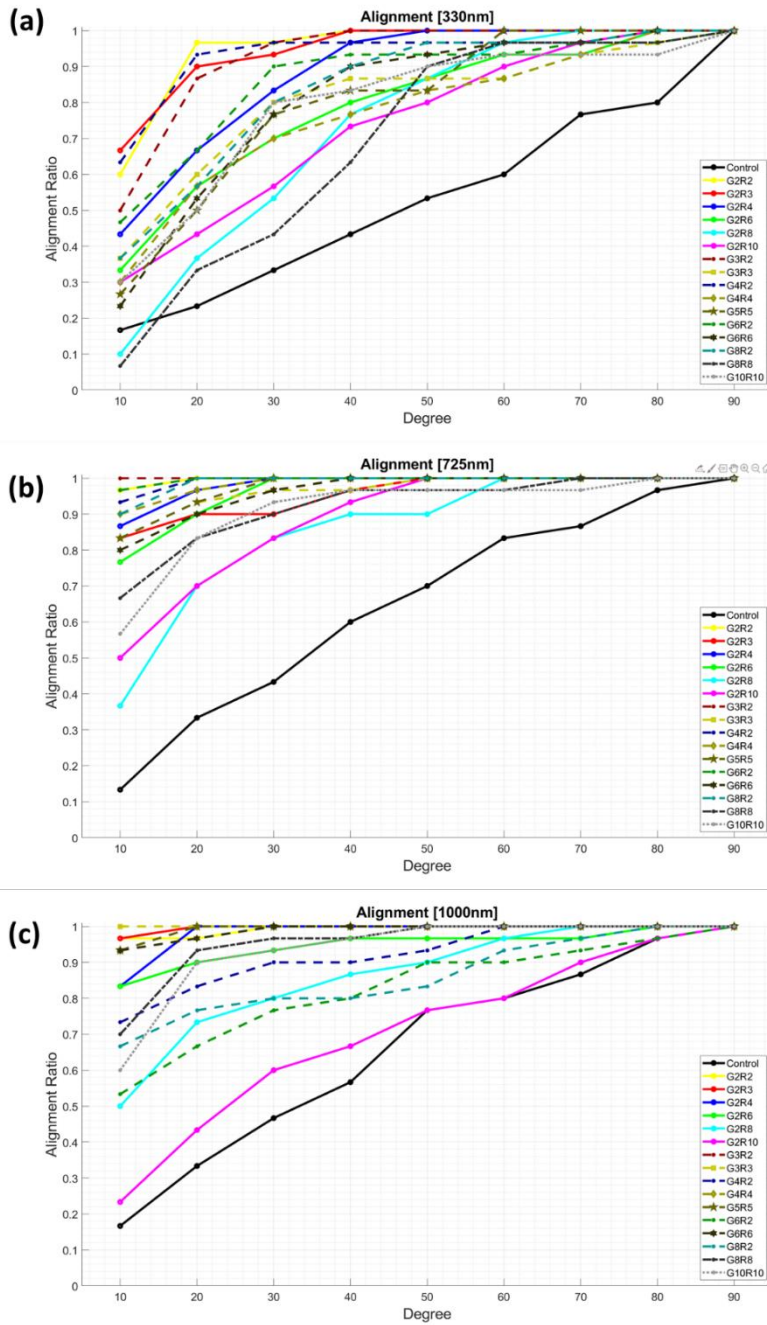
Figure 5-8. Graphs of the radial distribution of the major axes of Hs27 cells on various topographies. Distribution of ratio of aligned cells within a specific degree. Results for each substrate are labelled with different colors and line types ((a): 330 nm depth, (b): 725 nm depth, and (c): 1000 nm depth).

151

For more detailed analyses, Figure 5-9 (a) shows the cellular alignment angle (θ) for G2RN, GNRN, and GNR2. Note that θ increases with either the increase of G_w and R_w or the decrease of G_D. For $G_D = 725$ nm (the second row), the θ values for G2RN, GNRN, and GNR2, increase from $2.87°$ (N = 2 μm) to $17.15°$, $11.74°$, and $4.69°$ (N = 8 μm), respectively. The statistical analysis in Figure S5 indicates that the effect of G_D is more significant than R_w and G_w. Also, it appears that the relative influence of
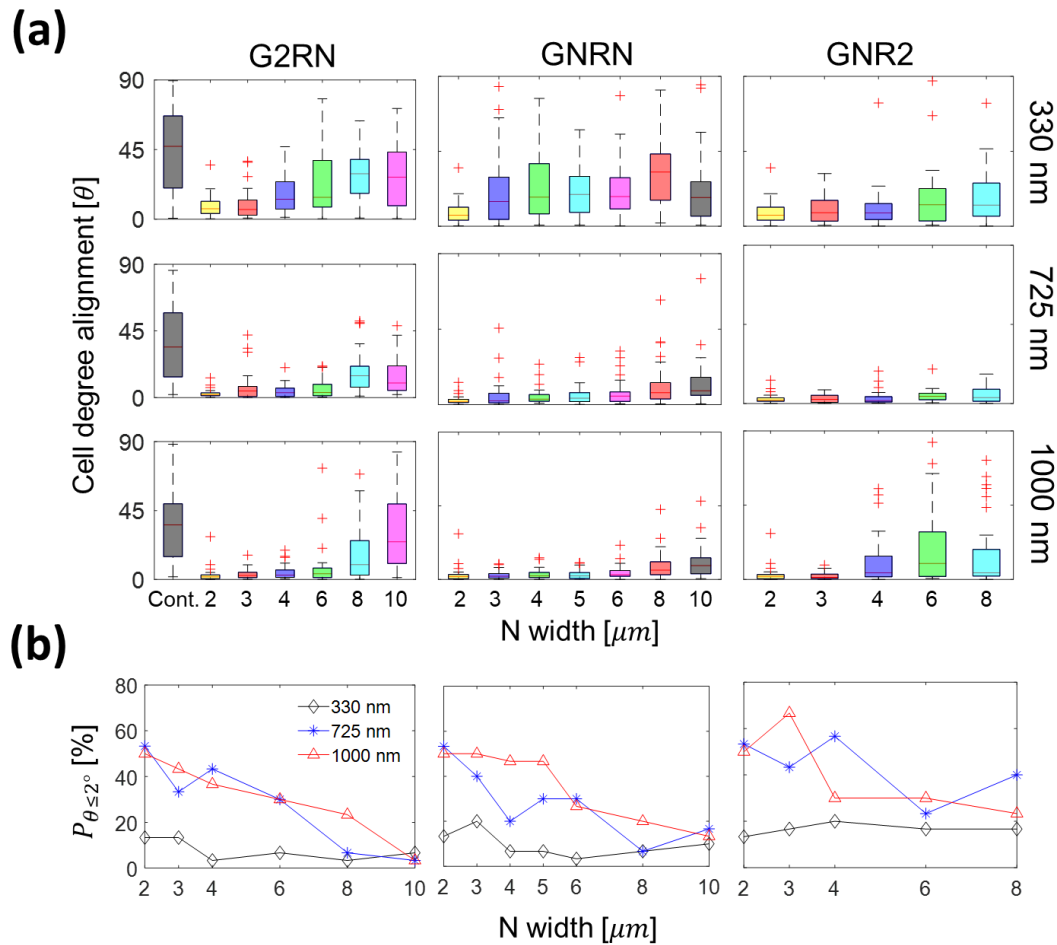
Figure 5-9. (a) Box-and-whisker diagrams of cell alignment angle ($θ$) with respect to groove patterns. (b) The percentage cell population ($P_{θ≤2°}$) within $θ ≤ 2°$ under different lateral conditions (G_w and R_w).

G_w on θ, compared to the other dimensional cues, is the weakest by the comparison of the corresponding p-values.

Figure 5-9 (b) shows the percentage population of aligned cells ($P_{\theta \leq 2\circ}$) for different G_w, R_w, and G_D values. It is worth noting that a new criterion ($\theta \leq 2°$) has been introduced to quantify aligned cells because of the following reasons Other prior studies [155, 246, 247] categorized $\theta = 0 \sim 15°$ as aligned cells, but their standard is not adequate for this study since $> 70\%$ cells on the patterned substrates are categorized as $\theta \leq 15°$. On the contrary, it is found that about 23% of cells on the chips satisfy $\theta \leq 2°$, which also corresponds to the percentage population of elongated cells in Figure 2b. Note that the new criterion allows us to consistently analyze the trends of $P_{\theta \leq 2\circ}$ using the comparable size in subpopulations as $P_{\overline{\alpha} \geq 2}$ and, arguably, the correlation between $P_{\overline{\alpha} \geq 2}$ and $P_{\theta \leq 2\circ}$ can be considered.

Data sets		Coefficient								R^2
		a	b	c	d	e	f	g	h	
Case 1	Control, 330 and 725 nm		-1.87	-1.43	81.3	0.350	-1.14	-6.64	0.0636	0.802
		3.33	p-value							
			0.269	0.290	3.13E-8	0.206	0.747	0.0244	0.907	
		a	b	c	d	e	f	g	h	
Case 2	Control, 330, 725, and 1000 nm		0.777	-1.462	77.8	0.0672	-6.43	-6.07	0.6127	0.771
		3.33	p-value							
			0.589	0.209	1.67E-13	0.774	0.00928	0.00223	0.0959	

Table 5-3. Regression results of normalized aligned cell population ($P_{\theta \leq 2\circ}$) with respect to G_w, R_w, G_D, and their cross terms. Frist and second represent estimated coefficients and their p-value with R^2 value for case 1 (Control, 330, and 725 nm) and case 2 (Control, 330, 725, and 1000 nm), respectively.

Equation 5-2

$$P_{\theta \le 2^{\circ}{}_i} = a + b \cdot G_{w_i} + c \cdot R_{w_i} + d \cdot G_{D_i} + e \cdot G_{w_i} \cdot R_{w_i} + f \cdot G_{w_i} \cdot G_{D_i} + g \cdot R_{w_i} \cdot G_{D_i} + h \cdot G_{w_i} \cdot R_{w_i} \cdot G_{D_i}$$

$$\begin{cases} i = 1,2,3, \dots, 32 \text{ for Case 1} \\ i = 1,2,3, \dots, 48 \text{ for Case 2} \end{cases}$$

For $G_D = 1000$ nm (red triangle), $P_{\theta \le 2^{\circ}}$ decreases from 50% (G2R2) to 23.3% (both G2R8 and G8R2), whereas the corresponding $P_{\theta \le 2^{\circ}}$ values for $G_D = 330$ nm (black diamond) are 13.3% (G2R2), 6.67% (G2R8), and 16.7% (G8R2). G_w and R_w effects are more noticeable when G_D values are 725 and 1000 nm. In addition, $P_{\theta \le 2^{\circ}}$ is sensitive to G_D up to $G_D = 725$ nm (p < 0.001), but no statical difference between $G_D = 725$ and 1000 nm (p ~ 0.493) as indicated in Figure 5-6 (b). As an example, the average $P_{\theta \le 2^{\circ}}$ values for $G_D = 0, 330, 725,$ and 1000 nm, regardless of G_w and R_w, are 3.33%, 10.6%, 29.8%, and 33.8%, respectively. It is worth noting that regression analyses of $P_{\theta \le 2^{\circ}}$ are performed by using Equation 5-2 and obtained similar conclusions (see Table 5-3)
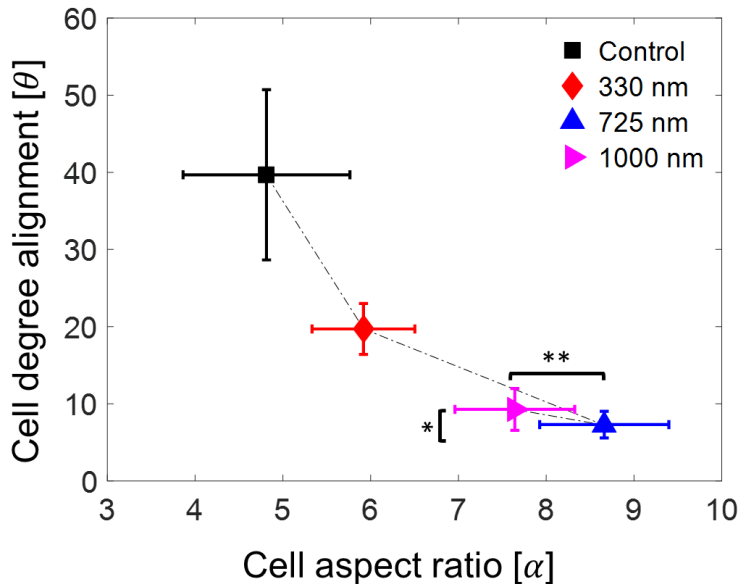
Figure 5-10. The cell alignment (θ) as a function of the cell aspect ratio (α) for different groove depths. The error bar denotes 95% confidence level interval.

compared to the regression results of the $P_{\alpha \geq 2}$ data. The effect of groove depth on the cell alignment is the most significant cue.

α and θ are the most sensitive to G_D among the controlled morphological cues in this study. To further consider the effect of G_D on both α and θ, regardless of G_w and R_w, Figure 5-10 correlates the cell alignment angles with the corresponding cell aspect ratios for different groove depth (G_D). Interestingly, the α-θ correlation appears to be inversely proportional. For example, for $G_D = 0$ (control), 325, and 725 nm, the trend is a decrease in θ with an increase in α. Then the direction of the trend gets reversed from 725 nm to 1000 nm as evidenced by a larger θ (* $p < 0.05$) and a smaller α (** $p < 0.001$) with considerable statistical significances.

As mentioned above, there is a significant discrepancy in the previous reported and the new θ values likely due to cell-type-dependent contact guidance. Moreover, Crouch et al. [155] studied human foreskin fibroblasts (HFF) only using G5R5 configuration with different depths from $G_D = 800$ nm to $G_D = 1024$ nm. Despite the nearly identical cell aspect ratio of HFF and Hs27 cells (Figure 5-11) as a function of the groove depth, the corresponding cell alignment again exhibits considerable cell type dependent discrepancy. Because of these cell type dependency, time-effective characterization of cellular response to contact guidance, e.g., using multiplexed contact guidance chips to concurrently consider a wide range of topographic design parameters within the same cell culture, becomes increasingly relevant for practical optimization and application of contact guidance technologies for biomedical applications and biological studies.
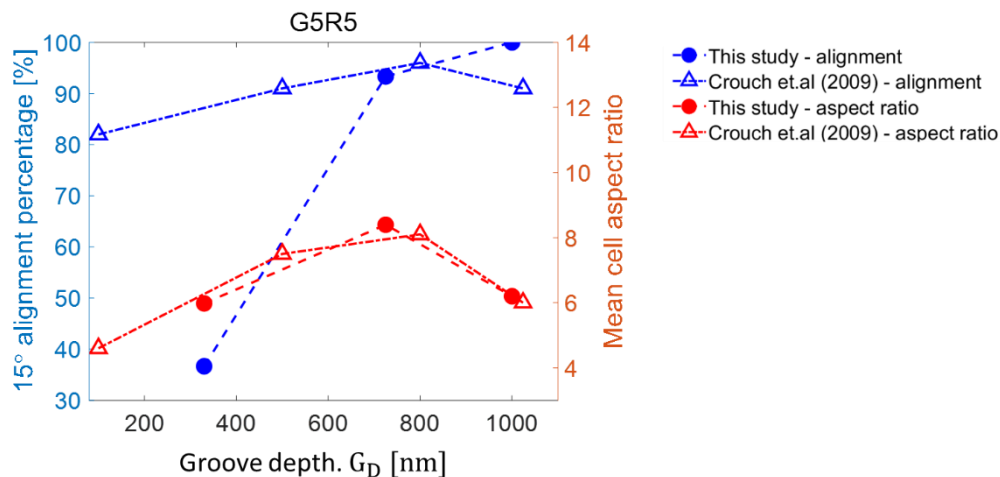
Figure 5-11. A plot for the 15° alignment percentage (blue) and mean cell aspect ratio (red). The solid circle represents the results of this study, while the empty triangular indicates the study from Crouch et al (2009).

5.2.2   Cell Migration: Dynamic Image Analysis

In this section, analyses are performed to quantify dynamic cell migration on contact guidance topographies with an emphasis on directional migration along the groove direction. Accurate characterization of dynamic cell behavior on various topographical cues is crucial for many biological applications such as embryological development, tissue formation/regeneration, immune defense/inflammation, and cancer progression [248-250]. For instance, it is known that the directional cell movement of fibroblast enables development of a larger contact area during wound healing process [251]. Furthermore, cell migration speed is directly linked to acceleration/deceleration of pathological matrix deposition processes in fibrosis [157]. Finally, an overall efficiency of cell migration [252-256], typically quantified by the directional motion and its ratio over the total travel distance, is relevant to rapid ECM synthesis and remodeling. This study may offer a means to efficiently guide cell migration in the scope of achieving a quicker recovery of the

156

microenvironments [257]. To clarify, all the directional characteristics of the dynamic cell migration in the following analyses are characterized with respect to the groove direction.

Figure 5-12 (a) and Figure 5-13 show the overall migration directionality. For this, vectors from the initial to final positions of the same individual cells migrational tracks >10-hour intervals were obtained from optical images. Then the angle between the vector and the groove direction was calculated for the migration directionality. Note that the percentage cell population near $0°$ monotonically increases with the groove depth. For example, the cell populations between $0°$ and $10°$ are 8.21%, 41.7%, 71.8%, and 75.3% on $G_D = 0$, 330, 725, and 1000 nm, respectively. For statistically significant conclusions on the G_D-sensitive directional orientation, a one-way ANOVA test has been performed as shown in Figure 5-14 (a). The average directional orientations are $43.8°, 21.6°, 10.7°,$ and $9.83°$ on $G_D = 0$, 330, 725, and 1000 nm, respectively. The results confirm that the directional orientation decreases from $G_D = 0$ to $=725$ nm ($p \ll 0.001$) and then the difference between $G_D = 725$ and $=1000$ nm becomes statistically insignificant ($p \sim 0.390$). It is worth noting that the effect of R_w and G_w on the cell directional orientation is statistically obvious ($p < 0.05$) only for $G_D = 330$ nm among three different depths (see Figure 5-14 (b) and (c)). Moreover, for $G_D = 330$ nm, R_w has a stronger influence on the cell directional orientation than G_w (i.e., R_w: $p \sim 0.0002$ and G_w: $p \sim 0.0207$).
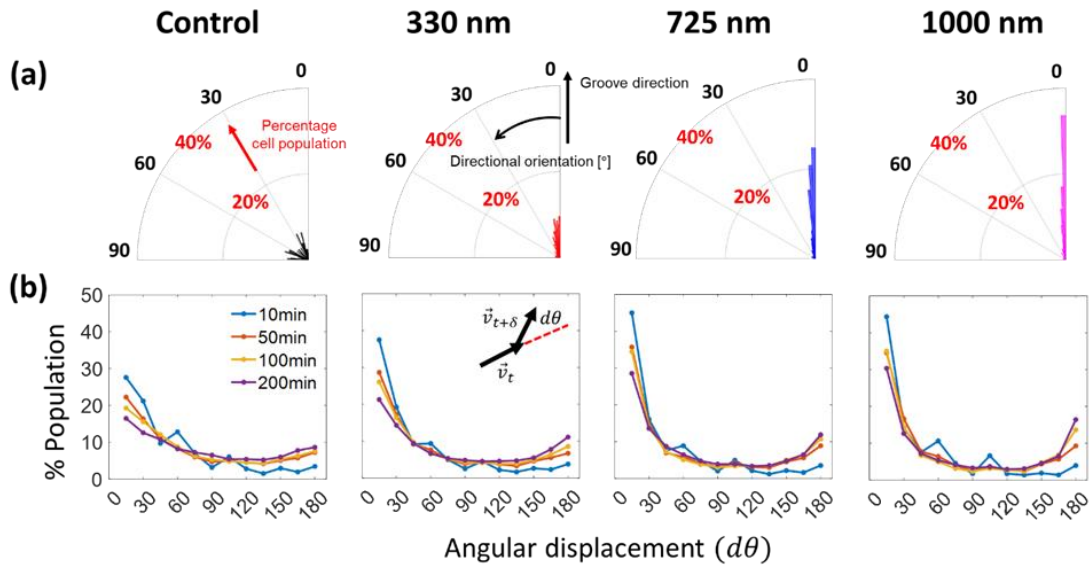
Figure 5-12. (a) Directional orientations of the fibroblasts on contact guidance with different groove depths. The angular and radial coordinates represent the cell orientation from 0 to 90° and the corresponding percentage cell population within the total population (each bin size is 2°). (b) The percentage population distribution of angular displacement ($d\theta$, see graphical definition in inset and δ represents a time interval) evaluated at four different time intervals (10, 50, 100, and 200 mins). For (a) and (b), each column represents the results of different groove depths (left to right) from 0 to 1000 nm.
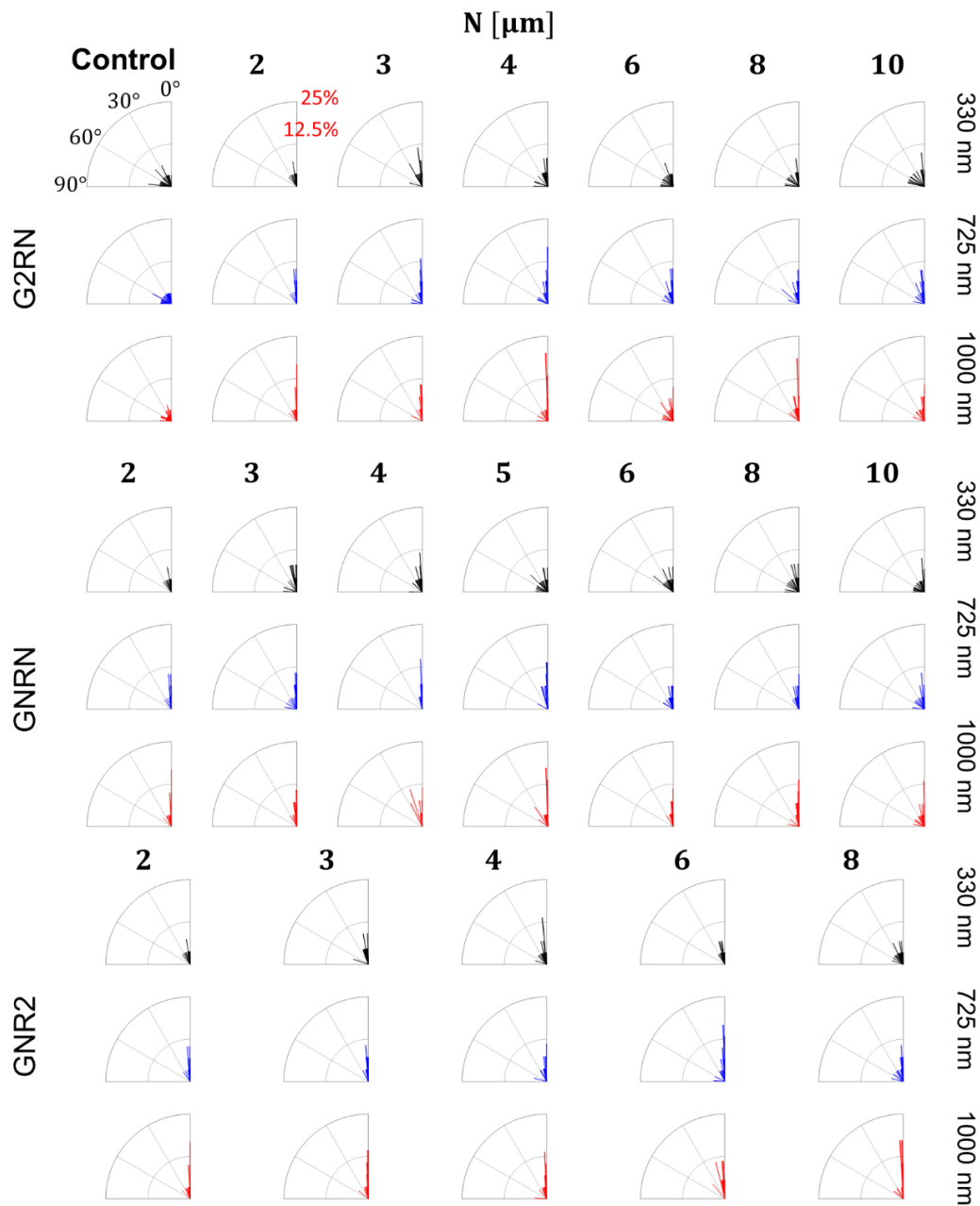
Figure 5-13. Directional orientations for the fibroblasts on all topographical cues in a polar plot. The range of the phase angle is from 0 to 90° (the bin is 2°). The radial coordinate represents the normalized number of cells having a directional angle within the phase angle intervals. The major grid intervals for phase and radial coordinates indicate 30° and 0.125, respectively.
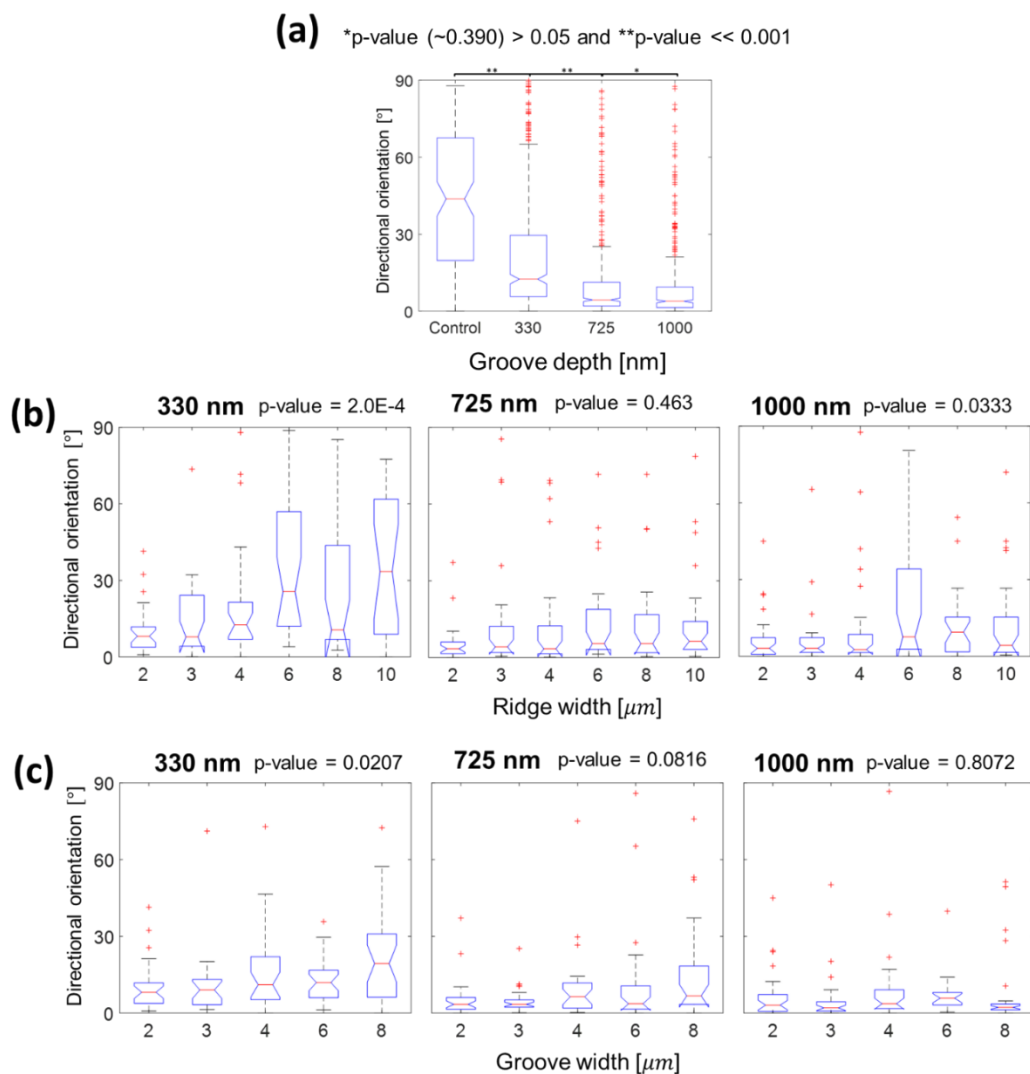
Figure 5-14. Box-and-whisker plot of the directional orientation as a function of groove depths (a), ridge widths (b), and groove widths (c) with the corresponding p-value from one-way ANOVA test.
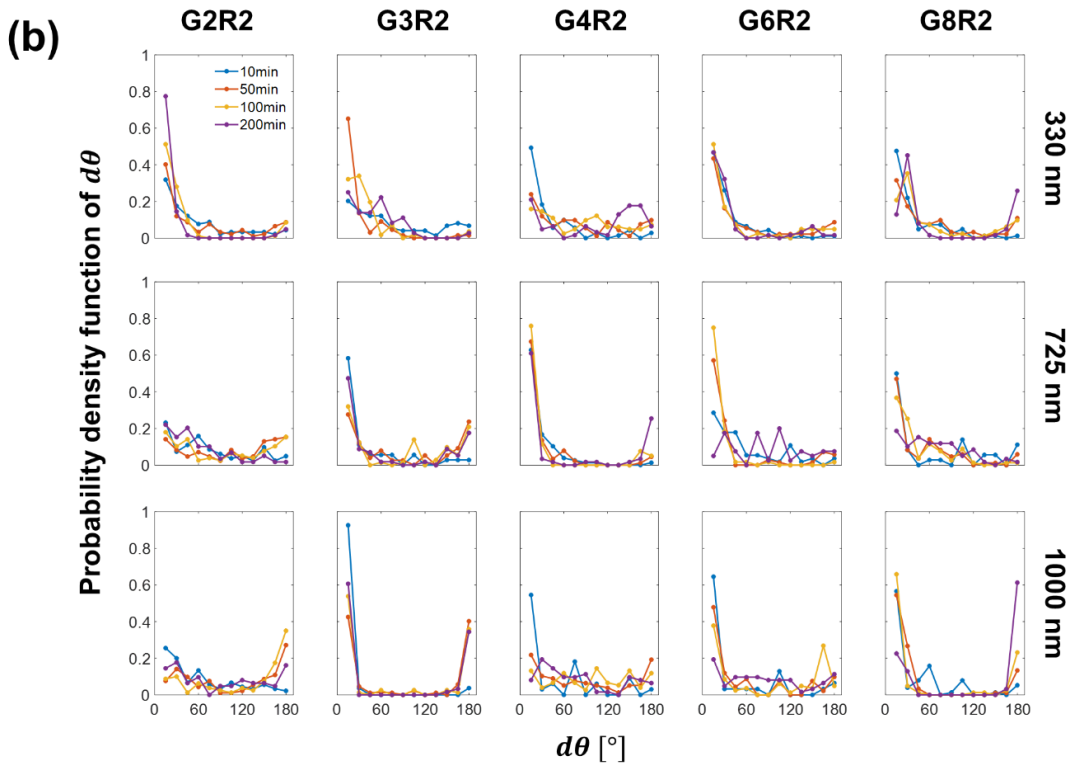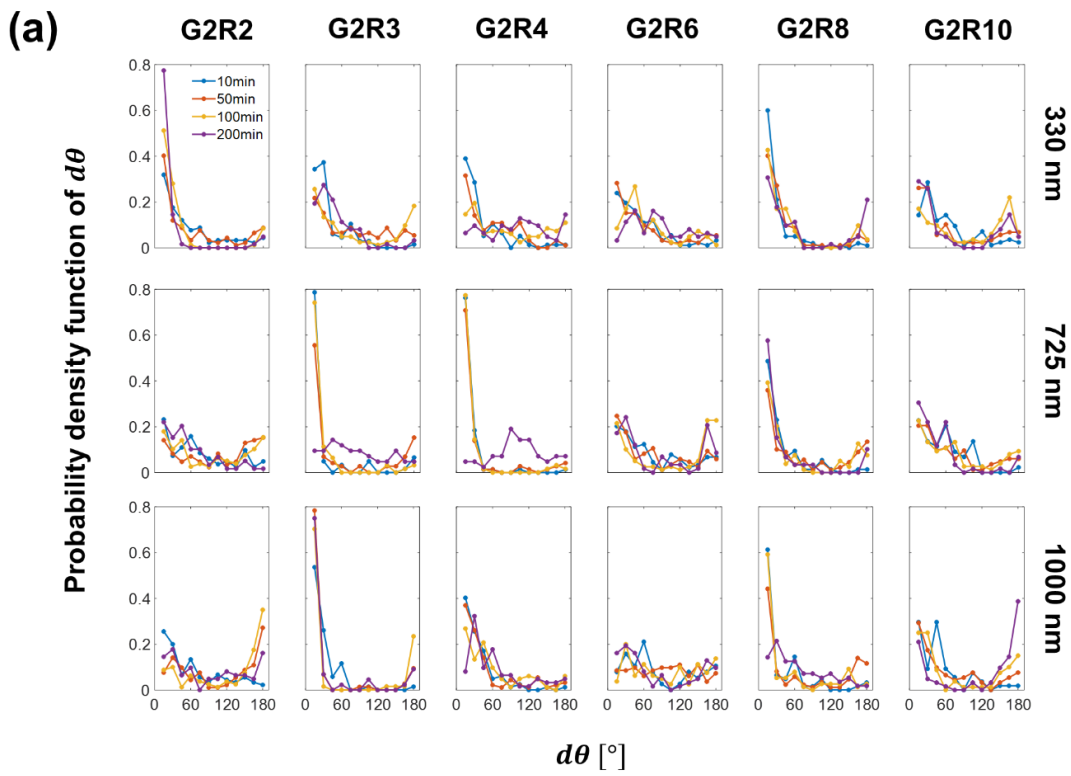
Figure 5-15. Probability density function of angular displacement ($d\theta$) for two different cases: G2RN (a) and GNR2 (b).

The cell directional orientation provides the general direction of cell migration over >10 hours but misses time-dependent dynamic characteristics in a shorter period. Because of this limitation, an angular displacement $(d\theta)$ of individual cells using different time intervals (i.e., $\delta = 10, 50, 100$ and 200 minutes) is computed and the occurrence distribution (i.e., the normalized cell population) with a $15°$-bin size is mapped by using the following expression [258]:

Equation 5-3
$$d\theta(t, \delta) = \cos^{-1}([\vec{v}_t \cdot \vec{v}_{t+\delta}]/|\vec{v}_t||\vec{v}_{t+\delta}|)$$

where $\vec{v}_t$ is a velocity vector of a cell between t and $t + \delta$ over a finite time interval (δ) (see the inset in Figure 5-12 (b)). The occurrence in Figure 5-12 (b) exhibits two general trends for all three G_D cases. First, the occurrence for $\delta = 10$ min exponentially decays with increasing $d\theta$, but a larger G_D value results in faster decay. Second, the occurrence in $0° \leq d\theta \leq 15°$ decreases, while the occurrence in $165° \leq d\theta \leq 180°$ increases, with increasing a time interval, respectively. These observed trends indicate that cell migration on deeper G_D is indeed more directional in the groove direction for any time interval. For example, note that the occurrence in $0° \leq d\theta \leq 15°$ on $G_D = 725$ and =1000 nm (e.g., 0.285 and 0.303, respectively, for $\delta = 200$ min) is considerably higher compared to $G_D = 0$ nm (e.g., 0.276 even for $\delta = 10$ min). In addition, the occurrence in $165° \leq d\theta \leq 180°$ for deeper G_D increases with increasing δ at a faster rate compared to the control, for example, from 0.04 ($\delta = 10$ mins) to 0.16 ($\delta = 200$ mins) for $G_D = 1000$ nm while the occurrence for the control remains low (i.e., 0.09 for $\delta = 200$ mins). In summary, cells on deeper G_D exhibit strong forward motion at shorter δ and back-and-forth motion at larger δ, respectively, along the groove patterns. The

162

additional analysis, while not discussed in detail here, indicates that the influence of R_w

and G_w on $d\theta$ is not significant (see Figure 5-15 (a) and (b), respectively).
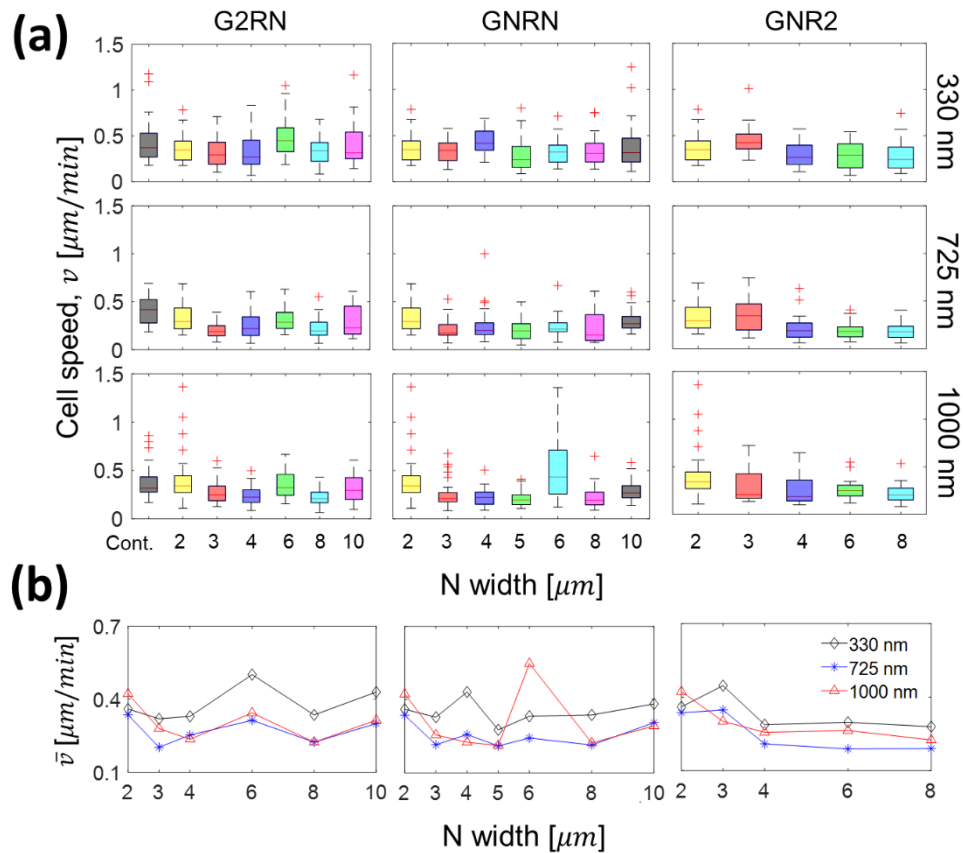
Figure 5-17. (a) Box-and-whisker diagrams of cell speed (v) with respect to individual topographic conditions. (b) The averaged cell speeds are plotted for different lateral conditions (G_w and R_w).
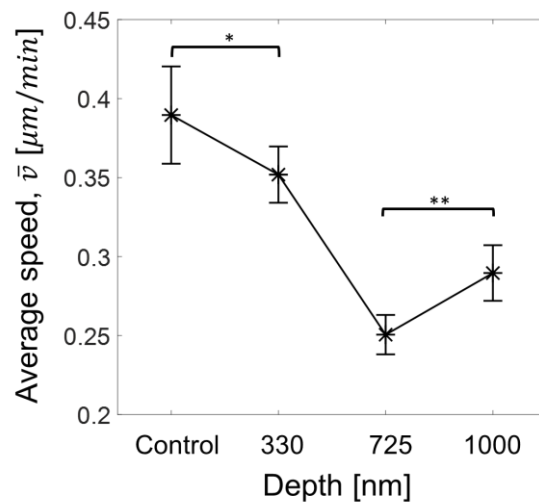
Figure 5-16. Cell migration speed with different groove depths. One-way ANOVA was performed to test for statistical significance (* $p < 0.05$ and ** $p < 0.001$). All error bars are mean $\pm$ standard error of mean (SEM).
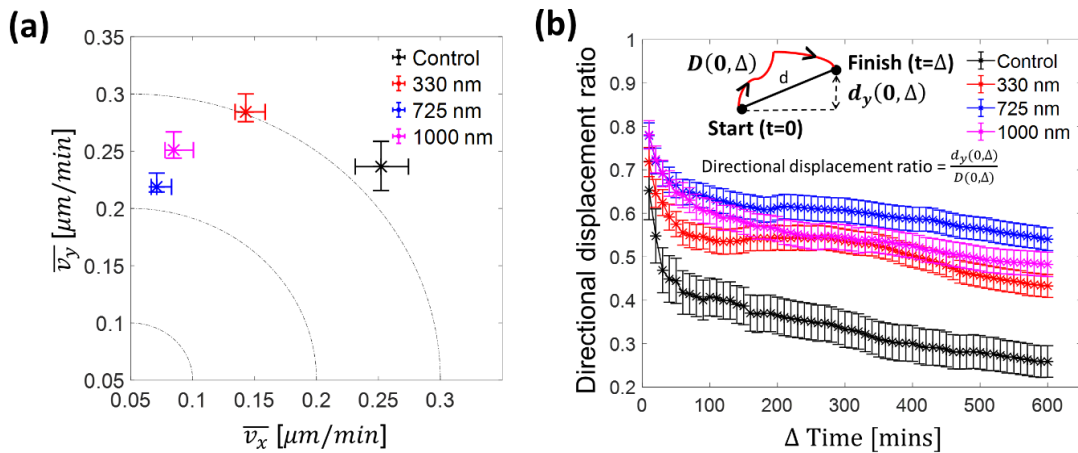
Figure 5-18. (a) Cell migration speed in the groove direction ($\bar{v}_y$) and perpendicular to the groove direction ($\bar{v}_x$). (b) Directional displacement ratio (i.e., y direction moving length ($d_y(0, \Delta)$)) divided by the total travel length ($D(0, \Delta)$) from start (t (time) = 0) to finish (t = Δ), see graphical definition in *inset*) as a function of the time interval (Δ) for different groove depths. All error bars are mean $\pm$ standard error of mean (SEM).

New, how individual topographical cues affect migration speed of Hs27 cells is identified. Surprisingly, the cell migration speed difference between G2RN, GNRN, and GNR2 is insignificant and the average migration speed ($\bar{v}$=total travel distance over total travel time) is insensitive to R_w and G_w. Again, $\bar{v}$ strongly depends on G_D (see Figure 5-17). Because of this reason, cell migration speed for different groove depth, G_D, is summarized in Figure 5-16 without separately considering R_w and G_w. The mean value of the cell speed on the flat substrate (control) is about 0.4 µm/min, which matches with the previous study using human skin fibroblasts [259]. The migration speed on the $G_D = 725$ nm is 0.25 µm/min, which is considerably lower than 0.39 and 0.35 µm/min on the control and $G_D = 330$ nm, respectively. The average cell speed on $G_D = 1000$ nm is 0.29 µm/min, slightly higher than $G_D = 725$ nm. Interestingly, the observed trend in the average cell speed is qualitatively similar to the cell alignment angle in Figure 5-9.

To quantify the directional speed, the average migration speed is decomposed into parallel ($\overline{v_y}$) and perpendicular ($\overline{v_x}$) directions with respect to the groove direction as shown in Figure 5-18 (a). The $\overline{v_y}$ to $\overline{v_x}$ ratio increases from 1 (control) to 3.1 ($G_D = 725$ nm) with an increase of G_D, but it slightly decreases to 3.0 with further increases of $G_D = 1000$ nm . Note that $\overline{v_y}$ is about 3.0-3.1 times larger than $\overline{v_x}$ for $G_D = 725$ and 1000 nm , indicating directional cell migration in the groove direction. In contrary, $\overline{v_x} \approx \overline{v_y}$ for the control experiment indicating that the cells move without a preferred direction.
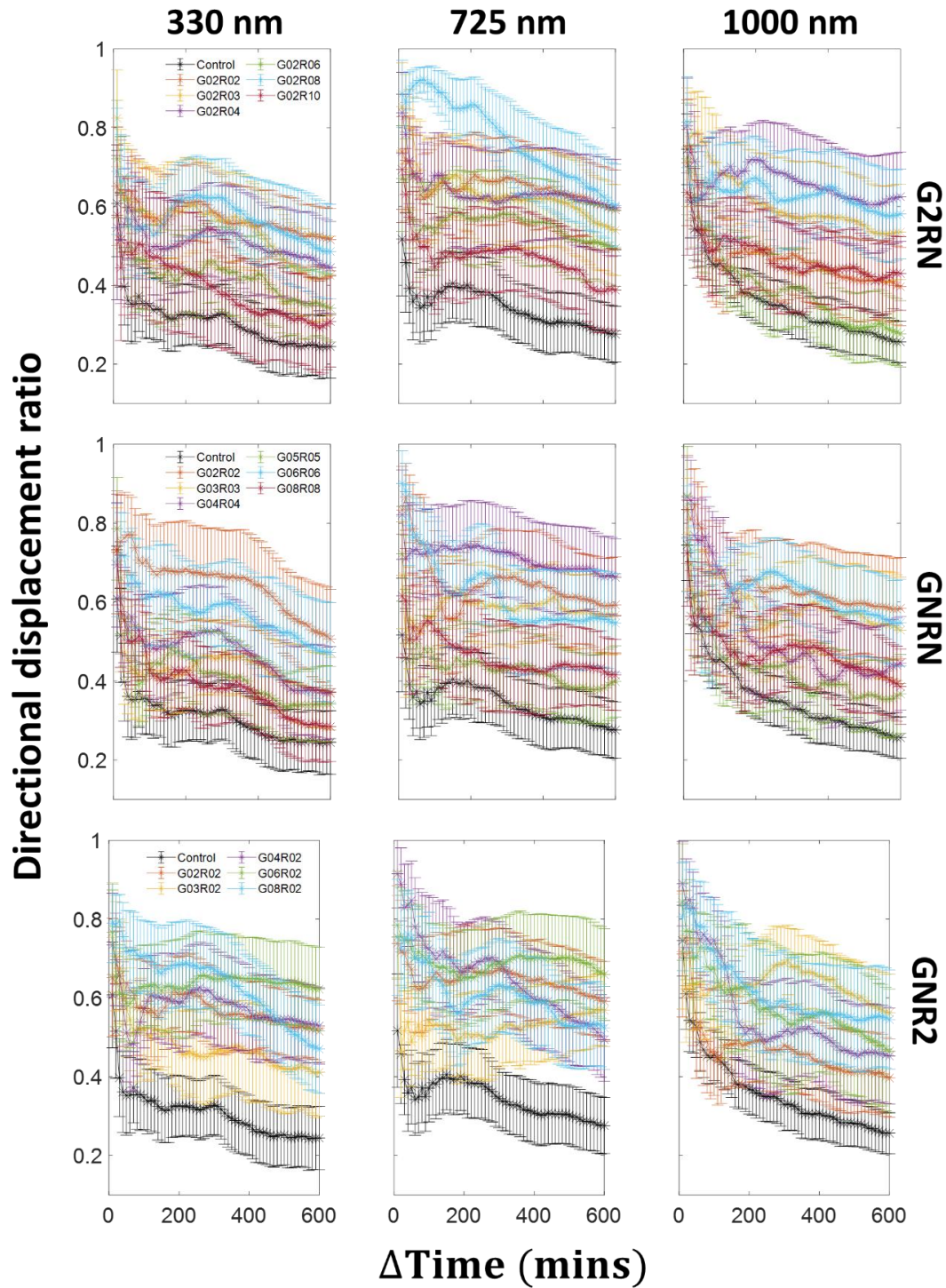
Figure 5-19. Directional displacement ratio (i.e., y direction moving length divided by the total travel length with error bars (mean $\pm$ standard error of mean (SEM) for the cells on all topographical cues as a function of the time interval (Δ). Each row and column represent three different regions and depths scales, respectively.

So far, the average cell speed has been quantified under the influence of contact guidance. However, it is still crucial to amplify the groove direction motion (along y-axis) of cells by minimizing their lateral motion (width direction along x-axis) to effectively guide cells to target locations, e.g., injured areas, using the contact guidance technology. For an increase of migration efficiency, the concept of y-axis directional persistence is considered through a directional displacement ratio. In this section, the emphasis is placed on the effect of G_D because the effect of G_w and R_w on cell speed is insignificant as discussed above (also see Figure 5-19).

The question to be addressed is whether as an efficient directional guidance, the G_D scales optimize the entire cell migration trajectories in order to rapidly reach the target point (i.e., somewhere along the groove direction). Similar with well-known directionality ratio (i.e., $\frac{d}{D}$, d = straight-line length between the start point and the endpoint of the migration trajectory, and D = the total length of the trajectory) [260], the directional displacement ratio has been utilized to characterize y-axis directional efficiency, which is defined as follows:

Equation 5-4

$$\frac{d_y(0, \Delta)}{D(0, \Delta)} = \frac{y(\Delta) - y(0)}{\sum_{k=1}^{\frac{\Delta}{10}} \sqrt{(x(10k) - x(0))^2 + (y(10k) - y(0))^2}}$$

In other words, instead of using d, the directional displacement is the ratio of a projection of d onto the y axis ($d_y(0, \Delta)$) over the total length of the trajectory ($D(0, \Delta)$) from start (t (time) = 0) to finish (t = Δ) in which the time interval (Δ [mins]) ranges from 10 to 600 mins with 10 mins increment as shown in the inset of Figure 5-18 (b). Since the

168

d_y and D depend on the Δ, this ratio can markedly change over the time period of a cell trajectory. The directional displacement ratio for all cases in Figure 5-18 (b) decays exponentially in Δ, but a larger G_D value result in slower decay. More specifically, the initial values of the directional displacement ratio are 0.65 (control), 0.72 ($G_D = 330$ nm), 0.78 ($G_D = 725$ nm), and 0.78 ($G_D = 1000$ nm) and then they decrease to 0.26, 0.43, 0.54, and 0.48, respectively, at $\Delta = 600$ mins. It is worth remarking that the directional displacement ratio for the control is consistently smaller than those for all three G_D cases as expected. The important observation, here, confirms that the cells require less total length of the trajectory to arrive at a target location along the groove direction with a deeper G_D.

5.3   Discussion

In this study, the influence of different topographical cues (i.e., R_w, G_w, and G_D) on the static and dynamic behavior of Hs27 fibroblast cells is characterized by utilizing a microfabricated contact guidance chip. To map the effect of the R_w and G_w beyond what has been reported in the literature, three different cases have been considered, namely, G2RN, GNRN, and GNR2. This study on the cell morphologies shows that the cells are likely elongated and aligned with the groove direction as G_D increases from 0 to 725 nm with the corresponding p-value $< 10^{-8}$. Within the same G_D range, the effect of R_w is also statistically significant (p $\sim$ 0.012). It appears that the trend in cell responses changes between $G_D = 725$ and 1000 nm because the cell elongation and alignment slightly decrease as evidenced by a considerable decrease in the R^2 value.

The experiments conclude that the groove depth, G_D, is the most dominant topographic cue for both static and dynamic responses of Hs27 fibroblasts, which agrees with other studies [139, 155, 261]. To provide feasible explanations of the G_D-dependent cell behaviors, the role of cell membrane on contact guidance is discussed. When G_D increases for a given ridge and groove width, cell membrane must undergo a larger degree of membrane deformation to occupy the space within the cross section of individual grooves defined by G_w and G_D. A cell membrane protrusion led by filopodia will sense topographic cues and move toward the groove bottom. Considering that the average length of filopodia is about $1\sim5\ \mu m$ [262-264], the Hs27 cells will likely reach the groove bottom and form focal adhesions as confirmed in the previous study [163]. For simplicity, it is assumed that the lateral filopodia protrusions occur on the ridge edge with their characteristic length (l_f). Then, the bending angle (θ_f) between filopodia and the groove bottom can be calculated as follows:

Equation 5-5

$$\theta_f = \sin^{-1}(G_D/l_f)$$

The Equation 5-5 shows that θ_f increases with increasing G_D. In [265], it was shown that larger θ_f increases the normal traction force component on the integrin-based filopodia adhesion. Such high normal stresses lead to an impairment of FA formation as well as severe buckling of the branched actin fibers in the filopodia [262, 265, 266]. As indicated by several studies [267-272], buckled F-actin filaments shorten and break the actin shaft and, therefore, filopodia forms in the lateral direction will likely be short-lived and retracting. Moreover, Dunn et al. reported that a larger bending angle, e.g., to follow discontinuous topographic patterns on a contact guidance chip, further limits lateral

protrusions of filopodia across the features [273]. Based on the previous studies, filopodia likely becomes thick, actin-rich, and stable in the groove direction compared to the lateral direction [274]. This may offer possible explanation for the directional cell orientation and migration because filopodia is known to be linked with the cell morphology [275] as well as the cell migration [276, 277].

For the R_w-dependent morphology of Hs27 fibroblasts, a model based on the constrained maturation of focal adhesions (FAs) [144, 278] can provide mechanistic insights. The anisotropic and oriented topographical cues, i.e., parallel ridges and grooves, likely induce cell membrane protrusions as well as FA formation and maturation along the topography. These laterally restricted FAs result in the formation of aligned actin stress fibers to along the parallel direction of the topography because the orientation of the stress fibers follows that of the FAs [163]. Note that the aligned actin stress fibers connected to large, long-lived, and oriented FAs are longer and more stable than small, short-lived, and non-aligned ones associated with non-oriented FAs [144]. With reduction of R_w, the formation of FAs is more confined along the groove direction and, as a result, the Hs27 fibroblasts tend to be more elongated and aligned in the same direction as shown in Figure 5-9.

The dynamic analyses also confirm G_D as the main geometrical parameter to influence cell behavior responses. The cells on deeper G_D are better guided along the groove direction. Cells on the flat control and $G_D = 330\ \text{nm}$ substrates move faster, compared to those on $G_D = 725$ and $1000\ \text{nm}$. This trend ($\bar{v} = 0.55\ \mu\text{m/min}$ for control and $\bar{v} = 0.36\ \mu\text{m/min}$ for the grooved pattern) has also been observed by other study which uses

171

NIH 3T3 fibroblasts with $R_w = G_w = 0.43$ µm and $G_D = 200$ nm [279]. However, these results are directly opposite with those of another study which reports that faster migration speed for MC3T3-E1 mouse osteoblast cells on various G_D ranging from 0 ($\bar{v} = 0.39$ µm/min) to 4.5 µm ($\bar{v} = 0.61$ µm/min) with $R_w = 6$ µm and $G_w = 4$ µm [148]. Based on a positive feedback loop between actin flow rates and the cell elongation, the elongated cells are likely to accelerate their actin retrograde flow such that it improves their motility as confirmed using several different cell types such as retinal pigment epithelial cells and bone marrow-derived mice dendritic cells [143]. This discrepancy may come from not only cell type-, but substrate topography dependent characteristics.

5.4   Conclusion

With growing interests in the development of the next generation biomaterials, a fundamental understanding of contact guidance offers the potential to guide specific cellular functions in vivo. The current work characterizes static and dynamic behaviors of the Hs27 fibroblasts in the wide range of groove and ridge dimensions and offers better understanding of individual geometric factor's contribution on the cellular responses. For static results, groove depth (G_D) as deep as 725 nm induces significant elongation ($\alpha_{ave} = 8.66$) and alignment ($\theta_{ave} = 7.23°$), while further increase of G_D to 1000 nm slightly decreases both elongation ($\alpha_{ave} = 7.64$) and alignment ($\theta_{ave} = 9.27°$) compared to the cells on a flat substrate (control, $\alpha_{ave} = 4.81$ and $\theta_{ave} = 39.7°$). The regression analyses show that G_D and $G_D \cdot R_w$ terms have a statistically significant effect on the cell elongation and alignment, whereas the effect of G_D as deep as 1000 nm has been diminished compared to that of $G_D = 725$ nm based on its coefficient reduction. In the

dynamic analysis, a deeper G_D better guided the cells migrating along the groove direction, even though their average speed slightly decreases from 0.39 μm/min (control) to 0.29 μm/min (1000 nm), respectively. The high occurrence of the $0° \leq d\theta$ (angular displacement) $\leq 15°$ and $165° \leq d\theta \leq 180°$ from the groove direction and its faster decaying rate with increasing $d\theta$ indicate the y-axis directional movement of the cells on the deeper G_D. The large ratio of directional speed and -directional displacement, both in the groove direction, for a deeper G_D suggest that the cells on the deeper G_D are better guided by minimizing their unwanted motion perpendicular to the groove direction. These findings demonstrate the importance of G_D for the Hs27 fibroblasts as a guideline of the efficient migration journey. The in-depth experimental and statistical studies would provide a way of creating an effective platform for the application of various topographical cues, which are shown to be successful in guiding and controlling cell morphological and migrating characteristics.

6.   CONCLUSION

Cavitation bubbles form in soft biological systems when subjected to a negative pressure above a critical threshold, and dynamically change their size and shape in a violent manner. The critical threshold and dynamic response of these bubbles are known to be sensitive to the mechanical characteristics of highly compliant biological systems. Several recent studies have demonstrated different biological implications of cavitation events in biological systems, from therapeutic drug delivery and microsurgery to blunt injury mechanisms. Due to the rapidly increasing relevance of cavitation in biological and biomedical communities, it is necessary to understand cavitation behavior in biologically relevant systems (e.g., tissue simulant and organs).

Despite the great importance, the onset of cavitation and its complex dynamics in biological materials remain unclear. In chapter 2, the experimental results using soft gels as a tissue simulant show that the critical acceleration (a_{cr}) at cavitation nucleation monotonically increases with increasing stiffness of gelatin A/B, while a_{cr} for agarose and agar initially increases but is followed by a plateau or even decrease after stiffness reach to ~100 kPa. The image analyses of cavitation bubbles and theoretical work reveal that the observed trends in a_{cr} are directly linked to how bubbles grow in each gel. Gelatin A/B, regardless of their stiffness, form a localized damaged zone (tens of nanometers) at the gel-bubble interface during bubble growth. In contrary, the damaged zone in agar/agarose becomes significantly larger (> 100 times) with increasing shear modulus, which triggers the transition from formation of a small, damaged zone to activation of crack propagation.

Although numerous efforts for mechanical response of tissue simulants under single impact have been made up to date, accurately characterizing soft matters, particularly under harsh conditions (i.e., high strain rate and repetitive loadings) at which other rheological techniques are not performed, remains limited due to their complex behaviors associated with ultra-soft nature and brittle manner from high water content. Chapter 3 shows a newly designed drop-tower-based repetitive impact tester, integrated with a motor system by converting rotational to translational energy. The experimental and theoretical approaches confirm that the system can tightly control impact characteristics, i.e., impact amplitude and the number of impacts over time, with a change of gear design and impact surface condition, continuously delivering a smooth, rapid impact-induced acceleration trajectory to the soft sample. As one of implications for the integrated system, the critical accelerations (a_{cr}) that corresponds to the onset of initial cavitation for pure water and 0.75w/v% agarose gel are experimentally quantified. This study indicates that the a_{cr}s for both materials strongly depend on the size of the sample and interestingly, the agarose sample shows impact characteristics dependent a_{cr}: its a_{cr} significantly decreases as an increase of total number of impacts before initial cavitation nucleation. Finally, a novel non-optical detection method of initial cavitation nucleation while conducting successive drop events based on cavitation collapse induced structural resonance of the sample holder along non-impact direction is introduced.

Even though the previous chapters 2 and 3 made significant progress on the dynamic response of tissue simulant under a wide range of loading conditions, the spatio-temporal response of live cells under mechanical impact has not been fully understood due to the lack of the experimental capability as well as of knowledge for cell complex responses. To

overcome these challenges, Chapter 4 demonstrates a newly designed in vitro experimental setup integrated with live cell microscopy and drop tower system to apply a well-controlled translational loading to actual live cells. On top of that, Chapter 5 systematically characterizes static and dynamic behaviors of Hs27 fibroblast, which plays a significant role in wound healing process, on varying dimensions of topography. The use of the multiplexed, microfabricated substrates aims at mimicking physiological topographies such as aligned fibers that most cells encounter *in vivo*.

In Chapter 4, to quantify potential blunt injuries and understand their main mechanism(s) under the extreme dynamic threats (>150g), an innovative experimental method that applies a well-characterized and -controlled mechanical impact to live cells cultured in a custom-built in vitro setup compatible with live cell microscopy has been developed. The studies using fibroblast cells as a model indicate that input acceleration (a_{in}) alone, even when it is much greater than the typical injury criteria, e.g., $a_{in} >$ 1000g, does not result in cell damage. On the contrary, a material-dependent critical pressure value above which a sudden decrease in cell population and cell membrane damage have been observed has been detected. It has been unambiguously shown that 1) this critical pressure is associated with the onset of cavitation bubbles in a cell culture chamber and 2) the dynamics of cavitation bubbles in the chamber induces localized compressive/tensile pressure cycles, with an amplitude that is considerably greater than the acceleration-induced pressure, to cells. More importantly, the rate of pressure change with time for cavitation-induced pressure is significantly faster (more than ten times) than acceleration-induced pressure. This in vitro study on the dynamic response of biological

systems due to mechanical impact is a crucial step towards understanding potential mechanism(s) of blunt injury and implementing novel therapeutic strategies post-trauma.

Finally, in Chapter 5, Cellular morphology and mobility play a key role in important biological processes, e.g., fibroblasts migration toward a wound site and regeneration of extracellular matrix. The morphological and dynamic cell responses are strongly influenced by topographic features such as lateral and vertical dimensions, namely, ridge and groove widths and groove depth ($R_w, G_w,$ and G_D , respectively). However, experimental studies that independently quantify the effect of the individual dimensions as well as their coupling on cellular function are still limited. In Chapter 5, extensive parametric studies in the dimensional space–well beyond the previously studied range in the literature–to explore topographical effects on morphology and migration of Hs27 fibroblasts via static and dynamic analyses of live cell images are performed. The static analysis reveals that the G_D is most significant, followed by the R_w. The fibroblasts appear to be more elongated and aligned in the groove direction as the G_D increases, but their trend changes after 725 nm. Interestingly, the cell shape and alignment show a very strong correlation regardless of G_D. The dynamic analysis confirms that directional cell migration is also strongly influenced by the G_D, while the effect of the R_w and G_w is statistically insignificant. Directional cell migration, as observed in the static cell behavior, shows the statistically significant transition when the G_D is 725 nm, showing the intimate links between cell morphology and migration. The experimental studies, combined with potential mechanistic explanation, are crucial for fundamental understanding of isotropic cell behavior and, therefore, relevant to development of new biomaterials/tools,

interpretation of biological processes in tissue regeneration, and promotion of wound repair, e.g., by achieving effectively guided cell migration.

REFERENCES

1. Brennen, C.E., *Cavitation and bubble dynamics*. 2014, New York: Cambridge University Press. xvii, 249 pages.

2. Sass, W., et al., *The mechanisms of stone disintegration by shock waves.* Ultrasound Med Biol, 1991. **17**(3): p. 239-43.

3. Sauerbruch, T., et al., *Fragmentation of gallstones by extracorporeal shock waves.* N Engl J Med, 1986. **314**(13): p. 818-22.

4. Holmer, N.G., et al., *On the mechanism of kidney stone disintegration by acoustic shock waves.* Ultrasound Med Biol, 1991. **17**(5): p. 479-89.

5. Chaussy, C.H., W. Brendel, and E. Schmiedt, *EXTRACORPOREALLY INDUCED DESTRUCTION OF KIDNEY STONES BY SHOCK WAVES.* The Lancet, 1980. **316**(8207): p. 1265-1268.

6. Kaude, J.V., et al., *Renal morphology and function immediately after extracorporeal shock-wave lithotripsy.* AJR Am J Roentgenol, 1985. **145**(2): p. 305-13.

7. Sokolov, D.L., M.R. Bailey, and L.A. Crum, *Use of a dual-pulse lithotripter to generate a localized and intensified cavitation field.* J Acoust Soc Am, 2001. **110**(3 Pt 1): p. 1685-95.

8. Ikeda, T., et al., *Cloud cavitation control for lithotripsy using high intensity focused ultrasound.* Ultrasound in Medicine & Biology, 2006. **32**(9): p. 1383-1397.

9. Pishchalnikov, Y.A., et al., *Cavitation bubble cluster activity in the breakage of kidney stones by lithotripter shockwaves.* J Endourol, 2003. **17**(7): p. 435-46.

10. Johnsen, E. and T. Colonius, *Shock-induced collapse of a gas bubble in shockwave lithotripsy.* J Acoust Soc Am, 2008. **124**(4): p. 2011-20.

11. Yoshizawa, S., et al., *High intensity focused ultrasound lithotripsy with cavitating microbubbles.* Medical and Biological Engineering and Computing, 2009. **47**(8): p. 851-860.

12. Kennedy, P.K., D.X. Hammer, and B.A. Rockwell, *Laser-induced breakdown in aqueous media.* Progress in Quantum Electronics, 1997. **21**(3): p. 155-248.

13. Zysset, B., J.G. Fujimoto, and T.F. Deutsch, *Time-resolved measurements of picosecond optical breakdown.* Applied Physics B, 1989. **48**(2): p. 139-147.

14. Husseini, G.A. and W.G. Pitt, *Micelles and nanoparticles for ultrasonic drug and gene delivery.* Advanced drug delivery reviews, 2008. **60**(10): p. 1137-1152.

15. Graham, S.M., et al., *Inertial cavitation to non-invasively trigger and monitor intratumoral release of drug from intravenously delivered liposomes.* J Control Release, 2014. **178**: p. 101-7.

16. Husseini, G.A., et al., *The role of cavitation in acoustically activated drug delivery.* Journal of controlled release : official journal of the Controlled Release Society, 2005. **107**(2): p. 253-261.

17. Li, F., et al., *Dynamics and mechanisms of intracellular calcium waves elicited by tandem bubble-induced jetting flow.* Proc Natl Acad Sci U S A, 2018. **115**(3): p. E353-e362.

18. Lo, C.W., et al., *Cavitation phenomena in mechanical heart valves: studied by using a physical impinging rod system.* Ann Biomed Eng, 2010. **38**(10): p. 3162-72.

19. Chao, T.-C. and A. Ros, *Microfluidic single-cell analysis of intracellular compounds.* Journal of The Royal Society Interface, 2008. **5**(suppl_2): p. S139-S150.

20. Goldsmith, W., *The state of head injury biomechanics: past, present, and future: part 1.* Crit Rev Biomed Eng, 2001. **29**(5-6): p. 441-600.

21. Lubock, P. and W. Goldsmith, *Experimental cavitation studies in a model head-neck system.* J Biomech, 1980. **13**(12): p. 1041-52.

22. Farjo, L.A. and T. Miclau, *Ballistics and mechanisms of tissue wounding.* Injury, 1997. **28**: p. C12-C17.

23. Hu, J., et al., *Injury patterns and sources of non-ejected occupants in trip-over crashes: a survey of NASS-CDS database from 1997 to 2002.* Annu Proc Assoc Adv Automot Med, 2005. **49**: p. 119-32.

24. Estrada, J.B., et al., *Microcavitation as a Neuronal Damage Mechanism in an In Vitro Model of Blast Traumatic Brain Injury.* Biophysical Journal, 2017. **112**(3, Supplement 1): p. 159a.

25. Wu, Y.-T. and A. Adnan, *Effect of Shock-Induced Cavitation Bubble Collapse on the damage in the Simulated Perineuronal Net of the Brain.* Scientific Reports, 2017. **7**(1): p. 5323.

26. Kanagaraj, J., et al., *Reparative Effects of Poloxamer P188 in Astrocytes Exposed to Controlled Microcavitation.* Annals of Biomedical Engineering, 2018. **46**(2): p. 354-364.

27.   Estrada, J.B., et al., *High strain-rate soft material characterization via inertial cavitation.* Journal of the Mechanics and Physics of Solids, 2018. **112**: p. 291-317.

28.   Kang, W., et al., *Cavitation nucleation in gelatin: Experiment and mechanism.* Acta Biomaterialia, 2018. **67**: p. 295-306.

29.   Kang, W. and M. Raphael, *Acceleration-induced pressure gradients and cavitation in soft biomaterials.* Scientific Reports, 2018. **8**(1): p. 15840.

30.   Jansen, L.E., et al., *Mechanics of intact bone marrow.* Journal of the Mechanical Behavior of Biomedical Materials, 2015. **50**: p. 299-307.

31.   Zimberlin, J.A., et al., *Cavitation rheology for soft materials.* Soft Matter, 2007. **3**(6): p. 763-767.

32.   Kang, W., et al., *Characterization and detection of acceleration-induced cavitation in soft materials using a drop-tower-based integrated system.* Review of Scientific Instruments, 2017. **88**(12): p. 125113.

33.   Kang, W., et al., *Mechanisms of cell damage due to mechanical impact: an in vitro investigation.* Scientific Reports, 2020. **10**(1): p. 12009.

34.   Santucci, R.A. and Y.J. Chang, *Ballistics for physicians: myths about wound ballistics and gunshot injuries.* J Urol, 2004. **171**(4): p. 1408-14.

35.   Maiden, N., *Ballistics reviews: mechanisms of bullet wound trauma.* Forensic Sci Med Pathol, 2009. **5**(3): p. 204-9.

36.   Crisco, J.J., et al., *Magnitude of head impact exposures in individual collegiate football players.* Journal of applied biomechanics, 2012. **28**(2): p. 174-183.

37.   Morse, J.D., et al., *An experimental and numerical investigation of head dynamics due to stick impacts in girls' lacrosse.* Ann Biomed Eng, 2014. **42**(12): p. 2501-11.

38.   Meaney, D.F., B. Morrison, and C. Dale Bass, *The mechanics of traumatic brain injury: a review of what we know and what we need to know for reducing its societal burden.* J Biomech Eng, 2014. **136**(2): p. 021008.

39.   Chen, H., et al., *Blood vessel deformations on microsecond time scales by ultrasonic cavitation.* Phys Rev Lett, 2011. **106**(3): p. 034301.

40.   Chen, H., et al., *Blood vessel rupture by cavitation.* Urol Res, 2010. **38**(4): p. 321-6.

41.   III, B.M., et al., *In Vitro Models of Traumatic Brain Injury.* Annual Review of Biomedical Engineering, 2011. **13**(1): p. 91-126.

42. Hemphill, Matthew A., et al., *Traumatic Brain Injury and the Neuronal Microenvironment: A Potential Role for Neuropathological Mechanotransduction.* Neuron, 2015. **85**(6): p. 1177-1192.

43. (CDC), C.f.D.C.a.P., *Sports-related recurrent brain injuries--United States.* MMWR Morb Mortal Wkly Rep, 1997. **46**(10): p. 224-7.

44. Thurman, D.J., C.M. Branche, and J.E. Sniezek, *The epidemiology of sports-related traumatic brain injuries in the United States: recent developments.* J Head Trauma Rehabil, 1998. **13**(2): p. 1-8.

45. Kleiven, S., *Why Most Traumatic Brain Injuries are Not Caused by Linear Acceleration but Skull Fractures are.* Frontiers in Bioengineering and Biotechnology, 2013. **1**(15).

46. Gennarelli, T.A., L.E. Thibault, and D.I. Graham, *Diffuse Axonal Injury: An Important Form of Traumatic Brain Damage.* The Neuroscientist, 1998. **4**(3): p. 202-215.

47. Gennarelli, T.A., et al., *Diffuse axonal injury and traumatic coma in the primate.* Annals of Neurology, 1982. **12**(6): p. 564-574.

48. Thibault, L.E. and T.A. Gennarelli, *Biomechanics of Diffuse Brain Injuries*. 1985, National Highway Traffic Safety Administration.

49. Gennarelli, T.A. and L.E. Thibault, *Biomechanics of acute subdural hematoma.* The Journal of trauma, 1982. **22**(8): p. 680-686.

50. Cairns, H. and H. Holbourn, *Head Injuries in Motor-cyclists: with Special Reference to Crash Helmets.* British medical journal, 1943. **1**(4297): p. 591-598.

51. Morrison B 3rd, C.H., Wang CC, Thomas FC, Hung CT, Ateshian GA, Sundstrom LE., *A Tissue Level Tolerance Criterion for Living Brain Developed with an In Vitro Model of Traumatic Mechanical Loading.* Stapp Car Crash Journal, 2003. **47**: p. 93-105.

52. Bain , A.C. and D.F. Meaney, *Tissue-Level Thresholds for Axonal Damage in an Experimental Model of Central Nervous System White Matter Injury.* Journal of Biomechanical Engineering, 2000. **122**(6): p. 615-622.

53. Gennarelli, T.A., et al., *Axonal injury in the optic nerve: a model simulating diffuse axonal injury in the brain.* Journal of Neurosurgery, 1989. **71**(2): p. 244-253.

54. Shreiber, D.I., A.C. Bain, and D.F. Meaney, *In Vivo Thresholds for Mechanical Injury to the Blood-Brain Barrier.* SAE Transactions, 1997. **106**: p. 3792-3806.

55.   Gross, A.G., *A New Theory on the Dynamics of Brain Concussion and Brain Injury.* Journal of Neurosurgery, 1958. **15**(5): p. 548-561.

56.   Adhikari, U., A. Goliaei, and M.L. Berkowitz, *Nanobubbles, cavitation, shock waves and traumatic brain injury.* Physical Chemistry Chemical Physics, 2016. **18**(48): p. 32638-32652.

57.   Haniff, S. and P.A. Taylor, *In silico investigation of blast-induced intracranial fluid cavitation as it potentially leads to traumatic brain injury.* Shock Waves, 2017. **27**: p. 929.

58.   Jeffrey, P., *Influence of Rotational Acceleration on Intracranial Mechanical Parameters Under Accidental circumstances*, in *Head Injury Biomechanics: Volume 2 the Brain*. 2011, SAE. p. 55-67.

59.   Huang, H.M., et al., *Finite element analysis of brain contusion: an indirect impact study.* Med Biol Eng Comput, 2000. **38**(3): p. 253-9.

60.   Lang, J., et al., *Cavitation causes brain injury.* Physics of Fluids, 2021. **33**(3): p. 031908.

61.   Rowson, S., et al., *Linear and angular head acceleration measurements in collegiate football.* J Biomech Eng, 2009. **131**(6): p. 061016.

62.   Walilko, T.J., D.C. Viano, and C.A. Bir, *Biomechanics of the head for Olympic boxer punches to the face.* Br J Sports Med, 2005. **39**(10): p. 710-9.

63.   Blankenship K, E.R., Allison S, Murphy M, Isome H, *Shoulder-Fired Weapons with High Recoil Energy: Quantifying Injury and Shooting Performance.* Natick, MA: Army Research Institute of Environmental Medicine, 2004: p. 63p.

64.   Benzkofer, P.D., *Dynamic analysis of shoulder-fired weapons.* Proceedings of the U.S. Army symposium on gun dynamics,Rhode Island, Newport 1993. **7**.

65.   Fu, Y., et al., *Size-dependent inertial cavitation of soft materials.* Journal of the Mechanics and Physics of Solids, 2020. **137**: p. 103859.

66.   Rayleigh, L., *VIII. On the pressure developed in a liquid during the collapse of a spherical cavity.* The London, Edinburgh, and Dublin Philosophical Magazine and Journal of Science, 1917. **34**(200): p. 94-98.

67.   Plesset, M.S. and R.B. Chapman, *Collapse of an initially spherical vapour cavity in the neighbourhood of a solid boundary.* Journal of Fluid Mechanics, 1971. **47**(2): p. 283-290.

68.   Liu, L., Y. Fan, and W. Li, *Viscoelastic shock wave in ballistic gelatin behind soft body armor.* Journal of the Mechanical Behavior of Biomedical Materials, 2014. **34**: p. 199-207.

69.   Liu, L., et al., *A spherical cavity expansion model of large elastic deformation and its application to ballistic gelatin penetration problems.* International Journal of Impact Engineering, 2014. **71**: p. 106-116.

70.   Nayar, V.T., et al., *Elastic and viscoelastic characterization of agar.* Journal of the Mechanical Behavior of Biomedical Materials, 2012. **7**: p. 60-68.

71.   Barney, C.W., et al., *Cavitation in soft matter.* Proceedings of the National Academy of Sciences, 2020. **117**(17): p. 9157-9165.

72.   Gozna, E.R., et al., *Mechanical properties of the ascending thoracic aorta of man1.* Cardiovascular Research, 1973. **7**(2): p. 261-265.

73.   Riahi, R., et al., *Advances in wound-healing assays for probing collective cell migration.* J Lab Autom, 2012. **17**(1): p. 59-65.

74.   Pham, Q.P., U. Sharma, and A.G. Mikos, *Electrospinning of polymeric nanofibers for tissue engineering applications: a review.* Tissue Eng, 2006. **12**(5): p. 1197-211.

75.   Bryant, S.J., et al., *Photo-patterning of porous hydrogels for tissue engineering.* Biomaterials, 2007. **28**(19): p. 2978-2986.

76.   Feng, K., et al., *A Flexible Bidirectional Interface with Integrated Multimodal Sensing and Haptic Feedback for Closed-Loop Human–Machine Interaction.* Advanced Intelligent Systems. **n/a**(n/a): p. 2300291.

77.   Di, J., et al., *Stretch-triggered drug delivery from wearable elastomer films containing therapeutic depots.* ACS nano, 2015. **9**(9): p. 9407-9415.

78.   Kuth, S., et al., *Oxidized Hyaluronic Acid-Gelatin-Based Hydrogels for Tissue Engineering and Soft Tissue Mimicking.* Tissue Engineering Part C: Methods, 2022. **28**(7): p. 301-313.

79.   Basak, S., J. Nanda, and A. Banerjee, *Multi-stimuli responsive self-healing metallo-hydrogels: tuning of the gel recovery property.* Chemical communications, 2014. **50**(18): p. 2356-2359.

80.   Domke, J. and M. Radmacher, *Measuring the elastic properties of thin polymer films with the atomic force microscope.* Langmuir, 1998. **14**(12): p. 3320-3325.

81.   Moreno-Arotzena, O., et al., *Characterization of fibrin and collagen gels for engineering wound healing models.* Materials, 2015. **8**(4): p. 1636-1651.

82. Hong, Y., et al., *Localized tissue surrogate deformation due to controlled single bubble cavitation.* Experimental Mechanics, 2016. **56**: p. 97-109.

83. Snedeker, J.G., et al., *Strain-rate dependent material properties of the porcine and human kidney capsule.* Journal of biomechanics, 2005. **38**(5): p. 1011-1021.

84. Zhu, F., et al., *The mechanical behavior of biological tissues at high strain rates*, in *Military injury biomechanics: the cause and prevention of impact injuries*. 2017, CRC Press. p. 418.

85. Itagaki, H., et al., *Water-induced brittle-ductile transition of double network hydrogels.* Macromolecules, 2010. **43**(22): p. 9495-9500.

86. Sun, T.L., et al., *Physical hydrogels composed of polyampholytes demonstrate high toughness and viscoelasticity.* Nature materials, 2013. **12**(10): p. 932-937.

87. Ahmed, S., et al., *Brittle–ductile transition of double network hydrogels: Mechanical balance of two networks as the key factor.* Polymer, 2014. **55**(3): p. 914-923.

88. Prevost, T.P., et al., *Dynamic mechanical response of brain tissue in indentation in vivo, in situ and in vitro.* Acta biomaterialia, 2011. **7**(12): p. 4090-4101.

89. Zhang, Z., et al., *Contactless rheology of soft gels over a broad frequency range.* Physical Review Applied, 2022. **17**(6): p. 064045.

90. Field, J.E., et al., *Review of experimental techniques for high rate deformation and shock studies.* International journal of impact engineering, 2004. **30**(7): p. 725-775.

91. Xu, P., et al., *SHPB experimental method for ultra-soft materials in solution environment.* International Journal of Impact Engineering, 2022. **159**: p. 104051.

92. Tiwari, S., et al., *Seeded laser-induced cavitation for studying high-strain-rate irreversible deformation of soft materials.* Soft Matter, 2020. **16**(39): p. 9006-9013.

93. Luo, J.C., et al., *Laser cavitation rheology for measurement of elastic moduli and failure strain within hydrogels.* Scientific reports, 2020. **10**(1): p. 13144.

94. Chen, W., B. Zhang, and M. Forrestal, *A split Hopkinson bar technique for low-impedance materials.* Experimental mechanics, 1999. **39**: p. 81-85.

95. Song, B. and W. Chen, *One-dimensional dynamic compressive behavior of EPDM rubber.* Journal of Engineering Materials and Technology, 2003. **125**(3): p. 294-301.

96. Nie, H., et al., *A versatile split Hopkinson pressure bar using electromagnetic loading.* International Journal of Impact Engineering, 2018. **116**: p. 94-104.

97.   Chen, W., F. Lu, and B. Zhou, *A quartz-crystal-embedded split Hopkinson pressure bar for soft materials.* Experimental mechanics, 2000. **40**: p. 1-6.

98.   Chen, W., et al., *Dynamic compression testing of soft materials.* J. Appl. Mech., 2002. **69**(3): p. 214-223.

99.   Robles, V., et al., *Soft material perforation via double-bubble laser-induced cavitation microjets.* Physics of Fluids, 2020. **32**(4).

100.   Kang, W., et al., *Characterization and detection of acceleration-induced cavitation in soft materials using a drop-tower-based integrated system.* Review of Scientific Instruments, 2017. **88**(12).

101.   Kim, C., et al., *Mechanically induced cavitation in biological systems.* Life, 2021. **11**(6): p. 546.

102.   Funk, J.R., et al., *Validation of concussion risk curves for collegiate football players derived from HITS data.* Annals of biomedical engineering, 2012. **40**: p. 79-89.

103.   Thurman, D.J., *Traumatic brain injury in the United States; a report to Congress.* 1999.

104.   Jin, W., et al., *Mechanisms of blunt liver trauma patterns: An analysis of 53 cases.* Experimental and therapeutic medicine, 2013. **5**(2): p. 395-398.

105.   Ling, G., et al., *Explosive blast neurotrauma.* Journal of neurotrauma, 2009. **26**(6): p. 815-825.

106.   McKee, A.C., et al., *The first NINDS/NIBIB consensus meeting to define neuropathological criteria for the diagnosis of chronic traumatic encephalopathy.* Acta neuropathologica, 2016. **131**(1): p. 75-86.

107.   Xiong, Y., A. Mahmood, and M. Chopp, *Animal models of traumatic brain injury.* Nature Reviews Neuroscience, 2013. **14**(2): p. 128.

108.   Courtney, A. and M. Courtney, *The complexity of biomechanics causing primary blast-induced traumatic brain injury: a review of potential mechanisms.* Frontiers in neurology, 2015. **6**: p. 221.

109.   Elder, G.A., J.R. Stone, and S.T. Ahlers, *Effects of low-level blast exposure on the nervous system: is there really a controversy?* Frontiers in neurology, 2014. **5**: p. 269.

110.   Leung, L.Y., et al., *Blast related neurotrauma: a review of cellular injury.* Mol Cell Biomech, 2008. **5**(3): p. 155-168.

111.	Sawyer, T.W., et al., *Primary blast causes delayed effects without cell death in shell-encased brain cell aggregates.* Journal of neurotrauma, 2018. **35**(1): p. 174-186.

112.	McEntire, B.J. and P. Whitley, *Blunt Impact Performance Characteristics of the Advanced Combat Helmet and the Paratrooper and Infantry Personnel Armor System for Ground Troops Helmet.* 2005.

113.	Blankenship, K., et al., *SHOULDER-FIRED WEAPONS WITH HIGH RECOIL ENERGY: QUANTIFYING INJURY AND SHOOTING PERFORMANCE.* 2004.

114.	Jin, W., et al., *Mechanisms of blunt liver trauma patterns: An analysis of 53 cases.* Exp Ther Med, 2013. **5**(2): p. 395-398.

115.	Parks, R.W., E. Chrysos, and T. Diamond, *Management of liver trauma.* Br J Surg, 1999. **86**(9): p. 1121-35.

116.	Franck, C., *Microcavitation: the key to modeling blast traumatic brain injury?* Concussion, 2017. **2**(3): p. CNC47.

117.	Hong, Y., et al., *Localized Tissue Surrogate Deformation due to Controlled Single Bubble Cavitation.* Experimental Mechanics, 2016. **56**(1): p. 97-109.

118.	Sun, S., et al., *Characterization of Subcellular Responses Induced by Exposure of Microbubbles to Astrocytes.* J Neurotrauma, 2015. **32**(19): p. 1441-8.

119.	Chen, B., et al., *Astrocyte Viability and Functionality in Spatially Confined Microcavitation Zone.* ACS Appl Mater Interfaces, 2019.

120.	Canchi, S., et al., *Controlled single bubble cavitation collapse results in jet-induced injury in brain tissue.* Journal of the Mechanical Behavior of Biomedical Materials, 2017. **74**: p. 261-273.

121.	Kang, W., et al., *Characterization and detection of acceleration-induced cavitation in soft materials using a drop-tower-based integrated system.* Rev Sci Instrum, 2017. **88**(12): p. 125113.

122.	Kang, W., et al., *Cavitation nucleation in gelatin: Experiment and mechanism.* Acta Biomater, 2018. **67**: p. 295-306.

123.	Kang, W. and M. Raphael, *Acceleration-induced pressure gradients and cavitation in soft biomaterials.* Sci Rep, 2018. **8**(1): p. 15840.

124.	Lai, E.S., et al., *Aligned nanofibrillar collagen regulates endothelial organization and migration.* Regenerative Medicine, 2012. **7**(5): p. 649-661.

125.   Ohta, S., S. Inasawa, and Y. Yamaguchi, *Alignment of vascular endothelial cells as a collective response to shear flow.* Journal of Physics D: Applied Physics, 2015. **48**(24): p. 245401.

126.   Lipowsky, R., *Remodeling of Membrane Shape and Topology by Curvature Elasticity and Membrane Tension.* Advanced Biology, 2022. **6**(1): p. 2101020.

127.   Sens, P. and J. Plastino, *Membrane tension and cytoskeleton organization in cell motility.* Journal of Physics: Condensed Matter, 2015. **27**(27): p. 273103.

128.   Morris, C.E. and U. Homann, *Cell Surface Area Regulation and Membrane Tension.* The Journal of Membrane Biology, 2001. **179**(2): p. 79-102.

129.   Harrison, R.G., *The reaction of embryonic cells to solid structures.* Journal of Experimental Zoology, 1914. **17**(4): p. 521-544.

130.   Weiss, P., *Experiments on cell and axon orientation in vitro; the role of colloidal exudates in tissue organization.* J Exp Zool, 1945. **100**: p. 353-86.

131.   Dunn, G.A. and J.P. Heath, *A new hypothesis of contact guidance in tissue cells.* Exp Cell Res, 1976. **101**(1): p. 1-14.

132.   Gadegaard, N., S. Mosler, and N.B. Larsen, *Biomimetic Polymer Nanostructures by Injection Molding.* Macromolecular Materials and Engineering, 2003. **288**(1): p. 76-83.

133.   Newgreen, D.F., *Physical influences on neural crest cell migration in avian embryos: contact guidance and spatial restriction.* Dev Biol, 1989. **131**(1): p. 136-48.

134.   Li, J., J. Chen, and R. Kirsner, *Pathophysiology of acute wound healing.* Clin Dermatol, 2007. **25**(1): p. 9-18.

135.   Friedl, P. and S. Alexander, *Cancer invasion and the microenvironment: plasticity and reciprocity.* Cell, 2011. **147**(5): p. 992-1009.

136.   Lynch, K.J., O. Skalli, and F. Sabri, *Investigation of surface topography and stiffness on adhesion and neurites extension of PC12 cells on crosslinked silica aerogel substrates.* PLoS One, 2017. **12**(10): p. e0185978.

137.   Kurniawan, N.A., *The ins and outs of engineering functional tissues and organs: evaluating the in-vitro and in-situ processes.* Curr Opin Organ Transplant, 2019. **24**(5): p. 590-597.

138.   Clark, P., et al., *Topographical control of cell behaviour: II. Multiple grooved substrata.* Development, 1990. **108**(4): p. 635-44.

139. Fraser, S.A., et al., *Sub-micron and nanoscale feature depth modulates alignment of stromal fibroblasts and corneal epithelial cells in serum-rich and serum-free media.* Journal of Biomedical Materials Research Part A, 2008. **86A**(3): p. 725-735.

140. Teixeira, A.I., et al., *Epithelial contact guidance on well-defined micro- and nanostructured substrates.* J Cell Sci, 2003. **116**(Pt 10): p. 1881-92.

141. Lee, G., et al., *Contact guidance and collective migration in the advancing epithelial monolayer.* Connective Tissue Research, 2018. **59**(4): p. 309-315.

142. Tamiello, C., et al., *Heading in the Right Direction: Understanding Cellular Orientation Responses to Complex Biophysical Environments.* Cellular and Molecular Bioengineering, 2016. **9**(1): p. 12-37.

143. Maiuri, P., et al., *Actin Flows Mediate a Universal Coupling between Cell Speed and Cell Persistence.* Cell, 2015. **161**(2): p. 374-386.

144. Ray, A., et al., *Anisotropic forces from spatially constrained focal adhesions mediate contact guidance directed cell migration.* Nature Communications, 2017. **8**.

145. Wieringa, P., et al., *Nanotopography induced contact guidance of the F11 cell line during neuronal differentiation: a neuronal model cell line for tissue scaffold development.* Nanotechnology, 2012. **23**(27): p. 275102.

146. Loesberg, W.A., et al., *The threshold at which substrate nanogroove dimensions may influence fibroblast alignment and adhesion.* Biomaterials, 2007. **28**(27): p. 3944-3951.

147. denBraber, E.T., et al., *Quantitative analysis of fibroblast morphology on microgrooved surfaces with various groove and ridge dimensions.* Biomaterials, 1996. **17**(21): p. 2037-2044.

148. Refaaq, F.M., X. Chen, and S.W. Pang, *Effects of topographical guidance cues on osteoblast cell migration.* Scientific Reports, 2020. **10**(1): p. 20003.

149. Tan, J. and W. Mark Saltzman, *Topographical control of human neutrophil motility on micropatterned materials with various surface chemistry*, in *The Biomaterials: Silver Jubilee Compendium*, D.F. Williams, Editor. 2002, Elsevier Science: Oxford. p. 191-201.

150. Liliensiek, S.J., et al., *Modulation of human vascular endothelial cell behaviors by nanotopographic cues.* Biomaterials, 2010. **31**(20): p. 5418-26.

151. Tang, Q.Y., et al., *Control of cell migration direction by inducing cell shape asymmetry with patterned topography.* Journal of Biomedical Materials Research Part A, 2015. **103**(7): p. 2383-2393.

152. Zhou, S.F., et al., *Substrates with patterned topography reveal metastasis of human cancer cells.* Biomedical Materials, 2017. **12**(5): p. 055001.

153. Pot, S.A., et al., *Nanoscale topography-induced modulation of fundamental cell behaviors of rabbit corneal keratocytes, fibroblasts, and myofibroblasts.* Invest Ophthalmol Vis Sci, 2010. **51**(3): p. 1373-81.

154. Leclech, C. and C. Villard, *Cellular and Subcellular Contact Guidance on Microfabricated Substrates.* Front Bioeng Biotechnol, 2020. **8**: p. 551505.

155. Crouch, A.S., et al., *Correlation of anisotropic cell behaviors with topographic aspect ratio.* Biomaterials, 2009. **30**(8): p. 1560-1567.

156. Biela, S.A., et al., *Different sensitivity of human endothelial cells, smooth muscle cells and fibroblasts to topography in the nano–micro range.* Acta Biomaterialia, 2009. **5**(7): p. 2460-2466.

157. Bainbridge, P., *Wound healing and the role of fibroblasts.* J Wound Care, 2013. **22**(8): p. 407-8, 410-12.

158. Evans, M.J., et al., *Attenuated fibroblast sheath around the basement membrane zone in the trachea.* Am J Respir Cell Mol Biol, 1993. **8**(2): p. 188-92.

159. Meyle, J., et al., *Fibroblast Shape Conformation to Surface Micromorphology.* Journal of Applied Biomaterials, 1991. **2**(4): p. 273-276.

160. Zhou, X., et al., *Cells cultured on microgrooves with or without surface coating: correlation between cell alignment, spreading and local membrane deformation.* Mater Sci Eng C Mater Biol Appl, 2013. **33**(2): p. 855-63.

161. Ingber, D.E., *Cellular tensegrity: defining new rules of biological design that govern the cytoskeleton.* J Cell Sci, 1993. **104 (Pt 3)**: p. 613-27.

162. Hohn, H.P., U. Steih, and H.W. Denker, *A novel artificial substrate for cell culture: effects of substrate flexibility/malleability on cell growth and morphology.* In Vitro Cell Dev Biol Anim, 1995. **31**(1): p. 37-44.

163. Robitaille, M.C., et al., *Monolithic quartz platform for cellular contact guidance.* Mrs Communications, 2020. **10**(2): p. 242-251.

164. Pervin, F. and W.W. Chen. *Mechanically Similar Gel Simulants for Brain Tissues.* in *Dynamic Behavior of Materials, Volume 1*. 2011. New York, NY: Springer New York.

165. Singh, D., S. Boakye-Yiadom, and D.S. Cronin, *Comparison of porcine brain mechanical properties to potential tissue simulant materials in quasi-static and sinusoidal compression.* Journal of Biomechanics, 2019. **92**: p. 84-91.

166. Mercey, E., et al., *The application of 3D micropatterning of agarose substrate for cell culture and in situ comet assays.* Biomaterials, 2010. **31**(12): p. 3156-3165.

167. Ulrich, T.A., et al., *Probing cellular mechanobiology in three-dimensional culture with collagen–agarose matrices.* Biomaterials, 2010. **31**(7): p. 1875-1884.

168. W M Tian, S.P.H., J Ma, C L Zhang, Q Y Xu, I S Lee, H D Li, M Spector, F Z Cui, *Hyaluronic Acid–Poly-D-Lysine-Based Three-Dimensional Hydrogel for Traumatic Brain Injury.* Tissue Engineering, 2005. **11**(3-4): p. 513-525.

169. Normand, V., et al., *New Insight into Agarose Gel Mechanical Properties.* Biomacromolecules, 2000. **1**(4): p. 730-738.

170. Ichinose, N. and H. Ura, *Concentration dependence of the sol-gel phase behavior of agarose-water system observed by the optical bubble pressure tensiometry.* Scientific Reports, 2020. **10**(1): p. 2620.

171. Normand, V., et al., *Gelation Kinetics of Gelatin: A Master Curve and Network Modeling.* Macromolecules, 2000. **33**(3): p. 1063-1071.

172. Pokusaev, B., et al., *Thermokinetics and rheology of agarose gel applied to bioprinting technology.* Thermal Science, 2019. **24**: p. 453-453.

173. Oates, C.G., P.W. Lucas, and W.P. Lee, *How brittle are gels?* Carbohydrate Polymers, 1993. **20**(3): p. 189-194.

174. Kwon, H.J., A.D. Rogalsky, and D.-W. Kim, *On the measurement of fracture toughness of soft biogel.* Polymer Engineering & Science, 2011. **51**(6): p. 1078-1086.

175. Markidou, A., W.Y. Shih, and W.-H. Shih, *Soft-materials elastic and shear moduli measurement using piezoelectric cantilevers.* Review of Scientific Instruments, 2005. **76**(6): p. 064302.

176. Schrieber, R., *Edible gelatin: types properties, use and application in the food industry.* Gordian, 1976: p. 356, 358, 360, 362, 364.

177. Baumberger, T. and C. Caroli, *Solid friction from stick–slip down to pinning and aging.* Advances in Physics, 2006. **55**(3-4): p. 279-348.

178. Czerner, M., et al., *Deformation and fracture behavior of physical gelatin gel systems.* Food Hydrocolloids, 2016. **60**: p. 299-307.

179. Haug, I.J. and K.I. Draget, *Gelatin.* 2009, Woodhead Publishing Ltd: Cambridge. p. 142-163.

180. Elharfaoui, N., M. Djabourov, and W. Babel, *Molecular Weight Influence on Gelatin Gels: Structure, Enthalpy and Rheology.* Macromolecular Symposia, 2007. **256**(1): p. 149-157.

181. Liu, L., et al., *Analytical and experimental studies on the strain rate effects in penetration of 10wt % ballistic gelatin.* Journal of Physics: Conference Series, 2013. **451**: p. 012035.

182. Gaudron, R., M.T. Warnez, and E. Johnsen, *Bubble dynamics in a viscoelastic medium with nonlinear elasticity.* Journal of Fluid Mechanics, 2015. **766**: p. 54-75.

183. Hamaguchi, F. and K. Ando, *Linear oscillation of gas bubbles in a viscoelastic material under ultrasound irradiation.* Physics of Fluids, 2015. **27**(11): p. 113103.

184. Zhu, J., et al., *Snap-through Expansion of a Gas Bubble in an Elastomer.* The Journal of Adhesion, 2011. **87**(5): p. 466-481.

185. Movahed, P., et al., *Cavitation-induced damage of soft materials by focused ultrasound bursts: A fracture-based bubble dynamics model.* The Journal of the Acoustical Society of America, 2016. **140**(2): p. 1374-1386.

186. Hauner, I.M., et al., *The Dynamic Surface Tension of Water.* The Journal of Physical Chemistry Letters, 2017. **8**(7): p. 1599-1603.

187. Hutchens, S.B., S. Fakhouri, and A.J. Crosby, *Elastic cavitation and fracture via injection.* Soft Matter, 2016. **12**(9): p. 2557-2566.

188. Raayai-Ardakani, S., D.R. Earl, and T. Cohen, *The intimate relationship between cavitation and fracture.* Soft Matter, 2019. **15**(25): p. 4999-5005.

189. Kang, J., C. Wang, and S. Cai, *Cavitation to fracture transition in a soft solid.* Soft Matter, 2017. **13**(37): p. 6372-6376.

190. Lin, Y.Y. and C.Y. Hui, *Cavity growth from crack-like defects in soft materials.* International Journal of Fracture, 2004. **126**(3): p. 205-221.

191. Gent, A.N. and C. Wang, *Fracture mechanics and cavitation in rubber-like solids.* Journal of Materials Science, 1991. **26**(12): p. 3392-3395.

192. Canchi, S., et al., *Controlled single bubble cavitation collapse results in jet-induced injury in brain tissue.* J Mech Behav Biomed Mater, 2017. **74**: p. 261-273.

193. Marsh, J.L. and S.A. Bentil, *Cerebrospinal Fluid Cavitation as a Mechanism of Blast-Induced Traumatic Brain Injury: A Review of Current Debates, Methods, and Findings.* Frontiers in Neurology, 2021. **12**(325).

194. Panzer, M.B., et al., *Development of a finite element model for blast brain injury and the effects of CSF cavitation.* Ann Biomed Eng, 2012. **40**(7): p. 1530-44.

195. Bass, C.R., et al., *Brain injuries from blast.* Ann Biomed Eng, 2012. **40**(1): p. 185-202.

196. Lubock, P. and W. Goldsmith, *Experimental cavitation studies in a model head-neck system.* Journal of Biomechanics, 1980. **13**(12): p. 1041-1052.

197. Malisa Sarntinoranont, S.J.L., Yu Hong, Michael A King, Ghatu Subhash, Jiwoon Kwon, David F Moore, *High-Strain-Rate Brain Injury Model Using Submerged Acute Rat Brain Tissue Slices.* Journal of Neurotrauma, 2012. **29**(2): p. 418-429.

198. Robert S. Salzar, D.T., Andrew Wardlaw, Greg Weiss, and Jacques Goeller, *Experimental Investigation of Cavitation as a Possible Damage Mechanism in Blast-Induced Traumatic Brain Injury in Post-Mortem Human Subject Heads.* Journal of Neurotrauma, 2017. **34**(8): p. 1589-1602.

199. Kraft, R.H., et al., *Combining the Finite Element Method with Structural Connectome-based Analysis for Modeling Neurotrauma: Connectome Neurotrauma Mechanics.* PLOS Computational Biology, 2012. **8**(8): p. e1002619.

200. Toma, M., et al., *Mechanism of Coup and Contrecoup Injuries Induced by a Knock-Out Punch.* Mathematical and Computational Applications, 2020. **25**(2): p. 22.

201. Kurosawa, Y., et al., *Basic study of brain injury mechanism caused by cavitation.* Annu Int Conf IEEE Eng Med Biol Soc, 2009. **2009**: p. 7224-7.

202. Goeller, J., et al., *Investigation of cavitation as a possible damage mechanism in blast-induced traumatic brain injury.* J Neurotrauma, 2012. **29**(10): p. 1970-81.

203. Budde, M., et al., *Primary Blast Traumatic Brain Injury in the Rat: Relating Diffusion Tensor Imaging and Behavior.* Frontiers in Neurology, 2013. **4**(154).

204. Sundaramurthy, A., et al., *Blast-induced biomechanical loading of the rat: an experimental and anatomically accurate computational blast injury model.* J Neurotrauma, 2012. **29**(13): p. 2352-64.

205. Hayes, J.P., et al., *The nature of white matter abnormalities in blast-related mild traumatic brain injury.* NeuroImage: Clinical, 2015. **8**: p. 148-156.

206. Riedy, G., et al., *Findings from Structural MR Imaging in Military Traumatic Brain Injury.* Radiology, 2016. **279**(1): p. 207-215.

207. Huang, A.P.-H., et al., *Cavitation-induced traumatic cerebral contusion and intracerebral hemorrhage in the rat brain by using an off-the-shelf clinical shockwave device.* Scientific Reports, 2019. **9**(1): p. 15614.

208. Estrada, J.B., et al., *Neural cell injury pathology due to high-rate mechanical loading.* Brain Multiphysics, 2021. **2**: p. 100034.

209. Wrede, A.H., et al., *Characterization of Astrocytic Response after Experiencing Cavitation In Vitro.* Global Challenges, 2020. **4**(7): p. 1900014.

210. Pernodet, N., M. Maaloum, and B. Tinland, *Pore size of agarose gels by atomic force microscopy.* Electrophoresis, 1997. **18**(1): p. 55-8.

211. Van Vlierberghe, S., et al., *Porous Gelatin Hydrogels: 1. Cryogenic Formation and Structure Analysis.* Biomacromolecules, 2007. **8**(2): p. 331-337.

212. Liu, X. and P.X. Ma, *Phase separation, pore structure, and properties of nanofibrous gelatin scaffolds.* Biomaterials, 2009. **30**(25): p. 4094-4103.

213. Mancia, L., et al., *Acoustic cavitation rheometry.* Soft Matter, 2021. **17**(10): p. 2931-2941.

214. Larson, K., *Can You Estimate Modulus From Durometer Hardness for Silicones? Yes, but only roughly … and you must choose your modulus carefully!* 2017.

215. Pervin, F. and W.W. Chen. *Mechanically similar gel simulants for brain tissues.* in *Dynamic Behavior of Materials, Volume 1: Proceedings of the 2010 Annual Conference on Experimental and Applied Mechanics*. 2011. Springer.

216. Daniel, R.W., S. Rowson, and S.M. Duma, *Head impact exposure in youth football.* Ann Biomed Eng, 2012. **40**(4): p. 976-81.

217. Urban, J.E., et al., *Head impact exposure in youth football: high school ages 14 to 18 years and cumulative impact analysis.* Ann Biomed Eng, 2013. **41**(12): p. 2474-87.

218. MacManus, D.B., et al., *A viscoelastic analysis of the P56 mouse brain under large-deformation dynamic indentation.* Acta Biomaterialia, 2017. **48**: p. 309-318.

219. Wilcox, B.J., et al., *Biomechanics of head impacts associated with diagnosed concussion in female collegiate ice hockey players.* Journal of biomechanics, 2015. **48**(10): p. 2201-2204.

220. Boulet, T., M.L. Kelso, and S.F. Othman, *Long-term in vivo imaging of viscoelastic properties of the mouse brain after controlled cortical impact.* Journal of neurotrauma, 2013. **30**(17): p. 1512-1520.

221. Slemmer, J.E., et al., *Repeated mild injury causes cumulative damage to hippocampal cells.* Brain, 2002. **125**(12): p. 2699-2709.

222.   Walker, A., et al., *Repeated in vitro impact conditioning of astrocytes decreases the expression and accumulation of extracellular matrix.* Annals of biomedical engineering, 2019. **47**: p. 967-979.

223.   Kim, C., W.J. Choi, and W. Kang, *Cavitation nucleation and its ductile-to-brittle shape transition in soft gels under translational mechanical impact.* Acta Biomaterialia, 2022. **142**: p. 160-173.

224.   Morovati, V., A. Bahrololoumi, and R. Dargazany, *Fatigue-induced stress-softening in cross-linked multi-network elastomers: Effect of damage accumulation.* International Journal of Plasticity, 2021. **142**: p. 102993.

225.   Munson, B.R., D.F. Young, and T.H. Okiishi, *fundamentals of fluid mechanics.* 4 ed. 2001: Wiley.

226.   Freshney, R.I., *Culture of animal cells: a manual of basic technique.* 17th ed. 2005, Hoboken, NJ: Wiley-Liss.

227.   Kumar, V., A. Abbas, and J. Aster, *Robbins Basic Pathology.* 2017, Elsevier: Philadelphia, PA.

228.   Walker, K.R. and G. Tesco, *Molecular mechanisms of cognitive dysfunction following traumatic brain injury.* Frontiers in Aging Neuroscience, 2013. **5**.

229.   Bar-Kochba, E., et al., *Strain and rate-dependent neuronal injury in a 3D in vitro compression model of traumatic brain injury.* Scientific Reports, 2016. **6**.

230.   Lehnert, D., et al., *Cell behaviour on micropatterned substrata: limits of extracellular matrix geometry for spreading and adhesion.* J Cell Sci, 2004. **117**(Pt 1): p. 41-52.

231.   Xia, N., et al., *Directional control of cell motility through focal adhesion positioning and spatial control of Rac activation.* FASEB J, 2008. **22**(6): p. 1649-59.

232.   Stevenson, P.M. and A.M. Donald, *Identification of three regimes of behavior for cell attachment on topographically patterned substrates.* Langmuir, 2009. **25**(1): p. 367-376.

233.   Thakar, R.G., et al., *Cell-shape regulation of smooth muscle cell proliferation.* Biophys J, 2009. **96**(8): p. 3423-32.

234.   Chin, L., et al., *Mechanotransduction in cancer.* Curr Opin Chem Eng, 2016. **11**: p. 77-84.

235. Wang, X., et al., *Electrospun Micropatterned Nanocomposites Incorporated with Cu2S Nanoflowers for Skin Tumor Therapy and Wound Healing.* ACS Nano, 2017. **11**(11): p. 11337-11349.

236. Yang, Y., et al., *Influence of Cell Morphology on Mesenchymal Stem Cell Transfection.* ACS Applied Materials & Interfaces, 2019. **11**(2): p. 1932-1941.

237. Rhee, S., *Fibroblasts in three dimensional matrices: cell migration and matrix remodeling.* Experimental & Molecular Medicine, 2009. **41**(12): p. 858-865.

238. Cady, E., et al., *Micropatterning Decellularized ECM as a Bioactive Surface to Guide Cell Alignment, Proliferation, and Migration.* Bioengineering (Basel), 2020. **7**(3).

239. McKinley, K.L., et al., *Cellular aspect ratio and cell division mechanics underlie the patterning of cell progeny in diverse mammalian epithelia.* Elife, 2018. **7**.

240. Chew, S.Y., et al., *The effect of the alignment of electrospun fibrous scaffolds on Schwann cell maturation.* Biomaterials, 2008. **29**(6): p. 653-61.

241. Hoehme, S., et al., *Prediction and validation of cell alignment along microvessels as order principle to restore tissue architecture in liver regeneration.* Proc Natl Acad Sci U S A, 2010. **107**(23): p. 10371-6.

242. Aubin, H., et al., *Directed 3D cell alignment and elongation in microengineered hydrogels.* Biomaterials, 2010. **31**(27): p. 6941-6951.

243. Mauriello, E.M.F., et al., *Localization of a bacterial cytoplasmic receptor is dynamic and changes with cell-cell contacts.* Proceedings of the National Academy of Sciences, 2009. **106**(12): p. 4852-4857.

244. Buskermolen, A.B.C., et al., *Cellular Contact Guidance Emerges from Gap Avoidance.* Cell Rep Phys Sci, 2020. **1**(5): p. 100055.

245. Kim, J., et al., *The mechanics and dynamics of cancer cells sensing noisy 3D contact guidance.* Proceedings of the National Academy of Sciences, 2021. **118**(10): p. e2024780118.

246. Yim, E.K., et al., *Nanopattern-induced changes in morphology and motility of smooth muscle cells.* Biomaterials, 2005. **26**(26): p. 5405-13.

247. Hu, W., et al., *Effects of nanoimprinted patterns in tissue-culture polystyrene on cell behavior.* Journal of Vacuum Science & Technology B: Microelectronics and Nanometer Structures Processing, Measurement, and Phenomena, 2005. **23**(6): p. 2984-2989.

248. Charras, G. and E. Sahai, *Physical influences of the extracellular environment on cell migration.* Nature Reviews Molecular Cell Biology, 2014. **15**(12): p. 813-824.

249. Mayor, R. and S. Etienne-Manneville, *The front and rear of collective cell migration.* Nature Reviews Molecular Cell Biology, 2016. **17**(2): p. 97-109.

250. van Helvert, S., C. Storm, and P. Friedl, *Mechanoreciprocity in cell migration.* Nature Cell Biology, 2018. **20**(1): p. 8-20.

251. Park, J., D.H. Kim, and A. Levchenko, *Topotaxis: A New Mechanism of Directed Cell Migration in Topographic ECM Gradients.* Biophys J, 2018. **114**(6): p. 1257-1263.

252. George, S.P., et al., *Regulation of directional cell migration by membrane-induced actin bundling.* J Cell Sci, 2013. **126**(Pt 1): p. 312-26.

253. Lombardi, M.L., et al., *Traction force microscopy in Dictyostelium reveals distinct roles for myosin II motor and actin-crosslinking activity in polarized cell movement.* J Cell Sci, 2007. **120**(Pt 9): p. 1624-34.

254. Oakes, P.W., et al., *Neutrophil morphology and migration are affected by substrate elasticity.* Blood, 2009. **114**(7): p. 1387-95.

255. O'Brien, X.M., et al., *Technical advance: introducing a novel metric, directionality time, to quantify human neutrophil chemotaxis as a function of matrix composition and stiffness.* J Leukoc Biol, 2014. **95**(6): p. 993-1004.

256. Heo, C., et al., *Cellular behavior controlled by bio-inspired and geometry-tunable nanohairs.* Nanoscale, 2017. **9**(45): p. 17743-17751.

257. Kirk, T., A. Ahmed, and E. Rognoni, *Fibroblast Memory in Development, Homeostasis and Disease.* Cells, 2021. **10**(11).

258. Wu, P.-H., et al., *Three-dimensional cell migration does not follow a random walk.* Proceedings of the National Academy of Sciences, 2014. **111**(11): p. 3949-3954.

259. Sales, A., et al., *Cell Type-Dependent Integrin Distribution in Adhesion and Migration Responses on Protein-Coated Microgrooved Substrates.* ACS Omega, 2019.

260. Gorelik, R. and A. Gautreau, *Quantitative and unbiased analysis of directional persistence in cell migration.* Nature Protocols, 2014. **9**(8): p. 1931-1943.

261. Kaiser, J.P., A. Reinmann, and A. Bruinink, *The effect of topographic characteristics on cell migration velocity.* Biomaterials, 2006. **27**(30): p. 5230-41.

262. Mogilner, A. and B. Rubinstein, *The physics of filopodial protrusion.* Biophys J, 2005. **89**(2): p. 782-95.

263. Schäfer, C., et al., *The filopodium: a stable structure with highly regulated repetitive cycles of elongation and persistence depending on the actin cross-linker fascin.* Cell Adh Migr, 2011. **5**(5): p. 431-8.

264. Husainy, A.N., et al., *Robust patterns in the stochastic organization of filopodia.* BMC Cell Biology, 2010. **11**(1): p. 86.

265. Albuschies, J. and V. Vogel, *The role of filopodia in the recognition of nanotopographies.* Scientific reports, 2013. **3**(1): p. 1-9.

266. Pronk, S., P.L. Geissler, and D.A. Fletcher, *Limits of filopodium stability.* Physical review letters, 2008. **100**(25): p. 258102.

267. Murrell, M.P. and M.L. Gardel, *F-actin buckling coordinates contractility and severing in a biomimetic actomyosin cortex.* Proceedings of the National Academy of Sciences, 2012. **109**(51): p. 20820-20825.

268. Leijnse, N., L.B. Oddershede, and P.M. Bendix, *Helical buckling of actin inside filopodia generates traction.* Proceedings of the National Academy of Sciences, 2015. **112**(1): p. 136-141.

269. Leijnse, N., L.B. Oddershede, and P.M. Bendix, *An updated look at actin dynamics in filopodia.* Cytoskeleton, 2015. **72**(2): p. 71-79.

270. Fujita, S., M. Ohshima, and H. Iwata, *Time-lapse observation of cell alignment on nanogrooved patterns.* Journal of the Royal Society Interface, 2009. **6**(suppl_3): p. S269-S277.

271. Bettinger, C.J., R. Langer, and J.T. Borenstein, *Engineering substrate topography at the micro-and nanoscale to control cell function.* Angewandte Chemie International Edition, 2009. **48**(30): p. 5406-5415.

272. Chang, K., et al., *Filopodia and viruses: an analysis of membrane processes in entry mechanisms.* Frontiers in microbiology, 2016. **7**: p. 300.

273. Dunn, G. and J. Heath, *A new hypothesis of contact guidance in tissue cells.* Experimental cell research, 1976. **101**(1): p. 1-14.

274. Jang, K.-J., et al., *Two distinct filopodia populations at the growth cone allow to sense nanotopographical extracellular matrix cues to guide neurite outgrowth.* PloS one, 2010. **5**(12): p. e15966.

275. Mattila, P.K. and P. Lappalainen, *Filopodia: molecular architecture and cellular functions.* Nature Reviews Molecular Cell Biology, 2008. **9**(6): p. 446-454.

276. Adebowale, K., et al., *Enhanced substrate stress relaxation promotes filopodia-mediated cell migration.* Nature materials, 2021. **20**(9): p. 1290-1299.

277. Song, K.H., et al., *T cells sense biophysical cues using lamellipodia and filopodia to optimize intraluminal path finding.* Integrative Biology, 2014. **6**(4): p. 450-459.

278. Leclech, C. and A.I. Barakat, *Is there a universal mechanism of cell alignment in response to substrate topography?* Cytoskeleton, 2021. **78**(6): p. 284-292.

279. Liang, E.I., et al., *Correlation of focal adhesion assembly and disassembly with cell migration on nanotopography.* Integr Biol (Camb), 2017. **9**(2): p. 145-155.